https://doi.org/10.15388/vu.thesis.983
https://orcid.org/0009-0005-7620-2199

VILNIUS UNIVERSITY
CENTER FOR PHYSICAL SCIENCES AND TECHNOLOGY

Evaldas Kažukauskas

Femtosecond Laser Ablation and Surface Roughness Control

DOCTORAL DISSERTATION

Natural Sciences
Physics (N 002)

VILNIUS 2026

This dissertation was written between 2022 and 2026 at Vilnius University Laser Research Center. The research was supported by the Research Council of Lithuania.

Academic Supervisor – Dr. Simas Butkus (Vilnius University, Natural Sciences, Physics, N 002).

Dissertation Defense Panel:

Chairman – Prof. Dr. Mikas Vengris (Vilnius University, Natural Sciences, Physics, N 002).

Members:
Prof. Dr. Saulius Juodkazis (Swinburne University of Technology, Natural Sciences, Physics, N 002),
Prof. Dr. Yves Bellouard (École Polytechnique Fédérale de Lausanne, Technology Sciences, Materials Engineering, T 008),
Dr. Gediminas Račiukaitis (Center for Physical Sciences and Technology, Natural Sciences, Physics, N 002),
Dr. Andrius Žemaitis (Center for Physical Sciences and Technology, Natural Sciences, Physics, N 002).

The dissertation shall be defended at a public meeting of the Dissertation Defense Panel at 15:00 on 22th of September 2026 in Room 306 at Laser Research Center.
Address: Saulėtekio al. 10, Laser Research Center, Room 306, Vilnius, Lithuania.
Tel. +370 5 236 6005;

https://doi.org/10.15388/vu.thesis.983
https://orcid.org/0009-0005-7620-2199

VILNIAUS UNIVERSITETAS
FIZINIŲ IR TECHNOLOGIJOS MOKSLŲ CENTRAS

Evaldas Kažukauskas

Femtosekundinė paviršių lazerinė abliacija ir medžiagų šiurkštumo kontrolė

DAKTARO DISERTACIJA

Gamtos mokslai
Fizika (N 002)

VILNIUS 2026

Disertacija rengta 2022–2026 metais Vilniaus universitete, Lazerinių tyrimų centre. Mokslinius tyrimus rėmė Lietuvos mokslo taryba.

Mokslinis vadovas – dr. Simas Butkus (Vilniaus universitetas, gamtos mokslai, fizika, N 002).

Gynimo taryba:

Pirmininkas - prof. dr. Mikas Vengris (Vilniaus universitetas, gamtos mokslai, fizika, N 002).

Nariai:
prof. dr. Saulius Juodkazis (Swinburne technologijų universitetas, gamtos mokslai, fizika, N 002),
prof. dr. Yves Bellouard (Lozanos politechnikos institutas, technologijos mokslai, medžiagų inžinerija, T 008),
dr. Gediminas Račiukaitis (Fizinių ir technologijos mokslų centras, gamtos mokslai, fizika, N 002),
dr. Andrius Žemaitis (Fizinių ir technologijos mokslų centras, gamtos mokslai, fizika, N 002).

Disertacija ginama viešame Gynimo tarybos posėdyje 2026 m. rugsėjo mėn. 22 d. 15:00 Lazerinių tyrimų centro 306 auditorijoje.
Adresas: Saulėtekio al. 10, Lazerinių tyrimų centras, 306 aud., Vilnius, Lietuva.
Tel. +370 5 236 6005;

CONTENTS

List of abbreviations **8**

Introduction **11**

Approbation **17**

1 Literature overview **22**

1.1 Surface roughness 22

1.1.1 Science and standards behind surface roughness 26

1.1.2 Parameters defining surface roughness 27

1.1.3 Guidelines for surface roughness assessment 32

1.1.4 Surface roughness measurement methods and their spatial resolution 41

1.2 Laser ablation 50

1.2.1 Linear absorption 50

1.2.2 Nonlinear absorption 52

1.2.3 Mechanisms of material removal 57

1.2.4 Laser-induced stress and rapid solidification 62

1.3 Attainable surface roughness levels after laser ablation 64

1.3.1 Different laser parameter impact on the surface quality after laser ablation 65

1.3.2 Different scanning strategy impact on the surface quality after laser ablation 71

2 Methodology **81**

2.1 Experimental setup and measurement equipment 81

2.2 Scanning techniques 84

2.3 Spectral analysis 85
2.4 Fractal analysis 88

3 Single-scan investigation **91**
3.1 Investigation framework 91
3.2 Laser ablation numerical model 94
3.3 Roughness dependence on the crater overlap 97
3.4 Other pulse positioning techniques 102
3.5 Summary 105

4 Multilayer ablation investigation **107**
4.1 Investigation framework 107
4.1.1 Multipulse exposure 109
4.2 Achieving stabilization of surface roughness 112
4.2.1 Rotation of the layers 112
4.2.2 Displacement of the layers 114
4.3 Control of the roughness stabilization level 117
4.4 Deep engraving with precise control of S_a 120
4.5 Summary 124

5 Spectral analysis of surface roughness evolution **126**
5.1 Investigation framework 126
5.2 Spectral analysis of S_q evolution from an initially smooth surface 129
5.3 Spectral analysis of S_q evolution from an initially rough surface 135
5.4 Spectral evolution of different texture components 139
5.5 Summary 144

6 Waviness formation during deep engraving: Origins and Mechanisms **146**
6.1 Investigation framework 147
6.2 Conditions for HALSFF formation 148
6.3 Acoustic wave propagation numerical model 154
6.4 The origins behind HALSFF formation 156
6.5 Methods to suppress HALSFF formation 160
6.6 Summary 162

7 Alternative laser-based surface roughness control method 163
7.1 Laser polishing 163
7.2 Laser polishing using bursts of femtosecond pulses 167
7.2.1 Investigation framework 168
7.2.2 Results 170
7.2.3 Summary 174
7.3 Non-thermal ablation 174

Outlooks 177

Main results and Conclusions 181

Santrauka lietuvių kalba 183

BIBLIOGRAPHY 197

Curriculum Vitae 214

Acknowledgements 216

List of abbreviations

IOL	Intraocular lens
PV	Peak-to-valley distance
WCA	Water contact angle
EDM	Electrical discharge machining
ISO	International Organization for Standardization
S-F surface	Surface after excluding spatial frequencies representing measurement noise and surface form
S-L surface	Surface after excluding all non-roughness spatial components
MPI	Multiphoton ionization
HAZ	Heat affected zone
UV	Ultraviolet part of the spectrum
IR	Infrared part of the spectrum
DOE	Diffractive optical element
SM	Sequential scanning method
IM	Interlacing scanning method
SEM	Scanning electron microscope
AFM	Atomic force microscope
FWHM	Full width at half maximum
FFT	Fast Fourier transform
RMS	Root mean square
RTC	Real time controller
LIPSS	Laser-induced periodic surface structures
FS	Fused Silica
PSD	Power spectral density
HALSFF	High-amplitude low-spatial-frequency features
TIS	Total integrated scattering
CW	Continuous wave
TCSPC	Time-correlated Single Photon Counting
MEMS	Micro-electro-mechanical systems
TPI	Tunneling ionization

Introduction

Surface machining for shape retrieval or change of its optical, chemical, mechanical, and other physical properties has garnered significant interest across numerous applications, with the size of the surface to be machined varying from microstructures to large surface areas. The biggest part of today's industry is based on conventional mechanical surface treatment methods such as CNC (computer numerical control) milling, turning, and abrasive polishing [1], although other more sophisticated methods like chemical treatment, electropolishing, or lithography have also found their place for smaller scale, more unique applications [2–4]. In recent decades, the development of powerful and reliable laser systems has introduced laser radiation as an attractive method for surface treatment of a wide range of materials. Compared to conventional techniques, laser-based processes offer several advantages, including high processing, precision, versatility, reduced tool wear, and others [5]. Further advancements in the development of femtosecond lasers introduced additional benefits such as reduced heat-affected zones and enhanced control over the modification structure [6]. Femtosecond laser ablation has been implemented across fields such as medicine, microfluidics, MEMS, and micro-optics [7–11] for both shallow surface modification and laser deep engraving. By performing only a few laser scans over the surface, a functional surface can be formed, exhibiting antibacterial or anti-icing behavior [12, 13]. In contrast, by selectively ablating the material layer by layer, the surface can be engraved to depths ranging from micrometers to millimeters, enabling the fabrication of precise, complex three-dimensional structures. The laser engraving technique is widely employed in the luxury goods industry for the precision engraving of watches and jewelry [14], where engraving depths often exceed 100 μm [15]. It is further utilized in the fabrication of complex, free-form molds [16] for casting and injection molding as well as medical components, including orthopedic implants [17],

where engraving depths ranging from several hundred micrometers to a few millimeters are required.

Alongside the ability to produce intricate geometries, laser engraving simultaneously affects the surface texture of the material being processed. The formed surface texture, which represents the entirety of surface spatial frequencies, including those corresponding to roughness, waviness, and other parts of the spectrum [18], dictates the majority of the surface's functionalities and properties. Numerous studies report that laser-induced surface roughness (representing the high-spatial-frequency part of the surface texture) can significantly influence the rate of corrosion [19, 20], wettability [21], biocompatibility [22], and other surface properties [23, 24]. However, unlocking specific surface properties necessitates attaining distinct levels of roughness. The formation of optical elements requires minimal roughness, as that is necessary to ensure surface transparency and minimize undesired scattering losses [25]. On the other hand, in the luxury goods industry, both glossy and matte surfaces are desired, which can be obtained by further tuning of surface roughness [26]. Other applications, like the formation of bacteria-repellent surfaces, require surface texture with a higher level of roughness ($R_q \approx 400$ nm) [27] to improve the adhesion of the cells. Whereas enhancing the heat dissipation efficiency of heat sinks requires an even higher level of surface roughness, with $R_a >> 1$ μm [28]. Such a level of roughness is also critical for enhancing the adhesion of paints or coatings [29]. The broad range of surface roughness levels necessary for the aforementioned applications underscores the critical need for precise surface roughness control during laser ablation. Without proper texture management, the engraved structure may fail to perform its intended function and be rendered unusable.

To address this challenge, numerous studies have investigated how various processing parameters, such as laser fluence, scanning speed, and pulse overlap, affect the final surface roughness during laser engraving [30–32]. Further insights were gained from studies examining how various scanning strategies impact final surface texture. The surface scanning approaches that included interlacing [33], radial scanning [34], rotation of the layers [35], and the displacement of the layers [36] have been tested on various materials to evaluate their respective advantages and limitations in controlling surface texture during laser engraving. Despite extensive research efforts, most studies examine roughness through parametric analyses confined to a narrow range of parameters

of interest, with a primary aim of identifying optimal conditions rather than gaining deeper insights into the formation and the development of surface texture. Hence, surface roughness after laser processing is still largely regarded as a byproduct of the process, an outcome defined by the values of laser parameters, rather than something that can be controlled or understood. Moreover, surface roughness in most of the studies is still predominantly assessed in terms of spatial parameters, such as R_a or S_a. At the same time, few studies provide clear details on the methods used for measuring roughness and the types of filters employed. As a result, analyses of surface roughness based solely on spatial parameters, without clear details behind their assessment, provide only limited information about the surface texture and may lead to misinterpretation of the results. The predominantly parametric nature of these studies, combined with the limited examination of surface texture, falls short of providing a comprehensive understanding of the mechanisms governing surface texture evolution and limits the ability to effectively control it. Thus, to address industrial demands that necessitate attaining diverse surface finishes, as well as broader technological and scientific needs, the control of surface roughness during laser ablation must be improved, which can only be achieved by gaining a deeper understanding into the development of surface texture.

The objective of the Thesis

This thesis seeks to investigate the physical mechanisms governing the formation of surface roughness and the evolution of surface texture during laser micro-machining, with the goal of achieving precise control over both roughness and texture.

The main tasks of the Thesis

- Investigate the formation of surface roughness during femtosecond laser ablation under single- and multi-pass scanning conditions, by considering roughness development in spatial and spectral domains.
- Investigate the ability to control surface roughness during femtosecond laser ablation through integrated approaches combining variations in scanning strategies and the adjustment of laser processing parameters.

- Investigate the evolution of surface roughness during femtosecond laser ablation, when the laser processing is applied on surfaces with different initial roughness levels.

Scientific novelty

The thesis provides new insights into the formation and development of surface roughness during femtosecond laser ablation, representing a novel contribution to the field of laser micromachining.

- This thesis presents the first demonstration of controlled surface roughness tuning during multilayer femtosecond laser ablation, enabling repeated, on-demand increase and reduction of roughness throughout the duration of deep engraving. This was accomplished through the development of novel laser processing strategies that integrate variations in scanning approaches with the use of diverse laser parameters.
- Through a detailed investigation of surface roughness evolution during laser processing, the fundamental limiting factor governing the minimum achievable roughness during femtosecond laser ablation was identified to be the formation of laser-induced periodic surface structures (LIPSS, commonly referred to as nanoripples), thereby contributing to a broader understanding of attainable roughness limits in laser ablation.
- The previously unexplored influence of initial surface roughness on its evolution during multilayer laser ablation was thoroughly investigated in this thesis, providing novel insights into its underlying mechanisms.
- Through experimental and numerical analysis, this thesis investigated the previously unknown origins behind the formation of high-amplitude, low-spatial-frequency features (commonly referred as waviness) during laser deep engraving, delivering the first systematic and qualitative explanation of their emergence.

Practical value

The generated knowledge and developed methods carry significant practical value and can be utilized for multiple applications, including but not limited to:

- Using precise control of surface roughness, surfaces featuring different transparency properties can be formed. Owing to the high precision of laser processing, the balance between transparency and scattering can be finely tuned, enabling the formation of diffusive and other surfaces.

- The achieved precise control of surface roughness enables the adjustment of roughness to a desired level, allowing for the optimization of bacteria-repellent or biocompatibility surface properties, which, according to the literature, are attained at specific roughness ranges.

- The developed precise control of surface roughness enables localized modification of surface texture, allowing adhesion properties to be enhanced in selected areas while reducing roughness in other regions. Practically, this is useful for enhancing bonding or coating adhesion only in targeted regions while preserving low-friction or anti-contamination properties in other areas, thereby improving the overall performance of the surface.

- Using precise control of surface roughness, it may be possible to form surfaces with different thermal emissivity but identical visual properties, targeting counter-theft applications. The developed capability to finely tune surface roughness enables the tailoring of surface properties sensitive to change in roughness, such as thermal emissivity, without affecting other, more inert characteristics, including visual appearance.

Statements to be defended

- In femtosecond laser ablation of glass materials, the lowest surface roughness is obtained at low crater overlap conditions, corresponding to overlap values of $\Omega_{x,y} \sim 10 - 25\%$.

- Precise ($\delta S_a = 20$ nm), on-demand control of surface roughness over a broad range of roughness values ($\Delta S_a \approx 500$ nm) can be achieved during multilayer femtosecond laser ablation by employing integrated approaches combining variations in scanning strategies - rotation of the layers and the displacement of the layers, and the adjustment of laser processing parameters, namely crater overlap $\Omega_{x,y}$, fluence F and wavelength λ.

- The surface roughness (S_q) evolution progression rate during femtosecond laser ablation depends on the initial surface spatial spectrum due to non-uniform attenuation rates of different spatial frequencies $k(f_r)$.
- High-amplitude (PV $\gtrsim$ 3 μm), low-spatial-frequency ($f \leq 3$ mm^{-1}) features formed during deep femtosecond laser engraving originate from the interaction between subsequent laser pulses and the residual acoustic field generated by the preceding laser–matter interactions.

Layout of the dissertation

The dissertation is divided into 7 main chapters. The first chapter provides the literature overview. It includes a detailed explanation of what surface roughness is and how it is measured, followed by a discussion of the main physical mechanisms underlying femtosecond laser ablation, and concludes with a summary of the surface roughness values achievable through laser ablation. The second chapter covers the main methodology behind the experiments performed in the thesis. The third chapter investigates the achievable surface roughness and its control through scanning algorithms during single-pass surface scanning. The fourth chapter extends the investigation to multilayer ablation and also presents methods for achieving precise control over surface roughness. The fifth chapter continues the investigation of surface roughness from a spectral perspective and presents results on roughness evolution when laser processing is performed on initially rough surfaces. The sixth chapter considers the formation of waviness during laser deep engraving, revealing the underlying physical mechanisms and presenting strategies for its prevention. Finally, the seventh chapter covers the alternative laser-based roughness control methods, which include laser polishing, burst polishing and non-thermal ablation.

Statement of contributions

The results presented in this thesis were generated at the Vilnius University Laser Research Center between 2022 and 2026 under the supervision of Simas Butkus. Although the majority of the experiments, data analysis, and manuscript preparations were carried out by the author himself, it is imperative to pay tribute to others who contributed to the thesis:

- **dr. Simas Butkus** supervised the thesis and made significant contributions to problem-solving, conceptualizing, research planning, and manuscript review.
- **dr. Vytautas Jukna** provided substantial support in numerical calculations, contributed greatly to the development of the numerical models, and took part in manuscript review.
- **prof. Domas Paipulas** contributed by providing the research environment and necessary tools, also took part in supervision and manuscript review.

- **Tadas Latvys** contributed to conducting the experiments and analyzing the data.

Approbation

List of publications on the dissertation topic

[A1] **E. Kažukauskas**, S. Butkus, V. Jukna, D. Paipulas, and V. Sirtukaitis, Scanning algorithm optimization for achieving low-roughness surfaces using ultrashort laser pulses: a comparative study, Mat. 16(7), 2788 (2023).

[A2] **E. Kažukauskas**, S. Butkus, V. Jukna, and D. Paipulas, Surface roughness control in deep engraving of fused silica using femtosecond laser ablation, Surf. and Interf. 50, 104471 (2024).

[A3] **E. Kažukauskas**, S. Butkus, T. Latvys, V. Jukna, and D. Paipulas, Spectral Domain Analysis of Surface Roughness Evolution during Femtosecond Laser Deep Engraving of Glass, Opt. Exp. 34, 10334-10350 (2026).

[A4] **E. Kažukauskas**, S. Butkus, T. Latvys, V. Jukna, and D. Paipulas, Low spatial frequency surface feature formation during femtosecond laser deep engraving: origins and mechanisms, Sci. Rep. 16, 22701 (2026).

Other publications

[B1] **E. Kažukauskas**, S. Butkus, P. Tokarski, V. Jukna, M. Barkauskas, and V. Sirtukaitis, Micromachining of Transparent Biocompatible Polymers Applied in Medicine Using Bursts of Femtosecond Laser Pulses, Micromac. 11(12), 1093 (2020).

[B2] S. Butkus, V. Jukna, **E. Kažukauskas**, Ž. Svirskas, D. Paipulas, and V. Sirutkaitis, High-contrast marking of stainless-steel using bursts of femtosecond laser pulses, Micromach. 14(1), 194 (2023).

Conference proceedings

[C1] **E. Kažukauskas**, S. Butkus, V. Jukna, D. Paipulas, and V. Sirutkaitis, Numerical simulations and experimental analysis of scanning techniques for low-roughness surfaces using UV femtosecond pulses, Proc. SPIE 12142, 1214219 (2022).

[C2] A. Vyšniauskas, **E. Kažukauskas**, and V. Stankevič, Generation and characterisation of different colors on 304 stainless steel using femtosecond laser pulses in GHz burst mode, Proc. Lim 2023, (2023).

[C3] D. Andriukaitis, V. Stankevič, **E. Kažukauskas**, and P. Gecys, Formation of through-glass vias (TGVs) in glass substrates using femtosecond laser operating in MHz/GHz burst mode, Proc. SPIE 13351, 1335102 (2025).

[C4] **E. Kažukauskas**, S. Butkus, V. Jukna, and D. Paipulas, Spectral domain analysis of surface roughness in deep-engraved surfaces, Proc. SPIE 13881, PC138810V (2026).

Conference presentations

Presented by the author

[D1] **E. Kažukauskas**, S. Butkus, V. Jukna, D. Paipulas, V. Sirutkaitis, Numerical simulations and experimental analysis of scanning techniques for low-roughness surfaces using UV femtosecond pulses, SPIE Photonics Europe 2022, April 3-7, 2022, Strasbourg, France, **POSTER presentation**.

[D2] **E. Kažukauskas**, S. Butkus, V. Jukna, D. Paipulas, V. Sirutkaitis, Numerical simulations and experimental analysis of scanning techniques for low-roughness surfaces using UV femtosecond pulses, Open Readings 2022, April 18-20, 2022, Vilnius, Lithuania, **ORAL presentation**.

[D3] **E. Kažukauskas**, S. Butkus, V. Jukna, D. Paipulas, V. Sirutkaitis, Numerical simulations and experimental analysis of scanning techniques for low-roughness surfaces using UV femtosecond pulses, LPM 2022, June 7-10, 2022, Dresden, Germany, **ORAL presentation**.

[D4] **E. Kažukauskas**, S. Butkus, V. Jukna, D. Paipulas, V. Sirutkaitis, Full control of surface roughness when engraving transparent materials using femtosecond laser ablation, LPM 2023, June 13-16, 2023, Hirosaki, Japan, **ORAL presentation**.

[D5] **E. Kažukauskas**, A. Vyšniauskas, V. Stankevič, High-quality laser cutting of heat-sensitive polymer materials using femtosecond laser pulses, LPM 2023, June 13-16, Hirosaki, Japan, 2023, **ORAL presentation**

[D6] **E. Kažukauskas**, S. Butkus, V. Jukna, D. Paipulas, V. Sirutkaitis, Full control of surface roughness when engraving transparent materials using femtosecond laser ablation, CLEO Europe 2023, June 26-30, 2023, Munich, Germany, **ORAL presentation**.

[D7] **E. Kažukauskas**, S. Butkus, V. Jukna, D. Paipulas, V. Sirutkaitis, Full control of surface roughness when engraving transparent materials using femtosecond laser ablation, 12th International Summer School "Trends and New Developments in Laser Technology", 28 August to 1 September, 2023, Dresden, Germany, **ORAL presentation**.

[D8] **E. Kažukauskas**, S. Butkus, V. Jukna, and D. Paipulas, Exploring the dynamic surface roughness evolution of fused silica under multilayer ablation conditions using femtosecond laser pulses, LPM 2024, June 11-14, 2024, San Sebastian, Spain, **ORAL presentation**.

[D9] **E. Kažukauskas**, S. Butkus, V. Jukna, and D. Paipulas, Exploring the dynamic surface roughness evolution of fused silica under multilayer ablation conditions using femtosecond laser pulses, UPLAMP 2024 summer school, July 1-6, 2024, Vilnius, Lithuania, **ORAL presentation**.

[D10] **E. Kažukauskas**, S. Butkus, V. Jukna, and D. Paipulas, Spectral domain analysis of surface roughness evolution in deep-engraved surfaces, LPM 2025, June 10-13, 2025, Ise, Japan, **ORAL presentation**.

[D11] **E. Kažukauskas**, S. Butkus, V. Jukna, T. Latvys and D. Paipulas, Spectral domain analysis of surface roughness evolution in deep-engraved surfaces, SPIE Photonics West 2026, January 17-22, 2026, San Fransico, California, US, **ORAL presentation**.

Other presentations

[E1] **E. Kažukauskas**, V. Jukna, V. Stankevič, High aspect ratio hole drilling in various glasses using long GHz burst packages, LPM 2024, June 11-14, San Sebastian, Spain, 2024, **ORAL presentation**

[E2] V. Stankevič, **E. Kažukauskas**, V. Jukna, A method for TGV Processing in Various Glasses with Burst Pulses Targeting Selective Metallization Applications, LPM 2024, June 11-14, San Sebastian, Spain, 2024, **ORAL presentation**

[E3] S. Butkus, **E. Kažukauskas**, D. Paipulas, Surface Roughness Control Using Femtosecond Laser Pulses and Different Scanning Strategies, EPIC meeting 2024, September 25-26,Vilnius, Lithuania, 2024, **ORAL presentation**

[E4] S. Butkus, **E. Kažukauskas**, Vytautas Jukna, Balys Momgaudis, and D. Paipulas, Numerical simulations on the ablation process and comparing with experimental results, PULMM 2025, June 29 - July 2, 2025, Villars-sur-Ollon, Switzerland, **ORAL presentation**

[E5] S. Butkus, **E. Kažukauskas**, Vytautas Jukna, Balys Momgaudis, and D. Paipulas, Digital Holography for Understanding Surface Roughness Evolution in Laser Deep Engraving, LIM 2025, June 23-26, Munich, Germany, 2025, **ORAL presentation**

[E6] A. Vyšniauskas, **E. Kažukauskas**, V. Stankevič, and P. Gečys, Inestigating efficient femtosecond laser processing conditions to enable the possibility of cold ablation in thin polyamide films, UPLAMP 2025, July 7-11, Vilnius, Lithuania, 2025, **ORAL presentation**

[E7] A. Vyšniauskas, **E. Kažukauskas**, V. Stankevič, and P. Gečys, Exploring parameter space for cold ablation in thin polymer film using femtosecond laser pulses, ICPEPA 2025, September 14-19, Lecce, Italy, 2025, **ORAL presentation**

Chapter 1

Literature overview

The thesis is centered around surface roughness and its control via laser ablation. For a qualitative analysis of the results, the overview of the fundamentals behind surface roughness, including definitions, methods of acquisition, and other aspects is imperative. Hence, this chapter aims to cover all essential information about surface roughness and how it is perceived in the context of laser micro-machining. Furthermore, the scope of the thesis is limited to laser machining and roughness analysis of dielectric materials, specifically soda-lime and fused silica glass. Accordingly, the fundamental principles of laser ablation of dielectric materials are also addressed in this chapter, with details on how different laser parameters influence final surface roughness. Finally, the attainable surface roughness levels during laser processing are listed with specifics of how they were acquired. This chapter lays the foundation for the chapters that follow, in which the main results are discussed.

1.1 Surface roughness

Surface roughness is a metric that characterizes the degree of roughness on a surface. It is quantified by the deviations in the direction of the normal vector of a real surface from its ideal form. If the deviations are large, the surface is considered to be rough. On the contrary, if the deviations are small, the surface is said to be smooth. The metric is linked to human physical and visual perception of the surface texture. The rough surfaces tend to exert higher levels of friction onto our fingers and may even result in physical damage. Low-roughness surfaces tend to have reduced resistance, often possess a more

appealing aesthetic appearance, and can exhibit higher levels of transparency. Furthermore, surface roughness not only governs human sensory perception but also significantly impacts various surface characteristics and functionalities.

For many types of metals, the roughness of the surface determines the rate of corrosion. It has been reported that an increase in the surface roughness of magnesium alloy AZ91 [37], stainless steel [19], copper [20], aluminium, and titanium-based alloys [38] increases the pitting susceptibility and general corrosion rate. Wettability is another surface attribute that is significantly affected by the surface roughness. Surface wettability is assessed through the measurement of the contact angle formed by a droplet when placed on the surface under examination. The relationship between roughness and wettability was first defined in 1936 by Wenzel, who stated that an increase in surface roughness enhances wettability due to increased of effective contact area [39]. The notion of roughness affecting the contact angle was further extended by Cassie and Baxter in 1944 when they focused on porous media, where liquid does not penetrate the grooves on rough surfaces and leaves air gaps [40]. The well-established theories have been experimentally verified on numerous occasions, demonstrating a robust correlation between surface roughness and surface wetting characteristics [21, 41–43]. What's more, it has been shown that surface roughness has a significant influence on the friction and wear rate of surfaces. The literature presents conflicting opinions on this matter, therefore, a single trend cannot be identified. The two-body shearing friction investigation at the atomic scale using molecular dynamics demonstrated that an elevation in surface roughness results in a higher friction coefficient [44], in a case when roughness R_a < 1 nm is considered. A similar trend was observed by another group [45], which investigated the influence of surface roughness on friction during contact with the human finger. Their findings indicate that friction increases with an increase in surface roughness up to a certain threshold (R_a - 25 μm), before stabilizing. However, other papers investigating the influence of surface roughness on the friction of human skin demonstrate that the friction coefficient tends to decrease with increasing surface roughness [46, 47] when R_a in a range from 1 to 10 μm is considered. They argue that reduced roughness leads to greater surface contact, consequently causing an increase in friction. Although it's undeniable that friction is influenced by surface roughness, the observed trend seems to be dependent on factors such as the range of roughness studied, surface texture, sliding direction, and other

variables, making it challenging to identify a singular pattern. Among other negative effects of high surface roughness in tribology, it was also demonstrated that a rough surface considerably increases the coating wear rate [24]. The dominant wear mechanisms were found to be crack nucleation/propagation with subsequent flake formation/chipping, and also fatigue (pitting). This is also of concern when fabricating glass micro-flexures and other components that operate under high mechanical stresses. For example, although glass possesses a high theoretical elastic strength (estimated to be 15 GPa or higher), it typically fractures at much lower stress values (on the order of a few tens of MPa) because surface flaws act as stress concentrators and preferential sites for crack initiation [48]. Consequently, minimizing surface roughness is essential to reduce the likelihood of crack nucleation and to ensure the reliable mechanical performance of such components. Furthermore, surface roughness governs the real area of contact between interacting surfaces, thereby influencing contact stiffness and load-bearing capacity. Rough surfaces initially transmit external loads through only a limited number of asperity contacts, leading to localized stress concentrations, increased elastic and plastic deformation, and reduced interface stiffness. As the surface becomes smoother, the real contact area increases, resulting in more uniform load distribution and improved mechanical stability of the contacting components [49]. What's more, surface roughness plays a tremendously important role in optics. It is well known that optical properties such as absorption, reflection, and transparency can be altered via a change in surface roughness. By roughening the surface, more and more valleys, pits, and hills are created that trap the incoming light and increase the absorption via multiple reflection phenomena [50]. This in turn results in a decrease of reflected and scattered light. Furthermore, as roughness increases, the distribution of reflected light intensity transitions progressively from being entirely specular (all light is reflected at an angle of incidence) to becoming fully Lambertian (reflects the same amount of light at all angles) [23]. In addition, this also influences the transparency of the surface. The Rayleigh roughness parameter (Ra_r) serves as a tool for evaluating the extent to which a surface's transparency is perceived by an average observer. The surface is qualified as very rough if the parameter $Ra_r > 1$ (according to [51]). If this condition is met for all the visible optical range, the surface will appear to an observer as completely white (if the material absorption is not accounted for) and non-transparent. The condition is satisfied if the roughness RMS (σ_{h}) is higher

than 120 nm [52]. Experimental evidence supporting the latter is given in [25]. Where it is demonstrated that after a typical laser micromachining procedure, the surface of acrylic polymer exhibits high surface roughness ($R_a \sim 1$ μm), which leads to the surface appearing as non-transparent with Lambertian-like properties. However, when the roughness of the very same surface is reduced to $R_a < 100$ nm, the full transparency of the surface is achieved. One more prosperous field, where the control of surface roughness is in huge demand, is the manufacturing of various implants. It was shown that the rate of success of an implant does not depend only on the biocompatibility properties of the material but also on its surface quality [53–56]. The importance of surface roughness becomes even more pronounced when talking about vision implants – intraocular lenses (IOLs). The optical properties, success of implantation, and even post-surgery complications of such lenses are greatly determined by the roughness of the lens [57]. The most common postoperative complication following cataract surgery is posterior capsule opacification (PCO), also known as secondary cataract. In the event of this complication, the patient's vision experiences a significant decline, necessitating the replacement of the IOL. This phenomenon is attributed to the migration of LE cells across the posterior surface of the IOL optic and in the space between the IOL and the capsular bag [58]. It was shown that the rate of LECs migration as well as the number of inflammatory cells adhesion to the optical surface linearly correlate with the amount of surface irregularities present on the surface [59]. Therefore, by minimizing the surface roughness, cell migration and adhesion can be prevented, reducing the likelihood of posterior capsule opacification.

In earlier times, prior to the availability of advanced metrology equipment we have today, surface roughness assessment relied on operators who visually or tactilely compared the roughness of a machined surface to reference surfaces featuring varying degrees of roughness. In 1933, Abbott and Firestone [60] developed the first analog surface tracking instrument for the assessment of surface roughness. The instrument used a contact stylus and could output actual numbers to quantify surface texture. Through the development of tools and techniques for assessing surface texture, it became apparent that the profile being measured could be viewed as a combination of numerous spatial wavelengths, each with its own unique amplitudes. In the early 1960s, this gave rise to the development of 2RC analog filters [61], a growing number of commercial instruments, and the popularity of basic roughness parameters such as R_a,

R_q, and R_z. Nonetheless, it was only during the digital revolution that the actual analysis of measured surface profiles started to take place, enabled by the capability to convert analog stylus output into digital data. Using digital tools, it became possible to separate a surface profile into different components representing roughness, waviness, and form by employing digital filtering techniques. International standards were established to define the foundational principles for accurate surface roughness assessment. The ISO 4287, first introduced in 1984 and subsequently revised in 1997, remains the cornerstone for assessing profile roughness parameters that continue to be in use today. The rapidly advancing machining techniques and the demand for measuring finer features than in the past spurred the development of novel surface texture measurement methods, such as atomic force microscopy (AFM), white light interferometry, laser microscopy, and others. In the present day, it is possible to accurately trace vertical variations in surface features within a picometer range [62] or measure the surface texture across a broad field (several hundred micrometers) in a matter of few minutes [63]. However, the multitude of surface roughness measurement methods, the vast amount of roughness parameters, and the varying guidelines on how to assess surface roughness are causing significant confusion within the community of laser micro-machining. Therefore, one of the goals of this thesis is to mitigate this confusion by providing explicit guidelines on the tools to use for the acquisition of surface texture after laser micro-machining and the procedures for processing data according to current ISO standards.

1.1.1 Science and standards behind surface roughness

In order to have the ability to compare surface roughness values, it is necessary to establish a set of rules that defines the fundamental criteria for determining what constitutes as surface roughness. The rules include the parameters that are used for evaluating surface roughness and the methodology describing the correct assessment of the roughness parameters. Furthermore, when discussing surface roughness, it is imperative to specify the type of surface under consideration, whether it be a primary surface prior to the filtration procedures or a surface with a partly filtered spatial spectrum. Therefore, valid comparisons of surface roughness values are possible only when measurements align with all established rules. The following chapters will provide a comprehensive explanation of

various surface roughness parameters and the methods employed in measuring them.

1.1.2 Parameters defining surface roughness

Surface roughness parameters can be computed in either two-dimensional (2D) or three-dimensional (3D) formats. The application of 2D profile analysis has been prevalent in science and engineering for over half a century. In recent decades, however, the demand for 3D surface analysis has grown, with recent studies [64, 65] emphasizing the advantages of analyzing surface roughness in 3D space. When using 2D parameters, the surface area is divided into multiple profiles, the roughness parameter of interest is calculated for each profile, and then an average is taken as a result. Whereas in the assessment of 3D roughness parameters, the surface is considered as a whole. As a result, the roughness measured using the 2D parameters can vary significantly depending on the measuring direction [66], resulting in variations or inconsistencies in the results. On the other hand, this allows for the provision of additional information about surface texture by investigating how roughness varies with the measurement direction. However, if the surface does not possess a specific texture and is homogeneous over the whole surface, the roughness assessed via 2D or 3D parameters is typically the same or very similar [67]. Next, roughness parameters are classified into amplitude, spatial, or hybrid categories. Amplitude parameters are the most important in characterizing surface topography, as they are utilized for measuring the vertical characteristics of surface deviations. Spacing parameters refer to measurements that assess the horizontal characteristics of surface deviations. The spacing parameters are of significant importance in some manufacturing operations, such as pressing sheet steel. In such a case, evaluating the spacing parameters is necessary to ensure consistent lubrication when pressing the sheets, to avoid scoring, and to prevent the appearance of the surface texture on the final product [68]. Finally, the hybrid parameters are a blend of amplitude and spacing, where alterations in either amplitude or spacing can impact the hybrid property. In tribology analysis, hybrid parameters such as surface slope, surface curvature, and developed interfacial area are regarded as crucial elements that influence the tribological properties of surfaces. However, since amplitude parameters are the most frequently cited in the literature, the primary focus will be on detailing them.

ISO 4287 standard provides a comprehensive introduction and detailed explanation of all the main 2D roughness parameters [69]. Among those, arithmetic average height (R_a, see equation 1.1) stands out as the most frequently encountered 2D roughness parameter in the literature, employed for the evaluation of surface roughness. It is defined as the average absolute deviation of the roughness irregularities from the mean line over one sampling length and is expressed as:

$$R_a = \frac{1}{l} \int_0^l |y(x)|\, dx. \tag{1.1}$$

Here, l - the length of a profile under consideration, $y(x)$ - the height deviation from an average value at x coordinate. This parameter is straightforward to define, simple to measure, and provides a concise, yet effective overall description of height variations. Another frequently employed parameter for measuring surface roughness is called root mean square roughness (R_q, see equation 1.2) or RMS in short. It is more sensitive to large deviations from the mean line and is defined as:

$$R_q = \sqrt{\frac{1}{l} \int_0^l y^2(x)\, dx}. \tag{1.2}$$

Although R_a and R_q are the most often used roughness parameters for characterizing 2D surface roughness in the community of laser micromachining, it is essential to introduce other roughness parameters as that provide additional information about important surface characteristics that cannot be fully captured by R_a and R_q alone. Largest peak-to-valley height (R_y) or PV in short represents the vertical distance between the highest peak and the lowest valley for the profile under the evaluation. This parameter is often employed in the assessment of optic quality. Typically, if the surface PV value is lower than $\lambda/10$, the surface (be it lens, mirror, etc.) is considered flat and aberration-free. Additional insights into the surface can be gained through the evaluation of skewness and kurtosis roughness parameters. The skewness (R_{sk}, see equation 1.3) of a profile is the third central moment of the profile amplitude probability density function, measured over the assessment length.

$$R_{sk} = \frac{1}{N R_q^3} \int_0^N Z^3(x)\, dx. \tag{1.3}$$

Here R_q is the RMS roughness parameter and *Z(x)* - is the height of the profile at point x. Skewness is used to measure the symmetry of the profile around the mean line. This parameter is sensitive to occasional deep valleys or high peaks. A symmetrical height distribution, i.e. with as many peaks as valleys, has zero skewness. Profiles with peaks removed or deep scratches have negative skewness. Profiles with valleys filled in or high peaks have positive skewness (see figure 1.1 part (A)). The skewness of a surface was shown to be highly related to the wetting properties of the surface [70]. Superhydrophobic properties are typically obtained for R_{sk} close to 0, whereas an increase or decrease of R_{sk} leads to a decrease of the water contact angle (WCA). Another roughness parameter that characterizes the distribution of peaks and valleys on the surface is kurtosis (R_{ku}), where:

$$R_{ku} = \frac{1}{NR_q^4} \int_0^N Z^4(x)\, dx. \tag{1.4}$$

It describes the sharpness of the probability density of the profile. If $R_{ku} < 3$, the distribution curve is said to be platykurtic and has relatively few high peaks and low valleys. If $R_{ku} > 3$ the distribution curve is said to be leptokurtic and has relatively many high peaks and low valleys (see figure 1.1 part (B)). The

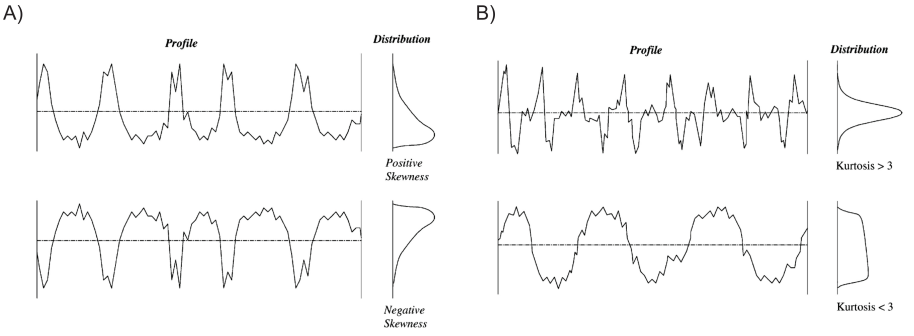


Fig. 1.1 The visual representation of roughness parameters skewness and kurtosis. Part (A) depicts the skewness roughness parameter. The upper profile represents a case when $R_{sk} > 0$, and the lower one a case when $R_{sk} < 0$. Part (B) shows the roughness parameter - kurtosis. The upper profile depicts a case when the profile is leptokurtic ($R_{ku} > 3$), whereas in the bottom part, a platykurtic case is shown ($R_{sk} < 3$) [68].

skewness and kurtosis parameters are usually considered when conventional surface roughness parameters like R_a or R_q are not enough. One of the cases where conventional roughness parameters prove insufficient is when assessing the tribological properties of contacting surfaces. It was shown that solely on the basis of conventional roughness parameters (R_a, R_q) tribological behavior

properties of contact surfaces cannot be anticipated. Whereas R_{sk} and R_{ku} show a good correlation to the tribological properties of contact surfaces and could be used for planning surfaces and surface topographies with desired tribological behavior in boundary lubrication regime [71]. Another field where skewness and kurtosis prove to be superior over conventional roughness parameters is in identifying the wear of the objects. When investigating the wear of human teeth it was seen that roughness parameters R_a and R_q fail in carrying out the task. In contrast, both skewness and kurtosis parameters demonstrated the ability to detect teeth wear, suggesting their potential utility in clarifying aspects of clinical issues [72].

Moving from profile-based to surface-based measurements allows the computation of 3D roughness parameters. A comprehensive explanation of the 3D roughness parameters is provided in the part 2 of the ISO 25178 standard [73]. The notation of earlier presented 2D amplitude roughness parameters when transformed into 3D undergo the change from $R_{a,q,sk,ku}$ to $S_{a,q,sk,ku}$ accordingly and are expressed as follows:

$$S_a = \frac{1}{A} \int \int_A |z(x, y)| \, dxdy, \tag{1.5}$$

$$S_q = \sqrt{\frac{1}{A} \int \int_A z^2(x, y) \, dxdy}, \tag{1.6}$$

$$S_{sk} = \frac{1}{AS_q^3} \int \int_A z^3(x, y) \, dxdy, \tag{1.7}$$

$$S_{ku} = \frac{1}{AS_q^4} \int \int_A z^4(x, y) \, dxdy. \tag{1.8}$$

Here, A - area under the evaluation, *z(x,y)* - the height deviation from a mean plane at *x,y* position. S_a - arithmetical mean height, S_q - root mean square (RMS) height, S_{sk} - skewness, S_{ku} - kurtosis. Unlike amplitude parameters, that only consider surface height deviations, the 3D spatial roughness parameters use the auto-correlation function in order to identify the extent of waviness on the surface as well as surface texture and its direction if such is identifiable. The parameter auto-correlation length (S_{al}) represents the distance in the transverse plane in the direction in which the auto-correlation function decays to the value s (0.2 by default) the fastest. In order to estimate (S_{al}) and other spatial parameters, first an auto-correlation function (f_{ACF}) that shows the correlation

between a surface and the same surface translated by (t_x, t_y) has to performed on the surface under the evaluation.

$$f_{ACF}(t_x, t_y) = \frac{\frac{1}{B}\int\int_B z(x,y)z(x+t_x, y+t_y)\,dxdy}{\frac{1}{A}\int\int_A z^2(x,y)\,dxdy}. \tag{1.9}$$

Here t_x, t_y - translations of a surface to x and y directions accordingly, and B - the intersecting area of two surfaces. The auto-correlation used here is normalized between -1 and 1. After performing f_{ACF} on the surface, the direction of the fastest decay is identified, and auto-correlation length towards that direction can be calculated as:

$$S_{al} = \min_{t_x, t_y \in R} \sqrt{t_x^2 + t_y^2}, \tag{1.10}$$

where

$$R = \{(t_x, t_y) : f_{ACF}(t_x, t_y) \leq s\}. \tag{1.11}$$

Here, s is the threshold value for f_{ACF}, if not specified, the default value (s = 0.2) should be used. For a better understanding of the procedure see figure 1.2. First, an auto-correlation function is performed on a surface (part a), then the boundaries where f_{ACF} decays to value s are identified (part b). Finally, from the threshold boundary at the center, the 3D spatial roughness parameters are evaluated. Another useful spatial roughness parameter is texture aspect ratio (S_{tr}). The value is obtained by dividing the distance in the transverse plane in the direction in which the auto-correlation function decays to the value s the fastest (equivalent to S_{al}) by the distance in the direction of the slowest decay of auto-correlation function to the value s. It is a measure of uniformity of the surface texture and is used for the evaluation of the surface anisotropy [74]. The last 3D spatial roughness parameter of high significance is texture direction (S_{td}). It is an angle of the absolute maximum value of the angular amplitude density and is useful for identifying the dominant texture direction on the surface (e.g., in the illustrative surface seen in the figure 1.2, the dominant texture direction is diagonal and is depicted by the angle θ in part (d) of the figure). As evident, the 3D spatial roughness parameters serve as effective tools for assessing surface texture, including aspects such as texture direction, periodicity, and more.

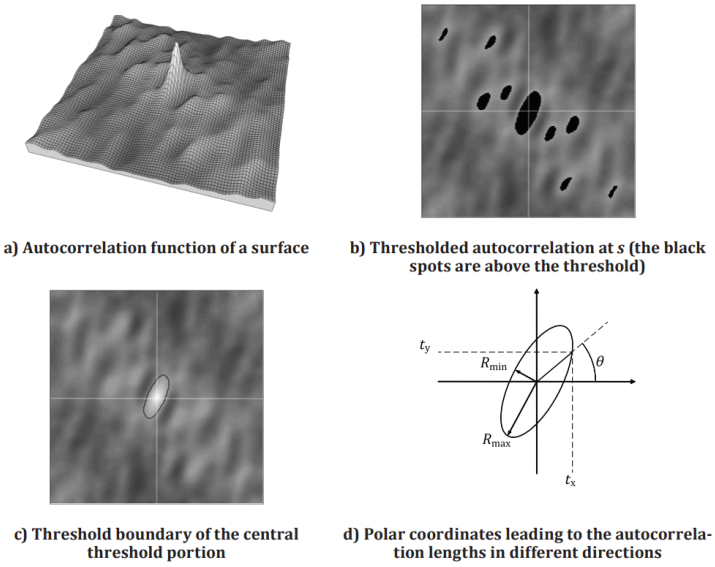


Fig. 1.2 The visual representation of the procedure to calculate spatial 3D roughness parameters. The picture was taken from the ISO 25178 part 2 [73].

1.1.3 Guidelines for surface roughness assessment

Understanding how to define surface roughness in terms of 2D or 3D roughness parameters is not enough in order to precisely quantify the surface roughness. For an effective comparison of measured surface roughness values, it is essential that the methodology for extracting roughness parameters from measured topographies remains consistent. This includes the rules for selecting the profile length or the surface area from which the roughness parameters are extracted and others. Furthermore, before calculating roughness parameters, it is necessary to filter the surface texture to eliminate the influence of the form and waviness inherent in the surface. Studies show that if these steps are done incorrectly the resulting values of surface roughness can vary tens of times [75], making the comparison of the absolute values invalid. However, the filtration of the surface, despite its importance, is commonly overlooked in the community of laser micromachining, due to the scattered and limited in availability literature regarding the filtration methodology. To bridge this gap, this chapter will concentrate on providing guidelines and methodology related to surface texture filtration and the selection of measurement windows, to ensure that the acquired surface roughness values are in accordance with the

international standards. There are several different international standards that describe the methodology of surface texture filtration to extract the roughness. Each standard varies slightly, offering distinct recommendations and guidelines for the selection of filters. The overview of different international standards and their distinct features is presented in the literature [76]. In this framework, only ISO standards will be discussed, as they are the most commonly used and referred to when talking about surface texture filtration. The surface topography can be

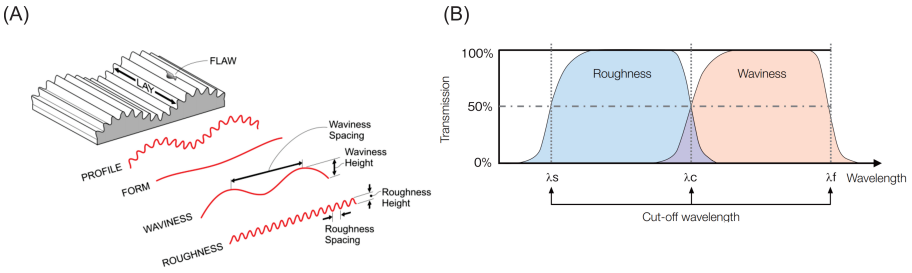


Fig. 1.3 A visual representation depicting that surface texture can be divided into form, waviness, and roughness (A). Filtration operation of the spatial spectrum (B). To obtain roughness cut-offs λ_s and λ_c are used. To obtain waviness λ_c and λ_f are used.

perceived as a composite of numerous periodic functions with different spatial wavelengths and amplitudes (see figure 1.3, part (A)). These are commonly classified into three categories: form, waviness, and roughness. The short wavelength components fall into the roughness category, the longer wavelength components represent waviness, and the longest ones - form (see figure 1.3, part (B)). The corresponding spectral regions of the 3 different wavelength groups are separated and defined by cut-off wavelengths (λ_s, λ_c, and λ_f). When performing surface texture filtering, the λ_s cut-off wavelength is used to remove the shortest wavelength surface components that constitute the measuring noise arising from the used equipment. The λ_c cut-off wavelength defines the boundary between surface components classified as roughness and those classified as waviness. Lastly, λ_f is used to remove the longest wavelength surface components that represent the form of the specimen that is being evaluated. When talking about surface roughness in its correct form, we refer to the variations in the height of surface components that belong to the category of roughness. Therefore, prior to calculating roughness parameters, the measured topography must undergo processing to selectively exclude non-roughness components. This is done by using filters to exclude unnecessary spatial wavelengths. Some of the filters

are convolution-based, and others apply filtering directly in the Fourier domain. After a filtered topography is obtained, the calculations of 2D or 3D roughness parameters are carried out. The part that brings the most confusion during this process is the correct selection of cut-off wavelengths that are used to remove the non-roughness surface components.

Profile roughness

The instructions on the methodology of measuring surface roughness and selecting the cut-off values when filtering surface components of a profile are provided in the ISO 4287, ISO 4288, and ISO 3274 standards [69, 77, 78]. As discussed above, the λ_s is a cut-off used to remove the measurement noise. The level of noise to be removed is determined by the measurement equipment used. The λ_s has to be selected to be 5 times larger than the spacing between adjacent measurement points in order to fully remove the measurement noise. λ_f is used to remove the longest spatial wavelengths that constitute the form of the specimen. Alternately, the form removal according to the standard can be carried out by using the best-fit least-squares method, instead of selecting a specific λ_f value. Moving onto the λ_c cut-off that is used to separate roughness from waviness, it is important to note, that this cut-off varies depending on the overall roughness of the surface. As stated in the standard the λ_c cut-off value has to be selected in accordance with the estimated surface roughness prior to the filtration. The provided cut-off values are different for surfaces that are periodic and non-periodic. The periodic surfaces are typically the result of traditional mechanical processes like milling or turning. On the contrary, when performing laser micromachining, the resulting surfaces are rarely periodic, therefore only the case of the selection of cut-off wavelengths for the surfaces that are non-periodic will be covered in the scope of this work. The guidelines for the selection of λ_c cut-off wavelength of non-periodic surfaces are provided in table 1.1. The table covers the roughness range from 6 nm to 80 μm and provides the sampling lengths l_r, cut-off values (λ_c), and evaluation lengths l_n that have to be used according to the initial roughness of the surface. Here, sampling length indicates the length of the profile that has to be used for the measurements of surface roughness. The λ_c cut-off value shall be chosen equal to this sampling length. Finally, the evaluation length denotes the length of the profile from which the assessment of the roughness parameters should be carried

Table 1.1 Roughness sampling lengths and evaluation lengths for surfaces with different roughness levels [77].

R_a, μm	Roughness sampling length l_r and λ_c cut-off value, mm	Roughness evaluation length, l_n, mm
$0.006 < R_a \leq 0.02$	0.08	0.4
$0.02 < R_a \leq 0.1$	0.25	1.25
$0.1 < R_a \leq 2$	0.8	4
$2 < R_a \leq 10$	2.5	12.5
$10 < R_a \leq 80$	8	40

out and is set to be 5 times larger than the sampling length. The roughness parameter of interest is calculated for each sampling length within evaluation length and the mean value is taken as a result. In summary, the filtration of a profile, aimed at removing the non-roughness elements from a surface, has to be performed by following these steps.

- The shortest spatial wavelengths constituting measurement noise are removed by applying λ_s cut-off. The cut-off is selected to be 5 times larger than the spacing between adjacent measurement points.
- The longest spatial wavelengths representing the form of the specimen are removed by performing the best-fit least-squares method and subtracting the reference line from the profile.
- The primary (before applying λ_c cut-off) surface roughness is evaluated, for example, by computing R_a of an unfiltered surface or through other methods.
- According to the primary roughness level, the sampling length and λ_c cut-off values are chosen from the table 1.1.
- Finally, the filtration is carried out on a profile that is 5 times larger than the sampling length, after which 2D roughness parameters are assessed for each sampling length and averaged to obtain the final values.

When specifying the absolute values of roughness parameters, it is essential to provide the mean value along with its upper and lower limits. The mean value is an average surface texture parameter derived from n (usually 5) sampling

lengths, whereas the upper and lower limits are specified by one standard deviation (σ) from the mean value. If the evaluation length of a profile according to the table 1.1 exceeds the dimensions of the processed area, the surface roughness can be evaluated on the shorter profile. However, if the evaluation length does not equal five sampling lengths, the standard deviation of the roughness parameter and its according upper and lower limits shall be recalculated and related to an evaluation length equal to five sampling lengths. This is realized using the following equation:

$$\sigma_n = \frac{\sigma_5}{\sqrt{n/5}}, \tag{1.12}$$

here, σ_5 - standard deviation of the evaluation length that is equal to 5 sampling lengths, σ_n - standard deviation of the evaluation length that is equal to n sampling lengths, where n is the number of sampling lengths.

Areal roughness

Next, the areal filtration of the surfaces for the evaluation of 3D roughness parameters will be discussed. The ISO 25178 standard, specifically in parts 2 and 3 [73, 79], provides a comprehensive explanation of the terminology and methodology employed in areal surface filtration. In contrast to the profile filtration mentioned earlier, areal filtration involves comparable steps; nonetheless, there are notable differences in terminology, and the criteria for selecting cut-offs deviate. Figure 1.4 depicts the areal filtration visually, showcasing the transformation of the topography after applying different filters. In areal filtration, cut-off wavelengths ($\lambda_{s,c,f}$) used for filtering different spatial wavelengths are replaced by the nesting indexes ($N_{is,ic,if}$ accordingly). The term nesting index was forged to widen the concept of cut-off which is only applicable to linear filters. In the ISO 16610 series [80], new filters are defined that are not linear filters, such as the Morphological filter and the Robust Spline filter. Hence, the term cut-off cannot be used for these filters and the term nesting index is used instead. However, when a conventional linear Gaussian filter is considered, the nesting indices perform the same function as the cut-off wavelengths. The N_{is} nesting index serves as a cut-off for the S filter, which is used to remove the shortest spatial wavelengths that constitute measurement noise. The N_{if} is a cut-off for the F-filter that is used to remove the form of the specimen, and

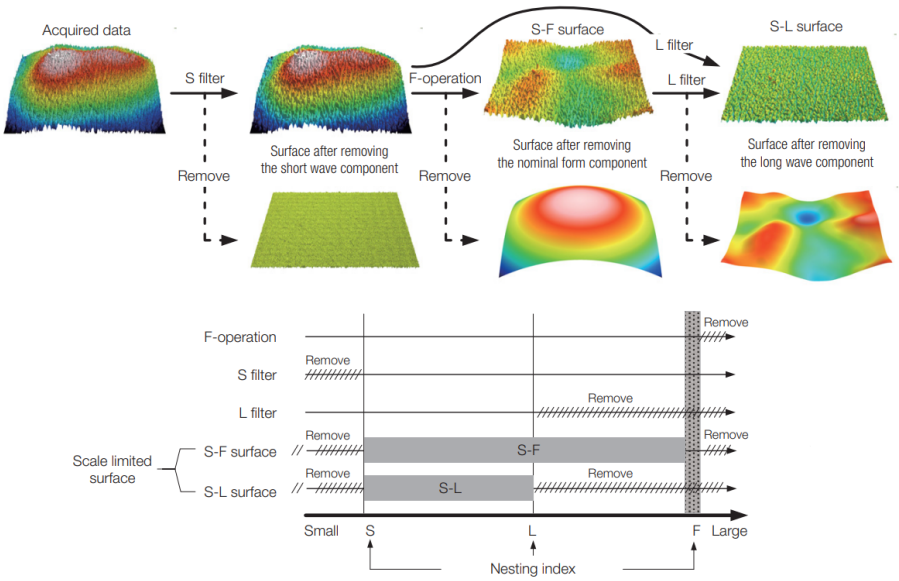


Fig. 1.4 The visual showcase of areal filtration workflow. The upper section of the image illustrates alterations in surface topography resulting from the application of various filters (S, F, and L). The bottom part of the figure shows the filtration operation in the spatial wavelength domain. The S filter is used to remove the shortest wavelengths, the F filter is used for the removal of the form, and finally, the L filter is used for the separation of roughness from waviness.

lastly, N_{ic} nesting index is a cut-off for the L filter that separates the roughness and the waviness surface components (see figure 1.4). In the process of areal filtering, the initial step involves the application of an S filter to the acquired raw data in order to eliminate the measurement noise. The S filter's nesting index is selected to be 3 times the sampling distance (the distance between adjacent data points in the lateral plane). After applying the S filter, the surface is designated as the primary surface. The following procedures include the F-operation to remove the form of the specimen and the application of an L filter to eliminate the waviness. If only the F-filter is applied to the primary surface, the resultant surface is denoted as the S-F surface. Conversely, if both F and L filters are employed, the surface is labeled as an S-L surface. When evaluating the 3D roughness parameters it is essential to specify the surface type (primary, S-F, or S-L) from which the parameters were derived. When removing the form of the surface, a best-fit least-squares method is employed. In the absence of any discernible shape on the surface, a basic tilt correction can function as an F-operation. While standards offer explicit instructions for the application of

S and F filters, the selection of an L-filter nesting index, on the other hand, is accompanied by recommendations rather than precise guidelines. It is specified that the typical selection for the value of an L-filter nesting index is five times the scale of the coarsest structure of interest. Therefore, for the selection of an L-filter, the coarsest structure on the surface has to be identified first. Once identified, the lateral dimensions are assessed, and the L-filter is adjusted to be five times larger. A set of values recommended for the selection of L filter is provided: *..., 0.1 mm, 0.2 mm, 0.25 mm, 0.5 mm, 0.8 mm, 1 mm, 2 mm, 2.5 mm, 5 mm, 8 mm, 10 mm, ...* Nevertheless, alternative values are also deemed acceptable. Once the nesting index is selected, the surface area from which roughness parameters are extracted can be selected. For an S-L surface, the evaluation area shall be a square whose sides are the same length as the L-filter nesting index value. As mentioned, the choice of an L-filter nesting index relies on the subjective judgment of the coarsest structure, thereby introducing uncertainty into the filtering process. The difficulties arising from subjective judgment underscore the reasoning why the guidelines behind the selection of an L-filter nesting index are presented as recommendations, rather than rigid rules. Therefore, if the identification of the coarsest structure poses too big of a challenge, alternative methods can be utilized to determine the L-filter nesting index. A straightforward approach involves employing various nesting index values to visually determine the extent of filtering needed to completely eliminate waviness. Regardless of the chosen method for determining the L-filter nesting index when specifying surface roughness parameter values for the S-L surface, it is crucial to present the value of the L-filter nesting index used and provide the rationale behind its selection. In summary, the areal filtering procedure to remove non-roughness components from the surface adhere to these steps:

- The S-filter is applied to the acquired raw data to remove the measurement noise. The S-filter nesting index N_{is} is chosen to be 3 times the sampling distance.

- The F-operation is performed on the primary surface to remove the form of the specimen. The operation includes performing the best-fit least squares method and removing the reference plane.

- The L-filter is applied to the S-F surface to eliminate the waviness of the surface. The L-filter nesting index N_{ic} is chosen by identifying the coarsest structure on the surface and setting the value of the nesting index to be 5 times larger than the lateral dimension of the structure.
- The evaluation area of the S-L surface is set to be a square, whose sides are the same length as the L-filter nesting index value.
- The assessment of the 3D roughness parameters is performed.

Filters and filtration procedure

Moving on, it is important to talk about the filter types that are employed in surface texture filtering procedures. Historically, in the previous century, before digitization took over, the very first filters implemented in analog surface texture measuring devices were the RC filters. Comprising a resistor and a capacitor, these physical filters could be configured into either high-pass or low-pass filters based on their arrangement. Subsequently, with the advent of digital processing for acquired data, digital filters emerged and gained widespread popularity. The most often encountered digital Gaussian filter, first introduced in 1996 [81], has been consistently utilized by the majority for profile and areal surface texture filtering ever since. Due to its popularity, the Gaussian filter is now available in most of modern surface texture acquisition devices, offering the quick and easy filtration of surface texture and preventing the need for manual post-processing of the data. A linear Gaussian filter has a weighting function of Gaussian shape and is described as:

$$s(x,y) = \frac{1}{\alpha\lambda_c} e^{-\pi(\frac{x}{\alpha\lambda_c})^2} \frac{1}{\alpha\lambda_c} e^{-\pi(\frac{y}{\alpha\lambda_c})^2}, \tag{1.13}$$

where

$$\alpha = \sqrt{ln2/\pi} = 0.4697. \tag{1.14}$$

Here, $\alpha \sim 0.5$ according to the definition of the cut-off wavelength, where the cut-off wavelength represents the wavelength in the spatial wavelength domain at which the transmission drops by 50 %. By performing the convolution of the S-F surface with the specified Gaussian weighting function, a mean surface representing waviness is obtained. Subtracting this mean surface from the primary surface results in the extraction of the surface's roughness component.

However, linear filters such as Gaussian have their drawbacks. One of them is that linear filters are sensitive to the outliers, which can heavily distort the filtered profile. This becomes very important when using optical metrological devices for the acquisition of surface texture. The sharp dips and peaks on the surface due to difficulties of measuring them commonly appear as distinct peaks in the dataset, forming outliers. In order to mitigate distortion caused by outliers, a viable solution involves employing a "robust" non-linear variant of the Gaussian filter. The filter uses an iterative technique that effectively alters the weighting of the Gaussian filter function in the region of an outlier [82]. Additional, less frequently used filter types include spline, wavelets, morphological, and various others [83]. Nevertheless, due to their lower frequency of use compared to the Gaussian filter, further elaboration on these filters will not be pursued within the scope of this work.

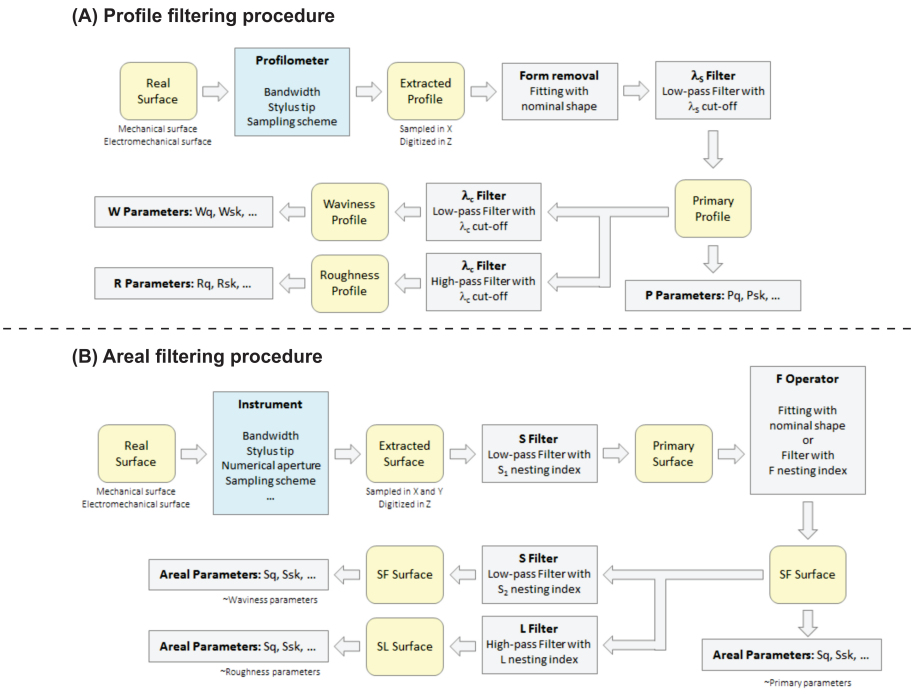


Fig. 1.5 The workflow summarizing the profile (part A) and areal (part B) filtration procedures.

Finally, to summarize this chapter, a workflow covering the profile and areal filtration procedures is presented in figure 1.5. Both procedures, despite different terminology, follow the same path. The profile or the surface is measured via

the means of mechanical or optical metrological devices (more about them in the following chapter). After acquiring the surface data, a filtration process is implemented. Initially, the shortest spatial wavelengths, which contribute to the measurement noise, are eliminated. Subsequently, the specimen's form is extracted and removed using methods such as the best-fit least squares method. After these two operations, the surface roughness parameters of the primary profile or SF surface can be evaluated. However, if the goal is to obtain the surface roughness parameters without the waviness component of the surface, an additional λ_c cut-off in profile filtering or N_{ic} nesting index in areal filtering is applied. The values for the cut-off wavelengths or nesting indices shall be selected according to the ISO standards. Finally, following the filtration of the waviness component, the 2D or 3D roughness parameters are assessed. It is important to note that when filtering a profile, the roughness of the primary profile is denoted as P_a instead of the usual R_a. In contrast, for areal filtration, the roughness of S-F or S-L surfaces is denoted the same - S_a. Therefore, specifying the surface type from which the parameter is derived is essential to avoid confusion.

1.1.4 Surface roughness measurement methods and their spatial resolution

The accurate acquisition of the surface topography is a vital part in the process of surface roughness measurement. The most primitive means of surface roughness inspection involve visible and tactile examination. While such means prove beneficial in a primary inspection of the roughness or the comparison of the two specimens, they fail to quantify the roughness and have a poor ability to store the data for later use. Even with the astonishing accuracy of the human fingers (studies show that individuals can perceive roughness levels as fine as 13 nm through tactile sensation with their fingers [84]), such qualitative assessment is of limited use for methodological purposes. To overcome these limits, devices capable of acquiring and quantifying surface roughness were developed.

Mechanical methods

Stylus instruments are by far the most common instruments used in the industry for measuring surface texture as of today. A typical stylus instrument consists of a stylus that physically contacts the surface being measured and a transducer

(linear variable differential transformer, an optical or a capacitance sensor) to convert its vertical movement into an electrical signal. The stylus arm is loaded against the sample and either the stylus is scanned across the stationary sample using a traverse unit at a constant speed, or the sample is transported across an optical flat reference. As the stylus or sample moves, the stylus rides over the sample surface, detecting surface deviations. The transducer produces an analog signal corresponding to the vertical stylus movement. This signal is then amplified, conditioned, and digitized [85]. Maximum vertical and spatial (horizontal) magnifications that can be achieved are on the order of 10^5 and 10^2, respectively. The vertical resolution is limited by sensor response, background mechanical vibrations, and thermal noise in the electronics. For smooth surfaces it is as low as 0.1 nm and 1 nm for rough surfaces. The scan lengths of such devices can be typically as high as 200 mm, and for three-dimensional imaging, the scan areas can be as large as 5 mm × 5 mm. The vertical range typically spans from 2 to 250 μm. The scan speed ranges from 1 μm/s to 25 mm/s. Despite the fact that stylus-based profilers are available and have been improved for almost a century now, they still fail to meet some of the current metrological demands. The main disadvantages of stylus-based profilers are stylus wear, long acquisition times, and surface scratching. The stylus devices are excellent for measuring single profiles but fall short in areal acquisitions due to long measuring times. It may be perfectly acceptable to take several minutes to make a single profile measurement, but if the same number of points are required in the y direction (orthogonal to the scan direction) as are measured in the x direction, then the acquisition times can increase to several hours, which becomes impractical. For example, if the drive mechanism can scan at 0.1 mm/s and 1000 points are required for a profile of 1 mm, then the measurement will take 10 s. If a square grid of points is required for an areal measurement, then the measurement time will increase to 10^5 s or approximately 2.7 h. In summary, the stylus-based devices are excellent for single profile measurements to extract the 2D roughness parameters but are not convenient in surface areal inspection due to long acquisition times.

Optical methods

Typically, when evaluating the roughness of the surface, the investigation of more than a single profile is preferable to rule out the influence of the outliers.

This is usually realized by measuring the roughness of an area that contains multiple profiles. As discussed, stylus-based profilers are not well-suited for this task. Hence, alternative methods are necessary for conducting areal surface roughness measurements. For such a task, optical instruments prove to be an excellent choice. There are many different optical methods that allow to acquire the surface texture. These are confocal microscopy, white light interferometry, coherence scanning interferometry, scatterometry, and others. Currently, confocal instruments stand as the most commonly employed tools

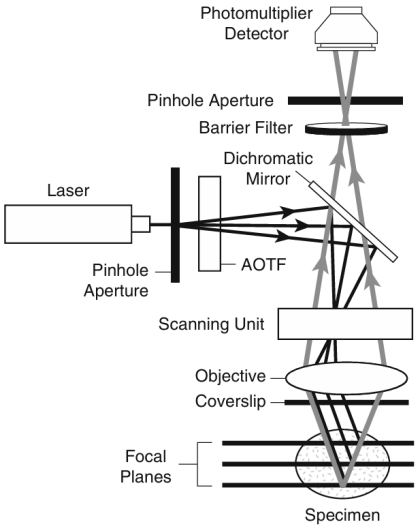


Fig. 1.6 The main components of a modern laser scanning confocal microscope. Light from one or more lasers passes through a pinhole, is attenuated through an AOTF (acoustic-optic tunable filter), bounces off a dichromatic mirror, and passes into the scanning unit. A scanned beam enters the back focal plane of the objective lens, which focuses the light at a point in the specimen. The reflected light undergoes filtration through a pinhole aperture to exclusively transmit the light gathered from the focal plane, which is then detected by a photomultiplier detector [86].

in the industry for surface texture acquisition. Confocal instruments offer great resolution, long working distances, fast acquisition rates, and many other benefits for which they are perfect in areal surface roughness measurements when laser-processed surfaces are considered. The basic principle of confocal microscopy is that the illumination and detection optics are focused on the same diffraction-limited spot, which is moved over the sample to build the complete image on the detector. While the entire field of view is illuminated during confocal imaging, anything outside the focal plane contributes little to the image,

minimizing the haze observed in standard light microscopy [87]. A schematic of a typical laser scanning confocal microscope is shown in figure 1.6. The working principle of such a microscope goes as follows: light from a laser source passes through a pinhole, is attenuated by a filter (neutral density, AOTF, or other), reflected by a dichroic mirror, and is focused on the sample. The reflected light is filtered by another pinhole to exclusively transmit the light gathered from the focal plane, which is then detected by a photomultiplier detector. To register the area, the laser beam is scanned over the surface using the scanning unit, which typically involves galvanometer mirrors or a spinning disk. The invention of the confocal microscope is attributed to Marvin Minsky, who built a working scanning optical microscope in 1955 with the goal of imaging neural networks in unstained preparations of living brains. All modern confocal microscopes, by definition, employ the principle of confocal imaging that he patented in 1957 [88]. A confocal microscope placed on a z-axis can be used to measure multiple planes at different z positions, from which a 3D surface texture can be reconstructed. The lateral and axial resolutions of confocal microscopes are determined by the numerical aperture (NA) of the objective used and the wavelength of the illumination radiation (λ). The equations used to determine lateral and axial resolution are as follows [87]:

$$R_{lateral} = \frac{0.4 \times \lambda}{NA}, \tag{1.15}$$

$$R_{axial} = \frac{1.4 \times \lambda \times n}{NA^2}, \tag{1.16}$$

where R is the resolution, λ is the wavelength of the light source radiation, n is the refractive index of the medium between the specimen and the objective, and NA is the objective's numerical aperture. A modern laser scanning confocal microscope with 0.8 NA objective and 405 nm wavelength illumination can achieve a lateral resolution of ($R_{lateral}$) 200 nm and axial resolution (R_{axial}) of 900 nm according to equations 1.16 and 1.15. However, through additional digital processing, including high-accuracy peak detection and intensity-based surface fitting of the confocal signal, modern confocal microscopes can perform effective height measurements with precision on the order of $\sim$ 10 nm (value corresponding to *Olympus Lext 5100* laser scanning microscope). Microscope objectives are available with working distances from about 100 μm to tens of millimeters. With increasing working distance, the NA normally decreases.

This also results in reduced lateral and axial resolution. Therefore, depending on the application, the objective parameters have to be chosen carefully. The field of view is limited by the objective magnification. Lower magnifying objectives with about 10× to 20× magnification provide a larger field of view of approximately one square millimeter. High-magnifying objectives with 100× magnification have a field of view of about 150 μm × 150 μm. Compared with stylus-based instruments, optical devices offer the advantage of non-contact measurements, thereby eliminating the risk of scratching or otherwise damaging the specimen under investigation. Moreover, while the stylus is typically scanned at 0.1 mm/s speed, the galvanometer mirrors can reach speeds up to 1 m/s and higher, reducing the acquisition times by a factor of 10^4. Further increase in acquisition times ($\times\ 10^{2-3}$) can be achieved by using MEMS scanners instead of galvo [89]. Lastly, stylus-based instruments often suffer from complicated relocation methods (the ability to reposition the sample precisely to its original location before removal). Whereas optical devices usually have integrated on-axis cameras, facilitating the monitoring of surface texture and aiding in the precise positioning of the sample.

An additional increase in resolution utilizing optical methods can be achieved by implementing interferometry. Interferometric optical profilers are based on standard microscopes where an interferometer built into the objective replaces the standard objective. During measurement, the interference signal is varied by changing the optical path difference between the object and reference beams. Finally, the vertical height data are deduced from the phase maps. Different types of interferometric objectives exist, each presenting unique pros and cons [90]. Commonly used Mirau interferometer contains two small glass plates between the objective and the test surface. One plate contains a small reflective spot that acts as the reference surface, and the other plate is coated on one side to act as a beamsplitter. At the beamsplitter, the radiation from the light source is split into two parts, where one is reflected back onto the reference mirror and the second incidences the specimen under investigation. The two beams, when reflected, will interfere if the conditions for the interference are met, and the interferogram will be registered on the CCD camera. The best contrast fringes will be achieved when the optical path difference between the reference mirror and the objective position is zero. By changing the optical path length towards the specimen and tracking the zero optical path difference's position on the CCD, it is possible to acquire the topography of the specimen's surface.

Using this technique, the scanning of the surface is no longer required, enabling further reduction in acquisition times of three-dimensional surfaces. One of the limitations of these instruments is that they can only be used for surfaces with similar optical properties. When dealing with thin films, incident light may penetrate the film and can be reflected from the film-substrate interface. This reflected light wave would have an additional phase shift, thereby introducing errors in determining the zero OPD point. Because the technique measures topographical features via wave interference, sub-nanometer axial resolution is achievable with step heights as small as 0.1 nm [91]. With a high lateral spatial resolution of 150 nm, white-light interferometry is accurate for distinguishing nearby objects along the axis. The working distance can be as large as 10 mm [92].

Other methods

When the task involves measuring the very finest features of a surface texture, the atomic force microscope (AFM) is the most effective tool for the job. In AFM, a sharp probe runs a raster scan across the sample surface with a positioning accuracy in the sub-nanometer level. During the scan, the probe is moved up and down by a closed feedback loop to maintain a constant probe-sample interaction. The vertical movements are recorded against XY position to form a surface topography of the sample. The AFM has several distinct modes of operation depending on the tip-sample interaction force (see figure 1.7, part A). Typically, two force regimes are distinguished: contact and non-contact modes. When the microscope is operated in a non-contact mode, the tip-sample separation is in the range of 10 to 100 nm. Under such conditions, forces such as Van der Waals, electrostatic, magnetic, or capillary can be sensed and give information about surface topography, distribution of charges, magnetic domain wall structure, or liquid film distribution. At smaller separations of the order of angstroms, the probing tip is in contact with the sample (therefore denoted - contact mode). In this mode, ionic repulsion forces allow the surface topography to be traced with high resolution. Under the best conditions, atomic resolution is achieved [93]. In addition, the AFM can be operated in static (DC) or dynamic (AC) modes. In static mode, the probe is static, and only the cantilever-type spring bends in response to the force that acts on the probing tip. Whereas in dynamic mode the cantilever is oscillating close to its resonant frequency, in such a way

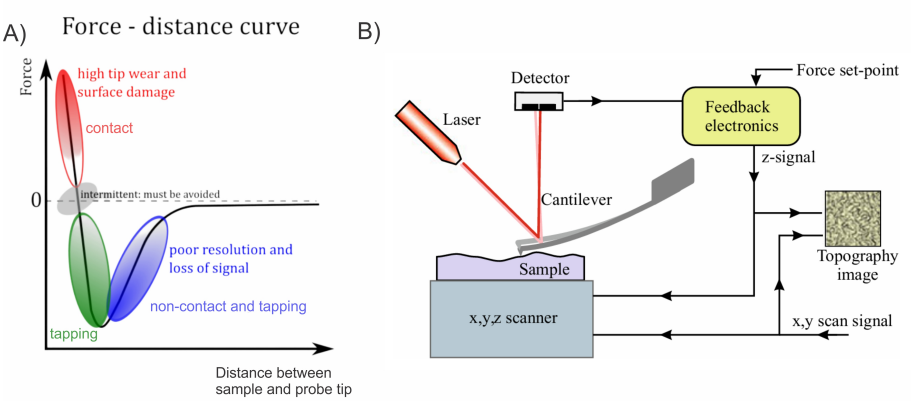


Fig. 1.7 Force - distance curve (A). The curve shows the force between the surface and the probe tip dependence on the distance between the two. Different color areas donate different modes AFM can be operated in. Schematic diagram of an atomic force microscope operating in contact mode (B) [94].

reducing the time when the probe is in contact with the sample. Such a mode is typically utilized when measuring soft samples, like polymers or biological samples. However, in laser micromachining, this is rarely the case. Therefore, further discussion will only cover AFM operating in contact static mode. The schematics of atomic force microscope operation in static mode are depicted in figure 1.7, part B. The microscope consists of a cantilever-type spring with a tip at the end, the laser source (usually laser diode), detector (PSPD), piezoelectric scanner, and feedback electronics (typically a PID controller). The laser beam from a laser diode is focused onto the end of the cantilever. The reflected beam from the cantilever surface is redirected to a quadrant photodiode (denoted as a detector), which is usually called position-sensitive photodiode (PSPD) in AFM. When the cantilever bends vertically (in case of a protruding or recessed feature on the surface), the direction of the reflected laser beam changes accordingly, causing the laser spot on PSPD to move vertically. The displacement of the reflected beam from the central position is considered an error. To eliminate this error, the controller will lift the probe or lower the sample (depending on the configuration) until the error becomes zero. With an optimized feedback loop, the probe tracks the surface with a constant force (hence, constant sample-tip distance) to form the topography of the sample [95]. Given the ultra-sharpness of AFM tips and the sensitivity of piezoelectric components, AFM is arguably capable of detecting vertical changes in picometers (the size of a typical atom is 30 to 300 picometers) [62]. However, the scanning scale of AFM is limited

to tens of micrometers [96]. Thus, a repeatable roughness measurement using AFM requires multiple scans at different locations of a sample surface. The practical scan speed limit for atomic resolution in a vacuum is 0.1 μm/s, while in water it increases to about 2 μm/s due to the additional damping of cantilever movements [97]. In summary, the AFM can be used to acquire surface texture at an atomic scale, but with a trade-off of long acquisition times.

In this chapter, the main surface texture measuring instruments that are usually employed for surface roughness acquisition were discussed. As apparent, each instrument possesses its own set of advantages and disadvantages, making it a superior choice for different applications. A thorough comparison of the main features and limits of discussed instruments is provided in table 1.2. The table, in addition to the discussed instruments, also includes the limits of the scanning tunneling microscope (STM). The former was not addressed in this chapter as it is yet hard to attain, is only used for scientific purposes, and the resolution it provides is excessive for measuring the roughness of laser-machined surfaces. A comprehensive description of STM and other surface texture measuring instruments that were not covered in the framework of this thesis can be found in the following literature source [98]. From the features and limits provided in table 1.2, several conclusions can be drawn. If the maximum resolution is needed, either AFM or STM (only for conductive samples) is the best choice. However, the acquisition times using the former instruments will be in the range of hours to days. If the roughness of a single profile is of interest and the sample is not prone to contact damage the stylus instruments are the best for the task, as they offer exceptionally good resolution and are straightforward to use. However, if the task includes measuring the roughness of an area instead of a profile, optical instruments prove to be the most time-efficient. The fast galvanometer mirrors allow to measure the entire field of view of an objective within a few minutes. The resolution of modern scanning confocal microscopes is usually sufficient for the measurement of laser-machined surfaces. However, if a higher resolution is needed, a WLI optical profiler can be used. In addition to fast acquisition times, optical instruments also provide a non-contact type of measurement, allowing to safely measure various biological or otherwise soft specimens. Given all that was said, the optical instruments, namely scanning laser microscope with or without the addition of an interferometric objective are the best choice for measuring the roughness of laser-machined surfaces as of today.

Table 1.2 Comparison of surface topography measurement techniques.

	Atomic force / scanning tunneling microscope	**Stylus profiler**	**White light interferometric optical profiler**	**Confocal microscope**
X, Y resolution	0–10 nm (AFM) / 0.1 nm (STM)	50 nm (stylus radius dependent)	0.5 μm (NA objective dependent)	0.5 μm (NA objective and lateral sampling dependent)
Z resolution	0.1 nm (AFM) / 0.01 nm (STM)	0.25 nm	0.3 nm	1–20 nm (dependent on objective magnification)
Field of view	Typically up to 120 $\times$ 120 μm	Up to 200 mm	100 $\times$ 100 μm to 10 $\times$ 10 mm, extendable by stitching	100 $\times$ 100 μm to 10 $\times$ 10 mm, extendable by stitching
Measurable height range	Up to 20 μm	1 mm	8 mm (or limited by the working distance of the objective)	Limited by working distance of objective
Sample preparation	Little or none	None	None	None
Contact technique	Optional	Yes	No	No
Special surface requirements	STM: only conductive surfaces	Surface damage possible due to high forces	Needs correction for dissimilar materials and film coatings	Needs correction for dissimilar materials and film coatings
Scanning	Point by point	Point by point	Full field of view	Point by point
Full-field dynamic motion of sample measurement	No	No	Yes	No
Through the glass measurement	Not possible	Not possible	Possible	Possible
Film thickness	Only if the film has a step	Only if the film has a step	Minimum 0.1 μm	Minimum 0.1 μm
Measurable optical properties of the surface or film	Indirectly, through correlation with topography	No	Yes	Yes
Other measurable material properties	Numerous: adhesive, electric, magnetic, visco-elastic, elastic, ...	No	No	No

In addition to the discussed tools, the scanning electron microscope (SEM) is also often utilized for the inspection of laser-processed surfaces. Unlike a laser scanning microscope or stylus profiler, the SEM cannot measure surface height deviations directly; Instead, it visualizes surface topography qualitatively by detecting variations in secondary electron emission caused by surface features, slopes, and morphology. The resulting images represent contrast related to surface structure rather than absolute height deviations, so topographical information typically has to be interpreted visually. However, since SEM

uses an electron beam for imaging, the achievable lateral resolution is in the range of 1-10 nm [99], greatly surpassing that of optical imaging devices. This property of SEM, makes it a compelling tool for imaging laser-processed surfaces when capturing the smallest surface features is of interest, for example, when investigating laser-induced periodic surface structures [100] and others. Furthermore, if a cross-section of the surface is available, by positioning it at a 90° angle in respect to the electron beam, the inspection and evaluation of surface roughness (to some extent) is also possible.

1.2 Laser ablation

Laser ablation refers to the process of using laser radiation to remove material from a surface by melting, fusion, sublimation, ionization, erosion, and/or explosion [101]. The amount of material removed will be determined by the laser radiation and material properties. Laser fluence, pulse duration, and wavelength define the laser input, whereas the material's absorption and reflection properties govern the acceptance of laser energy. Furthermore, once laser energy is deposited in the material, depending on the material's thermal properties and laser-matter interaction duration, the material can undergo different phases until it is removed from the surface in the form of nanoparticles, liquid droplets, or even solid exfoliations. Moreover, even after laser ablation is finished, the laser-matter interaction can continue, with residual heat dissipating in the vicinity of the formed crater. Eventually, a well-defined heat-affected zone is formed, where original material properties are altered. In this long chain of events, the first and foremost important mechanism is laser absorption in the material, as without it, the laser ablation wouldn't be possible. Hence, in the following, the mechanisms behind laser absorption in the material will be discussed in more detail.

1.2.1 Linear absorption

Laser absorption is described as the process by which electromagnetic radiation from a laser transfers energy to a material through light–matter interaction, resulting in a reduction of the laser's intensity as it propagates through or impinges on the medium. This reduction in radiation intensity as it travels through the medium follows an exponential decay governed by the Beer–Lambert

law [102]:

$$I(z) = I_0 e^{-\alpha z}. \tag{1.17}$$

Here, I_0 represents the initial intensity, $I(z)$ is the intensity after propagating a distance z, and α denotes the absorption coefficient. Given the exponential decay nature of this law, the light penetration depth δ can be derived. It shows the propagation length $z = \delta$, at which the intensity of laser radiation attenuates to the level of $1/e$. By substituting $I(z) = \frac{I_0}{e}$ in the equation 1.17, we get that:

$$\delta = \frac{1}{\alpha}. \tag{1.18}$$

It shows that the depth δ at which the laser radiation is absorbed is inversely proportional to the absorption coefficient. Consequently, a higher absorption coefficient leads to a shallower light penetration depth, resulting in the formation of modifications with smaller depth, and vice versa. As evident, the absorption coefficient α plays a crucial role in laser micromachining, determining the depth of the craters and other related features. In general form α expresses as:

$$\alpha = \frac{4\pi k}{\lambda}, \tag{1.19}$$

where k is extinction coefficient and λ - the wavelength of the laser radiation. The absorption coefficient α depends on both the irradiated material properties k and the characteristics of the laser radiation itself λ. Next, let's discuss the conditions when the α value peaks and absorption occurs.

In the simplest case, when considering single atoms, the absorption is described using the Lorentz model, in which the atoms are considered as sets of oscillating dipoles. Depending on the atomic composition (mass and restoring force), the dipoles exhibit characteristic natural resonant frequencies ω_0, that are expressed as [103]:

$$\omega_0 = \sqrt{\frac{K_s}{\mu}}, \tag{1.20}$$

where K_s is a restoring force and μ - reduced mass. If any of the natural frequencies ω_0 coincide with the frequency of an external electromagnetic wave ω - the resonance occurs, during which the energy is transferred from the external wave to the atom, resulting in peaked α value at ω_0. However, such a simplified explanation is only valid for a system of widely spread atoms, which

in reality closely corresponds only to gases. When the distance between atoms becomes sufficiently small (as in case of solids), the electrons of individual atoms begin to experience the electric fields generated by neighboring atoms, causing discrete absorption lines to broaden and form bands. The two broad bands are formed - valance and conduction [104]. Depending on the type of material the energy levels of the bands can overlap - as in case of metals or be separated by a bandgap as observed in dielectrics and semiconductors. In the latter, absorption occurs through interband excitations, meaning that only photons with energy greater than the bandgap E_g can be absorbed, promoting electrons from the valence band to the conduction. For example, the most commonly reported bandgap value E_g of fused silica - the material most extensively discussed in this thesis - is approximately 9 eV [105]. To excite an electron from valance band to the conduction across such a bangap would require a photon with $\lambda \leq 138$ nm. In practice, the fundamental absorption edge of FS is slightly higher, at $\lambda = 153$ nm [106], due to indirect nature of the gap, with its precise position strongly dependent on structural disorders and defects. Nevertheless, such short wavelengths already fall in the vacuum ultraviolet (VUV) range, meaning that it would be absorbed by the air. The requirement for vacuum conditions, together with the very limited availability of lasers capable of emitting at such wavelengths, makes linear absorption of laser radiation in fused silica nearly impossible. Furthermore, currently available industrial femtosecond lasers typically use Yb:KGW as the active medium, featuring a fundamental wavelength of $\lambda = 1030$ nm, which is far from that required for linear absorption in fused silica. Therefore, absorption in such materials must be realized through alternative means, such as nonlinear absorption mechanisms.

1.2.2 Nonlinear absorption

The local generation of free electrons through nonlinear mechanisms can transform a normally transparent material into a strongly absorbing one. The critical free electron density required to initiate optical breakdown - a turning point at which a typically non-absorbing material becomes strongly absorbing - is $n_{\mathrm{cr}} = 10^{21}$ cm^{-3} for laser radiation of $\lambda = 1030$ nm. It signifies a free electron density at which laser radiation ω matches plasma frequency ω_p (see

equation 1.21) and expresses as [103]:

$$\omega_p = \sqrt{\frac{n_e e^2}{\epsilon_0 m_e}}, \tag{1.21}$$

$$n_{cr} = \frac{\epsilon_0 m_e \omega^2}{e^2}, \tag{1.22}$$

here, n_e is the electron density, e is the elementary charge, ϵ_0 is the permittivity of free space, and m_e is the electron mass. The nonlinear mechanisms that generate free electrons are: tunneling, multiphoton and avalanche ionizations. Multiphoton and tunneling ionization are processes that excite electrons into an initially empty conduction band and are effective only at high laser intensities $I > 10^{13}$ W/cm^2 [107]. In contrast, avalanche ionization does not require such high intensities, but it only initiates when the conduction band is already populated by a certain amount of free electrons, which are typically generated by the other two ionization processes. Which mechanism will dominate the initial generation of free electrons - multiphoton ionization (MPI) or tunneling ionization (TPI) - is determined by the Keldysh parameter [108]:

$$\gamma = \frac{\omega}{e}\sqrt{\frac{mcn\epsilon_0 E_g}{I}}, \tag{1.23}$$

here γ is Keldysh parameter, ω - laser angular frequency, I - laser intensity, m and e are the reduced mass and charge of the electron, c is the velocity of the light, n stands for the refractive index of the material, E_g is the band-gap energy and ϵ_0 is the permittivity of free space. Figure 1.8 illustrates the different ionization processes and the conditions under which they occur, expressed in terms of the Keldysh parameter. When $\gamma \leq 1.5$, the ionization occurs predominantly via tunneling, where the strong laser field distorts the Coulomb potential of the atom, allowing the electron to escape through the potential barrier without absorbing multiple photons. In the intermediate regime, $\gamma \approx 1.5$, ionization involves contributions from both tunneling and multiphoton ionization mechanisms, representing a transitional behavior. For $\gamma \geq 1.5$, ionization is dominated by MPI, in which the electron absorbs several photons simultaneously to acquire enough energy to overcome the atomic binding potential. It should be noted that there is no sharp boundary between tunneling ionization and (MPI); as a rough guideline, the transition is often considered to occur over the range

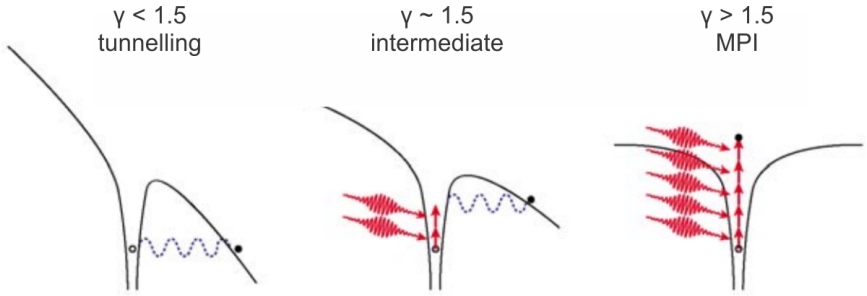


Fig. 1.8 Schematic diagram of the photoionization of an electron in an atomic potential for different values of the Keldysh parameter. In a solid, the electron is promoted from the valence to the conduction band, rather than ionized [108].

$0.5 \leq \gamma \leq 1.5$. Let us consider the typical parameters used in this thesis to determine the dominant ionization mechanism. By substituting $\lambda = 1030$ nm, $E_g = 9$ eV, and $I = 9.5 \times 10^{13}$ W/cm^2 (corresponding to $F = 20$ J/cm^2) into equation 1.23, we obtain $\gamma \approx 0.8$, indicating that both multiphoton and tunneling ionization contribute to the process, with tunneling ionization being the dominant mechanism.

Once MPI and TPI generate a certain number of free carriers, avalanche ionization begins. In this process, the free electrons in the conduction band gain energy from the laser electric field and through collisions with ions - a mechanism known as inverse Bremsstrahlung [109, 110]. These energized electrons can then collide with bound electrons in the valence band, ionizing them and producing additional free carriers. This leads to an exponential increase in electron density, even at laser intensities lower than those required for multiphoton or tunneling ionization, highlighting the effectiveness of avalanche ionization even during the trailing edge of the laser pulse. Considering the ionization mechanisms described above, the temporal evolution of the free-electron density can be expressed as [111]:

$$\frac{\partial N^e}{\partial t} = W_{MPI}(N_0 - N_e) + W_{TPI}(N_0 - N_e) + \eta N_e - \alpha N_e, \tag{1.24}$$

where N_e denotes the free-electron density, N_0 represents the atomic density, η represents the avalanche ionization rate, and α is the recombination rate of free electrons. The term W_{MPI} is the multiphoton ionization (MPI) rate coefficient,

defined as:

$$W_{MPI} = \sigma^K \left(\frac{I}{h\omega}\right)^K N_0, \tag{1.25}$$

where σ^K is the multiphoton ionization cross section (reported values for fused silica : $\sigma^4 = 2.05 \times 10^{-114}\text{cm}^8\text{s}^3$ and $\sigma^8 = 7.6 \times 10^{-240}\text{cm}^{16}\text{s}^7$ [112]), I is the laser intensity, and K is the number of photons required for multiphoton absorption. The term W_{TPI} stands for tunneling ionization rate coefficient and follows Ammosov, Delone, and Krainov (ADK) expression [113]. The last term in the rate equation, corresponding to the recombination of free electrons, is only relevant for pulse durations longer than $t_p \geq 1$ ps. Therefore, it can be neglected, since this thesis considers only femtosecond laser ablation. Figure 1.9 shows the temporal evolution of free electron density in fused silica when a high intensity $t_p = 100$ fs pulse is applied. In this example only MPI and avalanche ionization are considered. It is observed that at the early stage of the

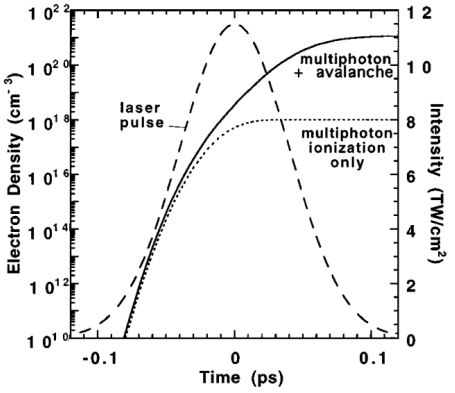


Fig. 1.9 Total (solid) and multiphoton produced (dotted) electron densities are plotted along with the Gaussian pulse shape. Seed electrons are produced by multiphoton ionization at the pulse peak after which an avalanche produces a critical density [111].

laser pulse, free electrons are primarily generated through the MPI process. As the electron density increases and the laser intensity approaches its maximum, avalanche ionization becomes significant, contributing to further growth of the free electron density. When the electron density produced by MPI approaches $\approx 10^{17}$ cm^{-3} [114], the avalanche ionization rate starts to exceed that of MPI. Although, the exact contribution from either ionization process depends strongly on the pulse duration and irradiance values [115]. The combined action of these two mechanisms enables the electron density to reach the critical plasma density

n_{cr} within the duration of a single laser pulse. Once the critical plasma density is generated, the dielectric is turned into a state similar to that of a conductor and the remaining incident laser energy is either absorbed in the plasma via inverse Bremsstrahlung heating or is reflected from it. Which effect will dominate depends on the scale length L - the characteristic spatial length over which the plasma density changes significantly, indicating the spatial sharpness of induced plasma boundary. The scale length approximates as $L_{max} \approx v_s \tau_p$, where $v_s = (ZkT_e/m_{ion})^{1/2} \approx 10^6$ cm/s is ion sound velocity for fused silica [114]. The laser radiation will be strongly absorbed if $L > \lambda$, where λ is laser radiation wavelength, and mainly reflected if $L < \lambda$. For the typical pulse duration value used in this thesis $\tau_p = 210$ fs, the estimated scale length is $L = 2.1 \times 10^{-3} \mu$m, indicates that most of the remaining pulse energy will be reflected. Figure 1.10 shows how the reflectivity of typically transparent fused silica depends on the incident laser intensity. The governing equations, which incorporate the complex dielectric function ϵ_t together with the Fresnel equations, are provided in Ref. [114]. The figure showcases that as the laser intensity increases, a progressively larger portion of the incident laser beam is reflected from the surface. Considering typical intensity values used in the thesis estimated earlier to be $I = 9.5 \times 10^{13}$ W/cm^2, we can see that only $\sim$ 30 % of the incident laser pulse will be absorbed in the surface of fused silica. By further considering the dynamic dielectric function ϵ_t, the skin depth l_{abs},

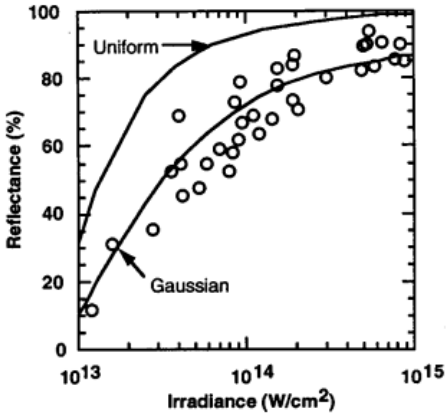


Fig. 1.10 Reflectivity of fused silica as a function of laser irradiance for $\lambda = 1053$ nm and $\tau_p = 350$ fs. Calculations of R values for two cases are given when laser beam has a uniform and gaussian intensity distributions. Governing equations are given in ref. [114].

which shows how deeply the electromagnetic field penetrates in the plasma before its amplitude falls to the level of 1/e, can be estimated. The skin depth is calculated as:

$$l_{abs} = c/(2\omega_l \kappa), \tag{1.26}$$

where $\kappa = Im(\sqrt{\epsilon_t})$ and $\omega_l = 2\pi c/\lambda_l$ is laser radiation angular frequency. More detailed expressions are given in ref. [116], where the authors estimate the skin depth in fused silica at the critical plasma density ($n_e \approx 3 \times 10^{21}$ cm^{-3}) to be $l_{abs} \approx 100$ nm for a femtosecond laser pulse with a fluence of $3.9F_{th}$. Equation 1.26 highlights that the light penetration depth during femtosecond laser ablation is a dynamic quantity, strongly dependent on the generated electron plasma density and the laser wavelength, and is typically on the order of hundreds of nanometers. The light penetration depth typically indicates the depth of the laser-induced modifications. However, while this is typically true at low fluence values (e.g. $F < 0.5$ J/cm^2 for copper), at higher fluences the resulting modification depth is extended due to increased effective penetration of hot electrons [117].

The discussion concludes that absorption in a typically transparent material, such as fused silica, is achieved through the initiation of optical breakdown. During this process, a dense local plasma of free electrons is generated via nonlinear ionization mechanisms, namely multiphoton, tunneling and avalanche ionization. The resulting free-electron plasma absorbs the remaining fraction of laser pulse through mechanisms similar to those occurring in metals, or reflects it, depending on the plasma scale length and laser pulse duration. The complex physical processes governing free-electron plasma formation and its subsequent coupling with electromagnetic waves have led to the development of numerous numerical models [118], each applicable under specific constraints, while a single universal model valid across the full range of materials and intensity regimes has yet to be established. Nevertheless, once the laser pulse energy is deposited in the material, it undergoes various phase transitions, which eventually lead to the removal of the material. The precise mechanisms behind it will be discussed in detail in the following section.

1.2.3 Mechanisms of material removal

After the laser pulse is absorbed, depending on its parameters (wavelength, pulse duration and irradiance) the laser-matter interaction composed of diverse

processes will take place with the final result of a material modification or removal. Within the scope of this thesis, the interaction between femtosecond laser pulses and dielectric materials is of primary importance and will be the main focus of discussion. The main stages of laser ablation during such interaction is given in Figure 1.11 parts (a)-(d). In the first picosecond, the incident laser

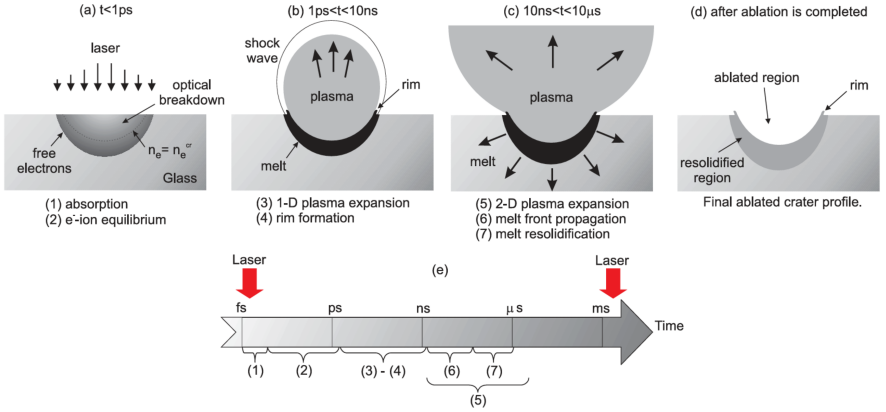


Fig. 1.11 A schematic description of ablation process of glass with a femtosecond laser pulse (a)–(d) and time scales associated with various processes (e) [119].

energy is absorbed by electrons through multiphoton and avalanche ionization to induce optical breakdown. Upon absorption the energy from the electrons is transferred to the lattice on the time scale of few picoseconds [120]. As the electrons and ions thermally equilibrate, a high-pressure and high temperature plasma of electrons and ions is formed above the surface. At early times (less than 10 ns), the plasma expands primarily in the direction perpendicular to the target surface [121]. In the later stages, the plasma expands in both the lateral and perpendicular directions and removes the ablated material from the surface. The largest portion of the absorbed energy is used in the formation of the plasma and its expansion in the ambient gas [122]. However, the Beer-Lambert law assumes that a small fraction of the laser pulse with fluence below the ablation threshold will remain in the target as thermal energy. The thermal energy deposited in the bulk of the glass forms a transient shallow molten zone below the expanding plasma. During plasma expansion, the front of the molten material propagates into the bulk as a result of the heat diffusion. When the temperature of the melt decreases below the melting temperature the melt resolidifies. The high pressure plasma (which can reach 10^7 atm at the initial moment [119]) acting on the molten material drive the liquid from the center to the edges of the crater

during the melt lifetime. Depending on the pulse duration, intensity and the size of the crater, the molten material can be either ejected on the surface and form an elevated rim around the ablated crater or remain within the ablated cavity if the plasma induced pressure gradient is insufficient to move the melt extended distances. The timescales governing these processes are given in figure 1.11, part (e). As observed, the entire sequence of events can extend across up to ten orders of magnitude in time, ranging from femtoseconds to microseconds or even milliseconds. Material ejection can occur multiple times throughout the described sequence of events, depending on the processing parameters, and may take several forms [101]. Under standard femtosecond laser irradiance (10^{10} – 10^{14} W/cm^2) the material is initially ejected in the form of hot electrons, followed by the emission of nano-sized particles or their clusters, which are mainly formed through the condensation of the expanding plasma plume of vaporized material and the release of accumulated pressure [118]. Additionally, liquid ejection of particles several micrometers in size can occur due to strong pressure gradient forces within the rapidly expanding vapor plume acting on the thin layer of remaining molten material. Finally, exfoliation of the solid sample pieces can also occur due to the large thermal stress gradients of the fast heating process; thermal stresses can break the sample into irregular-shaped particles, ejecting them from the surface. Contributing to the topic, Minok Park et. al. [123] have conducted a time-resolved scattering imaging of femtosecond laser ablation of Cu to unveil the dominant material ejection mechanisms. The scattering images showcasing the ablation dynamics of a single 500 fs pulse with fluence of 18.7 J/cm^2 are given in figure 1.12. The images disclose two different material ejection mechanisms. Within the first 200 ns, a continuous streak of ejected particles is observed (denoted in the figure as particles “A”). Based on an estimated velocity of 350 m/s and a size on the order of several hundred nanometers, these particles are attributed to a spallation mechanism [124]. Spallation is a photomechanical material ejection mechanism that occurs when significant tensile stresses build up within a confined volume. Upon relaxation of the laser-induced stress, the upper layer of the material is expelled in the form of nanometer-sized particles or droplets. Such stresses can be only realized when the laser heating (pulse duration) is shorter than the time required for the mechanical relaxation (expansion) of a material, a condition only achievable with ultrashort laser pulses [125]. Further analysis of figure 1.12 reveals a second material ejection mechanism occurring between 300 ns

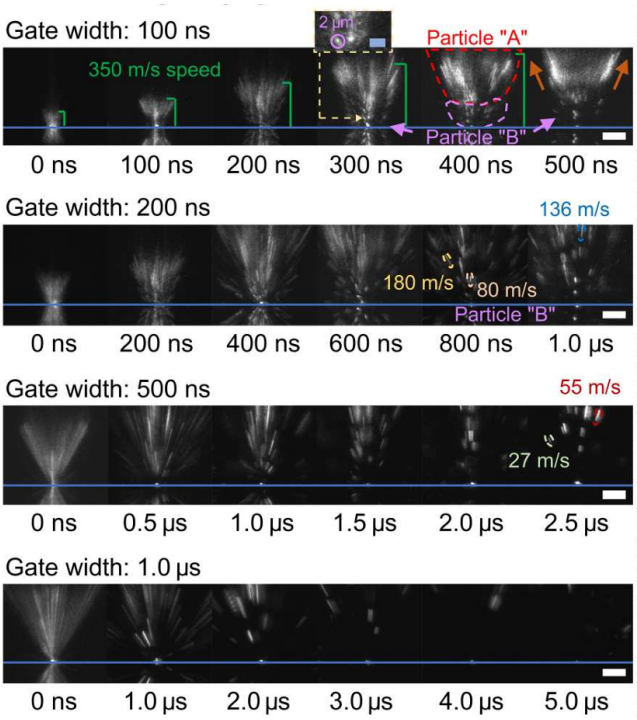


Fig. 1.12 Scattering images showing the ablation dynamics at a fluence of 18.7 J/cm^2 and pulse duration of 500 fs, across different time scales. Scattering images were acquired for varying ICCD gate widths of 100 ns, 200 ns, 500 ns, and 1 μs, respectively. The blue lines in these images represent the Cu target surface, and images below the lines are mirror reflections from the polished Cu surface. White scale bars, 50 μm [123].

and 4 μs after the initial laser–matter interaction. In this case, the material is ejected in the form of μm sized particles, denoted as particles "B" in the figure. The estimated velocity of 27 to 180 m/s, together with the particle size and ejection timing, suggests that these particles originate from hydrodynamic instabilities within the shallow melt layer, driven by the high-pressure plasma. It is further noted, that such particles were observed only when fluence values of $F > 18.7$ J/cm^2 were used, implying the need of high pressure plasma to drive the melt expulsion. In contrast, the ejection of particles "A" was observed in all cases, even with fluences as low as $F = 3.7$ J/cm^2. Furthermore, at even lower intensities, close to the ablation threshold, an additional material ejection mechanism during femtosecond laser ablation - Coulomb explosion - may occur [126]. In this process, highly excited electrons are emitted from the target surface, leading to charge separation between the escaping electrons and the

remaining positively charged ions. This separation creates a strong electric field, commonly referred to as the space - charge effect. Charge separation takes place when the energy absorbed by the electrons exceeds the Fermi energy - effectively the sum of the electron binding energy (in dielectrics) and the work function, allowing electrons to escape from the material. If the energy of these electrons is sufficiently high, the resulting electric field becomes strong enough to overcome the binding forces of ions within the lattice. At the same time, the loss of electrons from the surface induces electrostatic repulsion among the positively charged ions, driving them apart. As a result, ions are ejected from the surface, leading to the removal of the first few monolayers (on the order of several nanometers) within the optical skin depth. Such a gentle ablation mechanisms allows to machine the surface very precisely without any increase in surface roughness. However, existing literature [127, 128] suggests, that laser intensity range under which this regime is achievable is very narrow, making it difficult to maintain. It was demonstrate that even in the Coulomb explosion regime, small defects may form with each laser pulse [129]. With prolonged ablation (number of pulses > 20), increased absorption at these defect sites leads to a transition from the Coulomb explosion regime to a thermal ablation regime, despite the laser intensity remaining unchanged.

In summary, the material can be ejected in several different ways during femtosecond laser ablation of dielectric materials. At low intensities, near threshold values, a very gentle, non thermal ablation (few nm per layer) can be achieved via Coulomb explosion. Intensity values higher than threshold will result in material removal via other mechanisms such as - photomechanical spallation (already observed at $F = 3.7$ J/cm^2 when ablating FS [123]) and thermal vaporization. Finally, at much higher fluences $F > 18.7$ J/cm^2, in addition to already mentioned material ejection mechanisms, the melt expulsion in the form of μm sized particles and phase explosion, i.e., the explosive boiling of a superheated melt due to spontaneous vapor bubble nucleation, are observed. Additional material removal mechanisms such as fragmentation are discussed in the literature [130]. However, due to limited data on their presence in the femtosecond laser ablation of dielectric materials, further discussion regarding these mechanisms is omitted.

1.2.4 Laser-induced stress and rapid solidification

During ultrashort laser matter interaction, the fast rate of energy deposition leads to rapid localized heating (reaching rates of 10^{14} K/s [131]) of the target material, which unavoidably results in the generation of stress. The laser-induced stresses can be grouped into three categories: (1) dynamic transient stresses and stress waves generated due to the condition of stress confinement, (2) long-term quasi-static thermo-elastic stresses related to the temperature gradients, and (3) residual stresses due to the laser-induced structural changes (defects) in the material. Laser-generated stresses are particularly high under stress confinement conditions (in the range of GPa [132]), which are satisfied when the laser heating time (defined by the pulse duration) is shorter than the characteristic mechanical relaxation time. As discussed in the previous chapter, these stresses are often relieved through material removal in the form of spallation. However, in addition to material spallation the relaxation of strong compressive and tensile stresses may also result in subsurface void formations [133, 134]. Deeper in the target, the remaining deposited laser energy can create high temperature gradients, that result in thermo-elastic stress buildup. The thermo-elastic stresses (with magnitude in the range of hundreds of MPa [135]) in the bulk of the region cannot fully relax because lateral expansion is constrained by the surrounding material. The induced thermo-elastic stress can give rise to birefringence and subsurface structural defects. If the local fracture strength is exceeded, it may additionally result in the formation of surface and subsurface microcracks [135, 136]. If the induced defects and other kind of structural modifications remain in the target even after the material cools down, it said that residual stress is induced. Collectively, these stress-induced defects, cracks, voids, and structural modifications can alter the material's optical and mechanical properties, thereby modifying the coupling and energy deposition of subsequent laser pulses.

In addition to material removal and stress generation, during the laser matter interaction, a shallow transient melt zone is typically formed. As discussed in the previous section, the pressure exerted by the laser-generated plasma can displace the molten material and partly eject it from the ablated crater. The remaining melt eventually solidifies, forming the modified surface with which subsequent laser pulses interact. Therefore, it is important to understand the structural modifications that may occur during solidification, as they can directly affect

further coupling of laser energy into the target. The solidification process varies significantly between materials due to differences in their internal structure (e.g. crystalline, amorphous, or polycrystalline) and thermal properties, particularly thermal conductivity. Since the thesis focuses on ablation of glasses, only the solidification of such materials (e.g. fused silica glass) will be covered here.

After laser-induced melting of glass, the remaining melt cools primarily through heat conduction into the surrounding solid material. Owing to the highly localized energy deposition and the small dimensions of the molten region, extremely steep temperature gradients are established, leading to estimated initial quenching rates on the order of 10^7-10^9 K/s [137]. However, the cooling rate decreases rapidly as the material approaches thermal equilibrium. For example, [138] reported an effective cooling rate of approximately 50 K/s during the glass transition of laser-modified fused silica, demonstrating that the cooling rate evolves significantly throughout the solidification process. Unlike crystalline materials, amorphous glasses do not normally undergo crystallization during resolidification. Instead, the melt undergoes a glass transition, where the viscosity increases continuously over many orders of magnitude until atomic rearrangement becomes too slow and the liquid structure becomes frozen into a metastable amorphous state (see the transition in figure 1.13). The structure preserved after solidification therefore depends on the cooling rate and is commonly characterized by the fictive temperature (T_f). The fictive temperature is defined as the temperature at which the atomic arrangement of a glass becomes effectively frozen during cooling, i.e., the temperature at which structural relaxation can no longer keep pace with the decreasing temperature [139]. Faster cooling suppresses structural relaxation and freezes the glass at a higher fictive temperature, resulting in a less relaxed, higher-energy structure with greater free volume. Conversely, slower cooling allows the atomic network to rearrange toward thermodynamic equilibrium for a longer period, leading to a lower fictive temperature and a denser, lower-energy glass structure. Accordingly, glass resolidified following ultrashort laser irradiation features an elevated fictive temperature relative to the untreated material, suggesting altered density and refractivity index values. Furthermore, rapid quenching can preserve a high concentration of laser-induced point defects within the resolidified glass. In fused silica, the most commonly observed defects include oxygen-deficient centers (ODCs), E centers, and non-bridging oxygen hole centers (NBOHCs) [140, 141]. Together with the elevated fictive temperature,

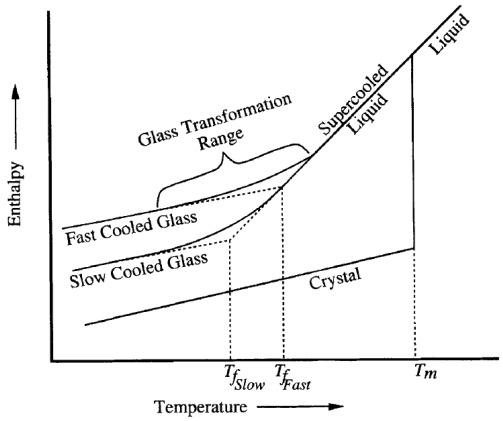


Fig. 1.13 Effect of temperature on the enthalpy of a glass forming melt. T_{fslow} here is fictive temperature for slow cooled melt, whereas T_{ffast} is a fictive temperature for fast cooled melt. T_m denotes melting temperature [139].

these structural modifications alter the optical and mechanical properties of the glass and may consequently influence the absorption and energy coupling of subsequent laser pulses.

1.3 Attainable surface roughness levels after laser ablation

The previous chapter discussed the laser-matter interaction, along with laser ablation and the dominant material removal mechanisms. It showed that a single laser pulse produces a crater whose shape closely follows the intensity distribution of the applied laser beam. Depending on the parameters of laser radiation and focusing conditions, craters of different depths and shapes can be formed. In addition to the formation of the crater, laser ablation may also result in the formation of heat affected zone (HAZ) surrounding the ablated cavity and the formation of the defects both on the surface and sub-surface. When performing laser ablation of an area, the laser beam is scanned on the surface in a chosen manner. The superposition of the individual craters results in an ablation of the cavity. The roughness and the texture of the bottom of the cavity will depend on all of the aforementioned laser and scanning parameters. Therefore a thorough understanding of different parameter impact on laser-matter interaction is essential in order to be able to predict and control the resulting

surface roughness during laser ablation. In this chapter, we will discuss how different laser parameters influence the quality of the surface after the laser processing. In addition, the discussion will address not only the effects of laser parameters but also the impact of scanning strategies on the resulting surface texture. Finally, the presented literature overview will serve as a foundation for the results developed in the course of this thesis.

It is further noted, that as the thesis is orientated around surface roughness control via laser ablation, the attainable surface roughness values via remelting of the top surface layer [26] using CO2 laser polishing or other laser based non-ablation techniques will not be discussed for now.

1.3.1 Different laser parameter impact on the surface quality after laser ablation

The laser parameters that have the greatest influence on the resulting surface quality are the laser wavelength, pulse duration, and pulse energy. How big of a difference the exact laser parameter will have on the resulting surface roughness will also depend on the material that is being processed.

When talking about pulse duration, it is imperative to understand the timescales at which different laser-matter interaction processes take place. As we can see from the figure 1.14 the energy transfer from the electrons to the lattice is happening within the first 10 ps. Shortly thereafter (after several hundred of ps after the laser pulse irradiates the surface) the plasma expansion in the ambient commences. If the pulse duration is in ns scale, the latter part of the pulse will interact with the expanding plasma plume. The interaction can include the absorption or the reflection of the laser radiation by the plasma plume as well as the distortion of the laser beam wavefront [142, 143]. The former typically have a negative impact on the quality of the ablation process. In addition, When using longer pulses (ns and longer), electrons and lattice have sufficient time to reach the thermal equilibrium during a single pulse excitation. After the thermal equilibrium is reached the rest of the laser pulse is used to heat the lattice. The heating of a lattice is described via a traditional heat conduction equation:

$$\rho c_p \frac{\delta T}{\delta t} - k \nabla^2 T = Q(r,t), \tag{1.27}$$

here ρ is the density, c_p is the specific heat at constant pressure, and k denotes the conductivity of the material. In such a case, the removal of the material is

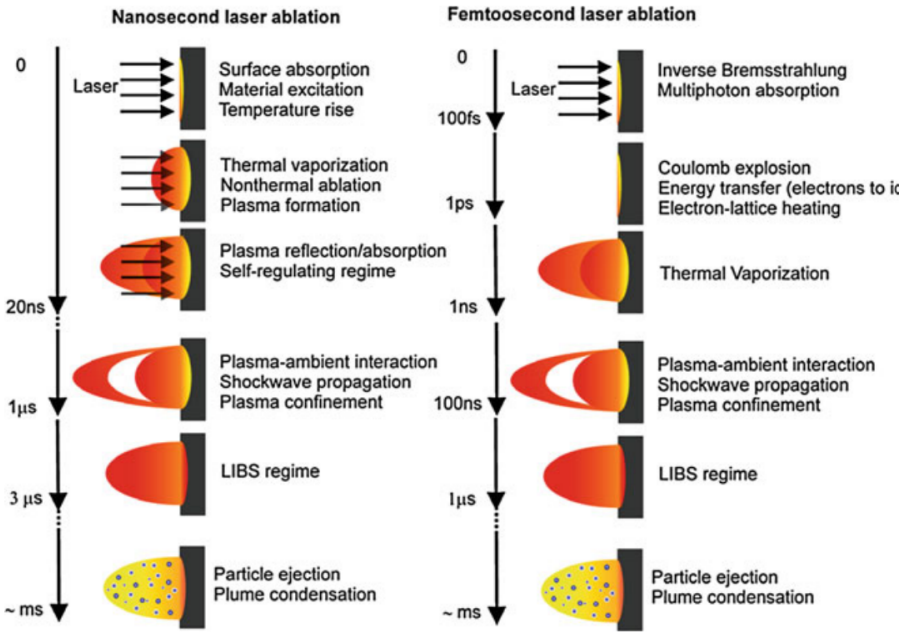


Fig. 1.14 Approximate time scales of nanosecond and femtosecond energy absorption and laser ablation along with various processes happening during and after the laser pulse [126].

achieved when the lattice is heated to the vaporization temperature. Therefore, the ablation of long laser pulses (ns and longer) is said to be purely thermal. During the heating of the lattice, the heat also diffuses into the bulk of the material. The heat diffusion length (l_t) can be evaluated using the following formula [144]:

$$l_t \approx 2\sqrt{D_T \tau_l}, \tag{1.28}$$

here $D_T = k(\rho c_p)^-1$ is the heat diffusivity, τ_l is the laser pulse duration. As evident from the equation 1.28, the heat diffusion length as well as the heat-affected zone will be larger for pulses with longer pulse durations. Under such conditions, the large volume of solidified molten material will lead to the formation of irregular crater shapes of poor surface quality. The example of a hole drilled using ns pulses is depicted in figure 1.15, on the left. As can be seen, the hole exhibits rims of high amplitude that are an indication of material melting during laser-matter interaction. In addition, it can be observed that the inner walls of the hole are also irregular and of high surface roughness. On the other hand, we can see that when performing laser drilling using fs pulses (see

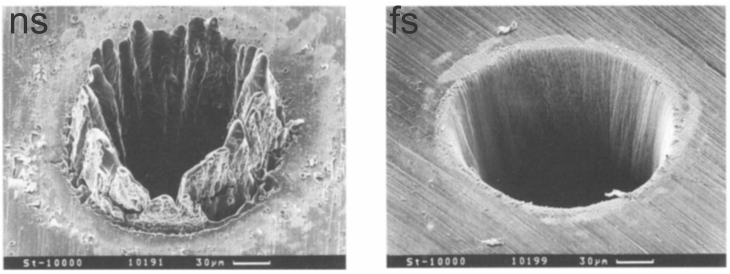


Fig. 1.15 A comparison of holes drilled using ns pulses (on the left) and fs pulses (on the right) [145].

figure 1.15, on the right) the hole quality is much better compared with the case when ns pulses are used. Due to the extremely short durations of ultrashort pulses (of fs scale), all the pulse energy is absorbed before the energy transfer from electrons to the lattice starts to take place [146]. Because of that, there is no interaction between laser pulse and plasma plume as well as no excessive heating of the lattice. In addition, due to the shorter pulse duration, the heat diffusion length is smaller, reducing the heat-affected zone (HAZ) substantially. Due to former reasons, the craters generated using fs pulses are of regular shape, high quality, and low surface roughness. The benefits of using femtosecond pulses in regard to surface roughness are supported by numerous studies. Andrius Žemaitis et al. investigated the machining of aluminum with ns and ps pulses [147]. The authors demonstrated that the use of picosecond (ps) pulses for laser micromachining of aluminum reduced the surface roughness by a factor of five, yielding an R_a of 0.2 μm compared with 1 μm obtained using nanosecond (ns) pulses. In another study, authors compared the ablation of molybdenum with ns and fs pulses [148]. The results showed that when fs pulses were used the achieved surface roughness was around 10 times smaller (R_a - 0.25 μm) compared to a case when ns pulses were used (R_a - 2.3 μm). Moreover, Utez el. al. [149] have demonstrated that reduced pulse duration, even on the fs scale, results in further increase of surface quality. Authors compared the quality of the craters formed on fused silica with pulse durations of τ_p = 7 fs and τ_p = 450 fs. The results disclosed that a crater formed with τ_p = 7 fs was of much better surface quality and exhibited a more regular shape. In addition, the craters were of smaller depth when using pulses with τ_p = 7 fs, due to early formation of overcritical plasma (corresponding to density of generated free carriers $n \gg n_{cr}$), which reflects the trailing edge of the laser pulse, preventing

further energy deposition in the material. The reduced depth of the crater enables a more precise laser processing with the possibility of achieving better final surface quality. In summary, pulse duration has a significant influence on the surface roughness produced by laser processing, with shorter pulses generally resulting in improved surface quality due to reduced thermal effects and greater processing precision.

Another important laser parameter that has a great influence on resulting surface quality after laser micromachining is laser wavelength. The absorption mechanism of each individual material heavily depends on the wavelength of the laser radiation, which directly correlates with the energy of individual photons (see previous chapters for more). The majority of today's femtosecond industrial lasers generate laser radiation in the near IR part of the spectrum (for example Yb:KGW based lasers generate λ - 1030 nm wavelength laser radiation). To initiate absorption in dielectrics with such laser radiation wavelength, high laser radiation intensities are necessary. This in turn require high laser fluence values, under which severe material ejection mechanisms, such as phase explosion, melt expulsion or fragmentation can take place (see previous chapter for details). Such processes tend to generate high volumes of debris, which contaminate the surface and contribute to further increase in surface roughness. In addition, high fluences also contribute to the increase of HAZ, which we have already seen to have negative impact on the final surface quality. Furthermore, the equation 1.26 highlighted that skin depth (indicated how deep EM penetrate) decrease for shorter-wavelength radiation. It suggests, that shorter λ values enable the formation of craters with smaller depth and therefore - a more precise ablation. In addition to that, with smaller penetration depth and increased absorption at smaller wavelength values the formed heat affected zone is reduced. HAZ exhibit different mechanical and chemical properties and can appear as burns, cracks, or even residues of molten material. All of the above contribute to the increase of surface roughness and are to be avoided if a smooth surface finish is required. N. Muhammad et. al. [150] have compared the nitinol and platinum-iridium alloy micromachining using different laser wavelengths. The authors showed that when using laser radiation with a wavelength of λ = 1064 nm, the resulting cuts exhibit burr formation, dross accumulation, and heat-affected zones extending up to 30 μm. However, when laser radiation with a wavelength of λ = 343 nm was used for material cutting, no dross was detected after machining, and the cut edges appeared smooth and clean. In addition, the HAZ was reduced down

to 15 μm. Another study [151] indicates that due to high photon energy and good absorption properties UV laser radiation is excellent for polymer ablation. Authors show that the polymer ablation with UV lasers is relatively cleaner with less HAZ when compared to mid-IR laser processing of polymers. In a separate recent study [152] it was shown that, when machining N-BK7 glass, surface roughness values of $S_a = 130$ nm can be achieved using laser radiation of a wavelength of $\lambda = 266$ nm, whereas values of $S_a = 400$ nm are obtained under same conditions with $\lambda = 1030$ nm. The benefits of using shorter wavelengths are further supported by Cheriyan et. al. [153]. The authors show that the line roughness of processed fused silica surface can be reduced from $R_a \approx 400$ nm at $\lambda = 1030$ nm, down to $R_a \approx 100$ nm when the wavelength of $\lambda = 515$ nm is used. In summary, it is evident that for most of the materials, the use of shorter wavelength laser radiation will result in better surface quality after laser processing due to reduced HAZ and light penetration depth.

Moving on, the pulse energy influence on the resulting surface quality after laser processing should not be overlooked as well. It is important to note that the quality after laser processing depends more on the laser fluence or intensity rather than the pulse energy. However, the former ones are the result of laser parameters (pulse energy and pulse duration) and focusing conditions, therefore they cannot be regarded as true laser parameters. But since the change in pulse energy changes both the fluence and the intensity of laser radiation, we can state that the influence of processing quality on laser fluence is the same as on pulse energy assuming that focusing conditions are fixed. The dependence of processing quality on fluence arises from the fact that excessive pulse energy can lead to undesirable effects such as overmelting, cracking, excess burning, and others. Lamia El Fissi et. al. [154] have demonstrated the influence of fluence on resulting surface quality when processing piezoelectric substrates. The authors show that with increasing fluence, the surface roughness increases accordingly despite what scanning speed is used. When processing piezoelectric material - LiTa03, the change in fluence from 0.5 J/cm^2 to 3 J/cm^2 resulted in the increase of surface roughness by 4-fold, from R_a - 0.5 μm to R_a - 2 μm. Next, R. Vilar et. al. [155] in their study investigated the ablation of sapphire using femtosecond pulses when different pulse energies are used (see figure 1.16). The authors observed that after increasing the intensity of laser radiation to a certain level, the cracking of the surrounding areas around the hole starts to take place (see figure 1.16, part B). Cracking typically occurs due

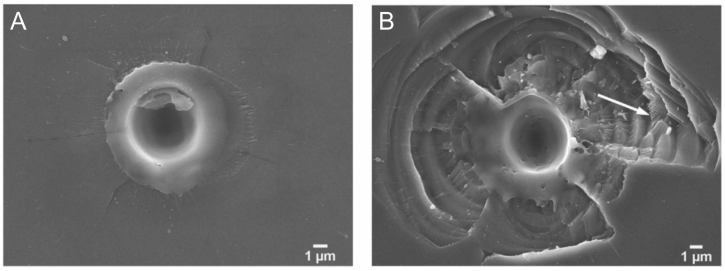


Fig. 1.16 Craters generated on sapphire with a stationary laser beam at a frequency of 1 kHz. (A) 30 μJ and 20 pulses, (B) 50 μJ and 40 pulses [155].

to an excessively high temperature gradient induced by the energy delivered through laser radiation (for more see section 1.2.4. A crater of such morphology exhibits high surface roughness and is typically regarded as a result of poor quality. These examples demonstrate that ablation at higher pulse energies tends to produce poor-quality craters as excessive energy deposition into the material leads to unfavorable laser–matter interactions, such as cracking and overmelting. Another study, led by A. Žemaitis et al. [156], building on the foundation of B. Neuenschwander [157], has shown the existence of an optimal fluence at which ablation efficiency is maximized while surface roughness is minimized. The authors investigated the ablation of cavities of pure copper substrates. They have found that ablation efficiency is maximized when operating at fluence $F_{optimal} = F_{th} \times e^2$, where F_{th} is threshold fluence. In addition, the authors observed that at the same fluence value where the ablation is the most efficient, the smallest surface roughness is achieved. The authors demonstrated that the minimum surface roughness achieved for copper after laser ablation was as low as R_a = 200 nm. The reasoning behind such coincidence that both main laser processing parameters (ablation efficiency and surface roughness) can be optimized under the same condition is not yet presented.

It is evident that laser processing parameters have a significant impact on the resulting surface roughness. When considering pulse duration, ultrashort laser pulses (fs and ps regimes) generally yield substantially improved processing quality compared to longer pulses (t_p > ns). This improvement is primarily attributed to the fact that, under ultrashort excitation, energy is deposited into the material on timescales shorter than those required for electron–lattice thermalization, thereby strongly suppressing heat diffusion and minimizing thermal effects that contribute to increased surface roughness. Next, the choice

of laser wavelength plays a crucial role in determining the dominant absorption mechanism. Shorter wavelengths, particularly in the ultraviolet (UV) spectral range, typically exhibit higher absorption in many materials and result in reduced heat-affected zones (HAZ), which in turn leads to improved surface quality after laser processing. Finally, pulse energy is another key parameter governing laser–matter interaction regimes. Excessive pulse energy can induce undesirable effects such as material cracking, overmelting, and increased debris formation, all of which contribute to higher surface roughness. Consequently, careful optimization of laser processing parameters is essential in order to achieve the desired surface finish. However, due to different laser-matter interactions, the optimal set of laser parameters is different and unique for each material. Moreover, the achievable roughness level at different depths is different and also parameter-dependent. Hence, achieving the desired surface finish at a specified processing depth typically requires a broad parametric study. However, this approach is often time-consuming and inefficient when used as the primary method for optimizing laser processing conditions. Currently, novel approaches are being introduced to replace the conventional parametric optimizations. Various effects of laser parameters on surface roughness are being investigated using machine learning models based on neural networks [158, 159]. While these methods show considerable potential for future applications, their current applicability is limited by the lack of sufficiently comprehensive databases required for model training. Another, completely different, but promising way to control the surface roughness is by implementing different scanning algorithms, rather than changing laser parameters.

1.3.2 Different scanning strategy impact on the surface quality after laser ablation

When processing surfaces, the laser beam is scanned over the surface in a chosen manner. To ablate a trench, the laser beam is scanned in a straight line. To ablate a rectangle, a superposition of multiple lines is realized. The scanning speed v and focusing conditions will determine the overlap of laser beams in a scanning direction, while offset between lines dy will determine the overlap of the beams in a perpendicular direction. Depending on the overlaps in x and y directions and the size of a laser beam at the focal plane, different surface morphologies will be realized. In order to attain sufficient depths during laser

processing the surface is scanned multiple times. During multilayer ablation, every layer can be positioned and scanned in a different manner. Every next layer can be rotated or shifted. The overlap in each layer can be changed or maintained. The layers can have different scanning patterns including linear, circular, etc. As evident, the variety of potential combinations in scanning techniques is extensive. The different scanning strategies can also be combined with varying laser parameters in order to achieve the desired surface finish. In this chapter, we will overview different scanning strategies presented in the literature, together with their influence on the resulting surface roughness.

When scanning the surface a single time one of the most important scanning aspects that determines the resulting surface roughness is the pulse overlap in x and y directions. The overlap of pulses is defined as:

$$\Omega_i = \left(1 - \frac{di}{D}\right) \times 100\%, \quad i \in \{x, y\}, \tag{1.29}$$

where $\Omega_{x,y}$ is the overlap of pulses in x and y directions, dx, dy - the distance between adjacent pulses in x and y directions, D - the diameter of a laser beam at a working distance. In some cases, crater overlap is considered, then, in equation 1.29, D denotes the diameter of a single crater instead of a beam diameter. Numerous studies are found in the literature that investigate the surface roughness dependence on the beam overlap. Typically, the studies focus on determining the optimal overlap value at which the roughness is minimized. In one study [160], the authors demonstrated that, during the ablation of soda-lime glass and fused silica, surface roughness is minimized at a pulse overlap of approximately 75%. The experiments were conducted using pulse energies below $E_p < 1$ μJ, which enabled the achievement of a surface roughness of R_a between 100 and 300 nm. The depth at which this roughness was obtained was not specified. The observation, that a combination of low pulse energy and high overlap results in a high-quality surface finish when ablating glasses was further validated by Tien-Li Chang [161]. He observed that when ablating soda-lime glass with femtosecond pulses of 5-10 μJ energy, the roughness is minimized when the overlap of pulses is Ω = 75 %. Under such conditions, the author managed to achieve roughness of 300 nm. The similar trend was reported by Žemaitis et. al. when ablating metals [162]. The group ablated copper using a picosecond laser and a conventional f-theta, galvo scanner combination for beam manipulation. The achieved surface roughness dependence on the

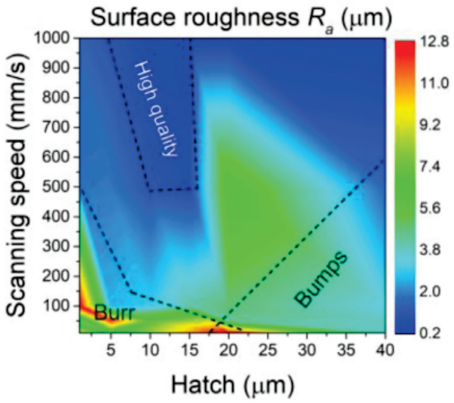


Fig. 1.17 The surface roughness of the bottoms of the cavities after one scan dependence on scanning speed and hatch distance with quality regions [162].

scanning speed and the hatch distance after a single scan is shown in figure 1.17. The authors have identified 3 different regimes that are achieved when using different laser scanning parameters: the regime where high-quality surfaces are formed after processing, a regime that results in the formation of surfaces with burr, and a regime where the surface after processing exhibits bumps. The parameters that led to the best surface finish were hatch - 10 μm and scanning speed 1000 mm/s, which recalculated in overlaps would appear as Ω_x = 96 % in scanning direction and Ω_y = 60 % in perpendicular to scanning direction. Under such conditions, authors achieved roughness of R_a = 0.2 μm. The search for optimal overlap values has also been reported in the ablation of silicon. In one study [163], authors indicate that Ω = 60 % results in the best surface finish when ablating silicon, while in another [164] it is shown that Ω = 20 % results in the lowest surface roughness during the same silicon processing. As can be observed, there is no universal optimal overlap value that yields minimum roughness across all materials. The optimal overlap value depends on the material and the combination of laser and focusing parameters. When using low fluences, typically high overlap values (Ω > 60 %) result in a high surface finish, as under such conditions the uniform energy deposition is achieved. On the contrary, if pulses are of higher energy values, the overlap yielding minimum roughness will be on the lower side (Ω < 30 %). Besides overlap, the laser beam intensity distribution can also have a significant impact on the resulting surface roughness. Reports in the literature [165–167] state, that the use of a top-hat intensity distribution beams for laser processing can

lead to improvements in surface roughness and structuring quality, especially in the reduction of taper angle of formed structures. However, generation of top-hat–shaped beams typically relies on diffractive optical elements (DOEs) [168] or other delicate techniques [169], which can complicate laser processing and impose additional constraints and attention requirements. Alternatively, the beam's intensity profile can be manipulated (elongated) by conducting laser processing at an angle rather than in the conventional perpendicular orientation. Nan Li et. al. [170] have demonstrated that laser ablation at small incidence angles (< 5 °) can be used very effectively in polishing surfaces that are initially rough. In their work, authors demonstrated that ablation of stainless steel at grazing angle - where the angle of incidence equals half of the beam divergence, enables the reduction of roughness from an initial S_a = 25 μm down to S_a = 0.2 μm, featuring the reduction of roughness equivalent to > 99 %. Authors reason this phenomenon by stating that at grazing angles, when the surface is ablated only by marginal rays, the formation of laser intensity-dependent zones (observed at other angles) is prevented, allowing the efficient and uniform polishing of the surface. Although laser processing at grazing angles is an effective polishing method for planar surfaces, it becomes impractical for deep cavities, pockets, and other geometries with shadowing sidewalls. Hence, in practice, perpendicular incidence remains the most commonly employed approach in laser processing. Beyond overlap, beam intensity distribution, and the factors already discussed, the laser scanning path can also influence the final surface roughness.

In a conventional manner, the desired-shaped area is scanned in a raster manner, line by line. Such a scanning strategy, where each line is scanned one after another is referred to as a sequential scanning method (SM). However, the scanning process can also be realized in manners other than sequential. Krystian L. Wlodarczyk et. al. [33] investigated an alternative scanning strategy called the interlacing scanning method (IM) and its influence on resulting surface roughness. The sequential (SM) and interlaced (IM) scanning methods are depicted in figure 1.18. During IM, some scanning lines are deliberately omitted at regular intervals during the first pass in order to be filled later in subsequent laser beam passes. In subsequent passes, the laser beam starts scanning at an offset equal to the hatch distance (ΔH) in relation to the previous pass, omitting an identical number of scanning lines as before. The interlacing is repeated until all the missing lines are filled in. The number of repetitions is defined as a

ratio of ΔIL to ΔH, where ΔIL is an interlacing distance [171]. The differences

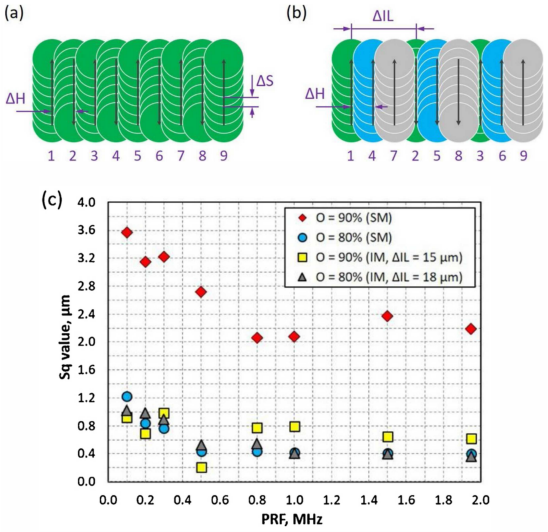


Fig. 1.18 Illustration of bi-directional: (a) sequential and (b) interlaced laser beam scanning methods. Symbols: ΔH – hatch distance, ΔS – pulse-to-pulse distance along the linear movement of the laser beam, and ΔIL – interlacing distance. Part (c) of the figure depicts the surface roughness (S_q) dependence on laser pulse repetition frequency (PRF) when different overlap values (O) and different scanning strategies are utilized [33].

in surface roughness of Borofloat 33 glass after laser processing, when different scanning strategies are utilized are shown in figure 1.18, part c. As is seen, the S_q values of the surfaces generated using overlap of O = 80 % are very similar for both SM and IM, however, in the case of O = 90 %, the differences are significant (e.g. 2.1 μm vs. 0.8 μm for PRF = 1 MHz). In addition, further analysis showed that IM also assists in reducing the HAZ after laser processing when compared to SM. After examining the plasma plume dynamics during laser processing with IM and SM observations were made that explain why a better surface finish can be achieved when the interlaced scanning method is used. The observed plume orientation disclosed that glass particles are ejected in the direction opposite to the laser beam scan movement, landing away from the hot region. Since the machined layers are relatively shallow, the glass particles can easily escape the machined area even at low laser-induced recoil pressure. In the case of SM, after a few laser scans glass particles seem to travel towards the steep wall. Most of these glass particles bounce off and land very close to the laser beam scanning path. Since this area is very hot, they melt and

merge with each other, forming a lump of partially fused white powder that sticks to the glass surface. However, during IM, the laser beam scanning path is always further apart, since several subsequent lines are skipped, hence avoiding the former problem.

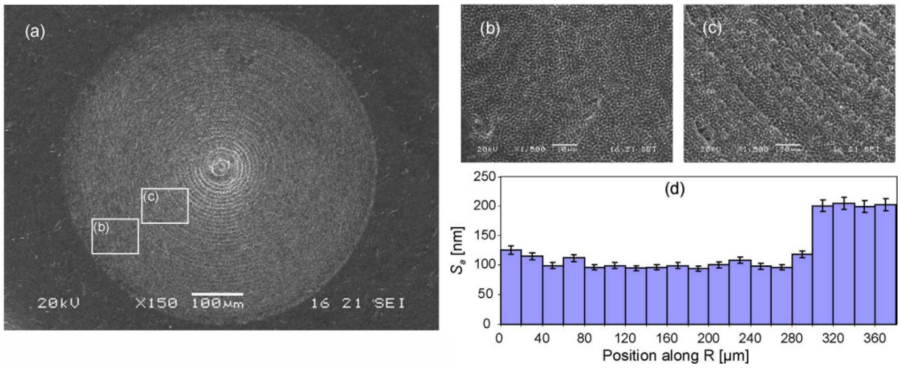


Fig. 1.19 Topography map of a sample machined at E_p = 15 μJ, v = 190 mm/s. Panel (a) shows the SEM top view of the ablated, panel (b) a magnification of the ablated surface close to the border with the bare surface, panel (c) a magnification at the middle of the ablated layer, panel (d) the variation of the areal roughness S_a measured on 20 μm × 20 μm square portions of the topography map. The error bars are evaluated on the basis of repeated measurements on different square portions [34].

What's more, the surface can also be scanned in patterns other than straight lines. L. Romoli [34] in his work has presented a spiral scanning method and investigated its effectiveness in flattening the roughness of AISI 316L stainless steel. In this work, the laser beam was scanned in a spiral manner, starting from the highest circle radius and going smaller with each rotation. After optimizing scanning and laser parameters, such as pitch, pulse energy, and others, the authors managed to achieve uniform ablation of the surface. The surface machined using optimal parameters and spiral scanning strategy is shown in figure 1.19, part a. Parts b and c show SEM images of close-up views of different areas within the scanned surface. On the outskirts of the ablated circle, the surface is mostly homogeneous, however, when approaching the center of a circle the individual trenches become more and more pronounced, increasing the local level of roughness. The increased roughness near the center is explained by pronounced heat accumulation within smaller radius circles. Despite the inhomogeneous appearance, the measured roughness values (given in part d of the figure) remained almost at a consistent level of $S_a \approx 100$ nm, with small deviations near the center of the circle. This suggests that spiral

scanning method, similar to raster scanning, allows to achieve uniform ablation, with small variations near the center of the spiral, where heat accumulation is increased. Hence, it appears that the scanning path itself has no significant impact to the final surface roughness, as long as the same values of overlaps in x and y directions are maintained. The differences only arise when heat accumulation is introduced, for example, when using high laser repetition rates.

Moving on, when scanning the surface multiple times, the number of possible scanning paths increases immensely. Under conventional conditions, when each layer is scanned line-by-line, with every subsequent layer positioned exactly on top of the previous one, the generation of periodic structures will start to take place. The positions to which beams are deflected experience higher levels of ablation, while positions at intersections of the beams - lower, forming periodic structures, whose contrast (peak-to-valley height) increases with each layer. This problem is typically approached by introducing the rotation of every subsequent layer. In such a way, more uniform energy distribution over the surface is achieved. Chong Chen et. al. [172] performed multilayer ablation of copper using femtosecond pulses. The authors showcased (see figure 1.20)

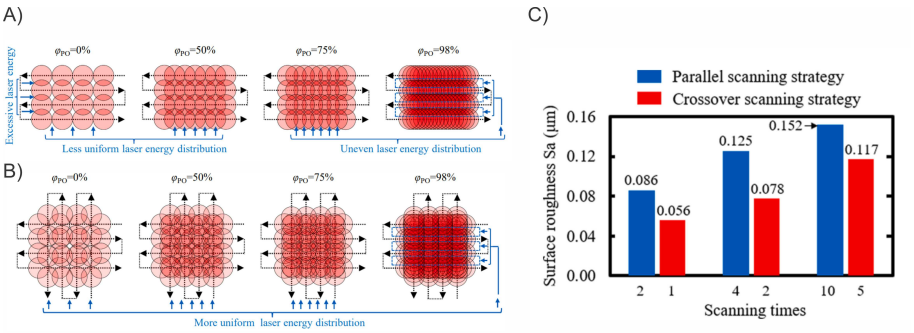


Fig. 1.20 Schematic diagram of the prototype of (A) parallel scanning strategy and (B) crossover scanning strategy with the line overlap rate of 60% and the pulse overlap rates ranging from 0 % to 98 %. Part (C) presents the statistics of the surface roughness (S_a) values achieved on the machined copper workpiece using the two scanning strategies [172].

that during parallel scanning depending on the overlap at some parts of the surface excessive amount of laser energy is deployed while at others insufficient, resulting in a non-homogeneous ablation. However, if every subsequent layer is rotated by an additional 90°, a more uniform laser energy distribution can be achieved. Such a way of scanning the surface is called the crossover scanning strategy. The comparison of achieved roughness values using conventional and

crossover scanning strategies is given in part C of figure 1.20. Results indicate that the crossover scanning strategy yields lower surface roughness (after 10 scans, S_a = 152 nm for parallel scanning and S_a = 117 nm for crossover scanning). This relation appears to be independent of the number of scans. However, the steady increase in surface roughness with each proceeding scan is observed for both scanning strategies. Another independent research group led by S.L. Campanelli [173] performed a similar study. The authors compared 4 different scanning strategies when ablating metal substrates. The scanning strategies included:

1. Only parallel lines to the scanning direction;
2. Parallel lines to the scanning direction for the first layer and rotation with 90° angular increase for the following layers;
3. Lines tilted at 45° for the first layer and an increase of 90° for the following layers;
4. Parallel lines to the scanning direction for the first layer and rotation with 45° angular increase for the following layers.

After performing multilayer ablation, authors determined that the lowest surface roughness was achieved using the 4^{th} scanning strategy, while the highest - the 1^{st} scanning strategy. This time rotating layers at an angle of 45° outperformed the crossover scanning strategy discussed earlier. This shows that other angles of rotation could yield even better results. An extended study on this topic was performed by Daniel et al. [35]. The authors performed multilayer ablation on carbide metal with primary roughness of S_a = 0.42 μm. In the study, authors experimentally examined surface roughness after laser processing when the layers are rotated at every integer angle in the range of 0 to 180 degrees. The investigation of angles φ = 180-360° was neglected, because they behave equally as angles φ = 0-180° due to geometrical symmetry. During each experiment, the surface was scanned n = 360 times, where each subsequent layer was rotated at a chosen hatching angle (φ). The results are shown in figure 1.21. The authors have categorized the findings into 3 groups (displayed by different colors) that represent different roughness formation mechanisms. Data points that are colored in red represent hatching angles at which high surface roughness is induced. Such angles are factors of 180°, like 90°, 45°, 30°, 15°, etc. When the

surface is scanned in a manner where each layer is rotated by former angles, the laser beam is often positioned in the same locations. For example, when using $\varphi = 180°$, the beam will be positioned in the same exact locations during each layer. When using $\varphi = 90°$ (crossover scanning strategy), the scanning pattern will coincide every 2nd layer, and in case $\varphi = 45°$ - every forth etc. Frequent ablation of the same locations results in the formation of periodic structures that constitute high surface roughness (e.g. the use of $\varphi = 0°$ resulted in surface roughness of $S_a = 2.9\ \mu$m). Another category, displayed in green represents

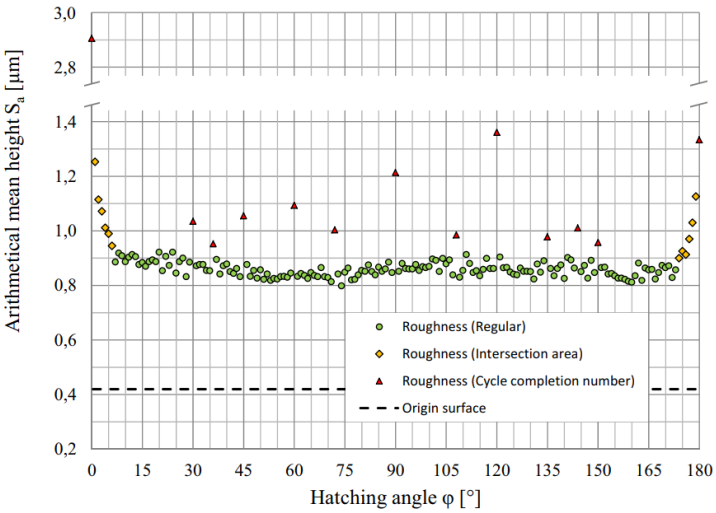


Fig. 1.21 Surface roughness dependence on hatching angle, when the surface is scanned 360 times [35].

hatching angles that result in minimum roughness. Such angles are arbitrary angles like $\varphi = 41°$, 73°, 13°, etc. When rotating layers at such angles, the scanning patterns rarely coincide with the ones in the previous layers, enabling the achievement of more uniform ablation. Under such conditions, the formation of periodic structures is reduced, resulting in minimal achievable roughness. The authors have demonstrated, that by carefully choosing a hatching angle the surface roughness could be reduced by a factor of 2-3.5 (e.g. $\varphi = 0°$ resulted in $S_a = 2.9\ \mu$m, while $\varphi = 42°$ resulted in $S_a = 0.84\ \mu$m). However, what authors have also observed was that independently to hatching angle, the roughness S_a increases with each subsequent layer (see figure 1.22). The figure shows that surface roughness increases with each layer, with the rate of increase depending on the hatching angle. The angles $\varphi = 90°$ and $\varphi = 3°$ lead to a faster rise in

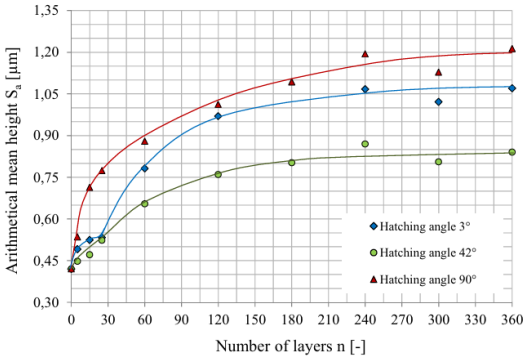


Fig. 1.22 Evolution of surface roughness, when different hatching angles are used [35].

surface roughness, while $\varphi = 42°$ exhibits a slower growth rate. The evolutions are in a good agreement with former discussion regarding the formation of periodic structures. The authors further observe that the roughness tends to saturate at higher numbers of layers; however, the reasons for this behavior are not provided. The same trend of increasing roughness with an increasing number of layers was also independently reported by Zubauskas et al. [10]. Such uncontrolled growth of surface roughness presents significant challenges for achieving precise control over surface texture, thereby necessitating further investigation on the topic.

The presented literature review demonstrates that, due to the significant influence of surface roughness on various material parameters, considerable research has been undertaken to investigate its nature and evolution during laser processing. The studies indicate that surface roughness is a complex parameter governed by multiple factors, that make its control particularly challenging. Despite the extensive efforts, complete control over the evolution of surface roughness during laser ablation has not yet been achieved nor demonstrated. Building upon the presented foundation, this thesis continues in this direction by exploring novel approaches to control surface roughness and by examining in greater detail the underlying mechanisms responsible for its formation.

Chapter 2

Methodology

2.1 Experimental setup and measurement equipment

The thesis investigates areal surface ablation using femtosecond laser radiation, with the primary objective of achieving control of surface roughness. To accomplish this, a generalized laser processing setup given in the figure 2.1 was used. For a laser source, Yb:KGW based femtosecond lasers "Carbide" and "Pharos" (Manufactured by Light Conversion) were employed. The lasers generated pulses with approximate duration of t_p = 210 fs (FWHM). A built-in harmonic generator unit enabled the upconversion of laser radiation to higher harmonics, resulting in emission of 1H (λ = 1030 nm), 3H (λ = 343 nm) and 4H (λ = 257 nm) laser radiation upon request. The lasers could output maximum of 40 W of laser power at 1H. The average laser power was further externally controlled via a combination of $\lambda/2$ waveplate and a Brewster-type polarizer. The laser beam was guided using mirrors with dielectric coatings optimized for the wavelength of laser radiation used. The two-dimensional laser beam scanning on the surface was achieved using a galvo-scanner. Several different scanners were employed over the course of experiments performed in the scope of the thesis, including “SCANLAB exelliSCAN14 “, “SCANLAB intelliSCAN14” and “SCANLAB intelliSCAN$_{se}$10” (all manufactured by ScanLab). The focusing of laser beam was achieved using a set of available f-theta lenses. For processing with λ = 1030 nm and λ = 343 nm, f-theta lenses with a focal length of f = 100 mm were employed, whereas for λ = 257 nm, an f-theta lens with a focal length of f = 160 mm was used. The use of different wavelengths and focusing conditions led to the varying beam sizes at the focal plane. The realized

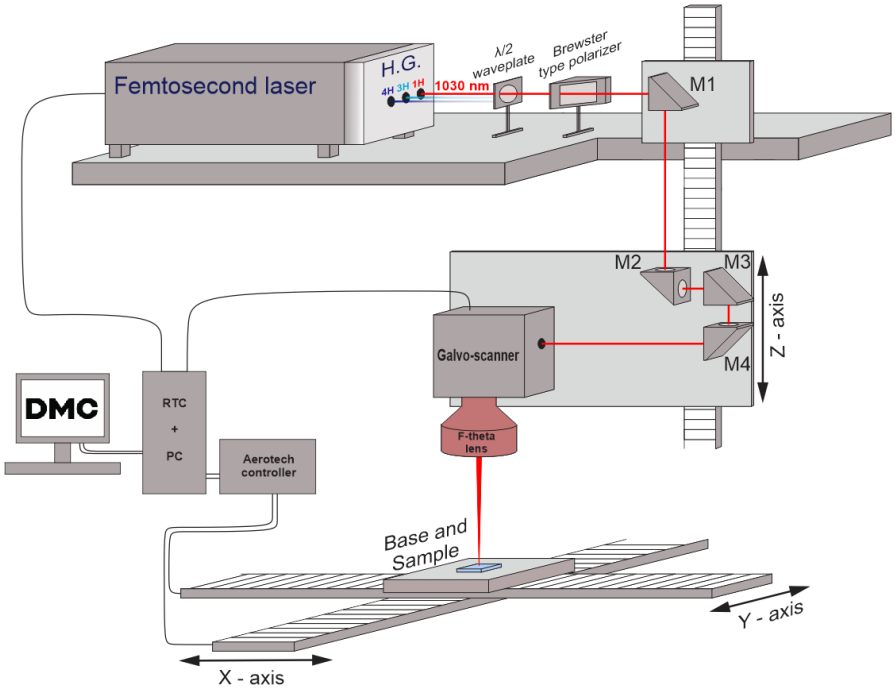


Fig. 2.1 Conceptual layout of the generalized experimental setup. *H.G.* stands for harmonic generator unit, *M* denotes different mirrors. *RTC* stands for "Real Time Controller" (Manufactured by ScanLab) and is used for the control of galvo-scanner and trigger of laser's pulse picker unit. *PC* here denotes personal computer, whereas *DMC* (Manufactured by Direct Machining Control) is a software that controls all active units within the experimental setup.

waist diameters under different experimental setup configurations are given in table 2.1. The beam diameters were measured using an Ophir "SP503U" beam profiler in combination with a 4F imaging system featuring a magnification of 6.6, enabling accurate characterization despite the limited pixel size (9.9 μm x 9.9μm) of the camera. The polarization state was fixed during all experiments through the duration of the thesis. No polarization-modifying optical components, other

Table 2.1 Focusing conditions and beam diameter at the waist under different experimental setup configurations.

	Laser	**Wavelength λ (nm)**	**f-theta focal length f (mm)**	**Beam diameter D (μm), at 1/e^2 level**
Config. 1	Yb:KGW (Carbide)	1030	100	42.8
Config. 2	Yb:KGW (Carbide)	343	100	12.6
Config. 3	Yb:KGW (Pharos)	257	160	22

than the external attenuator, were employed, resulting in a theoretically linearly polarized beam incident on the sample. For experimental setup configuration 1, the degree of linear polarization measured at the output of the galvo-scanner was (DoLP = 95 %), where $DoLP = (I_{\max} - I_{\min})/(I_{\max} + I_{\min})$, whereas the polarization orientation was found to be rotated by (15°) with respect to the vertical direction of the sample plane. Both the slight rotation of the polarization axis and the non-ideal degree of linear polarization are attributed to the cumulative effect of multiple reflections from mirrors along the optical path. The laser processing was performed on dielectric materials: soda-lime glass and fused silica slides, of various thicknesses. Soda-lime glass was mainly used in a single-scan experiments, while fused silica for multilayer ablation experiments. Soda-lime glass, due to its relatively high thermal expansion coefficient ($\alpha \approx 8 \times 10^{-6}$ K^{-1} [174]), is prone to cracking under increased thermal stress, as in the case of multilayer ablation; therefore, its use in these experiments was excluded. In contrast, fused silica, with a thermal expansion coefficient of $\alpha \approx 0.5 \times 10^{-6}$ K^{-1} [175], proved to be a highly suitable material for this task. The control of galvo-scanner mirrors was achieved via "Real Time Controller" (RTC in short, manufactured by ScanLab), while the beam path itself was preprogrammed using DMC software (manufactured by Direct Machining Control). Furthermore, the scanner was mounted on the air-bearing nanopositioning stage ("ABL1500", manufactured by AEROTECH) that allowed movement in the z direction, i.e. perpendicular to the sample surface. This allowed to adjust the distance from the lens to the surface of the sample during the deep-engraving procedure to ensure that the surface of the sample subject to the processing is maintained in the focal plane of the lens. Additionally, samples were placed on the nanopositioning stages ("ABL1500WB", manufactured by AEROTECH) enabling the precise positioning of the sample in x and y directions. Following laser processing the samples were cleaned in ultrasonic bath for 15 minutes and blown dry using a high-pressure air stream. The topographies were acquired and the surface roughness measurements were performed using either „Sensofar PLμ 2300" (manufactured by Sensofar) or "Olympus LEXT OLS5000" (manufactured by Evident Scientific, formerly Olympus) laser scanning microscopes. Complimentary microscope pictures were either taken with the latter or „Olympus BX51" (manufactured by Evident Scientific, formerly Olympus) optical microscope. Additional scanning electron microscope (SEM) measurements were performed using "Prisma E" SEM

(manufactured by Thermo Fisher Scientific), while the transmission spectra was measured using spectrophotometer UVProbe (manufactured by Shimadzu Corporation).

2.2 Scanning techniques

When performing laser processing experiments, the surface was scanned in a rectangular manner, following a raster scanning path in a sequential order. In the scope of this thesis, three main scanning algorithms were examined and employed:

- Change in overlap of the craters Ω (figure 2.2, part A);
- Rotation of the layers (figure 2.2, part B);
- Displacement of the layers (figure 2.2, part C);

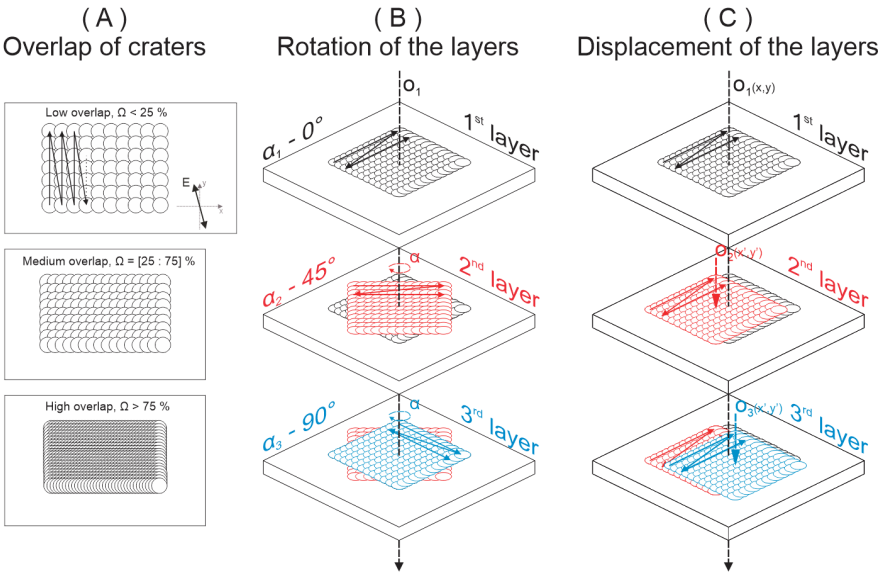


Fig. 2.2 The visual representation of different scanning algorithms used in the thesis. (A) the changing of the overlap of the craters Ω. The E vector represents linear polarization orientation, which was maintained during all experiments. (B) the rotation of the layers, where α is the angle of rotation and α_n is the cumulative angle. (C) the displacement of the layers, where O_n is the central point of the scanned pattern for each layer. Different colors stand for different layers.

The overlap of the craters were calculated using equation 1.29. The overlap in the x direction was varied by tuning the scanning speed (v), while the overlap in the y direction was varied by selecting different distance values between adjacent lines (dy). To maintain even ablation, the overlap of the craters Ω in both - x and y directions was maintained equal. When using the rotation of the layers, each subsequent layer was rotated around its central axis by a fixed additional angle. The angle at which the $n-th$ layer is rotated is described as:

$$\alpha_n = (n-1) \times \alpha, \tag{2.1}$$

here α is the angle of rotation and α_n is the cumulative angle at which the n-th layer is rotated. Another scanning strategy, the displacement of the layers, includes changing the position of each subsequent layer by a certain value. Instead of scanning each layer on top of each other, every following layer is displaced. The x' and y' coordinates of the n-th layer are then described as:

$$x' = x + (\mathfrak{R} - 0.5) \times \Delta, \tag{2.2}$$

$$y' = y + (\mathfrak{R} - 0.5) \times \Delta, \tag{2.3}$$

here, x' and y' are the coordinates of the n-th layer, while x and y are the coordinates of the first layer. The $\mathfrak{R}$ is a function that returns a random value from the interval [0, 1] at a uniform distribution and is recalculated for each layer. Finally, Δ is a scaling factor used to vary the maximum extent of the displacement. During the thesis each individual scanning strategy was examined, demonstrating their influence towards the final surface roughness. In addition to their individual examination, the combined use of all three scanning strategies was employed for the control of surface roughness. To the best of our knowledge, no other study has investigated such a complex, combined scanning approach.

2.3 Spectral analysis

For a more detailed characterization of surface roughness, spectral analysis of the acquired surface topographies was performed to examine the evolution of individual spatial frequency components. This approach enabled the waviness

and roughness components of the surface texture, as defined in ISO 25178, to be analyzed separately.

First, the acquired topographies were digitally preprocessed to remove the outliers that correspond to dust and other bodies that were unsuccessfully removed during the cleaning stage. This was necessary, as the outliers contribute to the distortion of the true roughness values. All data points with values exceeding 3 times the standard deviation were removed and filled according to the average values of the neighbors. In addition, the tilted plane (if present), arising from imperfect sample placement or microscope stage, was digitally removed. Following that, the digitally preprocessed topographies were subjected to a 2D Fourier transform:

$$Z_{u,v} = \sum_{n=0}^{N-1} \sum_{m=0}^{M-1} z_{n,m} e^{-j2\pi\left(\frac{un}{M} + \frac{vm}{N}\right)}, \tag{2.4}$$

here, the term $Z_{u,v}$, with $u = 0, \ldots, N-1$ and $v = 0, \ldots, M-1$, denotes the two-dimensional frequency-domain representation of the topography obtained through the discrete Fourier transform. To express the frequency indices in terms of their corresponding centered spatial frequencies, the following coordinate transformation from the spatial domain to the spectral domain was applied:

$$f_x = \frac{u - N/2}{N\Delta X}, \tag{2.5}$$

$$f_y = \frac{v - M/2}{M\Delta Y}, \tag{2.6}$$

where f_x and f_y are the spatial frequencies along the x- and y-directions, respectively. These relationships account for the frequency centering and provide the mapping between the discrete indices (u, v) and their physical spatial frequency values. The example of a calculated 2D spatial spectrum of a single-scanned surface, given in figure 2.3, part A, can be seen in the part B of the same figure. As can be observed, the spectrum contains multiple peaks distributed across the frequency domain. Such spectral data visualization makes it difficult to identify and track the positions and amplitudes of individual spatial frequencies, rendering it inconvenient for detailed analysis; therefore, more informative ways to visualize spectral data were proposed. In the first instance,

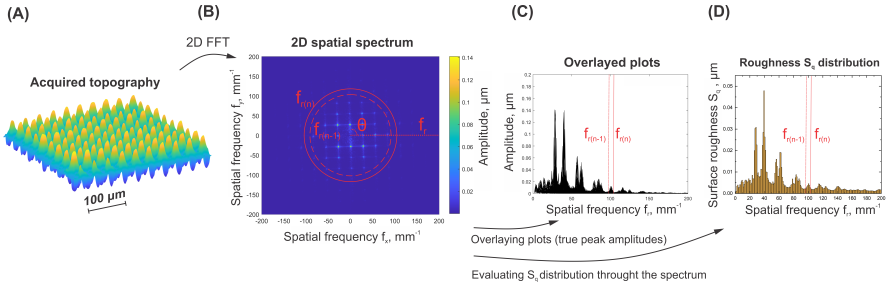


Fig. 2.3 The principle scheme of spectral analysis. (A) The surface texture is acquired using a laser scanning microscope and digital preprocessing is performed (more details in the text). (B) Fast Fourier transform is carried out to extract 3D spatial spectrum. The 3D spatial spectrum is represented in 2D either through overlaying all profiles in a polar coordinate system (C) or by segmenting it radially and examining the data from each segment (D).

the data was visualized in polar coordinates, where:

$$f_r = \sqrt{f_x^2 + f_y^2}, \tag{2.7}$$

$$\theta = \tan^{-1}(\frac{y}{x}). \tag{2.8}$$

All radial profiles f_r across every angle θ were overlaid on top of one another (see figure 2.3, part C), and their amplitudes were digitally scaled (multiplied by 4) to match the true amplitudes of the corresponding spatial features. This visualization method makes it possible to capture the dominant spectral peaks associated with key spatial features and track their amplitude evolutions over the laser processing duration. In the second instance, the spectral domain was divided into radial segments of matching radial spatial frequencies $\Delta f_r = f_{r(n)} - f_{r(n-1)}$ at the discretization step of $\Delta f_r = 1$ mm^{-1}. From the integrated data within the radial segments, the surface roughness S_q of each segment was calculated and plotted (see figure 2.3, part D). This was possible following Parseval's theorem [176], which states that the RMS roughness of a surface in the spatial domain is an equivalent measure of the area under the Power Spectral Density (PSD) of the same surface in the frequency domain. Hence, the RMS roughness of a single segment from the spectral data can be calculated following the equation:

$$S_q(f_r) = \sqrt{\int_{f_r - \Delta f_r}^{f_r} \int_0^{2\pi} PSD(f_r', \theta) f_r' df_r' d\theta}, \tag{2.9}$$

here $S_q(f_{r(n)})$ is the RMS roughness of a single radial segment. The PSD is expressed as:

$$PSD(f_r, \theta) = |Z(f_r \times \cos\theta, f_r \times \sin\theta)|^2 / A, \tag{2.10}$$

where $A = N \times M$ denotes the analyzed surface area. This type of data visualization reveals the contribution of individual spatial frequencies to the overall surface texture and is essential in order to understand surface texture evolution.

2.4 Fractal analysis

The concept of fractals was introduced by Benoit Mandelbrot in 1967 [177] to describe irregular geometrical structures that cannot be adequately characterized using classical Euclidean geometry. Unlike idealized Euclidean objects, many natural forms, such as coastlines, mountains, and clouds, exhibit complex, scale-dependent features that are more accurately described by fractal geometry. During the course of the thesis, it was observed that laser-processed surfaces subjected to multiple scans using diverse scanning strategies display fractal behavior as well, showing scale-dependent complexity in their surface morphology. To gain additional insights into their structure, such surfaces were characterized using fractal analysis methods introduced by Mandelbrot, where the complexity of the structure is quantified through the estimation of the fractal dimension (D).

The fractal dimension is a quantitative measure of the geometric complexity and scale-dependent roughness of an object [178]. It describes how the level of detail changes with the observation scale, providing a scale-independent descriptor of surface topography that complements conventional roughness parameters. Real objects, such as mountains, clouds, and laser-processed surfaces, are referred to as self-affine, meaning that their horizontal and vertical dimensions scale differently:

$$x = \lambda x, \tag{2.11}$$

$$z = \lambda^H x. \tag{2.12}$$

Here λ is a scaling factor and H is the Hurst exponent. The fractal dimension of such structures can be estimated using various fractal analysis methods, including

the roughness-depth (RD) method, correlation analysis, power spectral density (PSD) analysis, and other scaling-based approaches [179]. The D parameter in this thesis was evaluated using the PSD method, due to its compatibility with the spectral analysis introduced in section 2.3. The methodology for the estimation of fractal dimension via PSD analysis was developed by Richard F. Voss [180]. It relies on the relationship between the power spectral density (PSD) and the spatial frequency distribution of surface features. Self-affine fractal surfaces exhibit a power-law dependence of the power spectral density, $PSD(f) \propto f^{-\beta}$. Consequently, plotting the PSD in logarithmic coordinates yields a linear relationship, the slope of which corresponds to the spectral exponent β, characterizing the scaling behavior of the surface. The Hurst exponent (H) and the fractal dimension (D) can then be determined using the following relationships:

$$H = \frac{\beta - 2}{2}. \tag{2.13}$$

$$D = 3 - H. \tag{2.14}$$

Note that equation 2.14 is only valid for 2D self-affine surfaces. A value of D $\approx$ 2 represents a smooth Euclidean-like surface, intermediate values (e.g., D $\approx$ 2.5) indicate moderate multiscale roughness, and D approaching 3 corresponds to highly irregular, complex surfaces with strong small-scale variations. For self-affine surfaces, the fractal dimension is bounded by 2 < D < 3; values outside this range indicate that the assumptions underlying the self-affine fractal model are not satisfied. Let's consider an example by estimating the fractal dimension of a typical laser-processed surface (see figure 2.4, part A). First, the 2D FFT is performed on the surface, and the averaged PSD value for each radial spatial frequency f_r is extracted following the methodology given in section 2.3. The averaged PSD versus radial spatial frequency is then plotted in a log-log representation (see figure 2.4, part B). The frequency range that follows a linear trend is identified and fitted. In this example, the fitting frequency range corresponded to 2 $\text{mm}^{-1} < f_r < 110\ \text{mm}^{-1}$. The roll-off observed at higher frequencies ($f_r > 200\ \text{mm}^{-1}$) is attributed to the instrumental transfer function rather than the actual surface texture. Therefore, this frequency range was excluded from the fitting procedure. By using a robust linear regression model, the selected frequency range was fitted, and the β value was extracted, measuring $\beta = 2.164$. With the β value assessed, the fractal dimension D is

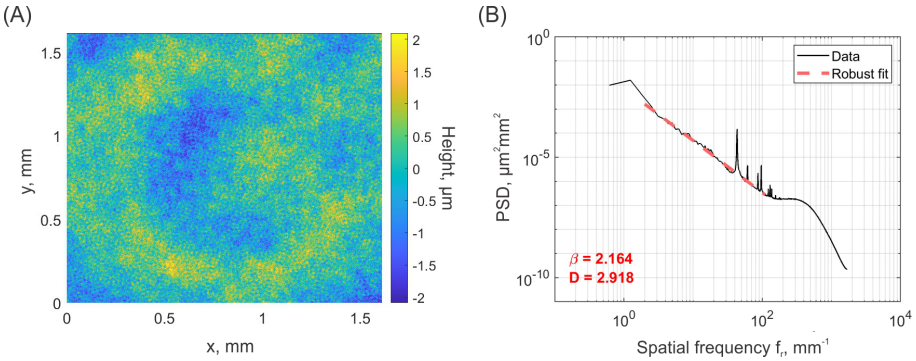


Fig. 2.4 A typical laser-processed surface topography (A). Averaged PSD versus spatial frequency f_r representation in a log-log format (B). The black curve is the raw data, while the red line represents the fit. β, H, and D are the parameters used in the fractal dimension calculation.

calculated using equations 2.13 and 2.14. In this example, D = 2.918, indicating the high complexity of the surface.

Chapter 3

Single-scan investigation

Results presented in this chapter were published in [A1] and presented at [D1], [D2], and [D3] conferences.

3.1 Investigation framework

First, a numerical and experimental investigation was conducted by scanning the surface of the sample a single time using different scanning algorithms. Each experiment was carried out by ablating 1x1 mm surface areas on a 1 mm thick soda-lime glass. The initial roughness of the glass samples was low, measuring $S_a < 10$ nm. The surface was scanned using different scanning algorithms. During the course of the study, three different scanning algorithms were investigated:

- Overlap of the craters in x and y directions.
- The uncertainty of line positions.
- Shift of every second line.

The visual explanation of the examined scanning strategies is given in figure 3.1. The uncertainty of line positions in this context refers to positional deviations caused by lack off synchronization between the laser and the scanning system. This results in a random displacement of each line along the x-direction. In contrast, the shift of every second line denotes a deliberate and precisely controlled displacement applied to alternating lines in the y direction. During the experiments the focal plane was maintained on the top surface of the sample,

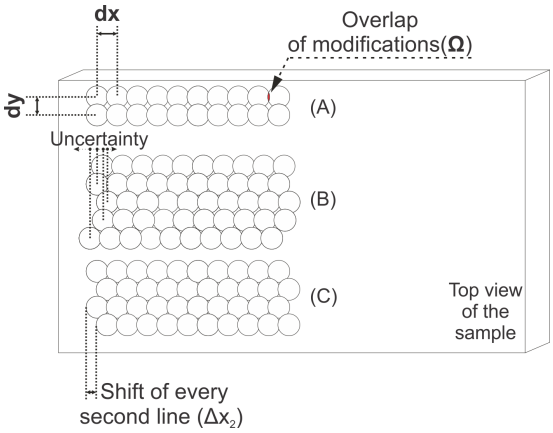


Fig. 3.1 Schematic explanation of different examined scanning strategies. (A) overlap of the craters, (B) uncertainty of first pulse positioning, (C) shift of every second line. *dx* - distance between single modifications in *x* direction, *dy* - distance in *y* direction, Ω - overlap of modifications, Δx_2 - shift of every second line.

where laser processing was performed. Following the ablation, the surface roughness was measured. A single measuring window 85x85 μm in size contained 256 profiles in *x* and *y* directions each. The measured surfaces were plane fitted to remove any tilt induced by possible sample positioning at an angle. For each profile, R_a parameter (described by equation 1.1) was calculated. To evaluate areal surface roughness in one of the directions an average of 256 profiles of a particular direction was taken. The areal *Ra* parameter (average of many profiles) considers the whole surface and not a single profile, thus provides more accurate results. Furthermore, utilizing this parameter allows for the assessment of surface roughness in various directions, which cannot be achieved by employing a single S_a parameter. For a better understanding of how this modified version of the parameter R_a is evaluated, see figure 3.2. As seen in the figure, the measured topography is sliced to profiles in direction of interest, for each profile R_a parameter is calculated. From the plotted $R_{a(y_i)}$ values it is evident that the roughness R_a parameter can vary quite significantly depending on the location of a profile from which it is calculated. Therefore, here for more accurate measurement of surface roughness we consider the average, directional R_a parameter - Ra_i, where *i* denotes direction of measurement. The error of areal roughness parameter is then a standard deviation from its average value.

Areal roughness parameter is then mathematically expressed as:

$$Ra_x = \frac{1}{N}\sum_{y=1}^{N} R_{a(y_i)}. \tag{3.1}$$

To calculate areal roughness parameter in perpendicular direction Ra_y, in

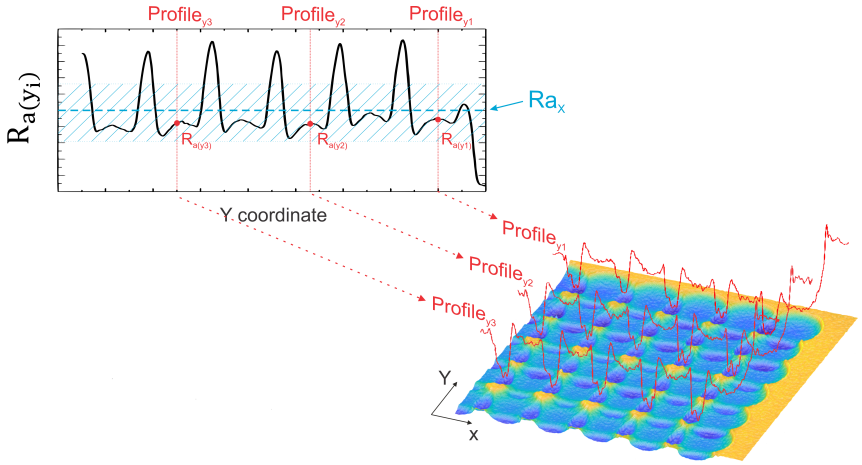


Fig. 3.2 Scheme explaining how areal roughness parameter is derived. The topography of a sample after single scan machining is examined. Red curves represent profiles at discrete locations. R_a parameter dependence on Y coordinate is calculated in preferred direction. The average of all R_a values is then an areal roughness parameter in a perpendicular direction Ra_x. Tilted blue lines represent the range of one standard deviation.

equation 3.1 the $R_{a(y_i)}$ should be substituted by $R_{a(x_i)}$. Furthermore, the measurement noise was estimated using the subtraction technique [181]. From a set of 100 measurements, the noise value of R_q = 4.6 nm was calculated. It is further noted that Ra_x here corresponds to the roughness of the averaged primary profile, where roughness and waviness components are not separated. Strictly speaking, the height deviations of the primary profile should be denoted as P_a (see section 1.1.3). However, since this notation is rarely used in the literature, the parameter is retained as R_a for consistency with common practice.

3.2 Laser ablation numerical model

The discussion in chapter 1.3 revealed that the number of possible combinations of different scanning strategies and laser parameters that could be tested in multi-shot laser ablation is vast. Therefore, in order to save time and resources that would be necessary for testing the extensive amount of combinations experimentally, a numerical model was developed, that could simulate laser ablation of surfaces. The model imitates laser ablation and enables the analysis of the resulting surface topographies. This is a semi-empirical model, whose working principle is based on experimentally acquired data. Prior to simulations, the material response function, representing the engraved depth as a function of fluence, of a target material is experimentally acquired. To retrieve it, the fluence profile of the laser beam at the working distance (in our case – focal plane) and the geometry of the crater produced with such laser are measured. The fluence profile was experimentally assessed using methods given in section 2.1. Simultaneous laser pulse energy measurements enabled normalization of the measured fluence distribution such that its integral matched the pulse energy. An example of the measured laser beam fluence profile, rescaled to its actual dimensions, together with the crater profile produced by this beam on target material (here soda-lime glass), is shown in figure 3.3(A). By matching

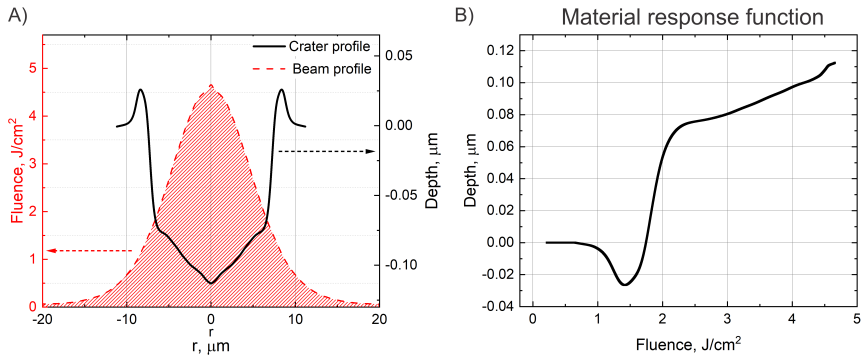


Fig. 3.3 An example of measured and rescaled to its actual size fluence profile of the laser beam at the focal plane and the measured geometry of the crater produced with such laser beam (A). The material response function derived from data in part (A) is given in part (B) of the figure. It shows how much of material is removed at a precise fluence value.

engraved depth at each fluence value, the material response function is extracted (given in figure 3.3 (B)). Following the acquisition of material response function,

numerical simulations of laser ablation are carried out. The standard workflow of the numerical model is illustrated in figure 3.4. The incident beam fluence is

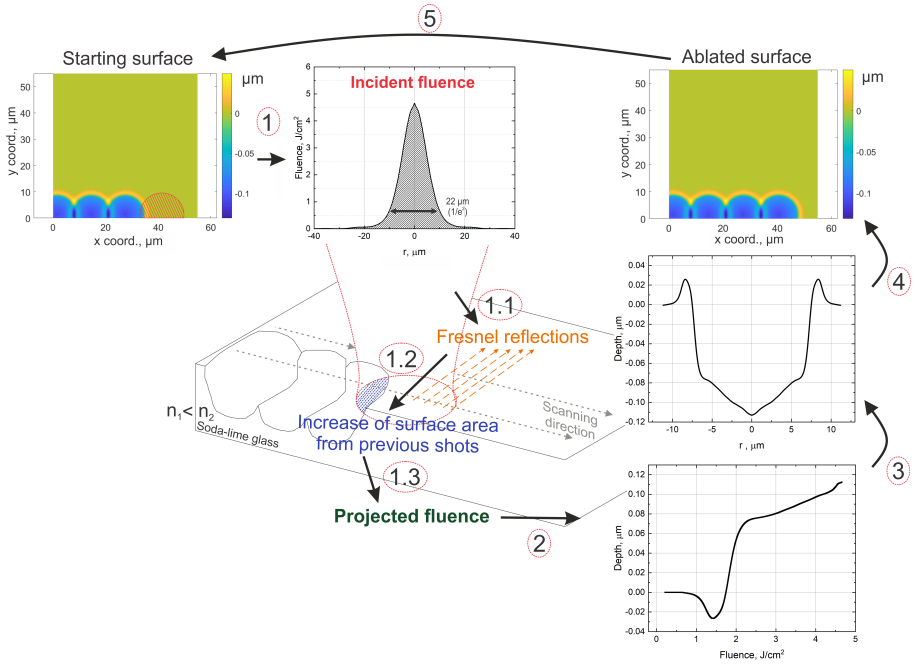


Fig. 3.4 Principle scheme showing the workflow of the numerical model. The incident fluence is projected on the surface (1). Fluence reduction due to fresnel reflections (1.1) and increase of surface area from previous shots (1.2) is taken into account. According to material response function and projected fluence (2) ablated volume is calculated (3). Finally, ablated volume is subtracted from the surface at the current beam location (4). The position of the beam is shifted and calculations are repeated (5).

positioned to a selected location on the surface (1). Reduction of the fluence due to Fresnel reflections (1.1) and increase of surface area due to the craters from previous shots (1.2) are taken into account. From recalculated projected fluence and material response function (2) the expected amount of ablated material at each pixel is calculated (3). Finally, the estimated ablated material is subtracted from the initial surface (4). The incident laser beam is shifted to a different location (5) and the process repeats. In addition, small beam positioning uncertainties (with magnitude of 0-4 μm) were introduced in order to imitate various vibrations present under real experimental conditions. The basic equations governing these steps can be written in the form:

$$H(x, y, N) = H(x, y, N-1) - h(x, y, F_{imp.}(x - x_N, y - y_N)), \qquad (3.2)$$

$$F_{imp.} = F \cdot L_{Fresnel} \cdot L_{proj.}, \tag{3.3}$$

$$L_{proj.} = \frac{1}{\sqrt{1 + H_x(x, y, N-1)^2 + H_y(x, y, N-1)^2}}, \tag{3.4}$$

$$L_{Fresnel} = 1 - R_s(H_x, H_y) \cdot I_s - R_p(H_x, H_y) \cdot I_p. \tag{3.5}$$

Here $H(x, y, N)$ - height value at x, y coordinates after N number of pulses, H_x and H_y are partial derivatives in x and y directions, h – a function that returns how much of the material is removed at a certain fluence value with accordance to the material response function. x_{N} and y_{N} are N'th pulse position on the surface, $F_{\mathrm{imp.}}$ – impinging on the surface beam fluence while F is the experimentally measured fluence. R_{s} and R_{p} are calculated Fresnel reflections [182] for impinging s or p polarization beam, that depend on the surface gradient while the I_{s} and I_{p} defines which polarization beam is used for laser micromachining and has to follow a rule of I_{s}+I_{p}=1, the ratio, therefore, $I_{\mathrm{s}}/I_{\mathrm{p}}$ defines ellipticity of the polarization. Equation 3.2 is used to calculate changes in surface height, while equation 3.3 is used for calculating the reduction of laser fluence due to Fresnel reflections and the increase of surface area from previous shots.

It is noted that the proposed simplified semi-empirical model is material dependent. Consequently, the simulated surface topography can be expected to agree with experimental results only when the laser processing is performed on the same material from which the material response function was derived. To simulate laser ablation of a different material, the corresponding representative material response function must first be experimentally determined. Furthermore, the model does not explicitly account for the complex physical mechanisms governing ultrashort laser–matter interaction, such as nonlinear light–matter coupling, laser-induced stresses, or defect formation. Instead, it considers only the final outcome of these processes, namely the resulting ablation crater, from which the material response function is derived. Incorporating these mechanisms would improve the accuracy of the proposed model; however, it would also increase the computational cost and prolong the calculation time. For example, molecular dynamics simulations of a single ultrafast laser–matter interaction, which explicitly account for the underlying physical processes, may require several days to weeks of computation, even when performed on high-performance computing systems. Therefore, to perform multi-layer ablation simulations with such accuracy, would require years, which is impractical.

Since the primary focus of this thesis is the simulation of multi-exposure laser processing, the developed semi-empirical numerical model was intentionally maintained in its present form.

3.3 Roughness dependence on the crater overlap

Over the course of the investigation it was observed, that surface roughness after a single pass is greatly determined by the overlap of modifications. The term - modification, here refers to a single pulse ablated volume on the surface of a sample (a.k.a. ablated crater). It is important to note, that here we are investigating the overlap of the craters and not the geometrical beam overlap. Although the geometrical overlap is more commonly addressed in the literature [183, 184], we propose that it is a parameter providing little information about resulting surface morphology. The spatial width of the beam (i.e. beam overlap) alone does not allow to predict the geometry of the modification (more precisely its width, edge steepness) as it depends on many more different factors like beam shape, pulse duration, material response, etc. That being said, we propose that spatial beam overlap as a parameter for surface evaluation should be avoided and overlap of modifications should be used instead. The overlap of modifications (Ω) was calculated using equation 1.29, with D - representing the diameter of a single modification, defined from the cross-sectional profile as the distance between the two points where the surface deviates below the original flat level and returns to it. In the experiments, the overlap of modifications in the x and y directions was kept equal to ensure uniform ablation. In figure 3.5 the areal surface roughness Ra_x dependence on the overlap of the modifications Ω when the surface is scanned once is given. The experimental results were achieved using the 3^{rd} experimental setup configuration (see section 2.1), featuring λ = 257 nm, and pulse energy of E_p = 8.72 μJ. The red curve represents the experimental roughness values evaluated as described in section 3.1, while the green curve corresponds to the roughness values obtained after applying a cutoff wavelength of λ_c = 10 μm. The latter was extracted to evaluate the influence of overlap on the smallest surface features. The corresponding surface profiles used for roughness evaluation with and without the application of λ cutoff wavelength are shown in part (C) of the figure. The numerical model employed in this part of the investigation is described in section 3.2. It can be observed that the results of numerical simulations (black curve) and experimentally acquired

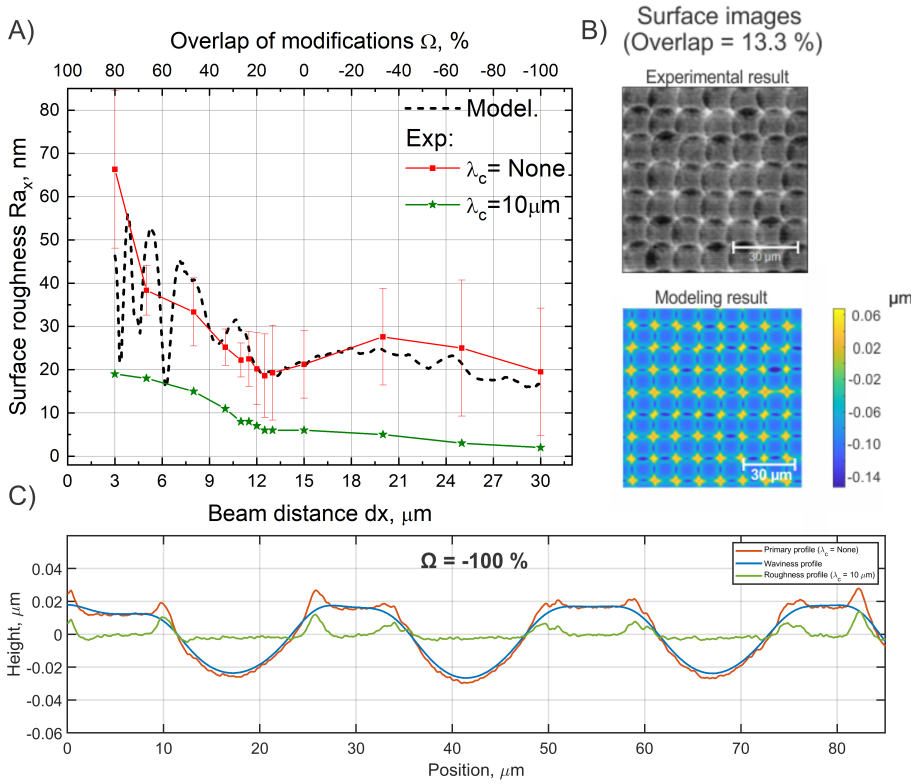


Fig. 3.5 Surface roughness (in the scanning direction) dependence on the overlap of modifications (A). The black dashed line represents the numerical modeling results, whereas the red and green curves correspond to the experimental results obtained without filtering and with a cutoff wavelength of λ_c = 10 μm, respectively. Surface images after single-pass machining acquired experimentally and via numerical calculations (numerical model description given in section 3.2) when the overlap of modifications is 13.3 % (B). Part (C) compares the surface profiles obtained without a λ_c filter (red) and with a cutoff wavelength of λ_c = 10 μm (green). The experiments were performed with 3^{rd} experimental setup configuration and E_p of 8.72 μJ.

values (red curve) are in good agreement. The lowest surface roughness (Ra_x ~ 20 nm) is achieved when Ω is in the range between 10-20 %. From the graph, it appears that even lower roughness values are attainable by further increasing beam distance to $dx > 30$ μm (Ω < -100 %). However, it is just a measurement artifact. When the beam distance is drastically increased, modifications are placed further and further apart to the point where the distance between single-shot modifications exceeds the dimensions of the measuring window. In that case, the initial surface roughness level is measured (Ra_x < 10 μm). At the other end of the curve, we observe increase in Ra_x as the overlap between

modifications increases. When Ω exceeded 80 %, the soda-lime glass began to fracture due to induced stresses, rendering such parameter values inapplicable, and therefore excluding them from further discussion here. After a more detailed examination of the numerical calculations, the periodic variations in surface roughness can be observed (see figure 3.5, black curve, where $dx \sim$ 3-15 μm). As discussed above, the minimum roughness is achieved when the distance between consecutive modifications is 13 μm (or 13.3 % overlap), however, other local minimums in the curve can be seen at beam distances - 6.3 μm and 3.2 μm. These results suggest that an optimal arrangement of modifications is achieved not only at a beam distance of 13 μm but also at twice smaller distances of 6.3 μm and four times smaller - 3.2 μm. In contrast, the experiments did not show the same variation in surface roughness as was observed in the case of numerical calculations. From the steepness of the dips in the curve, it can be assumed that highly precise pulse positioning is necessary for optimal arrangements to be established. However, in reality, all sorts of vibrations and inaccuracies exist, that likely restrict the formation of such patterns, therefore they were not observed experimentally. Further examination of the experimental results revealed that, after the removal of the longer spatial wavelengths (green curve), the distinct optimum overlap corresponding to the minimum roughness is no longer observed. Instead, the roughness decreases monotonically with increasing beam spacing dx. When craters no longer overlap ($\Omega < 0$ %), the $Ra_x(\lambda_c = 10\ \mu\text{m})$ remains approximately constant. A slight decrease is still observed, which can be attributed to the gradual reduction in the number of craters within the measurement window as dx increases. While the application of a cutoff wavelength isolates the highest-frequency roughness components and provides additional insights, the surface texture part considered as waviness here is still generally perceived as very fine and has a strong influence on various material properties. Therefore, all subsequent analyses will continue the evaluation of roughness values with no λ_c filter applied.

Additional experiments were carried out with other experimental setup configurations to test if the previously determined $Ra_x(\Omega)$ relation maintains when different laser parameters are applied. The results are given in figure 3.6. Looking at the figure, a few observations can be made. First, it is observed that lower surface roughness is achieved when using shorter wavelength laser radiation. The discussion in section 1.2.1 disclosed that absorption coefficient is highest for the shortest wavelength radiation. Moreover, the inverse relationship

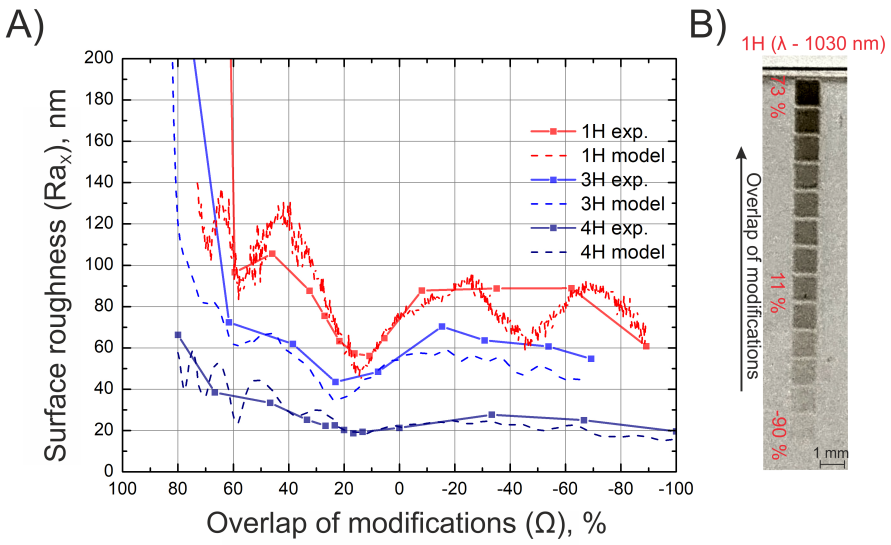


Fig. 3.6 Surface roughness dependence on the overlap of modifications, when different laser wavelengths are used (A). Surface roughness measured in scanning (x) direction. Solid lines represent experimental results, and dotted - modeling results. In part B, a macro picture of machined surfaces with λ = 1030 nm (1H) is shown. Pulse energies used: for 1H - E_p = 173 μJ, for 3H - E_p = 10.8 μJ and for 4H - E_p = 8.72 μJ.

between absorption coefficient and light penetration depth indicates that shorter wavelengths enable the formation of shallower modifications, which is also experimentally confirmed in figure 3.7, part B. The superposition of shallower modifications is therefore expected to produce topographies with reduced roughness, which is indeed observed in figure 3.6. Furthermore, it is observed that the minimum achievable surface roughness is reached when the overlap of the modifications Ω is between 10-25 %. This relationship holds across all examined system configurations, that include variations in wavelength, pulse energy, and beam diameter. To better understand why the best surface quality is achieved when the modifications are just barely overlapped, it is worth looking into the geometry of a single-shot modification (see figure 3.7 (B)). One of the key geometrical features of the modification that strongly influences the resulting surface roughness is the lateral ratio Γ between the sidewall and the crater diameter, given as $\Gamma = (\Delta r_{sw}/D) \times 100\%$, where sidewall lateral dimension Δr_{sw} is estimated at the depth of $1/e^2$. The visual correspondence of parameters $h(1/e^2)$, Δr_{sw}, and D for crater generated with 1H are given in figure 3.7 (B). The estimated Γ values for each modification are given in table 3.1. The

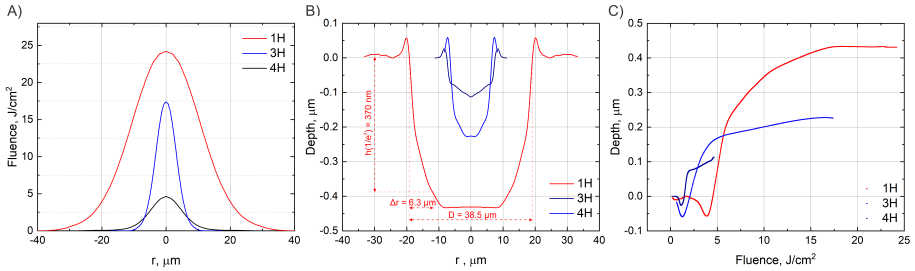


Fig. 3.7 Beam profiles for different laser wavelengths (A), cross-sectional profiles of single-shot modifications in soda-lime glass induced by different wavelengths (B), and material response functions corresponding to the various wavelengths (C). Red curve - 1H (E_p = 173 μJ; F = 24 J/cm^2), blue curve - 3H (E_p = 10.8 μJ; F = 17.3 J/cm^2), black curve - 4H (E_p = 8.72 μJ; F = 4.6 J/cm^2).

comparison of Γ and Ω_{opt} values show a strong correlation in their absolute magnitudes. It suggests, that the minimum roughness is achieved when the

Table 3.1 Geometrical characteristics of single-shot modifications given in figure 3.7 (B). $h(1/e^2)$ corresponds to the depth at 1/e^2 level, Δr_{sw} is the lateral dimension of sidewall (estimated at $h(1/e^2)$), D denotes the crater diameter, Γ is the lateral ratio between sidewall and the crater diameter, and Ω_{opt} is experimentally determined optimal overlap of craters, when minimum roughness is achieved.

Configuration	$h(1/e^2)$ (nm)	Δr_{sw} (μm)	D (μm)	Γ (%)	$\Omega_{opt.}$ (%)
1H, E_p = 173 μJ (F = 24 J/cm^2)	370	6.3	38.5	16.4	10.8
3H, E_p = 10.8 μJ (F = 17.3 J/cm^2)	210	2.9	13.32	21.7	23
4H, E_p = 8.72 μJ (F = 4.6 J/cm^2)	96	4.5	15	30	16.6

craters are overlapped by the fraction corresponding to the lateral length of the sidewalls. Under such conditions, only the sidewalls are ablated while relatively flat bottoms are left unaffected, resulting in smoothest surface. Additional parameters describing the surface roughness characteristics at optimal overlap values are presented in the table 3.2. The roughness parameters provided demonstrate a close correlation between our proposed areal Ra parameter and the conventional S_a (surface arithmetical mean height) parameter. Moreover, it can be seen that if the surface has different roughness values measured in different directions (such a case happens when the laser system is not synchronized), the S_a parameter is determined by the more rough direction of the surface. Hence, in a case when only the S_a parameter is measured, only half of the information about the roughness of the surface is retrieved. Therefore, measuring Ra_x and

Table 3.2 Different surface roughness parameters of experimentally produced surfaces using different system configurations at optimal overlap values. Ra_x and Ra_y - the arithmetic average height of a line averaged over the area in x and y directions accordingly, S_a - surface arithmetic average height, S_q - RMS roughness of the surface, S_{sk} - surface skewness, S_{ku} - surface kurtosis.

Configuration	Ra_{X} (nm)	Ra_{Y} (nm)	S_{a} (nm)	S_{q} (nm)	S_{sk}	S_{ku}
1H, Ω = 10.8%, E_p = 173 μJ	55.30	80.42	82.20	107.50	0.0887	0.572
3H, Ω = 23%, E_p = 10.8 μJ	42.61	62.07	62.17	84.00	-0.085	1.316
4H, Ω = 16.6%, E_p = 8.72 μJ	19.33	19.87	21.96	30.19	0.515	1.661

Ra_y separately provides more information about the roughness of the surface than a stand-alone S_a parameter. Other parameters, skewness (S_{sk}) and kurtosis (S_{ku}) indicate that all three surfaces have a relatively even distribution of peaks and valleys over the area. Moving on, additional advantage of using UV light in the context of surface roughness can be noted. When looking at figure 3.7 part C, we can notice that the material response function for the 4H is shifted to the lower fluence values when compared to the 3$^{\mathrm{rd}}$ and 1$^{\mathrm{st}}$ harmonics, which is attributed to linear absorption [185]. Reduced ablation threshold for 4H renders the requirement for high-power laser sources unnecessary, which simplifies the process and reduces the risks associated with operating such systems.

3.4 Other pulse positioning techniques

It was further observed that if the beam guiding system is not synchronized with the laser, the modified surface roughness in the x and y directions can differ significantly. In a non-synchronized system, the laser and the scanning unit operate independently without synchronization. The laser is generating pulses at a fixed (manually selected) repetition rate. To create desired scanning paths on the surface of the sample, the triggering of the pulse picker of the laser is controlled via an external signal (using Scanlab RTC5 control board). The pulse picker trigger signal does not account for the time position of the nearest generated pulse within the laser; therefore, when the pulse picker is triggered (e.g. at the starting position of the line), the time delay after which the first pulse will arrive is random. This introduces the uncertainty of the position of the first pulse in the line. The magnitude of the uncertainty is determined by the scanning speed and the repetition rate of the laser. The maximum possible shift

(δ) can be estimated using the following expression:

$$\delta = \frac{v}{f} = dx, \tag{3.6}$$

where v – scanning speed, f – laser repetition rate, dx – pulse distance. The laser ablated surface for two cases when the system is synchronized and not synchronized are depicted in figure 3.8. We see that when the beam guidance

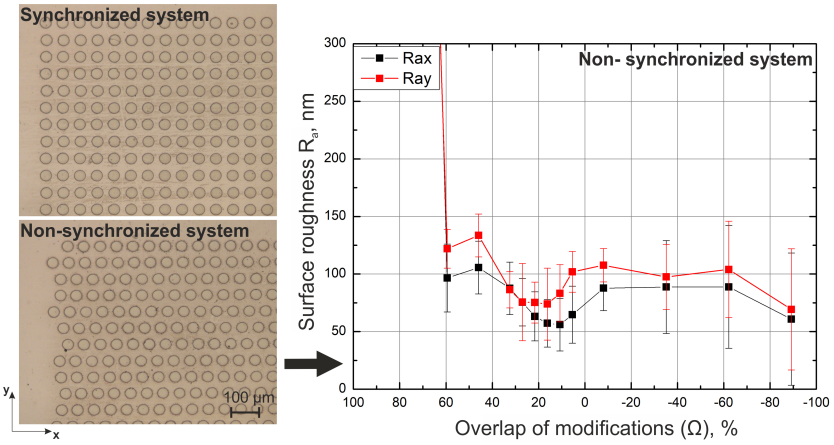


Fig. 3.8 Surface morphology after single-pass ablation with synchronized system (top left) and with non-synchronized (bottom left). Surface roughness as a function of modification overlap in the non-synchronized system (right). Results achieved with 1^{st} experimental system configuration (see section 2.1), E_p = 173 μJ, λ = 1030 nm.

system is synchronized all the modifications are nicely arranged in a rectangular manner. On the other hand, when the system is not synchronized all lines are shifted. While this does not affect surface roughness in the scanning direction (x direction), the surface roughness in the y direction changes. This can be observed from the surface roughness dependence on the overlap of modifications in the x and y directions. Surface roughness in the y direction is usually higher. The measured difference was as high as 37 % (when the overlap is 5.4 %). Since many different material parameters depend on the surface roughness the difference in surface roughness in x and y directions can be exploited. One of the possible applications would be the control of fluid and gas movement direction [186, 187].

Lastly, it was shown that surface roughness can be further improved by shifting every second line by a certain distance in the scanning direction. In

figure 3.9 a dependence of surface roughness on the shift of every 2nd line is depicted. The shift of every 2nd line was normalized to the pulse distance and plotted on the x-axis. It can be observed that the lowest surface roughness is achieved when every second line is shifted by half of the pulse distance. By realizing such conditions surface roughness can be further reduced by an additional 20%. When every second line is shifted by half a distance between single pulses a checker pattern is realized. A small portion of un-ablated material that is usually left in a cross-section of 4 pulses (see figure 3.5 topographies) is now being ablated while still maintaining the overlap of modifications close to optimal. If such conditions are met further reduction of surface roughness is possible.

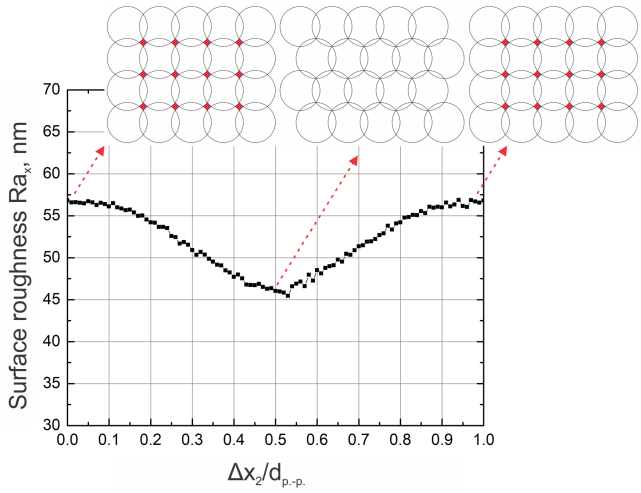


Fig. 3.9 Surface roughness dependence on the shift of every 2nd line, when pulse distance of 32 μm is maintained. On x axis shift between consecutive lines Δx_2 divided by the pulse distance is plotted. Used system configuration – 1 (see section 2.1), E_p = 173 μJ, λ = 1030 nm. Data of numerical simulations.

After a thorough investigation, it was demonstrated that surface roughness can be tailored or minimized by choosing an appropriate scanning algorithm. A detailed explanation has been introduced for the first time, establishing the underlying reasons for the attainment of minimum surface roughness when the overlap of craters is within the range of 10-25 %. In addition, the relation between surface roughness and used laser wavelength was demonstrated and reasoned. Next, a novel technique for attaining diverse levels of roughness in distinct orientations was introduced and discussed. A new perspective for

evaluating the areal surface roughness was introduced, offering areal surface roughness measurements based on its orientation. Besides, a novel scanning algorithm was introduced that involves shifting every second line and has the capability to achieve an even greater reduction in surface roughness. Moreover, it was shown that the developed model (for details see section 3.2) is capable of performing surface ablation simulations and accurately predicting final surface roughness. To the best of our knowledge, this is the first numerical model of such kind, that accounts for the fresnel reflections, fluence reduction due to the increase of surface area and allows for such accurate estimation of final surface roughness under provided conditions.

However, the study was limited by investigating only single-scanned surfaces. The achieved depths after a single scan were very low (usually < 1 μm). In practice, to retrieve any shape using laser ablation the surface must be scanned multiple times to remove a reasonable amount of material. This case, when the surface is scanned multiple times, is usually of more interest. Therefore, in the next chapter we will investigate how surface roughness behaves under multilayer ablation conditions and how it can be controlled via different scanning strategies.

3.5 Summary

It was found that, for single-pass scanning, the resulting surface roughness is primarily governed by the overlap of laser-induced modifications rather than the geometrical beam overlap. It was seen that the smoothest surface ($R_a \approx 20$ nm, achieved using $F = 4.6$ J/cm^2 and $\lambda = 257$ nm) is realized when the overlap of modifications Ω is in the range of $\Omega \sim 10 - 25\%$. This behavior was consistent across different experimental system configurations (featuring fluences $F \sim 4.6 - 24$ J/cm^2 and laser radiation wavelengths $\lambda \sim 257 - 1030$ nm), and is attributed to selective material removal, where mainly steep edge regions are ablated while relatively flat crater bottoms remain largely unaffected, leading to overall surface smoothing. In addition, it was observed that in non-synchronized systems, a significant anisotropy in surface roughness arises between the x and y scanning directions, with differences reaching up to 37%, which is linked to the formation of direction-dependent surface structures. Finally, a reduction in surface roughness by additional 20% (from $Ra_x = 57$ nm to $Ra_x = 45$ nm) was achieved by implementing a checkerboard scanning strategy, in which every second line is shifted by half a step between adjacent

modifications $\Delta x_2/d_{p.-p.} = 0.5$. This approach promotes the removal of residual unablated material that would otherwise remain at the intersection of four modifications (when $\Omega = 20\%$ is used), thereby further improving the final surface quality.

Chapter 4

Multilayer ablation investigation

Results presented in this chapter were published in [A2] and presented at [D4], [D6], and [D7] conferences.

Extending the investigation of the previous chapter, which examined the surface roughness after a single scan, in this chapter we investigate the surface roughness behavior during multilayer ablation. In a multilayer ablation the surface is scanned multiple times, until the desired depth is reached. From the literature overview in section 1.3, it is evident that surface roughness (measured as S_a) evolves continuously during multilayer ablation, making it challenging to maintain precise control over it. Thus, in this chapter we explore diverse means of controlling it through the use of combined scanning strategies. We propose that in order to achieve control over surface roughness, first, the stabilization of S_a evolution must be achieved. Once the roughness no longer changes with increasing depth, it can be further tuned by varying laser and scanning parameters.

4.1 Investigation framework

In this chapter, the first and second experimental setup configurations were used, featuring laser wavelengths of $\lambda = 1030\,\text{nm}$ and $\lambda = 343\,\text{nm}$, respectively. The detailed description of different configurations is given in section 2.1. Laser engraving experiments and surface microstructuring were performed on fused silica glass samples of varying thicknesses. The third harmonic was used only when the formation of smaller diameter and depth craters were needed to benchmark the lowest achievable surface roughness. The initial roughness of

the samples was measured to be S_a = 5 nm. The measured value falls within the range of the device's measurement noise, indicating that the real initial roughness value is $S_a \leq 5$ nm. The experiments consisted of scanning a surface area of 1 x 1 mm^2 multiple times by a chosen scanning algorithm. After the processing of a single area was completed, the sample was repositioned to the center of the lens field using the x and y translation stages, and the next machining algorithm was executed. This was done to eliminate aberrations of the f-theta lens, which become significant near the edges of the lens field. Next, to eliminate the uncertainty of the pulse positioning, observed in the previous chapter when the laser-scanner system is not synchronized, the laser and scanner were electronically synchronized using the Output Synchronization functionality of RTC5(SCANLAB Ltd.) control board. In this chapter, three different scanning strategies were examined:

- Change in overlap of the craters $\Omega_{x,y}$.
- Rotation of the layers.
- Displacement of the layers.

The detailed description and visual representation of each scanning strategy is given in section 2.2. The expression of the overlap of the craters Ω is given in equation 1.29. To maintain even ablation, the overlap of the craters in x and y directions was kept equal. Based on the findings in chapter 3, an Ω value of 20% was selected for use in the experiments presented in this chapter, unless stated otherwise. During the rotation of the layers, the rotation of every next layer at a fixed angle (α) relative to the previous one is performed. The axis of rotation is set to be fixed at the center of the machined area. By utilizing different angles of rotation, various patterns could be generated that produce different values of surface roughness. During the displacement of the layers, each successive layer is displaced by a random amount in x and y directions. This introduces more randomness in laser pulse positioning and assists in preventing the formation of periodic structures.

The laser-processed areas were subjected to the surface roughness measurements after the machining. The laser scanning microscope ("LEXT OLS5100", Evident Scientific, formerly Olympus) equipped with a 100x (0.8 NA) objective ("LMPlanFL N", Evident Scientific, formerly Olympus) was used for the acquisition of the surface topographies. When acquiring the topographies,

the machined samples were centered, and the surface area of 256×256 μm (comprising 2048×2048 measuring points) was acquired. The measurement noise was determined using the subtraction technique [181]: from a set of 10 measurements, the noise value, expressed as the root mean square of roughness ($S_{q(noise)}$) was estimated to be 6.5 nm. For the assessment of the surface roughness, a 3D roughness parameter - arithmetical mean height (S_a) was computed for each surface. The roughness parameter was evaluated as described in ISO 25178 standard, with the mathematical expression provided in the equation 1.5. Since here, only the assessment of the average roughness and its change was of interest, calculating only S_a parameter proved to be sufficient. The filtration of the primary roughness involved the use of the S (surface small-scale filter) and F (form removal) operations only, excluding the L (surface large-scale filter) operation from the filtration procedure. Therefore, within the framework of this chapter, the surface roughness parameter S_a constitutes the average roughness of a scale-limited S-F surface. For the removal of the small-scale lateral components that denote the measurement noise the nesting index N_{is} of 0.5 μm was applied. Furthermore, to remove the tilt induced by inaccurate positioning of the sample a best-fit least squared F operation was executed. After these operations, the primary surface was obtained from which the roughness parameter S_a was computed. For more details on the filtration procedures, see section 1.1.3.

4.1.1 Multipulse exposure

Section 1.2.4 concluded that during laser-matter interaction, laser-induced stresses and the rapid resolidification of the molten material can significantly alter the optical and mechanical properties of the processed surface, thereby affecting the coupling of subsequent laser pulses to the material. During multilayer laser ablation, the same surface is irradiated repeatedly. As the material properties evolve with each exposure, the absorption coefficient, optical penetration depth, and ablation rate are expected to change throughout the laser processing. Confirming that, different independent groups have observed a decrease in ablation threshold fluence when the surface is subjected to multiple pulses. Rosenfeld et al. [188] obtained a 75 % decrease in the damage threshold of fused silica, measuring a single-shot damage threshold of 3.7 J/cm^2, and 0.9 J/cm^2 when 20 laser pulses were used. Similar values were reported by

Ben-Yakar et al. [189], measuring $F_{th} = 2.6$ J/cm^2 in a single-shot case and $F_{th} = 1.74$ J/cm^2 when the surface is exposed to 50 shots. In addition to that, repeated laser exposure not only alters the material's internal properties but also leads to the continuous evolution of the surface texture. One of the key surface texture modifications induced during multipulse laser irradiation is the formation of laser-induced periodic surface structures (LIPSS), which can further modify the surface optical response. The surface coverage by LIPSS can further enhance absorptance of laser radiation, which is attributed to geometrical light-trapping, increased surface area, and other effects. Tianyu Wang et al. [190] report that absorptance is increased by 38 % when high-quality laser-induced periodic surface structures are formed. While the mechanisms underlying the formation of these features have been extensively studied [191], their formation appears to be unavoidable.

To evaluate the combined influence of the aforementioned factors on the material's optical response (e.g., light absorptance, optical penetration depth, and ablation rate), an experimental investigation was carried out comparing laser processing of pristine and previously laser-modified surfaces. For comparison,

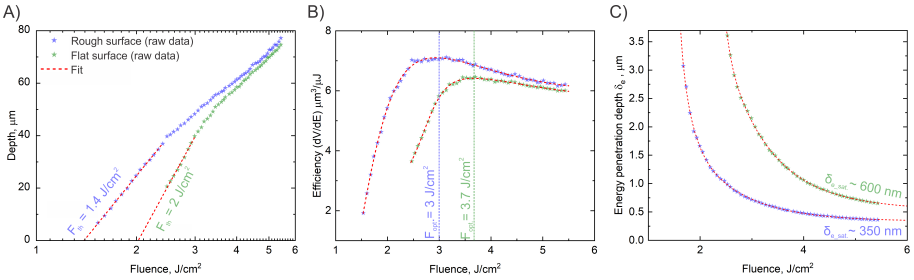


Fig. 4.1 Engraved cavity depth dependence on used laser fluence, when laser processing is applied on flat ($S_{a\_int} < 10$ nm) and rough ($S_{a\_int} = 420$ nm) surfaces (A). Ablation efficiency (dV/dE) dependence on used laser fluence (B). Assessed energy penetration depth δ_e dependence on used laser fluence. Each cavity measured 0.5×0.5 mm^2 is size. The engraving parameters were: laser repetition rate $f = 5$ kHz, scanning pitch $dx = dy = 12.3$ μm, scanning speed $v = 61.5$ mm/s, and included 50 scans per cavity.

0.5×0.5 mm^2 cavities were engraved on two different surfaces: an initially smooth, laser-unaffected surface ($S_{a\_int} < 10$ nm) and a laser-modified surface with roughness of $S_{a\_int} = 420$ nm, which was formed laser scanning the surface 100 times with chosen parameter set. Each cavity was scanned 50 times to achieve sufficient depth, while the laser repetition rate was maintained low ($f = 5$ kHz) to eliminate the influence of heat accumulation. The results

are given in figure 4.1. From part (A) of the figure, we see that the multishot ablation threshold $F_{\text{th.}}$ is lower in the case when laser processing is applied on rough surface ($F_{\text{th.}}^{\text{rough}} = 1.4$ J/cm^2), in comparison to when ablation is performed on a flat surface ($F_{\text{th.}}^{\text{flat}} = 2$ J/cm^2). This agrees well with the previous discussion regarding the influence of LIPSS on the optical material properties. Furthermore, the ablation efficiencies were estimated for both cases, where the efficiency is expressed as [192]:

$$\eta = \frac{V}{E} = \frac{z \cdot d_x^2 f}{N_{\text{scan}} P}, \tag{4.1}$$

here, z - engraved depth, d_x is a scanning pitch, f - fundamental laser repetition rate, N_{scan} is number of scans and P is average laser power. Part (B) of the figure unveils that the optimal fluence value at which maximum ablation efficiency is achieved also differs depending on the initial roughness of the surface ($F_{\text{opt.}}^{\text{rough}} = 3$ J/cm^2 and $F_{\text{opt.}}^{\text{flat}} = 3.7$ J/cm^2). This suggests that as laser processing progresses, the optimal fluence shifts to lower values. Finally, from the experimentally determined ablation efficiencies, the theoretical energy penetration depths were estimated, following the equation [193]:

$$\delta_e = \frac{2F_0\eta}{\ln^2\left(\frac{F_0}{F_{\text{th}}}\right)}, \tag{4.2}$$

where η is the ablation efficiency, F_0 laser fluence and F_{th} is ablation threshold fluence value. The corresponding δ_e dependencies on laser fluence when laser processing is performed on initially smooth and rough surfaces are given in figure 4.1, part C. As can be observed, the penetration depth decreases with increasing fluence, indicating an increasing free-electron plasma density until saturation is reached at $F_0 \gtrsim 6$ J/cm^2. In addition, it was shown that the $\delta_{\text{e\_sat.}}$ value is lower when laser processing is applied on an initially rough surface ($\delta_{\text{e\_sat.}}^{\text{rough}} \sim 350$ nm and $\delta_{\text{e\_sat.}}^{\text{flat}} \sim 600$ nm), further confirming that initial roughness greatly alters optical material properties.

In the previous chapter, it was demonstrated that the developed numerical model of laser ablation (see section 3.2) can accurately predict the surface roughness after a single scan. However, that model does not account for the dynamic evolution of the material's optical properties under multi-exposure conditions, the existence of which was demonstrated in this section. Simulating

defect accumulation and LIPSS formation would substantially increase the computational time. Consequently, the model predictions deviate significantly from the experimental results under multilayer ablation conditions. This defines the current applicability limits of the developed model, which remain until these physical effects are incorporated. Therefore, the following investigation of multilayer ablation will be based primarily on experimental observations.

4.2 Achieving stabilization of surface roughness

During the investigation of multilayer ablation, it was observed that the first step towards achieving precise control of surface roughness is to stabilize its evolution so that it no longer changes with increasing engraving depth. This condition is achieved when the topography of the surface is maintained in a similar state after each scan. This requires suppressing the formation of any kind of periodic structures, which are typically the source of ever growing roughness. This is accomplished by adjusting the laser scanning path to minimize the likelihood of irradiating the exact same locations in each layer.

4.2.1 Rotation of the layers

Initially, an investigation of surface roughness evolution when every consecutive layer is rotated by a particular angle was carried out. The angle at which the n-th layer was rotated is given in equation 2.1. Each processed area was scanned 30 times with a fixed angle of rotation (α) and the resulting surface roughness was measured. The full range of angles from 0° to 360° was investigated. However, given the directional symmetry of the layer rotation, where both clockwise and anti-clockwise rotations have an identical effect on the quadratic pattern, the complete angular range could be truncated to [0°; 45°] interval using triangular function:

$$\alpha^* = \frac{1}{4}\cos^{-1}[\cos(4\alpha)], \tag{4.3}$$

here α^* is a truncated angle. The surface roughness dependence on the compressed domain of angles of rotation is shown in figure 4.2, part (A). After examining the results, it was observed that two categories of angles can be identified: the category 1 comprises arbitrary angles (depicted in the figure as green circles) and include primary numbers such as 3°, 29°, 73°; while the category 2 include particular angles that are factors of 90° (shown as red stars).

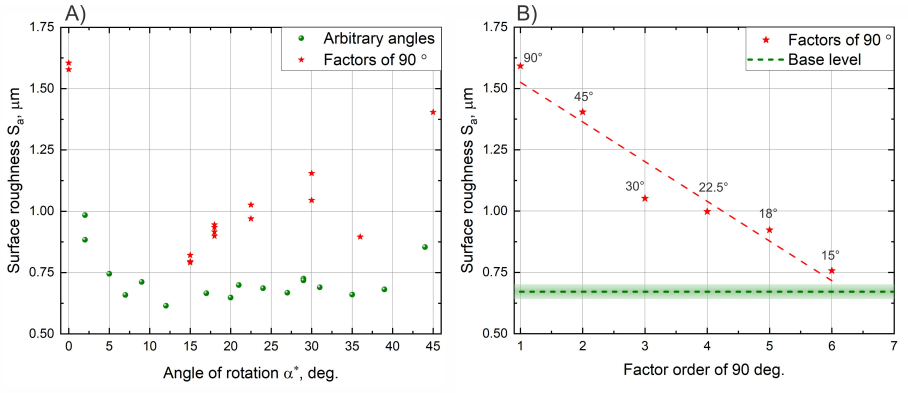


Fig. 4.2 (A) The surface roughness dependence on the angle (α) of layer rotation, when surface is scanned 30 times. Two distinctive angle categories are depicted: arbitrary angles and factors of 90°. (B) The dependence of the surface roughness on the angles of rotation that are factors of 90°. The fit is presented as a red dashed line, whereas the base level formed of arbitrary angles is presented as a green dashed line with a standard deviation (1σ) shown as a green area. Processing parameters: Fluence F = 52 J/cm^2, overlap of the craters Ω = 20 %, wavelength λ = 1030 nm.

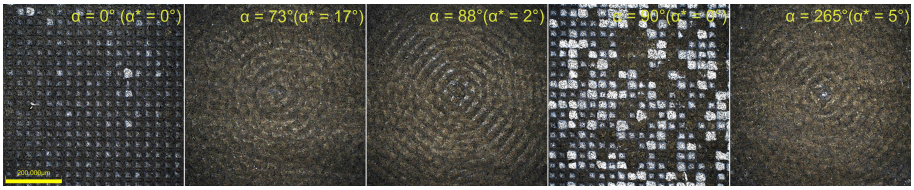


Fig. 4.3 Color images of surface structures induced by scanning the surface 30 times with different angles of rotation (α). Fluence F = 52 J/cm^2, overlap of the craters Ω = 20 %, wavelength λ = 1030 nm.

The use of arbitrary angles results in an almost constant surface roughness level (here, $S_a \sim 0.65\,\mu$m), which constitutes the minimum achievable surface roughness value. In contrast, category 2 angles exhibit surface roughness values that are higher than the baseline, with the exact magnitude varying depending on the α value. When a category 2 rotation angle is used, the laser beam positioning frequently coincides with the same locations as in previous layers, leading to the formation of deeper localized craters. Consequently, high-contrast periodic structures are produced (see figure 4.3, $\alpha = 0°$ and $\alpha = 90°$), resulting in elevated surface roughness ($S_a > 0.8\,\mu$m). To further analyze the category 2 angles, the surface roughness dependence on the factor order of 90° was extracted and plotted in figure 4.2, part (B). Results show that increasing the factor order linearly reduces surface roughness. Rotation of layer by 90°, yield

the same pattern during each scan (for the quadratic pattern with rotational axis fixed on the center); whereas when a 30° angle is used, the scanning pattern coincides only with every 3^{rd} layer, and so on. Hence, the factor order shows how often the scanning pattern coincides with the one in the preceding layers, indicating the magnitude of induced periodic structure. When category 2 angle exceeds the 6^{th} factor, the surface roughness approaches the values comparable to the ones achieved with arbitrary angles. The results are in a good agreement with the ones presented in the literature [35]. However, even when category 1 angles are used, the periodic structures develop after multi-scan machining which are clearly seen in the microscope pictures, given in figure 4.3 (see $\alpha = 73°, 88°, 265°$). In these cases, the periodic structures exhibiting a high degree of cylindrical symmetry are observed. It is reasoned to be the result of a fixed axis of rotation, which is positioned at the center of the processing area. Periodic structures, of any kind, are generally considered undesired phenomena, as they are attributed to the continuous growth of the surface roughness. Hence, this demonstrates that the layer rotation scanning strategy alone is insufficient in order to stabilize the surface roughness evolution.

4.2.2 Displacement of the layers

The formation of cylindrical symmetry exhibiting periodic structures during the rotation of the layers can be mitigated by implementing "moving axis of rotation" technique. This method involves shifting the axis of rotation to a different position during each scan. In practice, this can be realized by introducing the uncertainty of layer positioning defined by the equations 2.2 and 2.3. In such a case, instead of scanning each layer on top of each other, every next layer is shifted by a random amount in x and y directions, with a maximum displacement magnitude of Δ (see section 2.2 for more details). The impact of this scanning technique on the resulting surface roughness, while maintaining the rotation of the layers at a category 1 angle ($\alpha = 73°$) is given in figure 4.4. The results reveal that displacement of the layers significantly influences the evolution of the surface roughness, with its effectiveness strongly dependent on the maximum displacement amplitude Δ. As is shown, the surface roughness evolution mainly consists of 3 stages (depicted as I, II, and III regions in the figure): the initiation (I), the transition (II), and the saturation (III). In the first stage, which typically happens within the first 10 layers, the roughness

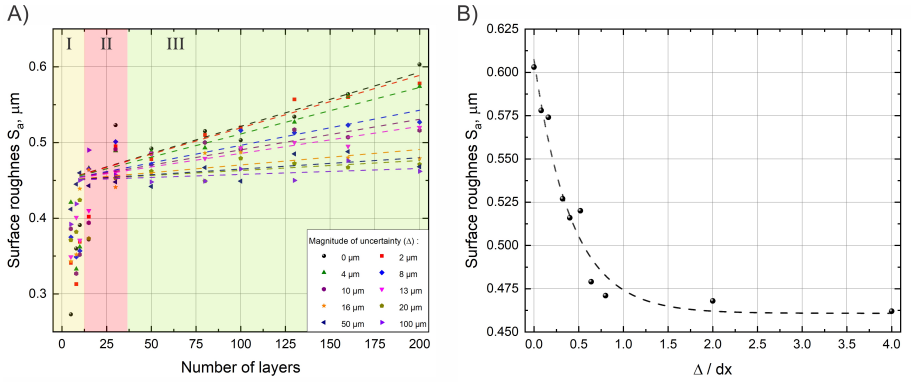


Fig. 4.4 Surface roughness (S_a) dependence on the number of layers, when different levels of uncertainty of layer positioning are introduced (A). Symbols represent raw data, dashed lines - linear fits of the data within the region III. The roughness evolution is divided into 3 different regions governing different roughening mechanisms. In part (B) of the figure a surface roughness dependence on the maximum displacement Δ divided by a pulse-to-pulse distance after 200 layers is shown. Symbols represent raw data, whereas the dashed lines show a decaying exponential fit. Processing parameters: overlap of the craters $\Omega = 22\%$, fluence $F = 20.8$ J/cm^2, wavelength $\lambda = 1030$ nm, diameter of a single crater $D = 32$ μm, pulse-to-pulse distance = 25 μm.

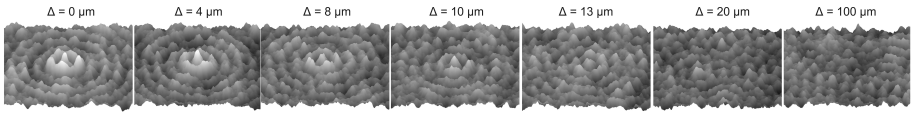


Fig. 4.5 3D views of surfaces after 200 layers when different levels of uncertainty of layer positioning are utilized. Dimensions of a single window 250×250 μm. Processing parameters: overlap of the craters $\Omega = 22\%$, fluence $F = 20.8$ J/cm^2, wavelength $\lambda = 1030$ nm, diameter of a single crater $D = 32$ μm, pulse-to-pulse distance = 25 μm.

of the surface increases very rapidly. The rapid growth is caused by several factors. At the beginning, each layer contributes to the formation of the final structure which is a superposition of individual craters within each layer. After the final structure is formed (which takes around 10 layers) each subsequent layer is used to further engrave the surface, while maintaining the the final structure. At the same time, following the scanning of several layers, nanoripples begin to form, contributing to an increase in surface roughness. The formation of self-organized nanostructures in multipulse laser treatment of metals and dielectrics is a widely known and intensely studied phenomena [194–196]. Stage II here spans across 15 to 30 layers and represents the surface morphology transition from semi-clean to fully covered by nanoripples. Since the formation

of nanoripples requires multiple pulses, the duration of stage II depends on the pulse density per layer and can vary significantly depending on the scanning parameter configuration. It was observed, that formed nanoripples tend to alter the altitude and the roughness of the surface. As a result, when the surface is only partly covered by nanoripples the surface roughness peaks (this can be seen by the outliers in region II). Once the formation of nanoripples across the entire surface is completed, the elevations become uniform, resulting in a reduction in surface roughness. After the transition stage, the subsequent phase, denoted as the final (III) - saturation stage, commences. When the entire surface is covered by nanoripples, the only variables influencing the final roughness is the induced surface structure and its contrast. It can be seen that when the axis of rotation is fixed we observe the linear growth of the surface roughness, which is attributed to the growth of the contrast of the periodic structure. However, when the uncertainty of layer positioning is introduced the formation of periodic structures can be prevented (see figure 4.5). By moving the axis of rotation to a slightly different location in each layer and maintaining the rotation of the layers, the likelihood of positioning the laser beam to the same location as in the previous layers decreases. Consequently, the sufficient introduction of layer position uncertainty prevents the formation of the periodic structures, resulting in a randomly patterned structure at the bottom of the cavity. Upon the prevention of the periodic structure formation, the final roughness saturates at the beginning of the 3rd stage of the roughness evolution and remains constant with the increasing number of layers. This, in consequence, results in the reduction of the final roughness compared to the fixed axis of rotation case.

The maximum reduction of the surface roughness (from 600 nm down to 460 nm (S_a)) was achieved after 200 layers when the uncertainty parameter $\Delta \geq 25$ μm was used. Since the absolute value of the Δ parameter necessary for the maximum reduction of surface roughness depends on the used processing parameters, a more appropriate way of expressing the prior condition is by linking it to the result of the combined laser and scanning parameters - the distance between the adjacent craters (pulse-to-pulse distance). Given that the distance between the adjacent craters was fixed at $dx = 25$ μm, the surface roughness after 200 layers dependence on the uncertainty parameter divided by pulse-to-pulse distance (Δ/dx) was derived (see figure 4.4, part (B)). From the derived relationship, we observe that 90% of the maximum reduction ($\delta S_{a(max)} = 140$ nm) is reached at $\Delta = dx$. Therefore, saturation and the

minimization of the resulting surface roughness can be considered achieved at $\Delta \geq dx$. The discussion concludes that the introduction of the uncertainty of the layer positioning (also refereed to as displacement of the layers) results in the saturation of the surface roughness, implying that the number of scans performed on the surface, whether it be 50, 100, or 200, becomes irrelevant as the resulting roughness remains constant. This capability allows for the prediction of the resulting roughness following the machining process for deep engraving applications. Nevertheless, in order to attain complete control over the roughness, it is necessary to possess the ability to change the level at which the roughness stabilizes.

4.3 Control of the roughness stabilization level

We identified two distinct methods that enable the control of the level at which roughness is stabilized. The first one includes tailoring the overlap of the craters. It was already demonstrated in the chapter 3, that the formed structure and it's roughness heavily depends on the overlap of the craters Ω after single-scan processing. Here, we extend the investigation of the latter dependence towards a multilayer processing scenario, aiming to evaluate its effectiveness in controlling the surface structure under deep engraving conditions. The results on roughness evolution versus crater overlap after multilayer scanning are shown in the part A of the figure 4.6, whereas part B, depicts results for the initial and final layers. It is clear, that the optimal overlap of the craters, required for the achievement of the lowest roughness is maintained even when the surface is scanned multiple times (up to 40 times), falling in the range of $\Omega = 10 - 25\%$. When the overlap $\Omega \geq 60\%$ is used, the total deposited energy per unit area increases to a point where the cracking of the glass initiates due to induced stresses, leading to significant fluctuations in height that resemble waviness. This dependence is unique for the glass-type substrates that are prone to cracking and could differ for other materials. The rise in S_a observed at lower Ω values results from entirely different mechanism. When the surface is scanned multiple times in a manner where the craters do not overlap, certain regions remain unablated, whereas others experience substantial material removal. Such irregularities in height over the surface cause the increase in surface roughness that is visible at the lower overlap values ($\Omega \leq -10\%$). Furthermore, in figure 4.6-A, we can see that with additional introduction of layer displacement (where maximum

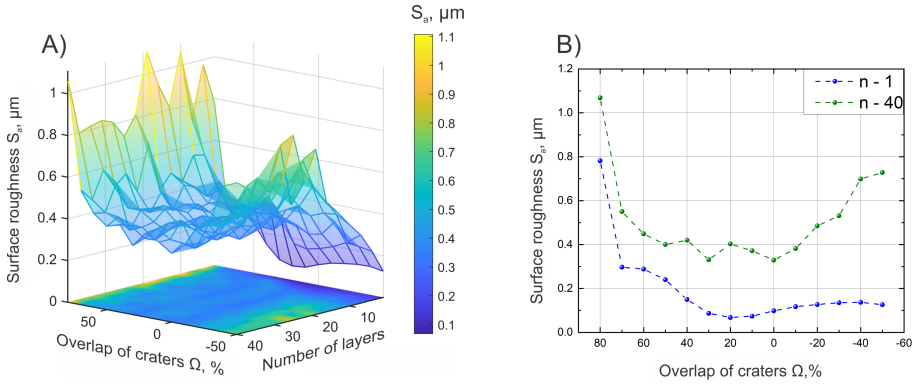


Fig. 4.6 (A) Surface roughness evolution when different overlaps of the craters are used. (B) Surface roughness dependence on the overlap value in single and multi-scan (40) cases. Processing parameters: Fluence $F = 26.1$ J/cm^2, angle of rotation $\alpha = 73°$, wavelength $\lambda = 1030$ nm. The uncertainty of layer positioning of a maximum magnitude $\Delta \geq dx$ was maintained.

shift is $\Delta > dx$) and rotation of the layers at an angle of type 1 (here $\alpha = 73°$), roughness stabilization can be achieved over multiple scans as was proposed previously. This demonstrates that roughness stabilization and the control of the roughness saturation level can be achieved using a combination of different scanning techniques. However, in some cases, roughness sensitivity to change in Ω is quite severe - i.e. change from $\Omega = 70\%$ to $\Omega = 80\%$ results in $\delta S_a \sim 500$ nm (when $n = 1$). This in turn restricts the continuous and precise tunability of S_a level, implying that the fine-tuning of the roughness level must be realized in a different manner.

We have already observed that once the stabilization of the roughness is achieved, the shape of the structure that constitutes the roughness is set via the overlap of the craters. However, the contrast, or PV value, of the resulting structure is governed by the depth of a single crater. This suggests that through the control of the depth of an individual craters, further fine-tuning of the surface roughness could be achieved. Here we show that the adjustment of the single crater's depth can be realized by tuning the pulse energy E_p and wavelength λ values of incident laser radiation. Profiles of the ablated craters produced with a single pulse of different pulse energies and wavelengths are depicted in figure 4.7-A. Based on the visual representation, it is evident that the craters sidewalls exhibit an extremely minimal level of roughness (R_a was measured to be < 10 nm), akin to the presence of background noise. When using lower pulse

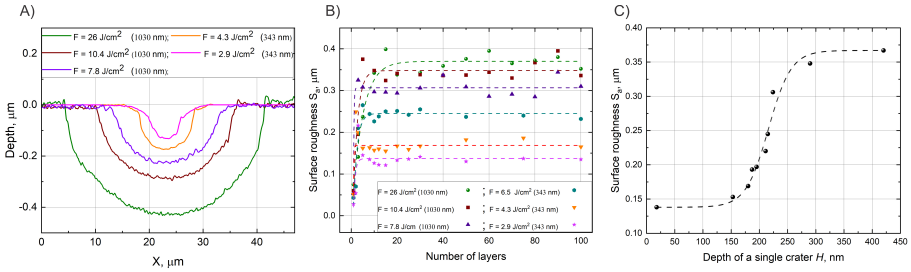


Fig. 4.7 (A) Cross sections of the craters produced using different pulse energies and wavelengths. (B) Surface roughness evolutions when utilizing craters of different dimensions. (C) Surface roughness dependence on the depth of a single crater after 100 scans when the stabilization of surface roughness is reached. Dots represent experiment data, dashed line - fit of the data. The scanning speed was adjusted to maintain the optimal overlap ($\Omega = 20\%$) in all the cases. In addition, each layer was rotated by 73°. The uncertainty of layer positioning of a maximum magnitude $\Delta \geq dx$ was maintained.

energies or shorter wavelengths, the crater dimensions decrease not only in depth but also along the longitudinal direction. Therefore, to preserve the required Ω value, the reduction in crater width had to be compensated by lowering the scanning speed. The surface roughness evolutions using craters of varying depths are shown in figure 4.7-B. As observed, when lower pulse energies (shallower craters) are used, the level at which roughness stabilizes shifts to lower S_a values. However, the available range of achievable crater depth values between the non-ablation regime and the maximum achievable depth restricted by optical penetration depth is narrow. Moreover, when using IR laser radiation, ablation with lower fluence values ($F \lesssim 5$ J/cm^2) results in the inconsistency of crater geometry with low repeatability of crater shape. The aforementioned factors establish the boundaries for the variety of crater depths attainable by manipulating only the pulse energy. It was demonstrated earlier (see chapter 1.2.1) that the light penetration depth can be reduced using shorter wavelength laser radiation. Facilitating on it, we were able to produce even smaller craters (with depths down to 20 nm) using UV ($\lambda = 343$ nm) radiation, thus extending the boundaries for the tunability of the surface roughness stabilization level. The determined relation between surface roughness and the depth of a single crater is depicted in figure 4.7-C. The relationship between surface roughness and the depth of a single crater exhibits an approximately linear increase within the range 150 nm < H < 300 nm, with saturation of achievable S_a values observed beyond both limits. This validates the proposal that by reducing the crater's

depth, the PV value of the structure is reduced leading to the decrease of the final surface roughness. The minimum roughness ($S_a \sim 130$ nm) is reached when the depth of the crater matches ($H \sim 130$ nm), and any further reduction in the crater's depth no longer results in decreased roughness, setting the lower boundary for the attainable minimum roughness using the presented methods. We propose, that this limit is governed by the fact, that at such low S_a values, the roughness is no longer determined by induced structure and it's PV value, but by the laser-induced nanoripples. The generation of such self-organized nanostructure was observed during multilayer ablation, as shown in figure 4.8. Therefore, achieving a further reduction in surface roughness below $S_a < 130$ nm during deep engraving would require suppressing the formation of nanoripples. However, to the best of our knowledge, no practical methods have yet been demonstrated to achieve such conditions during femtosecond laser ablation. Thus, it remains a challenge for future research endeavors.

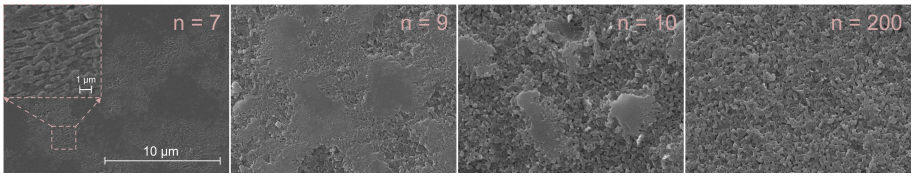


Fig. 4.8 SEM images of the ablated regions produced after different numbers of scans. Processing parameters: fluence $F = 2$ J/cm^2, overlap of the craters $\Omega = 20\%$, angle of rotation $\alpha = 73°$, wavelength $\lambda = 343$ nm. The uncertainty of layer positioning of a maximum magnitude $\Delta \geq dx$ was maintained.

4.4 Deep engraving with precise control of S_a

Finally, the developed surface roughness control methods were tested during deep engraving of fused silica. To evaluate repeatability, ten areas were processed using identical scanning parameters. Surface roughness control was demonstrated by applying the process in sequential steps, each using different scanning parameters on the previously processed surface. The results are given in figure 4.9. In part A, the roughness control via the change of overlap of the craters Ω is shown. Each parament set was scanned for 100 layers to ensure complete transition from one S_a level to another. An exception was made when Ω value of 70 % was used, due to high ablation rate and limited sample thickness, this parameter set was scanned for 30 layers only. The experiment

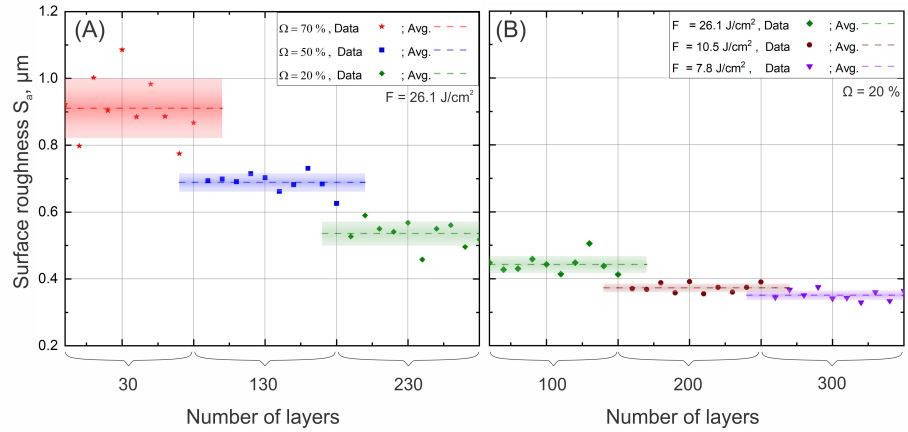


Fig. 4.9 Surface roughness dependence on the number of scans when different scanning algorithms are utilized. Graph (A) shows engraving with different overlaps of the craters, while graph (B) when different pulse energies are used. In both cases, additional scans with different scanning algorithms were scanned on the structures induced by the previous scanning algorithm (see text for clarification). Dots represent raw data, while dashed lines - average values. The extent of the colored area surrounding the average values stands for a range equivalent to one standard deviation. Other processing parameters: $\alpha = 73°$, $\lambda = 1030$ nm. The uncertainty of layer positioning of a maximum magnitude $\Delta \geq dx$ was maintained.

was conducted in such a way, that an initial scanning parameter set that produces the highest roughness was used first (in this case 30 layers of $\Omega = 70\%$). It was followed by additional 100 scans of new set of scanning parameters featuring $\Omega = 50\%$. The procedure was repeated for another 100 layers at $\Omega = 20\%$. The results disclose that by using different Ω values, the control of roughness stabilization level can be achieved. In part B of the figure, a similar experiment was conduced, only this time the variable parameter was fluence. As before, the initial parameter set was selected to yield the maximum surface roughness and the first 100 layers were ablated. Proceeding that, the pulse energy was reduced, and additional scans were conducted on the already processed surface. The engraving involved 3 steps in total, comprising different values of pulse energies and resulting in the stabilization of the roughness at different levels. In this case, we can see that the difference between the stabilization levels is significantly smaller. Showcasing that by varying the pulse energy the fine-tuning of the roughness stabilization level can be achieved, while changing the overlap of the craters results in a more coarse adjustment of the roughness stabilization value. These observations agree well with the previous discussion. The findings

suggest that by utilizing a combination of different scanning algorithms and varying laser parameters, namely inducing different surface structure via control of the overlap of the craters and tuning the PV value of induced structure via change in single crater depth, the fine (δS_a = 20 nm) control of the roughness stabilization level within a wide range of roughness values (300 ÷ 900 nm) is achievable.

To show that established methods are effective over extended range of engraved depths, the samples were engraved up to 750 μm in depth while maintaining the control over the surface roughness. The results are shown in figure 4.10. Each experiment was repeated 10 times to investigate its

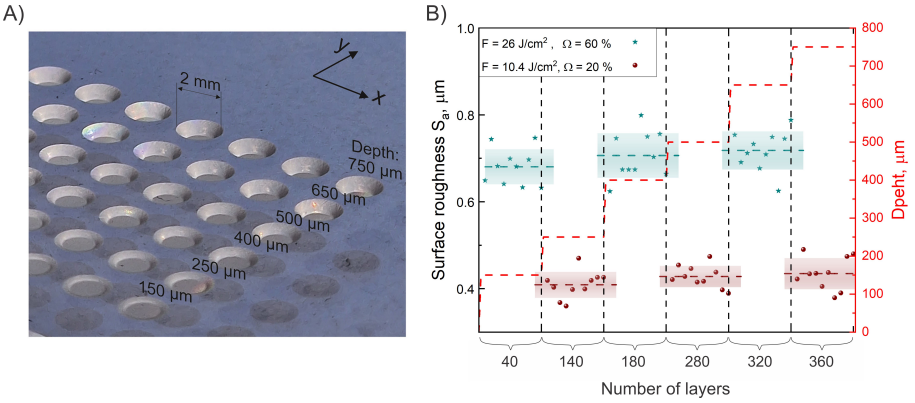


Fig. 4.10 (A) A photo of the sample after deep-engraving. In the y direction cavities of different depths can be seen, whereas in the x direction, cavities ablated using identical parameter sets are shown. In part (B) of the figure, surface roughness and depth of the cavity dependencies on the number of scans are presented. Dots represent raw data, while dashed lines - averaged values. The extent of the colored area surrounding the average values represents the range equal to one standard deviation. Other processing parameters: $\alpha = 73°$, $\lambda = 1030$ nm. The uncertainty of layer positioning of a maximum magnitude $\Delta \geq dx$ was maintained.

reproducibility. While engraving the material, the surface roughness was varied between two stable roughness levels of our choice. The combination of E_p = 181 μJ (F = 26 J/cm^2) and Ω = 60% resulted in the roughness stabilization at $S_a \sim 700$ nm, whereas the combination of E_p = 72.5 μJ (F = 10.4 J/cm^2) and Ω = 20% produced roughness of $S_a \sim 420$ nm. Each successive scanning step was performed on a surface formed by the previous scanning algorithm. An image of a deeply engraved sample is shown in figure 4.10-A, whereas part B shows how the surface roughness was varied during the engraving. It can be seen that throughout the engraving process, the roughness was changed 6

times. In addition, the roughness was not only reduced but also enlarged in a controlled manner via a change in the scanning algorithm. By the end of the deep-engraving experiment, the roughness of S_a = 420 nm at the depth of 750 μm was achieved. Demonstrated results show that full control (reduction as well as enlargement) of surface roughness while engraving can be achieved by applying the strategies presented in this chapter.

The presented methods are effective for controlling surface roughness of dielectric materials, particularly fused silica. While the application of the presented scanning protocols to other material systems is expected to yield similar trends in terms of surface roughness stabilization and control, the specific achievable roughness levels and optimal processing parameters are expected to vary. The developed scanning protocols rely on the optimal geometrical arrangement of single hemispheres, representing laser-induced craters. Their successful implementation therefore requires the formation of regular and reproducible laser-induced craters with high surface quality ($R_a \lesssim 10$ nm). This condition is typically satisfied during femtosecond-laser ablation of dielectric materials, including glasses and crystals, primarily due to the strong spatial confinement of energy deposition associated with nonlinear absorption (when considering standard IR laser sources). In contrast, during the femtosecond-laser ablation of metals, the combination of linear absorption and comparatively lower melting temperatures (e.g., $T_m \sim 1100$,°C for copper compared with $T_m \sim 2000$,°C for sapphire [197]) results in more pronounced melting. The instabilities in melt flow, spallation and rapid solidification rates of metals (reaching 10^{12} K/s [131]), may result in the formation of laser-induced craters of lower quality [198], making the application of presented protocols more challenging and less predictable. Besides that, in crystalline or polycrystalline materials, such as metals and alloys, the roughness of laser-induced modifications may depend on crystallographic orientation, as demonstrated for chromium [199], further reducing the predictability of the resulting surface morphology. Another significant difference between metals and glasses or crystals is that the latter generally exhibit brittle behavior and are more susceptible to cracking and fracture under laser-induced stresses. In contrast, many metals exhibit greater ductility, allowing stresses to be partially accommodated through plastic deformation. The optimal crater overlap determined in this thesis ($\Omega_{opt.} \sim 20\%$) is therefore primarily applicable to brittle materials, whereas the greater ability of metals to accommodate laser-induced stresses may shift the optimal processing

conditions toward higher overlap values. However, when processing metals at higher Ω values, increased heat accumulation may promote excessive melting, resulting in surface roughness degradation [200]. Hence, whether and to what extent the optimal processing conditions would change remains unknown. The applicability of the presented protocols to polymers is expected to be strongly material dependent. Polymers can exhibit amorphous or semicrystalline structures, while their response to ultrashort-pulse irradiation may involve not only melting but also photochemical bond breaking, thermal decomposition, carbonization, and gas formation [201]. Consequently, the resulting crater morphology and surface quality depend strongly on the polymer composition and irradiation conditions. Nevertheless, provided that regular and reproducible single-pulse craters with sufficiently low roughness can be generated, the geometrical principles underlying the developed scanning protocols should remain applicable, although material-specific optimization would be required. The discussion concludes, that the presented scanning protocols are expected to yield qualitatively similar results for material families with properties comparable to glasses and crystalline dielectrics, whereas their applicability to other material systems remains uncertain due to substantial differences in internal structure, optical response, and thermomechanical properties.

Lastly, most of the experiments provided in this chapter were carried out on optically flat fused silica samples, highlighting the effectiveness of the established methods only under such conditions. It is yet unknown, whether the methods presented in this chapter would be successful when performing laser processing on surfaces that are initially rough. Since only a minority of the materials in practice have very low initial surface roughness (as the samples used here), the ablation of rough surfaces and the control of surface roughness of such materials is of huge interest. To find this out, in the next Chapter the investigation and implementation of developed methods will be extended to the ablation of the surfaces that are initially rough.

4.5 Summary

In summary, methods for the control of the surface roughness while deep engraving were developed. It was demonstrated that the stabilization of the surface roughness can be achieved via implementation of combined scanning strategies. These include the rotation of every subsequent layer at an angle

α that is not a factor of 90° (e.g. $\alpha = 73\ °$), with the addition of intentional randomized layer displacement, where maximum displacement Δ is higher than pulse pitch dx. Under such conditions, the formation of periodic structures is prevented and the stabilization of the roughness is achieved within the first 30 layers (achieved here using $F = 20.8$ J/cm^2 and $\Omega = 20\%$). The level at which the roughness will stabilize is then determined by the initial overlap of the craters and their depths. The former can be scaled by tailoring pulse energy or adjusting the wavelength to smaller values, effectively reducing the light penetration depth. The developed methods enabled the control of surface roughness over a broad range of different roughness values ($\Delta S_a \sim 550$ nm) with a resolution of $\delta S_a = 20$ nm under deep-engraving conditions. The appearance of self-organized nanostructures after multipulse ablation remains the limiting factor for the minimum attainable roughness ($S_a = 130$ nm).

Chapter 5

Spectral analysis of surface roughness evolution

Results presented in this chapter were published in [A3] and presented at [D8] and [D9] conferences.

Continuing the series of investigations on surface roughness control via combination of different scanning algorithms and change of laser parameters, in this chapter we explore the ablation of initially rough surfaces. We aim here to examine the applicability of methods established in Chapter 4 on the surfaces that are initially rough. Furthermore, as the standard roughness parameters, such as S_a and R_a, carry only limited information about surface texture, in this chapter we extend the investigation of surface texture evolution by performing spectral analysis of the laser-processed surfaces. We examine how different spatial frequencies change over the coarse of laser processing. Such kind of analysis enables us to unveil the underlying causes behind the formation and alternation of surface roughness and texture.

5.1 Investigation framework

In this chapter, the first experimental setup configuration was used, featuring laser wavelength of $\lambda = 1030$ nm. The detailed description of the experimental setup used here is given in section 2.1. The laser processing experiments were carried out on 4 mm thick fused silica (FS) samples with varying initial surface roughness. Such samples were prepared by performing mechanical grinding on the surfaces that initially exhibited an optical-quality roughness level. By using

aluminum oxide grains of different sizes, different levels of surface roughness were generated. Following mechanical grinding, the surfaces were cleaned in an ultrasonic bath to ensure the removal of residual contaminants. The topographies of mechanically-created initial surfaces are shown in figure 5.1, with corresponding 3D roughness parameters in table 5.1 and spatial spectrum distributions in figure 5.2.

Table 5.1 Main 3D surface roughness parameters of initial surfaces (in accordance to the ISO 25178 [73]). The roughness parameters were calculated from 1600x1600 μm areas.

Nr	S_q [μm]	S_{sk}	S_{ku}	S_{sp} [μm]	S_v [μm]	S_z [μm]	S_a [μm]	S_{dq}	S_{dr} [%]
1	0.02	1.603	121.401	2.131	1.459	3.590	0.016	0.065	0.212
2	0.62	-0.440	4.390	7.574	8.528	16.102	0.496	1.418	62.337
3	1.64	0.108	10.946	27.038	19.550	46.587	1.317	2.245	102.603
4	3.53	-0.646	4.693	21.720	29.075	50.795	2.822	3.496	152.061
5	8.07	-0.492	3.411	33.855	46.873	80.728	6.422	4.864	199.692

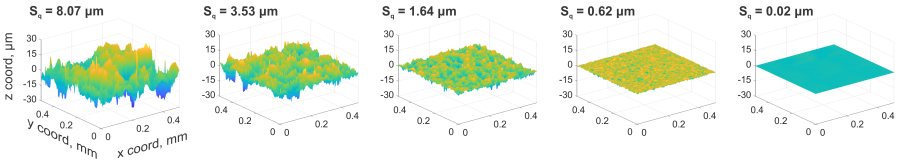


Fig. 5.1 Topographies of initial surfaces with varying surface roughness (see roughness values S_q at the top left corner above each topography). The surfaces were prepared using conventional mechanical grinding means.

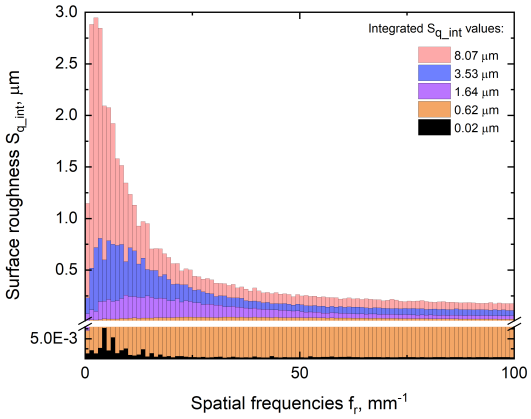


Fig. 5.2 Spatial spectra of initial surfaces with varying surface roughness levels.

The mechanically generated initial surfaces were then subjected to laser processing. The surfaces of the samples were scanned line by line in a raster

manner. Each experiment consisted of scanning a surface area of 3x3 mm in size. When performing laser processing, the scanning strategies established in the chapter 4, namely - rotation of the layers and the displacement of the layers, were applied. The α value of 73°and Δ value of $5 \times dx$ were used, to ensure the complete mitigation of periodic structure formation. See section 2.2 and chapter 4 for more details regarding these scanning algorithms and their corresponding variables α and Δ. The scanning path with all aforementioned scanning strategies and layer compositions was realized using a commercial laser processing software DMC PRO (Direct Machining Control, UAB). Following laser engraving, laser-processed surfaces were cleaned in an ultrasonic bath for 15 minutes and measured using a laser scanning microscope ("LEXT OLS5100", Olympus Corporation) equipped with a long working distance 50x objective with NA of 0.6 ("LMPlanFLN 50x", Olympus). When necessary, the topographies were additionally examined using a scanning electron microscope ("Prisma E", Thermo Fisher Scientific). When using a laser scanning microscope, each surface was measured over an area of 1600 x 1600 μm (corresponding to 5400x5400 data points). The acquired topographies were exported, and their further digital processing was performed in the MATLAB environment. First, the F operator (form removal procedure in accordance to ISO 25178 [79]) was applied. The surface was fitted with 2^{nd} order polynomial function, and the approximated reference surface was subtracted from the surface texture, as it does not contribute to the surface roughness. The S operator, which removes the measurement noise was not applied in this case, as it had a negligible effect on the dataset. Similarly, the L operator, used to separate the roughness and waviness components of the surface texture, was omitted as our aim was to analyze the evolution of the entire surface texture. More about filtration procedures read in section 1.1.3. Such digitally processed surfaces (S-F surface in ISO25178 terms) were then subjected to the evaluation of 3D roughness parameters and spectral analysis. In the scope of this chapter, in order to observe the general trend of the roughness evolution, only the S_q (RMS roughness) parameter of S-F surfaces was calculated. This parameter, which is equivalent to the standard deviation of surface heights, is widely used in the literature and therefore provides a simple and convenient measure for comparing surface roughness. The expression of S_q parameter is given in equation 1.6. For a more in-depth examination of texture evolution, spectral analysis of laser-processed surfaces was performed. Details on the methodology behind spectral analysis

are provided in section 2.3. It enables extraction of the surfaces' spatial spectra and evaluation of the S_q parameter from the spectral domain. This in turn allows for the evaluation of S_q parameters of separate surface texture parts. Such analysis permits to observe corresponding evolutions of waviness and roughness parts of surface texture separately, offering significant insights regarding overall texture evolution, that would not be observed otherwise.

5.2 Spectral analysis of S_q evolution from an initially smooth surface

Initially, an experiment was conducted in which the surface of an optical-grade fused silica sample (S_a < 10 nm) was scanned a single time, followed by a spectral analysis, in order to understand what individual peaks in the spatial spectrum correspond to. The spatial spectrum of a single-scanned surface is shown in figure 5.3 part B. As can be seen, the spectrum of a single-scanned

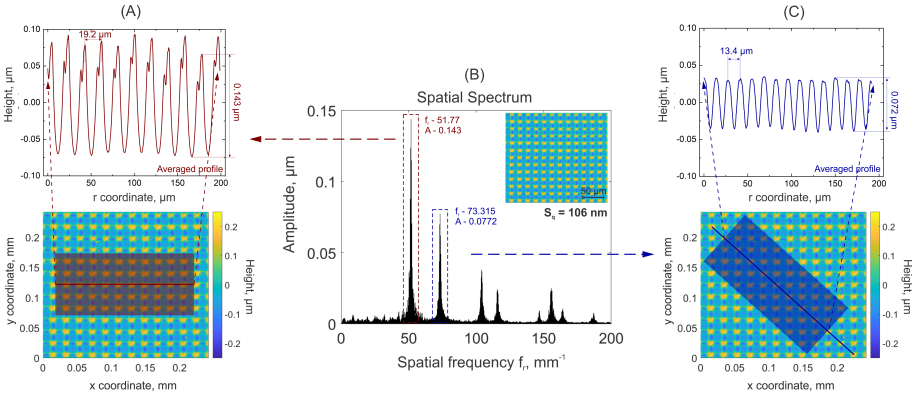


Fig. 5.3 A horizontal profile averaged over red-colored area (A). Spatial spectrum of a single-scanned surface (B). A diagonal profile averaged over blue-colored area (C). Laser processing parameters: fluence F = 8.23 J/cm^2, scanning speed v = 1937 mm/s, scanning pitch dx = 19.36 μm.

surface has several distinctive peaks. The two dominant ones correspond to radial spatial frequencies of f_{r1} = 51.77 mm^{-1} and f_{r2} = 73.31 mm^{-1}, which translates to spatial periods of T_{r1} = 19.3 μm and T_{r2} = 13.6 μm. Laser scanning microscopy revealed that the first peak T_{r1} = 19.3 μm corresponds to the scanning pitch in x and y directions, which was originally set to be dx = dy = 19.36 μm (see part A of figure 5.3). Whereas the second peak T_{r2} = 13.6 μm corresponds to the half of the diagonal scanning pitch $dx_{diag.}$ = 26.8 μm.

To better understand this relationship, it is important to note that the Fourier transform (FT) procedure analyzes entire surfaces rather than individual profiles. Therefore, if we take a diagonal profile and average it across multiple parallel profiles, the resulting averaged diagonal profile of a rectangular grid will exhibit a period equal to half the original diagonal pitch (see part C of figure 5.3). Other spectral peaks, that appear in the spectrum above $f_r > 100$ mm^{-1} are the higher harmonics of the two that were discussed. Moreover, from the figure, it is also evident that the amplitudes of the spectral peaks are in a good agreement with PV (peak-to valley) values of retrieved profiles. The results of figure 5.3 conclude, that the surface roughness after a single scan is purely determined by laser scanning parameters (scanning speed v, scanning pitch dy, and the scanning pattern) and the depth of a single crater, which sets the amplitudes for the spectral peaks.

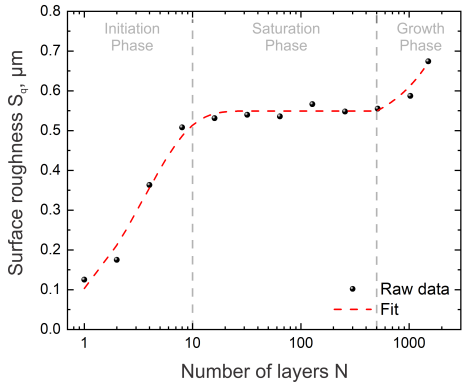


Fig. 5.4 Surface roughness parameter S_q dependence on the number of layers N. Processing was performed on a surface of an optical quality roughness level. Dots show data points, while the dashed line represents the fit. Laser processing parameters: fluence $F = 12.2$ J/cm^2, scanning speed $v = 2324.8$ mm/s, scanning pitch $dx = 23.24$ μm, overlap of the craters $\Omega_{x,y} = 20$ %. The ablation rate under such parameters was $R_t = 2.27$ mm^3/min (0.7 μm/layer). Spatial spectra of different data points are depicted in figure 5.5.

Next, we examine how surface roughness evolves when the surface undergoes multiple scans. The values for the number of layers N, representing how many times the surface was scanned, were chosen as powers of 2 (1, 2, 4, 8, 16...) with an additional final value of $N = 1500$. The ablation rate during the experiments was found to be approximately $R_t = 2.27$ mm^3/min (0.7 μm/layer), with minor variations depending on the specific parameter set employed. The evolution of surface roughness parameter S_q, when a multilayer laser processing is performed

on an optical quality FS glass, is shown in figure 5.4, while spatial spectra of various data points from the evolution are depicted in figure 5.5. As can be seen, the evolution of surface roughness can be divided into three distinct stages. In the initiation phase ($N < 10$), roughness increases rapidly. This is followed by a saturation regime ($10 < N < 500$), where the roughness stabilizes and remains nearly constant, forming a plateau. Finally, once the number of layers exceeds $N > 500$, the roughness resumes its growth, increasing linearly with N. To gain better insight into what is causing such behavior of S_q it is worth looking at the spatial spectra depicted in figure 5.5. As discussed

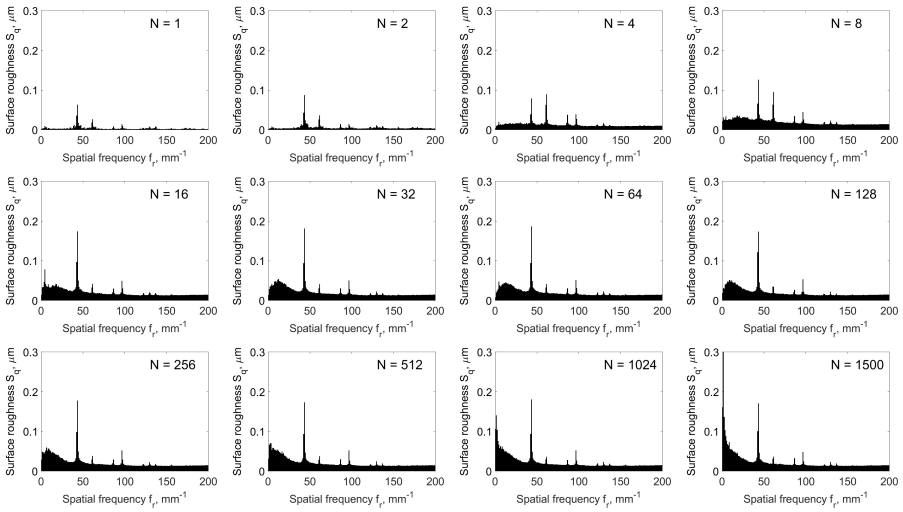


Fig. 5.5 Spatial spectra of processed surfaces after different numbers of scans (N). Processing was performed on a surface of an optical quality roughness level. Laser processing parameters: fluence $F = 12.2$ J/cm^2, scanning speed $v = 2324.8$ mm/s, scanning pitch $dx = 23.24$ μm, overlap of the craters $\Omega_{x,y} = 20$ %.

before, after a single scan ($N = 1$, $h \sim 0.7\,\mu$m), the spectra only show peaks whose positions and amplitudes are described by scanning parameters and the depth of a single craters. After several scans ($N \geq 4$, $h \gtrsim 3\,\mu$m), the spectrum develops a low-amplitude background spanning the entire frequency range, indicating the emergence of random height fluctuations across multiple length scales - a sign of stochastic surface modification. Such a type of modification mainly arises from the implemented scanning strategies (see section 5.1 for details), that intentionally introduce randomness in laser pulse positioning. The stochastic effects from these strategies predominantly contribute to the low- and mid-spatial-frequency background of the spectrum, while the high-

spatial-frequency background is primarily generated by the progressive surface coverage of nanoripples (as observed in figure 5.6). Such uneven nanoripple

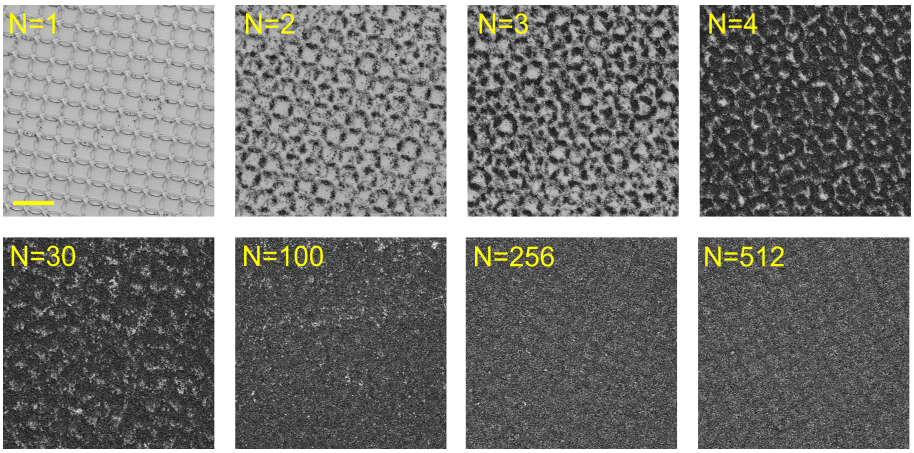


Fig. 5.6 Optical microscope images of laser-processed surfaces after different numbers of scans (N). Scale bar is 50 μm. Laser processing parameters: fluence F = 12.2 J/cm^2, scanning speed v = 2324.8 mm/s, scanning pitch dx = 23.24 μm, overlap of the craters $\Omega_{x,y}$ = 20 %.

coverage of the surface locally enhances ablation rates due to the multireflection phenomena [202]. Furthermore, the nanoripples themselves act as sources of high-spatial-frequency roughness. Within the first 10 layers, a statistically steady surface morphology is established; subsequent processing reproduces this morphology, stopping the rapid increase in S_q. This compliments the discussion presented in chapter 4. However, unlike in figure 4.4, the "transition" stage characterized by outliers is not observed here. This is because the area used for roughness evaluation here is significantly larger (1600 μm × 1600 μm) compared to that in figure 4.4 (256 μm × 256 μm). Further analysis of the spectra reveal that after more scans (N = 32, $h \sim 22.5\,\mu$m), the spectrum develops a new set of low spatial frequencies seen at $f_r < 40$ mm^{-1}. These low spatial frequencies also originate from the scanning algorithms - rotation of the layers and the displacement of the layers described earlier. Although the scanning strategies are designed to maximize randomness and prevent the formation of high-contrast periodic structures, they still lead to the emergence of certain types of patterns that represent the discussed spatial frequencies. However, since the new spectral features are generated in a limited spectral range and exhibit amplitude comparable to that of the background, their addition to the total PSD is minimal. Therefore, the S_q evolution in figure 5.4 shows

that the additional low spatial frequency features generated due to the scanning strategies have a negligible effect on the roughness of the overall surface texture. Finally, after further examination of the spectra, it can be observed that after multiple scans ($N > 500$, $h \gtrsim 350\,\mu$m), additional spectral components emerge at low spatial frequencies ($f_r \lesssim 3$ mm^{-1}) that are of high amplitude. These low-frequency, high-amplitude features are responsible for the increase of the S_q parameter at high N values seen in figure 5.4. It is evident that the newly generated low spatial frequencies arise from the multilayer ablation. It appears to be a cumulative effect, influenced by a modulation in ablation rate at specific surface sites predisposed to form long spatial wavelength patterns over multiple scans. The underlying physical mechanisms are complex. Therefore, a detailed analysis of the emergence of high-amplitude, low-spatial-frequency components at high N values will be presented in a separate chapter, given further in the thesis.

To gain a deeper understanding of the physical meaning behind the different spatial spectrum components and their quantitative contribution to the PSD, the corresponding surface texture features were examined, as shown in figure 5.7. The figure examines the texture of the surface after 32 laser scans. Based on the previous discussion, four main groups of spectral components can be identified. Group I (violet) represents the laser-induced waviness, group II (blue) corresponds to the low-spatial-frequency components introduced by the scanning strategy, group III (green) contains the spectral peaks associated with the scanning pitch, and group IV (pink) represents the spectral background. The different groups are represented by accordingly colored regions in figure 5.7. The surface topographies corresponding to the different spectral component groups were reconstructed by isolating the respective regions in the Fourier domain and applying the inverse Fourier transform. For each spectral component group, the corresponding S_q value and its percentage contribution $C = S^2_{q(i)}/S^2_{q(total)} * 100\%$ to the overall surface roughness were determined and are listed in the figure. As shown in this example, the largest fraction of the surface roughness ($C = 60$ %) is contained within the spectral background, which was previously attributed to the stochastic nature of the surface modification introduced by the applied scanning strategies. Since spectral component group II is also associated with this mechanism, the total roughness contribution arising from stochastic surface modification can be estimated as $C = C(\mathrm{II}) + C(\mathrm{IV}) \approx 78$ %. The remaining $C \sim 20\%$ of roughness is contained in the descrete spectral peaks

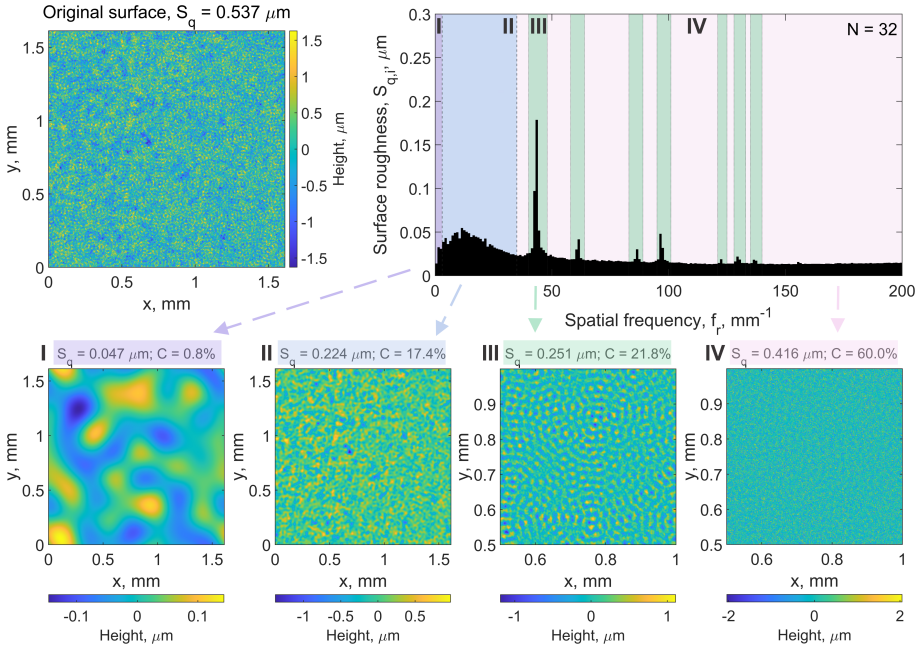


Fig. 5.7 Surface topography and its corresponding spatial spectrum after 32 laser scans applied on an initially smooth surface (top). Laser processing parameters were: fluence $F = 12.2$ J/cm^2, scanning speed $v = 2324.8$ mm/s, scanning pitch $dx = 23.24$ μm, and crater overlap $\Omega_{x,y} = 20$ %. The bottom part of the figure presents the surface topographies corresponding to different texture components identified in the spatial spectrum. Region I (violet) represents laser-induced waviness, region II (blue) corresponds to low-spatial-frequency components introduced by the scanning strategy, region III (green) contains the spectral peaks associated with the scanning pitch, and region IV (pink) represents the spectral background. The S_q value shown above each topography denotes the root-mean-square roughness of the corresponding texture component, while C indicates its percentage contribution to the overall surface roughness.

that belong to the spectral component group II. Although these observations indicate that stochastic surface modification is the primary contributor to surface roughness generation, the applied scanning strategies are essential in enabling the control of surface roughness level. It should be noted that the discussed S_q fractional distribution is specific to this surface and should not be considered universal. Examination of surface texture after 1500 scans revealed a significant redistribution of roughness among different spectral component groups: C(I) increased from 0.8 % to 30 %, while C(IV) decreased from 60 % to 39 %. Thus, demonstrating the progressively increasing contribution of laser-induced waviness to the overall surface roughness as the laser processing progresses.

5.3 Spectral analysis of S_q evolution from an initially rough surface

Next, the laser processing experiments were carried out on surfaces that were initially rough. The initial roughness values of different surfaces are detailed in table 5.1. The S_q evolutions of surfaces with varying initial roughness are shown in figure 5.8. As can be seen, the evolution of the surface roughness S_q

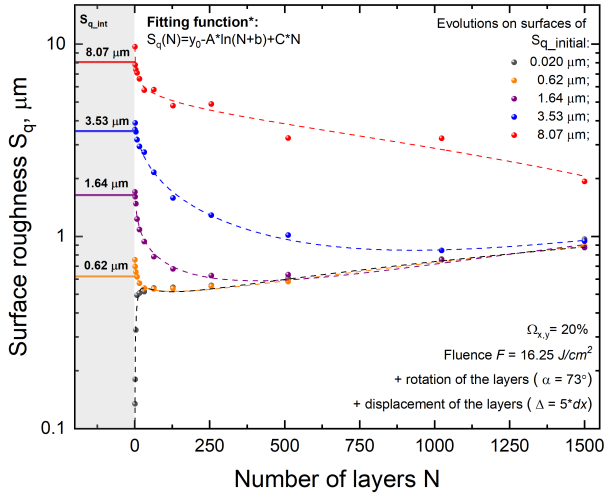


Fig. 5.8 Surface roughness S_q dependence on the number of scans N, when laser processing is performed on surfaces with varying initial roughness (S_{q_int} values given in the legend). Dots represent raw data, while the dashed lines represent the fit. The fitting function is outlined in the upper-left corner of the figure (except for the case S_{q_int} = 0.02 μm; see the text for details). Laser processing parameters: fluence F = 16.25 J/cm^2, scanning speed v = 2324.8 mm/s, scanning pitch dx = 23.24 μm, overlap of the craters $\Omega_{x,y}$ = 20 %.

varies depending on the initial roughness of the surface S_{q_int}. The general trend shows that the S_q parameter of surfaces with initial roughness of S_{q_int} of 0.62, 1.64, and 3.53 μm is reduced with each additional scan, until it converges to the evolution of the surface with initial roughness of S_{q_int} = 0.02 μm. Moreover, it is seen that after the evolutions converge, they then follow the same path of linear growth due to laser-processing-generated low spatial frequencies. It is further observed that the parameter S_q decrease rate depends on the initial surface roughness. The evolution of S_{q_int} = 8.07 μm stands out as it does not converge as all other evolutions within the observed window of N $\leq$ 1500. While a gradual decrease in S_q is observed, the rate of change remains very

slow. This indicates that convergence with the other evolutions would likely occur at higher N values. Moreover, it was observed that the data describing the evolutions of laser processing conducted on initially rough surfaces can be accurately approximated using the following equation:

$$S_q(N) = y_0 - A \times ln(N + b) + C \times N, \tag{5.1}$$

here N is the number of layers, S_q - surface roughness, and y_0, A, b, C are the fitting parameters. The corresponding fits are displayed in figure 5.8, seen as dashed lines. The average coefficient of determination R^2, indicating the goodness of fit of the model [203], exceeded 0.97 for all datasets. The fitting function consists of two main components: a decay that follows the logarithmic saturation and the linear growth. The logarithmic decay describes the attenuation of various spectral components during laser processing, whereas the linear growth represents the generation of new low spatial frequencies that begin in the latter stages of the evolution, as discussed before. However, the evolution of laser processing on an optically flat surface (denoted in black color) does not follow these physical mechanisms; therefore, that dataset was fitted using a different, more complex function, which features a variable exponential growth with a saturation factor, followed by linear growth.

To gain further insight into the distinctive behaviors of these evolutions, we next examine the evolution S_{q_int} = 1.64 μm in more detail by considering its spectral development during laser processing, shown in figure 5.9. The figure depicts how the spectrum evolves (shown in black) with respect to the spectrum of the unprocessed surface (shown in gray). Furthermore, the right y-axis shows the difference in S_q across spatial frequencies, obtained by comparing the surface after N layers with the spectrum of the unprocessed surface. The results reveal that laser processing affects all spatial frequencies. However, it is evident that the rates of attenuation or amplification of different spatial frequencies vary across the spectrum. The data show that high spatial frequencies ($f_r > 100\,\mathrm{mm}^{-1}$) are affected first, within the initial layers. Subsequently, the mid-spatial frequencies ($100\,\mathrm{mm}^{-1} > f_r > 10\,\mathrm{mm}^{-1}$) undergo attenuation within the first 100 layers. Finally, low spatial frequencies ($f_r < 10\,\mathrm{mm}^{-1}$) exhibit noticeable changes only after several hundred scans. Moreover, it is observed that the final shape of the spectrum (when $N > 1000$) converges to the same shape as in the case discussed above, when the processing was performed on a surface of an optical

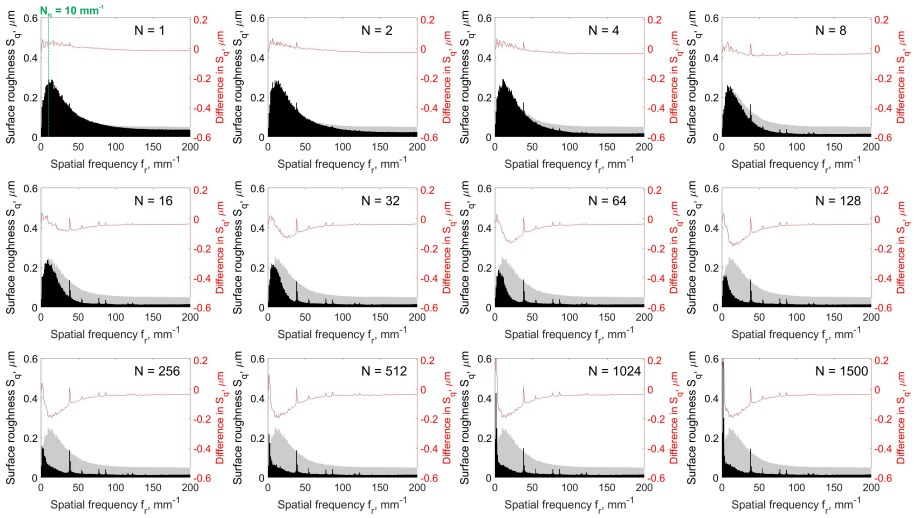


Fig. 5.9 Spatial spectra of surfaces after varying numbers of scans (N) are shown in black, while the grey background represents the spectra prior to laser processing. The left y axis indicates the roughness level S_q as a function of spatial frequency. The right y axis displays the change in roughness across spatial frequencies, obtained by comparing the spectra after N scans with that of the unprocessed surface. Processing was performed on a surface with initial roughness of S_{q_int} = 1.64 μm. Laser processing parameters: fluence F = 16.25 J/cm^2, scanning speed v = 2595.2 mm/s, scanning pitch dx = 25.95 μm, overlap of the craters $\Omega_{x,y}$ = 20 %. The ablation rate under such parameters was R_t = 0.68 μm/layer. The green line indicates the nesting index position that divides the spectra into waviness and roughness parts.

quality. This observation is consistent with the results shown in figure 5.8, which demonstrate that the evolutions of the roughness parameter S_q converge at high values of scan numbers ($N > 1000$). It suggests that laser processing alters the surface morphology in different ways depending on the initial surface texture, but after prolonged engraving, all the surface textures converge to the same state governed by the laser processing conditions.

To further investigate the evolution of surface texture when laser processing is applied on the surface of initial roughness S_{q_int} = 1.64 μm, a fractal analysis of the laser-processed surfaces was performed. A comprehensive description of the principles and implementation of the fractal analysis can be found in section 2.4. The fitted $PSD(f_r)$ plots with corresponding estimated fractal dimension (D) parameters are given in the figure 5.10. First, we observe that the fractal dimension of the mechanically pre-roughened surface measures D = 2.656, suggesting that the surface exhibits a moderate level of self-affinity and irregularity. After prolonged engraving (N = 1500), the D value is increased to

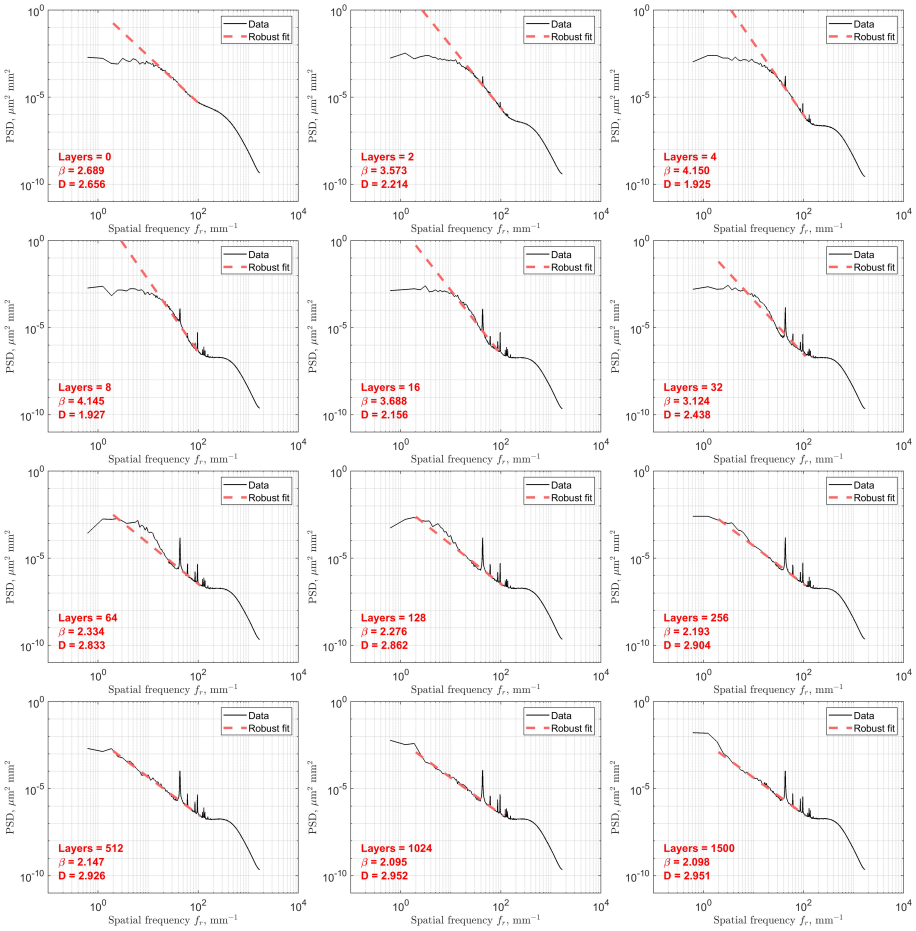


Fig. 5.10 Averaged PSD dependencies on radial spatial frequency f_r in a log-log representation of laser-processed surfaces after different numbers of scans. The initial surface roughness of the surface S_{q_int} = 1.64 μm. The black curve represents raw data, while the red dashed line is a fit over a selected region of frequencies (for more detail see section 2.4). β here is a scaling exponent, and D is the fractal dimension.

2.951. It indicates that laser processing using the presented methods increases the surface complexity significantly. This is expected, as the randomization of pulse positioning introduced by the applied scanning strategies promotes stochastic surface modification. On top of that, it can be assumed that prolonged laser engraving promotes the accumulation of debris and defects, which may further contribute to the increase in the fractal dimension D. The figure also indicates that, in some cases (when $N = 4-8$), the estimated fractal dimension D falls below 2. However, this does not represent the actual fractal characteristics of the surface. Instead, it is an artifact arising from inaccurate fitting of the

$PSD(f_r)$ spectrum during its transition from the initial to the laser-modified state. During this transition, the initially single linear region of the spectrum splits into two distinct regions: the low-spatial-frequency region retains the characteristics of the initial surface, whereas the high-spatial-frequency region already reflects the laser-induced modifications. The fractal analysis revealed that despite the fact that the application of laser processing resulted in the final S_q value reduction, the complexity of the surface was significantly increased.

5.4 Spectral evolution of different texture components

In the following, we investigate how the roughness and waviness parts of surface texture change by considering their respective S_q parameter evolutions. To acquire that, the spectrum seen in figure 5.9 was separated by a hard-cut filter into two parts, corresponding to waviness (low f_r part) and roughness (high f_r part). The separation nesting index N_{ic}, which determines the cut-off frequency, was selected according to ISO 25178-3 [79] guidelines and was set to $N_{ic} = 10\ \mathrm{mm}^{-1}$ (depicted in figure 5.9 as green, dashed line). From the spectral data of the separated parts, S_q parameters for waviness S_{q_W}, roughness S_{q_R}, and entire surface texture S_{q_P} were calculated. The corresponding evolutions are plotted in figure 5.11, part A. The results reveal that the roughness part ($f_r > 10\ \mathrm{mm}^{-1}$) of the surface texture experience a rapid decrease within the first 100 layers ($h \sim 70\,\mu\mathrm{m}$), after which it stabilizes and remains at a constant level. In contrast, the waviness part ($f_r \leq 10\ \mathrm{mm}^{-1}$) of the surface texture continues to evolve throughout the entire laser processing period. In the initial stage of processing ($N < 500$, $h \lesssim 350\,\mu\mathrm{m}$), the waviness decreases, as the initial low spatial frequencies are being reduced due to laser processing. In the subsequent stage ($N > 500$, $h \gtrsim 350\,\mu\mathrm{m}$), the waviness begins to increase due to the generation of new laser-processing-induced low spatial frequencies. As it appears, the waviness evolution is driven by two competing mechanisms: (1) the attenuation of the initial waviness components and (2) the generation of new, laser-processing-generated waviness components. The first mechanism predominates during the early stages of laser processing, whereas the second becomes dominant in the later stages. To sum up, since the roughness part of the surface texture stabilizes relatively quickly, the evolution of the waviness components is the primary factor governing the overall development of the surface texture. Part B of the figure 5.11 shows the local derivatives of the

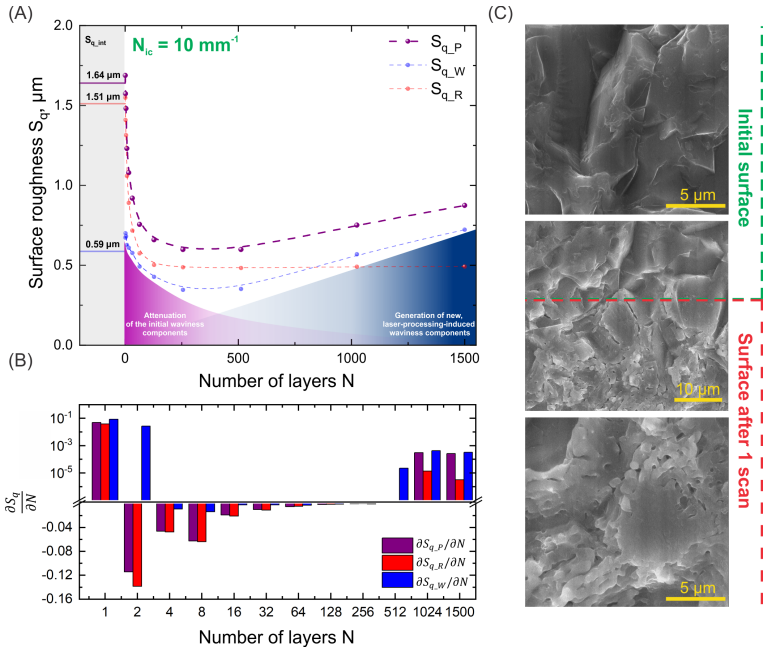


Fig. 5.11 Surface roughness S_q dependance on the number of layers scanned N (A). The S_q values associated with the waviness and roughness parts of the surface texture are denoted as S_{q_W}, S_{q_R} respectively, while the S_q value of the entire surface texture is indicated as S_{q_P}. Variation of the local derivatives $\partial S_{p,r,w}/\partial N$ as a function of the number of layers N (B). SEM images of initial surface texture (initial roughness of S_{q_int} = 1.64 μm) and surface texture after a single scan (C). Laser processing parameters: fluence F = 16.25 J/cm^2, scanning speed v = 2595.2 mm/s, scanning pitch dx = 25.95 μm, overlap of the craters $\Omega_{x,y}$ = 20 %. The nesting index used to separate waviness and roughness components was set to N_{ic} = 10 mm^{-1}.

discussed evolutions, expressed as:

$$\frac{\delta S_q}{\delta N} = \frac{S_q(N_i) - S_q(N_{i-1})}{N_i - N_{i-1}}. \tag{5.2}$$

As can be seen, at the very beginning (first layers) of each evolution, we observe a slight increase in the corresponding S_q parameters - depicted as positive derivatives. This phenomenon can be seen in other examples as well, such as the evolutions displayed in figure 5.8. It appears that this slight increase in roughness is a result of the initial interaction between laser radiation and the rough surface. We assume that it is governed by a local field enhancement at sharp edges and surface irregularities [204, 205], which promotes the formation of nanoripples and enhanced localized ablation (as seen in part C of figure 5.11).

The spatial modulation of the ablation rate leads to a further increase in the surface roughness S_q relative to its initial value. However, since the fluence values used in the study were well above the ablation threshold, during the first several scans all sharp edges and other surface features are expected to be reduced by ablation and melting processes. Therefore, field enhancement can occur only during the initial scans. This explains why an increase in the S_q parameter was registered only during the initial interactions between the laser radiation and the rough surface. Following that, we observe that the amplitudes of the S_q parameters decrease at rates that progressively slow with extended laser processing. Finally, after multiple layers ($N > 500$, $h \gtrsim 350\,\mu$m), the derivatives turn positive again, indicating a resumption of amplitude growth. However, this time, the growth rates of the S_{q_P} and S_{q_W} amplitudes are two orders of magnitude lower than those observed at the onset of the evolution, yet remain constant until the end of the process. Hence, as the growth rate of the induced waviness is extremely low, it can only be observed after prolonged ablation ($N > 500$, $h \gtrsim 350\,\mu$m).

Finally, we sought to understand why the evolutions shown in figure 5.8 unfold at varying rates. To address this, we calculated the attenuation rates of different spatial frequencies. This was accomplished by fitting the temporal evolutions of different spatial frequencies with an exponential decay function and extracting their corresponding decay rates. The decaying exponential function is expressed as:

$$S_q(f_r, N) = y_0(f_r) + A(f_r) \times e^{-k(f_r)N}, \tag{5.3}$$

here $y(N)$ is the fitting function, N is the number of layers, y_0 and A are the fitting parameters, and k is the decay coefficient. The average coefficient of determination R^2 exceeded 0.95 for all datasets. The decay coefficients were extracted for all spatial frequencies that are $f_r > 4$ mm^{-1}. The very low spatial frequencies were excluded, as they exhibit both decay and growth behaviors, for which a simple exponential decay model is insufficient to achieve an accurate fit. Nevertheless, the explored frequency range was more than adequate to support the validity of the findings. The extracted decay coefficients $k(f_r)$ are displayed in figure 5.12, part A. The results exhibit a clear trend, showing that the decay rate increases with increasing spatial frequency value. It suggests that surfaces containing multiple low spatial frequencies of high amplitude need substantially

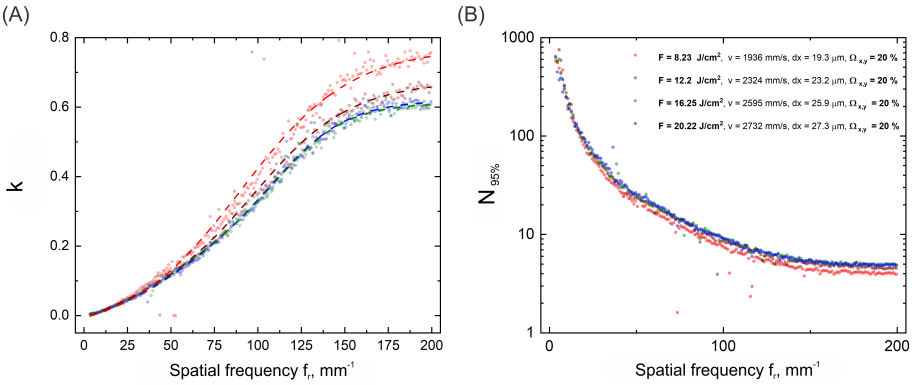


Fig. 5.12 Decay coefficient k dependence on the spatial frequency (A). The number of layers $N_{95\%}$ necessary to reach 95% reduction of the corresponding spatial frequency amplitude (B). Dots represent raw data, while the dashed lines - a visual guide of a trend for the reader. Different colors correspond to different processing parameters. The legend is shared between both figures. The processing was performed on a surface of initial roughness S_{q_int} = 1.64 μm.

more scans to achieve comparable roughness reduction than those composed mainly of high spatial frequencies. This provides a clear explanation for the varying evolution rates observed in figure 5.8, as the initial surfaces of these evolutions exhibit different compositions of low and high spatial frequencies (see figure 5.2). When the PSD is predominantly concentrated in low spatial frequencies, the evolution unravels slowly; in contrast, a dominance of high spatial frequencies corresponds to a faster evolution rate. What's more, we calculated how many scans were necessary to reach 95% reduction of the amplitude of each spatial frequency. This was calculated using the following expression:

$$N_{95\%}(f_r) = -\frac{ln(0.05)}{k(f_r)}, \tag{5.4}$$

here, $N_0(f_r)$ is the number of scans necessary to achieve 95% reduction of the corresponding spatial frequency amplitude, and $k(f_r)$ is the decay coefficient. The results are shown in figure 5.12, part B. As can be seen, the high spatial frequencies are reduced within the first 5 scans (resultant depth $h \sim 3.5\,\mu$m), while the full reduction of low spatial frequencies can take thousands of scans (resultant depth $h \gtrsim 700\,\mu$m). It explains well why the attenuation segments of S_q evolutions in the figure 5.8 follow a logarithmic decay behavior. We can see that in the beginning of the evolution, multiple spatial frequencies are being attenuated at once, therefore we have a fast decay of the S_q parameter.

However, as the evolution advances, progressively fewer spatial frequencies remain reducible, and their corresponding reduction rates also decrease. This results in slower decay of the S_q parameter, until the decay stops entirely. It is further observed that the value of the decay rate k reaches saturation at high spatial frequency values. This is related with the fact that features of such scale typically have low amplitude and are strongly affected by laser radiation. Therefore, these features are fully suppressed within the initial scans, corresponding to the highest reduction rate measurable under the circumstances used here. Lastly, an investigation was carried out to determine how diverse laser processing parameters affect the decay rates of different spatial frequencies (see table 5.2). During the experiment, the fluence values F were varied while maintaining the overlap of the craters to be $\Omega = 20\%$. The results show that the differences are most pronounced at higher spatial frequency values, when $f_r > 100\ \mathrm{mm}^{-1}$ (see figure 5.12). It can be seen that the decay rate increases as the fluence value decreases, which is a somewhat counterintuitive observation. It must be noted that to maintain a constant overlap of the modifications, both the scanning speed and the scanning pitch were adjusted, thereby altering the density of shots per layer, expressed as $N_L = \left\lfloor \frac{L^2}{dx \times dy} \right\rceil$. Here L stands for the side length of the cavity (3 mm in our case), and $dx = dy$ represent scanning pitches in x and y directions accordingly. Considering that, the total fluence incident on the surface per one scan can be estimated as $F_L = N_L \times F_0$, where F_0 is the fluence of a single pulse. However, even the calculated total fluence values per layer (see table 5.2) yield the same outcome - the decay coefficient increases as the fluence decreases. It appears that fluence may not be the critical processing parameter governing the decay rate. Instead, the determining factor is likely the shot density - that is, the effective coverage of the surface by the laser radiation.

Table 5.2 Laser processing parameters and resulting decay coefficient values k.

Scanning speed v (mm/s)	Scanning pitch $dx = dy$ (μm)	Overlap Ω (%)	Shots per layer N_L	Fluence F_0 (J/cm^2)	Total fluence F_L ($\times 10^3$ J/cm^2)	Decay coefficient k ($f_r = 200\ \mathrm{mm}^{-1}$)
1936	19.3	20	24025	8.23	197.7	0.74
2324	23.2	20	16641	12.2	203.0	0.65
2595	25.9	20	13456	16.25	218.6	0.61
2732	27.3	20	12100	20.22	244.6	0.61

The discussion concludes that femtosecond laser engraving can be effectively used to reduce the initial surface roughness. Furthermore, it shows that any reduction in S_q using this approach is inherently coupled to the removal of a

certain amount of material (with precise amount depending on laser parameters used), which imposes a fundamental limitation on the method. If the allowable engraving depth is restricted, only partial attenuation of the spatial spectrum may be achieved (depending on the composition of the spectrum), since different spatial frequencies require different numbers of scans to fully suppress their corresponding amplitude components (as given in figure 5.12). Nevertheless, the presented femtosecond laser engraving influence on the initial surface texture provides valuable insight into surface texture evolution and opens new directions for further research.

5.5 Summary

In this chapter, a thorough investigation of surface roughness evolution was conducted from both spatial and spectral perspectives, providing new insights into the mechanisms governing surface roughness formation. The spectral analysis indicated that the early stages ($N < 10$, $h \lesssim 7$ μm) of roughness evolution are primarily determined by the scanning parameters and strategy. Additionally, a pronounced increase in roughness during these initial stages was shown to be attributed to the stochastic surface modification and the uneven surface coverage by laser-induced nanoripples. We observed that approximately 10 scans are required for the surface to reach a statistically steady state, indicating the saturation of surface roughness. The further increase in roughness observed at the latter stages of the evolution ($N > 500$, $h \gtrsim 350$ μm) was attributed to the newly generated high amplitude, low-spatial-frequency features induced by the laser processing. When investigating the effect of laser processing on the surfaces that had different initial roughness, we found that in all cases the surface texture evolves towards the same fundamental state that would be reached if the processing was applied on an initially smooth surface. The engraving duration (number of scans) required to reach the fundamental state depends on the initial spatial spectrum and laser processing parameters. The shape of the overall surface texture evolution (S_{q_P}) follows the evolution of the waviness part of the surface texture (S_{q_W}), that is governed by two competing mechanisms - the reduction of the initial low-spatial frequencies and the generation of new, laser-processing-induced features. Furthermore, we observed that the decay of amplitudes of different spatial frequencies ($k(f_r)$) varies across the spatial spectrum, having a decreasing trend towards the lower part of the spatial

spectrum. Moreover, we demonstrate that the decay coefficient $k(f_r)$ values at high spatial frequencies ($f_r > 100$ mm^{-1}) are sensitive to laser processing parameters, especially the shot density per layer, that affect the effective surface coverage by laser radiation.

Chapter 6

Waviness formation during deep engraving: Origins and Mechanisms

Results presented in this chapter were published in [A4].

In the last chapter, it was demonstrated that during laser deep engraving (depth > 500 μm), the unforeseen growth in surface roughness is observed that cannot be attributed to algorithm-related effects. It was revealed that the observed roughness increase is associated with the formation of high-amplitude, low-spatial-frequency features (HALSFF), corresponding to the generation of new waviness components within the surface texture. The generated low-frequency ($f_r \lesssim 3$ mm^{-1}) components exhibited a high amplitude of PV (peak-to-valley) > 3 μm, significantly increasing overall surface roughness. The formation of such features disrupts the stabilization of the surface roughness level (established in section 4.2) under prolonged engraving conditions. This in turn limits precise control over surface texture, making the resulting surfaces unsuitable for certain applications, such as free-form mold manufacturing. To address that, in this chapter we conduct an in-depth investigation that considers the formation of new high-amplitude, low-spatial-frequency features during laser deep engraving, with the aim of understanding their origins and identifying strategies to eliminate them. We first determine the conditions, under which these features are formed. Following that, based on numerical and experimental results, we establish strategies that mitigate the formation of HALSFF.

6.1 Investigation framework

To identify the conditions that result in the formation of HALSFF, the first experimental setup configuration was used, featuring laser wavelength of λ = 1030 nm. The detailed description of the experimental setup used here is given in section 2.1. The experiments performed on optical quality fused silica samples consisted of scanning the surface area of 4x4 mm (or similar) in size multiple times, until the desire depth was reached. During laser processing, the focal plane was maintained at the sample surface. The Rayleigh length, calculated as z_r = 1.35 mm, was sufficiently long to sustain efficient ablation across the entire deep engraving procedure, eliminating the need to adjust the focus between the scans. The scanning was performed in a raster manner, line by line, with a line pitch of dy. To maintain even ablation, the overlap of the craters Ω in x and y directions was kept equal, with expression of given in equation 1.29. The overlap in the x direction was varied by changing the scanning speed (v), while the overlap in the y direction was varied by selecting different line pitch values (dy). Furthermore, when scanning multiple times, to avoid the formation of the periodic structures that arise from the raster scanning, additional scanning strategies - rotation of the layers and the displacement of the layers were implemented. The visual representation of laser engraving employing the aforementioned scanning strategies is shown in figure 6.1. When

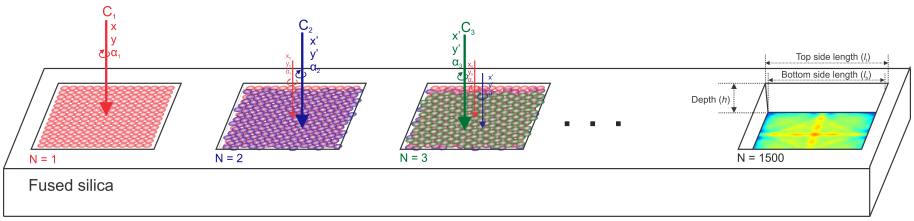


Fig. 6.1 Schematic of the laser engraving process and scanning strategies. Arrows, denoted as c_1, c_2 and c_3 display the central axis of each layer with corresponding spatial coordinates x, y and angle of rotation α_n. Different colors stand for different layers. N stands for number of scans performed on the surface.

layer rotation is applied, each successive layer is rotated about its central axis by a fixed incremental angle α. In addition, layer displacement involves shifting the central rotation axis of the current layer by a randomly generated offset in the x and y directions, thereby further reducing the likelihood of laser irradiation at the same locations. The detailed description of scanning strategies in use

is given in section 2.2. The figure 6.1 additionally displays, that the laser processing this time was strictly confined within a rectangle, resulting in a rectangular shaped cavities (with top side length of l_t and bottom side length of l_b), as opposed to previous experiments, where the resultant structures were of circular shape (see figure 4.10, part A).

After laser processing, the engraved structures were subjected to the cleaning procedure which included cleaning the samples in an ultrasonic bath filled with distilled water for the duration of > 15 min and subsequently drying them using high-pressure air. Next, the engraved surfaces (with areas ranging from 3x3 mm^2 to 7x7 mm^2) were measured using the LEXT OLS5100 laser scanning microscope (Olympus Corporation) equipped with a long working distance 50x objective with NA of 0.6 ("LMPlanFLN 50x", Olympus). Due to the limited single field of view (256 × 256 μm^2), multiple adjacent measurements were stitched together to obtain a complete image of the engraved surfaces. The acquired surface topographies were digitally processed to remove measurement noise and the form of the surface, which does not contribute to the surface roughness. Following digital processing, 3D surface roughness parameter S_q was calculated. It represents the root mean square value of ordinate values within the definition area with its expression given in equation 1.6. This parameter was chosen for the evaluation of the surface roughness as it gives a good approximation of general roughness value and is widely used within the literature. Note that S_q values here were calculated for S-F surfaces, which include both roughness and waviness parts of the surface texture. The decision to compute S_q for S-F surface, rather than the S-L surface, is motivated by the importance of evaluating the influence of induced high-amplitude low-spatial-frequency features on the overall surface unevenness.

6.2 Conditions for HALSFF formation

To establish the conditions under which HASLFF are formed, a systematic investigation of their geometric constrains dependence on various processing parameters was conducted. We first examined how the structural characteristics of the formed HALSFF depend on the laser fluence values used during the processing. The fluence was varied by changing the pulse energy (E_p) and is expressed as: $F = 2E_p/(\pi\omega_0^2)$. To ensure the same depth was reached while using different F values, the number of scans N was varied according to the

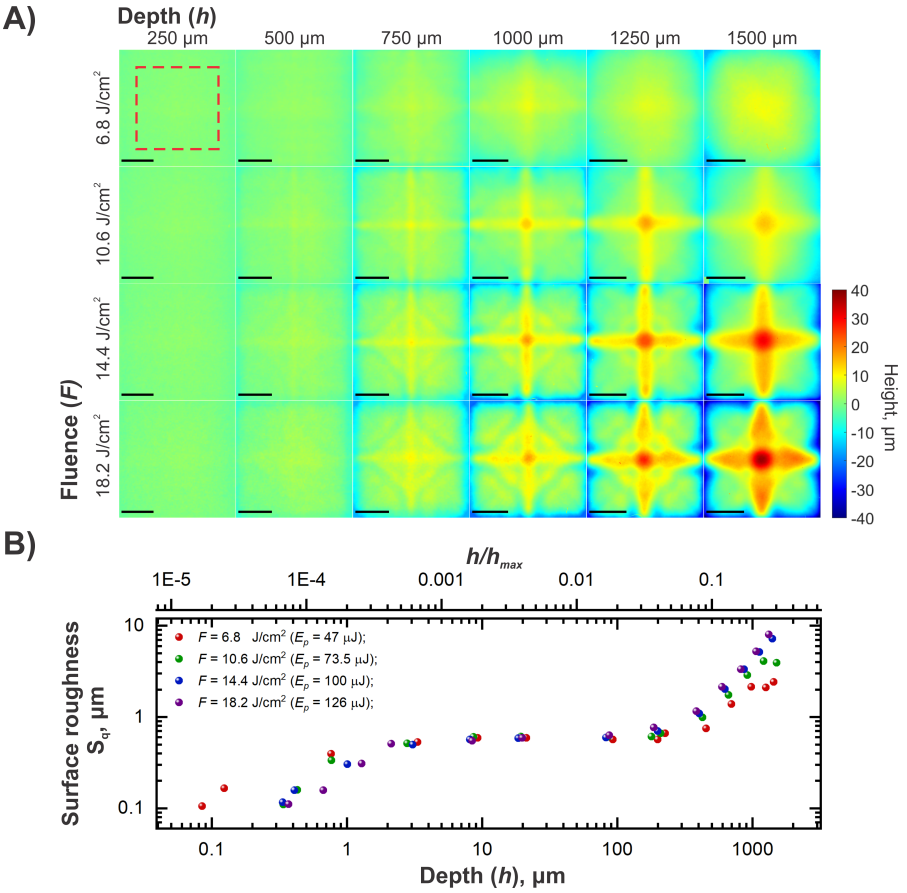


Fig. 6.2 Height maps of the bottom surfaces of deep ablated rectangular cavities of varying depths produced using different fluences F (A). Surface roughness parameter S_q dependence on the engraved depth, when different F values are used (B). The top x axis shows engraved depth normalized to the sample thickness h_{max} (5 mm). Other laser parameters were fixed: scanning speed v = 2325 mm/s, scanning pitch $dy = dx$ = 23.3 μm. The black bar indicates a length of 1 mm, the red dashed rectangle shows the area from which the roughness was calculated (representing 2.1 mm x 2.1 mm in size).

change in ablation rate. The resulting bottom surfaces of the ablated cavities are presented in figure 6.2, part A. As can be seen, when deep ablating 4x4 mm size cavities, HALSFF exhibiting cross-like shapes are formed. The patterns begin to surface when the engraved depth of $h \geq 500$ μm is reached. The measured surface roughness S_q values, given in part B of figure 6.2, confirm that the formation of HALSFF is responsible for the increase in surface roughness observed after prolonged engraving, as was suggested in the previous chapter. It is observed that the formed surface features are ablation depth h and fluence

F dependent. Once surfaced, their peak-to-valley (PV) values increase with engraved depth h, leading to a corresponding rise in surface roughness. The rate of increase in S_q is governed by the fluence, with higher F values producing a more rapid growth of surface roughness. At a Fluence value of 18.2 J/cm^2, the surface roughness S_q reaches 8 μm at an engraved depth of approximately 1500 μm, whereas at 6.8 J/cm^2 the roughness is only 2.4 μm. Accordingly, at F = 18.2 J/cm^2 the height maps reveal pronounced HALSFF with well-defined shapes of high PV values, whereas at F = 6.8 J/cm^2 these features are barely discernible. It is plausible that at even lower fluence values ($F \leq$ 6.8 J/cm^2), HALSFF formation could become negligible, indicating that fluence is one of the critical factors in the formation of these surface features. It is further observed that in addition to the increase of PV and S_q values, the features shape gradually changes and broadens as engraving progresses. It suggests that this phenomenon may be cavity size dependent, as with increasing depth of the cavity, the bottom surface area narrows due to the sidewalls being non-perpendicular. Therefore, the subsequent analysis focuses on investigating the dependence of HALSFF formation on the ablated cavity size. The top side length of the ablated rectangular cavities was varied from 3.2 mm to 5 mm, while keeping the laser processing parameters constant. The resultant morphologies of the bottom surfaces of deep ablated cavities are shown in figure 6.3. As can be observed in

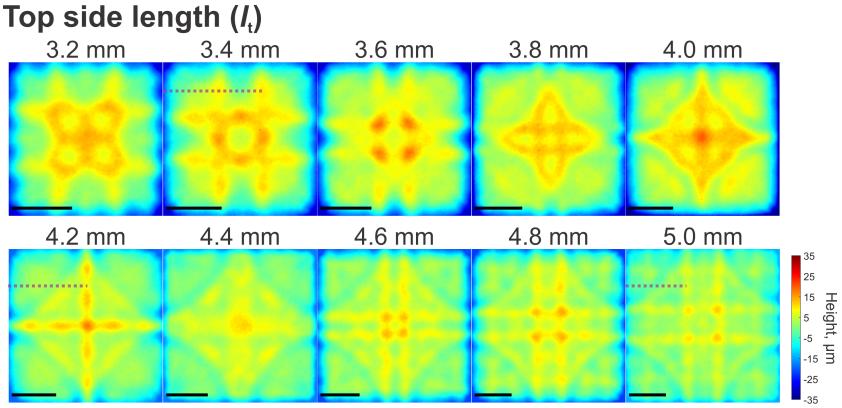


Fig. 6.3 Height maps of the bottom surfaces of deep ablated rectangular cavities with top side lengths of l_t. Laser processing parameters used: fluence F = 18.2 J/cm^2, scanning speed v = 2325 mm/s, scanning pitch $dy = dx$ = 23.3 μm, number of scans N = 775, engraved depth h = 820 μm. The black bar indicates a length of 1 mm. The dashed purple line indicates the length of 1.78 mm.

the figure, HALSFF were formed in all cases; however, the resulting surface

features exhibit different patterns depending on the side length of the ablated cavity. The patterns, despite their different shapes, show signs of rectangular geometry, suggesting that the contour of the cavity plays an important role in their formation. Furthermore, a more detailed analysis of the pattern shapes revealed the presence of a characteristic fixed distance of 1.78 mm (displayed as dashed purple line in the figure) that is common to all patterns. For a cavity with a side length of 4.2 mm, the distance from the sidewall to the cross maximum is approximately 1.78 mm. For a cavity with a side length of 5 mm, the same distance (1.78 mm) is observed between the sidewall and the first major parallel ridge. Similarly, for a cavity with a side length of 3.4 mm, a distance of 1.78 mm is measured between the sidewall and the second major parallel ridge. A certain evolution of the pattern shape with decreasing side length l can be observed. First, when the cavity side length is 5 mm, the pattern exhibits four major ridges-two horizontal and two vertical-each located 1.78 mm from the sidewalls. As the cavity size decreases, the distance between the ridges and the sidewall remains constant, causing the ridges to move closer together until they merge at a cavity side length of 4.2 mm. With a further decrease in cavity size, the ridges split again, this time maintaining a fixed distance of 1.78 mm between the sidewall and the second ridge. The characteristic evolution of the HALSFF shapes, together with the consistent fixed distance observed in all patterns, suggests that the shape of the formed surface features is determined by the cavity size and shape.

Next, an investigation was conducted to examine the influence of temporal and spatial scanning parameters on the formation of HALSFF. The temporal scanning parameter - pulse repetition period τ_{p-p}, here is defined as the time interval between consecutive laser pulses and expresses as $\tau_{p-p} = 1/f_{trigg}$, where f_{trigg} is laser triggering frequency. To maintain constant pulse pitch dx, while changing τ_{p-p}, the scanning speed v was varied accordingly. As a result, the surfaces were scanned under identical conditions-maintaining the pulse pitch dx, line pitch dy, pulse energy E_p, scanning strategy, and number of passes N, with only varying parameter being the τ_{p-p}. Surfaces formed with different pulse repetition period values are displayed in the figure 6.4. The results show that diverse τ_{p-p} values lead to the formation of different HALSFF patterns, while the PV value of the structures remains mostly preserved. Furthermore, it is seen that when the pulse repetition period is $\tau_{p-p} \geq 30\ \mu s$ (f_t = 33.3 kHz) no distinguishable HALSFF are observed, with the only

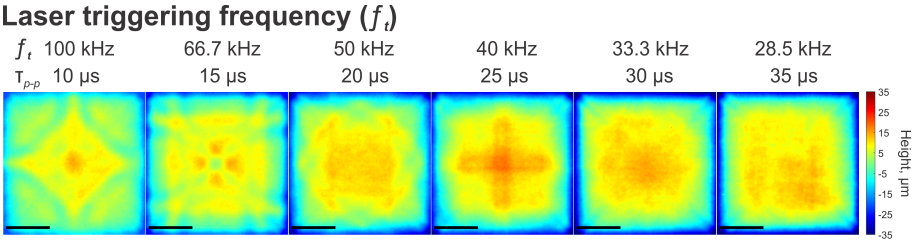


Fig. 6.4 Height maps of the bottom surfaces of deep ablated rectangular cavities, when scanning is performed under identical conditions, with only varying parameter being the pulse repetition period τ_{p-p}. Laser processing parameters used: fluence F = 18.2 J/cm^2, overlap of the craters Ω = 20 %, number of scans N = 775, engraved depth h = 820 μm. The black bar indicates a length of 1 mm.

remaining low ($f_r \lesssim 1\text{mm}^{-1}$) spatial frequency surface feature being the peripheral grooves. The formation of such grooves during multilayer laser ablation is a well known phenomena and is documented in the literature [206]. It is attributed to the partial reflection of incident laser pulses by non-perpendicular sidewalls toward the bottom surface near the sidewalls, which enhances local ablation and eventually results in trench formation. The absence of HALSFF at large temporal separations between laser pulses indicates that the physical mechanism underlying HALSFF formation relies on a high laser repetition rate (here $f \gtrsim 40$ kHz). It was demonstrated, that HALSFF formation can be suppressed by performing laser processing at $f_t \leq 30$ kHz; however, this approach is impractical, as it significantly prolongs the processing duration. For instance, ablating a $4 \times 4\,\text{mm}^2$ cavity to a depth of 820 μm required 10 minutes (corresponding to 775 scans) at $f_r = 100\,\text{kHz}$, whereas at $f_r = 33.3\,\text{kHz}$, the process took 25 minutes, resulting in approximately 2.5-fold increase in duration.

Subsequently, the influence of spatial scanning parameters on HALSFF formation was examined. In this case, the temporal separation between laser pulses was kept constant, corresponding to a fixed laser repetition rate of 100 kHz, while the cavities were engraved using different overlap of the craters (Ω) values. The overlaps in both the x and y directions (Ω_x and Ω_y) were varied simultaneously to ensure uniform ablation. It should be noted that number of scans N was adjusted for each Ω value to ensure the same engraved depth of $h \approx 1000$ μm is achieved. The obtained surfaces after engraving with different overalp of the crater values are shown in figure 6.5. The morphologies indicate that the pattern of generated HALSFF is independent of the spatial scanning

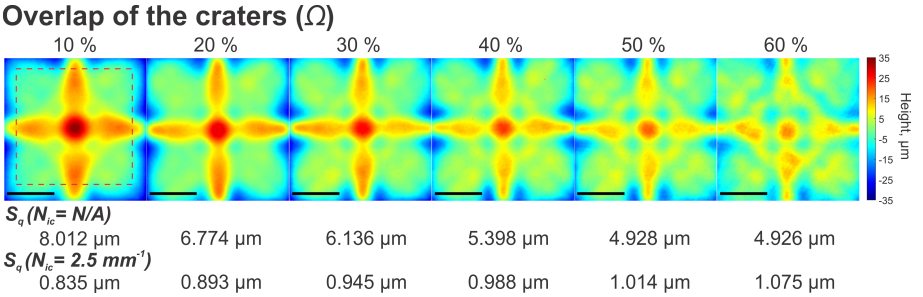


Fig. 6.5 Height maps of the bottom surfaces of deep ablated rectangular cavities obtained using different crater overlap values Ω. For each surface, the S_q values estimated from a 2.5×2.5 mm^2 rectangular area (indicated by the red dashed rectangle) are reported for both the unfiltered case (N_{ic} = N/A) and after eliminating low spatial frequencies (N_{ic} = 2.5 mm^2). Laser processing parameters used: fluence F = 18.2 J/cm^2, scanning speed v, line pitch dy and number of scans N were varied to reach an engraved depth of $h \approx 1000$ μm. The black bar indicates a length of 1 mm.

parameters. Across all cases, the pattern remains essentially the same, while the PV values vary (from PV = 67 μm at Ω = 10% to PV = 36.2 μm at Ω = 60%). These can be attributed to the fact that the number of scans N applied for different Ω values was not equal. The number of scans required to reach a 1 mm engraved depth was 224 for a crater overlap of Ω = 60%, compared to 1428 scans for Ω = 10%, corresponding to more than a sixfold increase. It has been previously shown that HALSFF formation is a cumulative process, with the PV value increasing as the number of layers grows. This characteristic of the HALSFF formation mechanism explains well why the PV value of the pattern generated at Ω = 10% exceeds that obtained at Ω = 60%. Moreover, a closer examination of the figures reveals that as Ω increases, not only does the PV value of the pattern change, but the pattern itself becomes increasingly distorted. The estimated S_q values obtained after removing low spatial frequencies (using N_{ic} = 2.5 mm^2) indicate that the distortion observed at higher Ω values is associated with increased surface roughness at higher spatial frequencies. This is supported by the measured values $S_q(N_{ic} = 2.5 \text{ mm}^2) = 0.835$ μm at Ω = 10 % and $S_q(N_{ic} = 2.5 \text{ mm}^2) = 1.075$ μm at Ω = 60 %. This aligns well with the discussion given in chapter 3, where it was shown that when ablating brittle dielectric materials, such as fused silica, the optimal crater overlap for minimal surface roughness is Ω ≈ 20 %, any further increase or decrease in overlap beyond this value leads to higher surface roughness. This is exactly what is observed in the figure 6.5, at low overlap value of Ω = 10%, the HALSFF

surface is smoother, whereas at Ω = 60‰, the same HALSFF is observed, however this time it's surface roughness is much higher (by ~ 20 ‰), giving the impression of the form distortion. Taken together, although spatial scanning parameters influence surface roughness, they do not affect HALSFF formation; these surface features form independently of the scanning speed or scanning pitch used.

6.3 Acoustic wave propagation numerical model

During laser ablation, each incident laser pulse, in addition to material removal, also generates a pressure disturbance in the surrounding environment [207]. This disturbance initially propagates as a shock wave and rapidly relaxes into an acoustic wave that continues to travel across the ablation region. Because these acoustic waves persist much longer than the typical inter-pulse separation in high-repetition-rate laser systems, they remain present when subsequent pulses arrive. In this work, we propose that the interaction between consecutive pulses and the residual pressure field generated by earlier pulses plays a defining role in the formation of HALSFF observed in our experiments.

To examine this hypothesis, we developed a numerical model to estimate the acoustic field distribution over the processing area at different time delays after the initial laser-matter interaction. Rather than simulating the full thermo-mechanical dynamics of the material, our model focuses specifically on the propagation of the pulse-generated pressure wave through the surrounding air and its reflections from the ablated cavity boundaries. The complete acoustic field dynamic would ordinarily be governed by the pressure-wave equation:

$$\nabla^2 p - \frac{1}{v_0^2}\frac{\partial^2 p}{\partial^2 t} = 0, \tag{6.1}$$

where p is the acoustic pressure and v_0 is the speed of sound. Solving this equation directly across the entire ablation domain, including multiple reflections, is computationally prohibitive for the timescales of interest; therefore, appropriate approximations were introduced. Each laser pulse was approximated as a point-like emitter of a spherical pressure wave originating from the laser-matter interaction site. Reflections from ablated cavity walls were incorporated using the method of images [208], where each planar boundary is substituted

by a virtual source placed symmetrically across the boundary plane. Due to large differences in impedance between the air ($Z_{\text{air}} \approx 4.1 \times 10^2$ Rayls) and fused silica ($Z_{\text{FS}} \approx 3 \times 10^7$ Rayls), almost all of the acoustic wave energy is reflected ($R = \frac{Z_{FS}-Z_{air}}{Z_{FS}+Z_{air}} \approx 1$). Therefore, the virtual sources were assigned the same amplitudes as the original sources. This simplified geometric-acoustics description captures the essential reflection and interference behaviors without resorting to computationally expensive numerical integration of the full wave equation 6.1. The temporal evolution of the pressure at each point was assumed to follow a modified Friedlander waveform [209], which characterizes the typical pressure dynamics of laser-induced shock waves in the air, featuring a rapid rise to peak overpressure, followed by an exponential decay and a subsequent negative rarefaction phase [210]. To account for a finite rising time of the pressure wave, an additional, second exponential term was introduced. The resulting pressure-time dependence is expressed as:

$$P(t) = P_{max} C \left(1 - \frac{(t+t_0)}{\tau_p}\right) exp\left(-\frac{(t+t_0)}{\tau_p}\right)\left(1 - exp\left(-\frac{(t+t_0)}{\tau_r}\right)\right), \quad (6.2)$$

here, P_{max} denotes the peak pressure, while C and t_0 are numerically determined normalization constants, with t_0 defining the temporal location of the pressure peak. τ_p is the characteristic decay time (positive-phase duration) and τ_r is the rise time. For the present calculations, the characteristic values of $\tau_p = 1$ μs, $\tau_r = 0.25$ μs were chosen according to the literature [210]. To account for spherical spreading, the pressure amplitude at a distance r from the source is given by $P(r,t) = P(t)/r$.

The numerical model was used to compute acoustic field distributions at various time delays after the initial laser-matter interaction. The rectangular cavity was assigned a length $l = 3.43$ mm (to be comparable with experimental conditions), and the speed of sound in air was set to $v_0 = 343$ m/s. The computed pressure distributions are displayed in figure 6.6, with different parts of the figure corresponding to scenarios where the acoustic wave source is positioned at different locations on the surface. Part (A) corresponds to the source located at the center of the processing area ($x = \frac{1}{2}l$, $y = \frac{1}{2}l$), part (B) to a source shifted laterally ($x = \frac{3}{4}l$, $y = \frac{1}{2}l$), and part (C) to a source shifted diagonally ($x = \frac{3}{4}l$, $y = \frac{3}{4}l$). In all three parts, the evolutions of an acoustic fields are observed, highlighting the emergence of complex field distributions resulting from multiple reflections and interference effects. Upon reflection, the

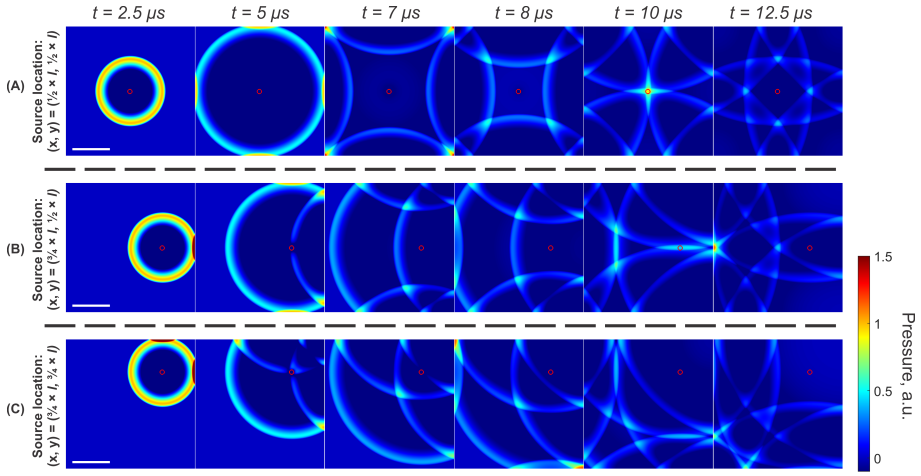


Fig. 6.6 Pressure distributions of a propagating acoustic wave at different time delays (2.5 ; 5 ; 7 ; 8 ; 10 ; 12.5 μs) after initiation. Parts A, B, and C illustrate scenarios with a single source located at different positions (indicated by a red circle). Initial peak amplitude equals 1. The scale bar represents 1 mm in length and variable l stands for a side length of a rectangular cavity.

fields develop localized overpressure regions, whose positions are governed by the cavity's size, geometry and the initial source location. As observed, fields with strong localized overpressure regions can persist for extended durations ($t > 10$ μs), lasting until the arrival of a subsequent laser pulse on the surface. This opens the possibility for interaction between a subsequent laser pulse and the overpressure regions, provided their locations coincide.

6.4 The origins behind HALSFF formation

The experimental results presented earlier provide valuable insights into the conditions necessary for HALSFF formation; however, they are insufficient on their own to elucidate the underlying physical mechanisms governing this process. Observations show that HALSFF formation requires short pulse repetition periods ($\tau \lesssim 25$ μm), the presence of the sidewalls, and high fluence values ($F \gtrsim 6.8$ J/cm^2), suggesting the involvement of both the laser pulse and residual laser-induced phenomena behind the formation of these features. Using the developed numerical model (see section 6.3) the residual acoustic fields generated during the laser processing were studied. An imaginary plane was constructed and populated with multiple spherical wave sources imitating laser

scanning. Using the numerical model, the propagation and reflection of each spherical wave within the ablated cavity was traced over the temporal delay between two laser pulses, recording the final positions of the wavefronts. By superposing the contributions from all spherical wave sources, the final pressure map could be obtained, showing the residual pressure amplitude distribution over the ablated cavity at the moment the second laser pulse arrives. The calculated pressure maps for different size cavities are displayed in figure 6.7, top row. The bottom row of the figure shows the experimentally generated HALSFF during laser deep engraving of similarly sized cavities. Comparison

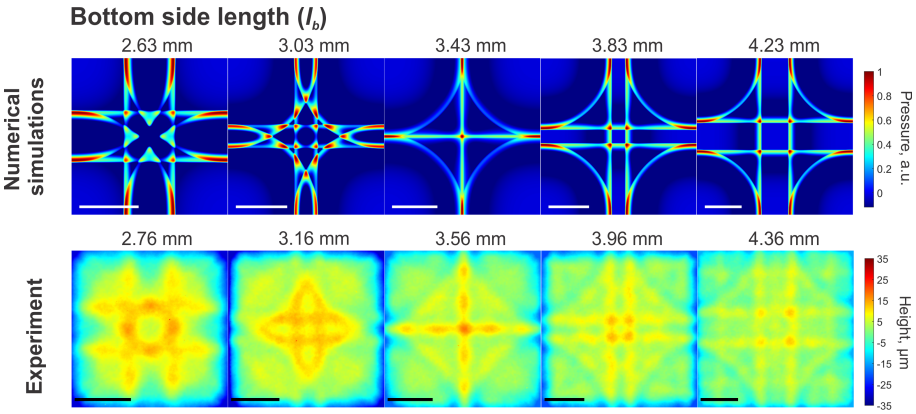


Fig. 6.7 Pressure maps of surfaces with different bottom side lengths of l_b generated using the numerical model presented in the study (top row). The amplitudes in each pressure map are normalized. Height maps of the bottom surfaces of deep ablated rectangular cavities with bottom side lengths of l_b (bottom row). Laser processing parameters used in the experiments are detailed in figure 6.3 caption.

of the pressure maps with the formed HALSFF reveals a clear similarity in their pattern shapes. It can be observed that regions of highest pressure correspond to protrusions in the HALSFF, whereas areas of minimal pressure exhibit a relatively homogeneous surface. This suggests that during laser processing, a laser pulse passing directly through the wavefront of a propagating acoustic wave generated by a preceding pulse results in the formation of protrusion. Reports in the literature [211] show that the initial pressure of the shock wave generated during femtosecond laser–matter interaction can reach GPa levels. After traveling a distance of 4 mm (in line with experimental observations), its pressure is reduced to the range of 10 kPa to 1 MPa, following an approximate $\sim r_0/r$ scaling. Applying the simplified relation of refractive index change to pressure change , $\Delta n \approx (n_0 - 1)\Delta p/p$, the estimated pressure variations of

traveled acoustic wave correspond to a refractive index change of $\Delta n \approx 10^{-5}$ to 10^{-3}. Such refractive index variations are sufficient to introduce local phase distortions in the propagating laser beam, leading to degraded focusing and consequently reduced ablation rate. The experimentally estimated decrease in ablation rate was found to be $\delta R_t \leq 5\%$. While resultant local depth variations are negligible for a single scan, the cumulative buildup over multiple passes ($N > 100$) becomes significant, leading to the formation of high-amplitude, low-spatial-frequency features. This theory aligns well with the observation that HALSFF formation occur only under deep engraving conditions, when the cavity sidewalls are established, as they are necessary for confining the acoustic waves within the processing cavity. Furthermore, the analysis of experimental results have shown that higher fluence values ($F \geq 6.8$ J/cm^2) are required for pronounced HALSFF formation. This can now be explained by considering that the pressure of the generated shock wave is directly proportional to the pulse energy applied [212]. As a result, higher pulse energies (fluence values) produce stronger perturbations for subsequent laser pulses, facilitating HASLFF formation. However, while the figure 6.7 offers a compelling explanation of HALSFF formation, it also reveals certain discrepancies between the model and the experimental results. As shown in the figure, the cavity lengths required to produce identical HALSFF patterns differ between the model and the experiment by up to 5 %. Furthermore, although the main patterns coincide in both the model and the experiment, the experimentally generated surfaces exhibit additional small-scale features surrounding the main pattern that are not captured in the modeling results. These discrepancies between the model and the experiment are believed to arise from additional factors not accounted for in the model, such as non-perpendicular side walls, textured side walls, variations in airborne acoustic wave speed due to surface heating, and higher-order reflections (second, third, etc.) that may also influence the results. Nevertheless, the model provides a comprehensive explanation of the governing physical mechanisms and enables the prediction of the main HALSFF pattern formed during multilayer laser engraving. To further validate the proposed physical mechanism underlying HALSFF formation, an attempt was made to reproduce identical HALSFF patterns under different processing conditions. It was observed in figure 6.4 that different pulse repetition period τ_{p-p} values yield different HALSFF patterns, as longer delays allow the acoustic wave to propagate extended distances, thereby perturbing the laser processing at different locations. Using the presented

numerical model, the cavity side lengths required to generate the same pattern for different pulse repetition periods τ_{p-p} were calculated. The generated HALSFF patterns under different pulse repetition periods τ_{p-p} and side lengths l are shown in figure 6.8. The top row shows numerical simulation results,

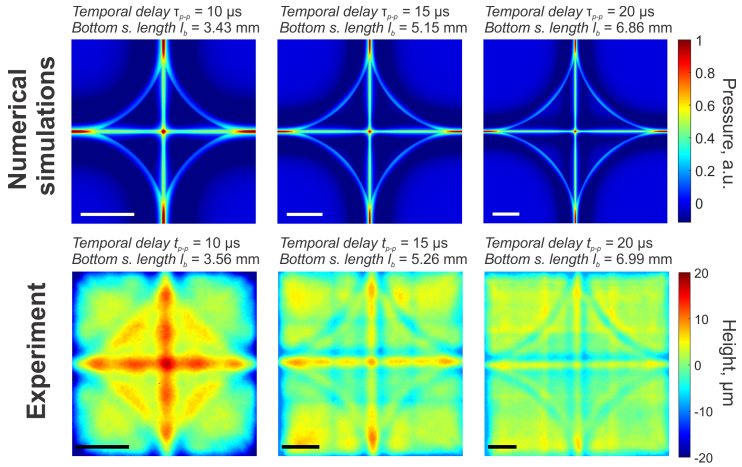


Fig. 6.8 Pressure maps of surfaces with different bottom side lengths l_b and pulse repetition periods τ_{p-p} generated using the numerical model presented in the study (top row). The amplitudes in each pressure map are normalized. Height maps of the bottom surfaces of deep ablated rectangular cavities with bottom side lengths l_b and pulse repetition periods τ_{p-p} (bottom row). Laser processing parameters used: fluence F = 18.2 J/cm^2, overlap of the craters Ω = 20 %, number of scans N = 775, engraved depth h = 820 μm.

while bottom row - experimental results. As can be seen, identical cross like pattern was formed in all the cases, showcasing the accuracy of the model and validating proposed physical mechanism governing the formation of HALSFF. Furthermore, it is observed that when the cavity's length is large (l_b = 6.99 mm), the HALSFF PV value is much smaller compared to the case when the cavity's length is small (l_b = 3.56 mm). This effect is caused by the pressure loss of the acoustic wavefront due to its expansion during propagation, since the amplitude of a spherical wave decreases with distance according to $A \propto 1/r$, where r is the distance traveled. In addition, when processing larger areas, due to longer temporal delays between successive scanned lines, the heat accumulation is less pronounced, eliminating the influence of variable sound speed in heated media and other morphological phenomena that might occur under increased temperature conditions. The eliminated additional factors, result in the better

agreement between model and the experiment, as seen in the case where $l_b \approx 7$ mm.

6.5 Methods to suppress HALSFF formation

Since the formation of HALSFF is an undesirable effect that leads to an uncontrollable increase in surface roughness during prolonged laser engraving, we propose several strategies to prevent its occurrence. One way to prevent the formation of HALSFF has already been demonstrated and relies on increasing the pulse repetition period τ_{p-p}. Increasing the τ_{p-p} value causes the spherical wave to propagate over a longer distance, resulting in a greater loss of wavefront pressure. If the propagation distance is sufficiently long, the wavefront pressure of the spherical wave becomes too weak to perturb the laser pulse, preventing a decrease in ablation efficiency. Furthermore, extended acoustic wave travel increases the number of reflections and may even cause the wave to exit the processing area. The results in figure 6.4 disclosed that $\tau_{p-p} \geq 30$ μs (corresponding to $f_t = 33.3$ kHz) was necessary for the HALSFF to be barely distinguishable, suggesting that such duration of acoustic wave travel was sufficient for the wave to escape the cavity or loose its pressure to a negligible level. However, although this solution prevents the formation of HALSFF, it significantly prolongs the processing duration (≥ 2.5 times, as demonstrated previously), making it ineffective. Another, more efficient approach in preventing the formation of these features relies on controlling the propagation direction of the spherical acoustic waves. It was observed that for the patterns to form, the presence of the steep sidewalls is necessary. Since the angle of reflection is identical to the angle of incidence [213] (in the consideration of ray optics), the cavity side-wall angle determines the pointing vector of the reflected acoustic spherical wave. Under typical processing conditions, the sidewalls with an angle of $\alpha \approx 10°$ are formed, where α is the angle between the sidewall and the vertical. Such steep side-walls reflect the spherical waves back over the processing area, creating conditions for them to interact with subsequent laser pulses and perturb them. However, if a side-wall angle $\alpha \geq 45°$ would be achieved, the spherical waves would be reflected outside the cavity, eliminating their perturbation of the subsequent laser pulses. In order to test it, the cavity with side-wall angle of $\alpha \approx 60°$ was formed. This was achieved by initiating the ablation process with increased cavity side length l_t and reducing the side length of each subsequent

layer by a constant amount of δl_t, thereby forming a cavity with identical depth and bottom side length l_b as before, but with different side-wall angle. The results are shown in figure 6.9. From a comparison of the height maps of the

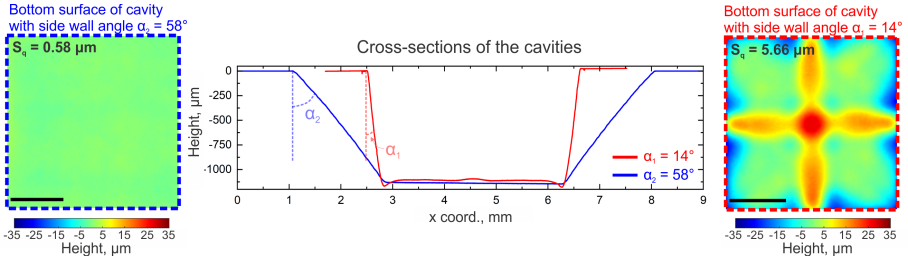


Fig. 6.9 Cross-sections of the cavities with sidewalls of different angles (in the middle). eight maps of the bottom surfaces of deep ablated rectangular cavities with sidewalls of different angles (on the sides). Laser processing parameters used in both cases: fluence F = 18.2 J/cm^2, overlap of the craters Ω = 20 %, number of scans N = 1111, engraved depth h = 1130 μm. The black bar indicates a length of 1 mm. See in text for explanation on how different side-wall angles were achieved.

bottom surfaces of cavities with different side-wall angles, it is evident that a high side-wall angle $\alpha = 58°$ prevents the formation of HALSFF, thereby confirming the previously proposed hypothesis. Furthermore, in addition to preventing the formation of HALSFF, a large side-wall angle also suppresses the formation of trenches around the perimeter of the bottom surface near the side-walls. The introduced benefits of large side-wall angle resulted in the total reduction of the bottom surface roughness by ten-fold, from S_q = 5.66 μm when $\alpha = 14°$ was used to S_q = 0.58 μm at α value of 58°. However, producing cavities with shallow sidewalls requires removing more of the material, thereby extending the processing duration. The ablation of a 4×4 mm^2 cavity with sidewalls of 14° to a depth of 1130 μm required 14 minutes, whereas producing an identical cavity with sidewalls of 58° took 24 minutes, corresponding to a 1.7-fold increase in processing time. Compared to mitigation strategy based on reducing the laser repetition rate, which prolonged processing duration by 2.5 times, this approach comes superior, offering a more effective solution for mitigating HALSFF formation. Beyond the solutions presented, other plausible approaches for suppressing HALSFF formation may also exist, including performing laser processing in a vacuum, applying a high-pressure gas stream, or operating in a burst regime. However, these methods were not tested in the framework of this study, and their effectiveness therefore remains unknown.

6.6 Summary

In this chapter an in-depth investigation was carried out to reveal the governing physical mechanisms behind the formation of high amplitude low spatial frequency features (HALSFF) that are formed during laser deep engraving. The experimental results and numerical calculations revealed that HALSFF are formed due to the laser pulse generated acoustic wave perturbation of the consecutive laser pulse wavefront, which results in the reduced local ablation efficiency. Each laser pulse generates a shock wave that upon expansion transforms into an acoustic wave, continuing its propagation further over the processing area. If the subsequent incident laser pulse overlaps with the propagating acoustic wave, its wavefront is perturbed, resulting in reduced ablation efficiency at incident location. The cavity size and form determines the locations where this effect takes place, thereby defining the pattern of formed HALSFF. The effect was only observed when fluence values of $F \geq 6.8$ J/cm^2 were used, as such a magnitude of fluence was required to generate sufficiently strong acoustic waves capable of inducing perturbations. Furthermore, this effect occurs only in the presence of steep side-walls, which confine the propagating acoustic waves over the processing area. It was demonstrated that the formation of HASLFF can be suppressed by increasing the temporal delay between consecutive laser pulses. At longer delays (in our case, $\tau_{p-p} \geq 30$ μs, achieved at $f_t = 33.3$ kHz), the laser-induced acoustic wave undergoes sufficient amplitude attenuation such that it can no longer perturb the subsequent laser pulses or may even exit the processing area due to multiple reflections. Another suggested approach in omitting HALSFF formation includes forming cavities with sidewall angles of $\alpha > 45°$. Under these conditions, the laser-induced acoustic waves, after reflecting from the sidewalls, are directed to exit the processing region, thereby eliminating their interaction with subsequent laser pulses. It was shown that suppression of HALSFF formation can reduce the surface roughness by an order of magnitude, with S_q decreasing from 5.66 μm to 0.58 μm during laser deep engraving to a depth of 1 mm. The physical mechanism underlying HALSFF formation identified in this study constitutes a novel contribution to the field of laser micromachining.

Chapter 7

Alternative laser-based surface roughness control method

Although this thesis primarily focuses on controlling surface roughness through laser ablation, it is essential to also consider other laser-based surface processing techniques and their ability to influence surface roughness. Doing so allows conventional laser ablation to be understood within the broader context of all laser-based processes, providing a more comprehensive perspective.

7.1 Laser polishing

Laser polishing is a surface finishing process that uses laser radiation to improve surface quality by reducing surface roughness. It is most commonly referred to when the discussion revolves around achieving the highest surface finish. When talking about optical components, this is achieved when the surface scatters light to a negligible extent. The total amount of light scattered by a surface can be evaluated by measuring the total integrated scatter (TIS) parameter [214], which approximates as TIS$\approx (4\pi R_q/\lambda)^2$. By considering visible and near-IR wavelengths, to achieve TIS < 5 % (level of scattering typically acceptable for most optical components), would require $R_q \approx 10$ nm. Such a level of surface roughness is practically near impossible to achieve via laser ablation alone and is typically reached by implementing the remelting of the surface texture via laser radiation. Hence, usually (but not only) when talking about laser polishing the remelting of the surface is considered.

The schematic depicting the typical laser polishing procedure is shown in figure 7.1. The laser polishing can be realized using continuous wave (A) as well as pulsed (B) laser radiation. In both cases, laser radiation is used to heat up the substrate until it melts. The molten material, driven by surface tension, redistributes itself to form a smooth surface.

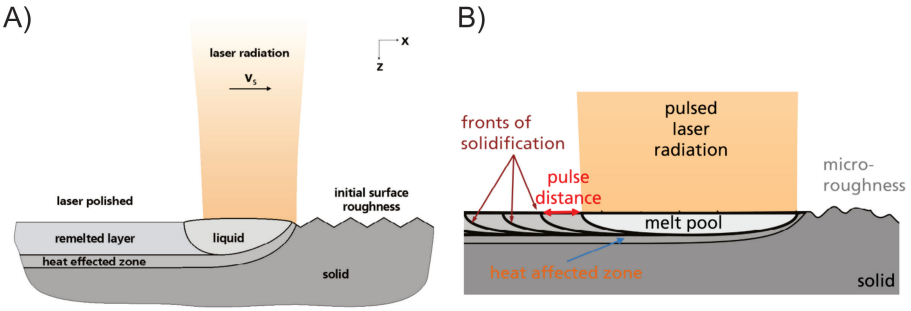


Fig. 7.1 Schematic of laser polishing by remelting a thin surface layer using continuous laser radiation (A) and pulsed laser radiation (B) [26].

The different mode of laser operation (continuous wave or pulsed) is picked depending on the initial roughness of the surface. Continuous wave (macro) polishing is used to smooth surfaces with spatial frequencies of f_r = 12.5-0.8 mm^{-1}. The smoothing of higher frequencies than f_r = 12.5 mm^{-1} is not attainable using continuous wave laser radiation due to a large remelted surface layer (ranging between 10-80 μm [26]) and complex solidification processes under extended heating conditions, such as the formation of martensite structures in metals and others. To further improve the quality of a surface that has a relatively smooth initial surface with spatial frequencies of $f_r \gtrsim 12.5$ mm^{-1} (e.g. diamond-milled surfaces) the pulsed laser radiation is used. This is achieved through the formation of a shallower remelted layer (< 5 μm [26]) and faster cooling rates (due to short pulse duration with $\tau \sim$ hundreds of ns and less). Therefore, for polishing of milled or turned surfaces that exhibit high initial roughness, continuous wave laser radiation is used. In such cases, a CO2 or high-power diode lasers are utilized [215]. Whereas, for fine polishing of grinded or diamond-milled surfaces that exhibit small initial roughness, the pulsed laser radiation is used. For such applications, Nd:YAG or Yb:KGW lasers are utilized [216]. However, it should be noted that although laser polishing effectively modifies surface roughness through remelting, it does not remove material from the sample surface and is therefore unsuitable for shape formation.

Thus, laser polishing is typically used as a post-processing technique to further tune the surface roughness, but not as a stand alone tool.

A perfect example of laser polishing in use was demonstrated by Zubauskas et al. [10], where authors formed a micro-lens array on the surface of fused silica using ultrashort laser ablation and polished by implementing laser polishing technique. First a micro lens array was formed using ablation with ultrashort laser radiation. The surface was scanned multiple times, until desired shape was achieved. A lens array consisting of 30 lenses 1 mm apart was formed. After shape retrieval procedure, the surface roughness measured $S_a = 0.4$ μm, when using femtosecond laser radiation and $S_a = 0.88$ μm, when using picoseconds. Next, using CO2 laser radiation the lens arrays were polished by remelting the top surface. The S_a values before and after laser polishing are given in table 7.1. It is evident that laser polishing was effective in reducing the final surface

Table 7.1 Surface roughness and lens radius comparison before and after laser polishing [10].

	Surface roughness S_a (μm)		Surface radius (mm)	
	No polishing	With polishing	No polishing	With polishing
Picosecond	0.88	0.06	0.73 ± 0.14	0.81 ± 0.21
Femtosecond	0.40	0.029	0.88 ± 0.009	0.88 ± 0.014

roughness, with displayed reduction in surface roughness from $S_a = 0.40$ μm down to $S_a = 0.029$ μm. In addition to the reduction of roughness, authors also observed that due to remelting of the top surface layer, the surface shape changed, with lens radius changing from 0.73 to 0.81 mm. Therefore, when using laser polishing to reduce the final surface roughness, the possible change in surface shape should be considered, especially when processing is performed on curved surfaces.

Furthermore, other studies confirm that laser polishing can be successfully realized not only on glasses, but also on metals. In one study [217], authors achieved a reduction of steel surface roughness from $S_a = 210$ nm down to $S_a = 75$ nm by remelting the top surface layer using pulsed ultrashort laser radiation. In another study [26], authors claimed that in order to minimize the micro-roughness (here defined as $f_r \geq 10$ mm^{-1}) and maximize the gloss level, a combined treatment of CW and pulsed laser radiation has to be used. The results from that study are given in figure 7.2. The figure shows that a reduction of roughness is achieved throughout the whole spectrum of spatial wavelengths

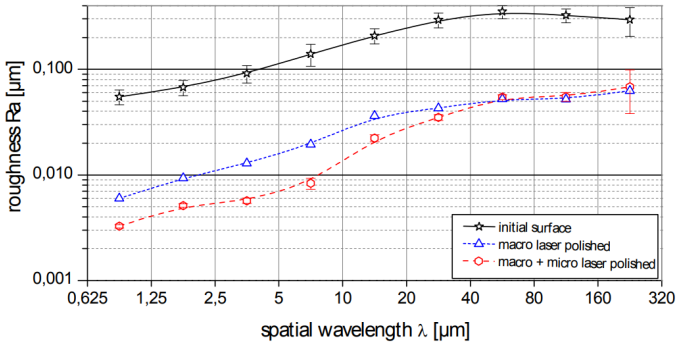


Fig. 7.2 Roughness dependence on spatial wavelength. Black curve represents initial surface roughness, blue curve - after macro laser polishing, while red - after combined macro and micro laser polishing procedures [26].

when performing macro laser polishing with CW laser radiation. After this first step, the achieved reduction in roughness ranges from 70% - 90% depending on the spatial wavelength. A subsequent laser polishing step using pulsed laser radiation leads to a further reduction of micro ($\lambda < 10$ μm) and meso (10 μm $< \lambda < 80$ μm) roughness up to 50%, with reduction of spatial wavelengths of up to $\lambda = 40$ μm. The final surface roughness is reduced down to $R_a = 3$ nm at spatial wavelength $\lambda = 0.93$ μm, accounting for the total reduction of surface roughness by 94 %. However, at $\lambda = 240$ μm the minimum achieved roughness value is only around $R_a \approx 75$ nm. It shows that a combined laser polishing approach, incorporating CW and pulse laser radiations is an effective technique in reducing surface roughness, especially at lower spatial wavelength values ($\lambda < 40$ μm). A similar level of roughness was achieved by another group [218], where the authors also utilized a two-pass method incorporating CW and pulse laser regimes. In such a way authors managed to reduce the roughness of Ti6Al4V from $S_a = 172$ nm down to $S_a = 47$ nm.

The main disadvantage of laser polishing is that during such a process the surface is enriched with regularly spaced ripples. The melt pools formed during pulsed laser polishing exhibit a non-uniform temperature distribution that mirrors the laser beam's intensity profile, which is typically a Gaussian distribution. Since, the surface tension is a function of temperature, the driving force of the melt pool towards the higher surface tension regions is formed, which is often referred as the Marangoni flow [219]. Once the melt-pool reaches the liquid-solid boundary, it is pushed upwards and forms local material

upwelling as resolidification occurs. Since pulsed laser polishing is performed at a constant pulse repetition rate, the overlapping local material upwellings manifest as regularly spaced ripples, whose amplitudes are primarily governed by the melt-pool velocity.

The discussion concludes that, depending on the material and laser source, different levels of polishing can be achieved. Continuous wave (CW) lasers are used to polish the surfaces with high initial roughness; however are limited in complete attenuation of low spatial frequencies. For further polishing of surfaces with low initial roughness, pulsed laser sources are used. It should be noted that typically long-pulse-duration lasers are used (ns lasers) due to the need for continuous surface heating, as under these conditions the widest range of surface features has been shown to be attenuated [216]. Moreover, pulsed laser polishing is generally limited to materials with strong absorption, such as metals, since only this enables surface remelting without inducing ablation. The combined use of CW and pulsed laser polishing techniques allows the reduction of the surface roughness from high initial roughness ($R_a > 10$ μm) down to minimal roughness ($R_a < 100$ nm) [220]. In addition, some literature sources indicate that the reduction of surface roughness below $R_a < 1$ nm is possible when using laser polishing [221, 222]. Yet, such low roughnesses are only achieved at spatial frequencies of $\lambda < 100$ μm ($f_r > 10$ mm^{-1}). At higher spatial wavelengths, roughness cannot be reduced to such extents due to the side effect of laser polishing - the formation of periodic ripples on the surface. While some post-processing techniques are present that allow the selective removal of the induced waviness, they are typically time-consuming, prolonging the overall manufacturing process greatly. Despite its disadvantages, laser polishing is still the leading laser processing technique for achieving of ultra-fine surface finish. Laser polishing is used for polishing of dental orthopedic implant materials [223], medical implants made of titanium [224], various glass [225], and others.

7.2 Laser polishing using bursts of femtosecond pulses

Results presented in this section were published in [B1].

With the rapid advancement of femtosecond laser technology, a recent innovation has emerged: the ability to split a single pulse into multiple sub-pulses with temporal separation in the range of MHz or GHz repetition rates. This operating mode is referred to as the burst regime, offering distinctive

advantages in regard to ablation rate and surface quality [193, 226]. The GHz intraburst repetition rate creates conditions for quasi-continuous heating of the material, similar to those observed with long pulse (> 10 ns) lasers, even when femtosecond pulses are used. This in turn opens the avenue for performing both processes: laser ablation and laser polishing with a single femtosecond laser. In the following, results will be presented that explore the use of the burst regime for polishing a dielectric material-hydrophobic acrylic polymer (Contamac CONTAFLEX 26% UV-IOL). This material is commonly used in the production of intraocular lenses (IOLs), where achieving extremely low surface roughness is of critical importance.

7.2.1 Investigation framework

In this investigation, the first experimental setup configuration was used (see section 2.1), featuring $\lambda = 1030$ nm laser radiation wavelength. When operating in burst mode, individual laser pulses with a duration of $t = 210$ fs were split into trains of sub-pulses, featuring an intra-burst temporal separation of 400 ps and a burst repetition rate of 100 kHz. The Carbide laser (manufactured by Light Conversion) used in this investigation featured a tunable burst envelope control, enabling the generation of bursts with ascending, descending, and flat intensity profiles, as well as intermediate shapes. To test this feature, the burst regime was examined using "Time-correlated Single Photon Counting" (also known as TCSPC) method [227]. The corresponding burst configurations when single pulse is split into packets of 2 and 10 sub-pulses are given in figure 7.3, parts (A) and (B) accordingly. As evident from the measurements, the pulses can be effectively split, with precise control over their amplitude profile achieved through adjustment of the burst envelope parameter. However, it was observed that when the burst packets containing 10 and more sub-pulses are generated, the parasitic pre-pulses are formed (see part C of the figure). Furthermore, it is seen that the trailing sub-pulse within the burst carries exaggerated amount of energy, measured to be 62 % more than other sub-pulses within the burst, when the envelope of 10 sub-pulses is leveled flat. While contribution of the exaggerated trailing pulse amplitude towards the laser-matter interaction remains unexplored, this feature is unavoidable due to the inherited technology of burst generation in this particular laser [228]. However, if the number of sub-pulses within the burst is reduced to five or less, then all of the pulses within the burst can be

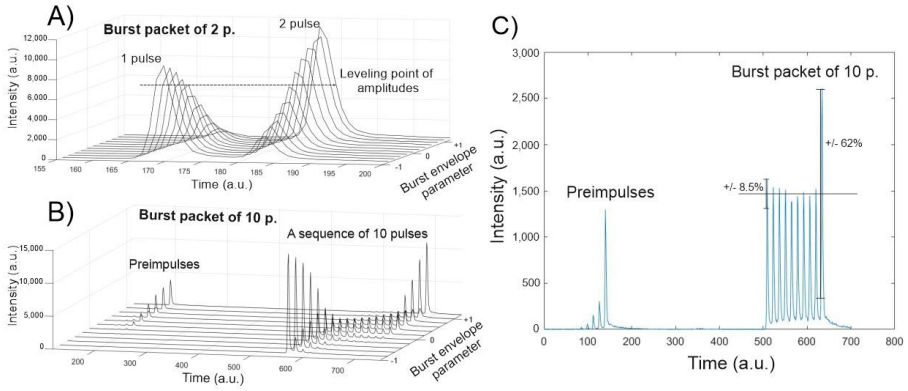


Fig. 7.3 The dependence of the intensity of the sub-pulses in the burst versus the envelope parameter when a single pulse is divided into 2 sub-pulses (A) and into 10 sub-pulses (B). Amplitudes of a leveled burst packet of 10 sub-pulses are displayed in (C).

leveled to an 10 % error margin. Another interesting insight is that the burst envelope parameter under which the burst profile is flat takes on different values depending on the length of the burst. Hence, when performing laser polishing experiments, the burst envelope parameter was varied accordingly to the burst length, to maintain the flat burst intensity profile.

The laser processing experiments consisted of 2 steps: first, rectangular cavities 10 mm x 10 mm in size and 0.5 mm in depth (such dimensions are typical for eye implants) were ablated while operating in a conventional femtosecond regime, followed by polishing of their bottom surfaces with bursts of femtosecond pulses. The ablation was performed in a raster scanning manner, with the overlap of beams Ω (given by equation 1.29) kept equal in both x and y directions to ensure uniform surface modification over the whole area. The laser was operating at 100 kHz repetition rate, no additional advanced scanning strategies were applied. The ablated surfaces were laser polished using varying burst configurations, with the aim of achieving minimal surface roughness. During the processing the surface temperature was monitored using a thermal vision camera "FLIR A600-Series" (manufactured by FLIR systems). The laser-processed surfaces were measured using "Sensofar PLU 2300" optical profiler. For the evaluation of the surface roughness, mainly the R_a (see equation 1.1) parameter (featuring sampling length of l = 125 μm) was calculated, with

complimentary 3D roughness parameters [229] measured for surfaces of higher importance.

7.2.2 Results

Initially, the cavities were ablated and prepared for laser polishing. During the ablation step, the primary focus was on maximizing the ablation rate. The maximum ablation rate R_t = 50.4 mm^3/min was achieved when using the fluence of F = 78.5 J/cm^2, which corresponded to an average laser power of P = 29 W. Other laser parameters were fixed, with scanning speed of v = 3.6 m/s and scanning pitch $dx = dy$ = 36.57 μm. With such processing parameters it took approximately 1 min to ablate the 10 mm × 10 mm × 0.5 mm (50 mm^3) shape. It is worth mentioning, that 50 mm^3 is a common value which would be required to produce a custom 3D lens shape applicable for eye implants; therefore, it represents a realistic estimation of the time needed for the ablation task. After ablating the samples to a depth of 0.5 mm, one to few additional scans were performed with a low average power setting of P = 2.5 W to further decrease surface roughness. This way we were able to achieve the lowest surface roughness of R_a = 0.991 μm using the single pulse regime.

Next, the bottom surfaces of ablated cavities were laser polished using bursts of femtosecond pulses. During the experiments, the average laser power P, scanning speed v, scanning pitch dy, and number of sub-pulses within each burst N_p were varied to assess how these parameters influence laser polishing. The summarized results are given in figure 7.4. The results indicate that appropriate burst pulse settings can significantly reduce the initial surface roughness. With 5 sub-pulses and medium average laser power ($P \approx$ 15 W), the roughness is already reduced 2.5 folds (from 1 μm to 400 nm, seen in part D of the figure). A further increase in laser power ($P \approx$ 24 W) allowed the surface roughness to be reduced down to $R_a <$ 100 nm. This shows that smoothing of the surface requires sufficient power for effective surface melting, but excessive power, especially at low scanning pitch values, can increase roughness due excessive thermal accumulation, which results in material boiling and overmelting. On the other hand, insufficient thermal accumulation, observed at high scanning speeds, leads to incomplete polishing and only mild reduction in surface roughness ($R_a \approx$ 520 nm at v = 2000 mm/s, see fig. C). A similar trend is observed in part (B), where high N_p values result in only minor roughness reduction, as dividing

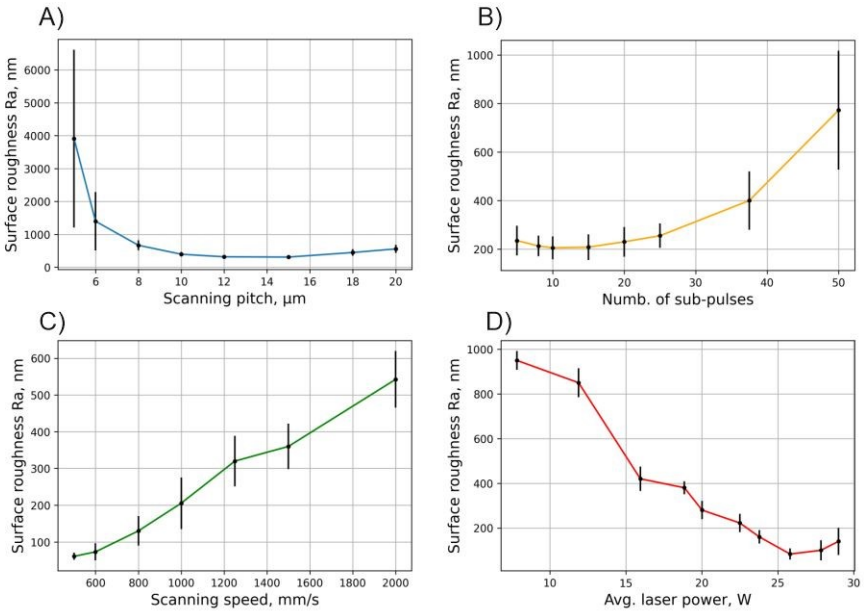


Fig. 7.4 Surface roughness after polishing ablated samples dependencies on different polishing parameters. Other fixed parameters in case of (A): P = 29 W, N_p = 10 and v = 1000 mm/s; in case of (B): P = 19 W, dy = 10 μm and v = 1000 mm/s; in case of (C): P = 25.8 W, dy = 10 μm and N_p = 10; and in case of (D): v = 1000 mm/s, dy = 10 μm and N_p = 5.

the pulse into that many sub-pulses lowers the energy of individual sub-pulse to a level where the intensity is insufficient for efficient nonlinear absorption. A more detailed analysis of selected laser-polished surfaces, including visual representations and 3D roughness parameters, is presented in the figure 7.5. As seen from the figure, the transparency of the surfaces correlates closely with measured surface roughness values. Surface in part A, with S_a = 0.991 μm appears to be completely opaque, while surface in part B with S_q = 0.692 μm is only semi-opaque and finally, surface in part C, with S_q = 0.088 μm is already completely transparent. An exception in this regard is seen in part D of the figure. Here, the surface appears to be visually transparent, but the roughness measures S_a = 3.89 μm. Such high roughness is measured due to excessive thermal accumulation which resulted in surface overmelting. However, despite the induced waviness, all shorter spatial wavelengths were effectively suppressed. Hence, these results indicate that surface transparency and scattering properties are mainly effected by shorter spatial wavelengths.

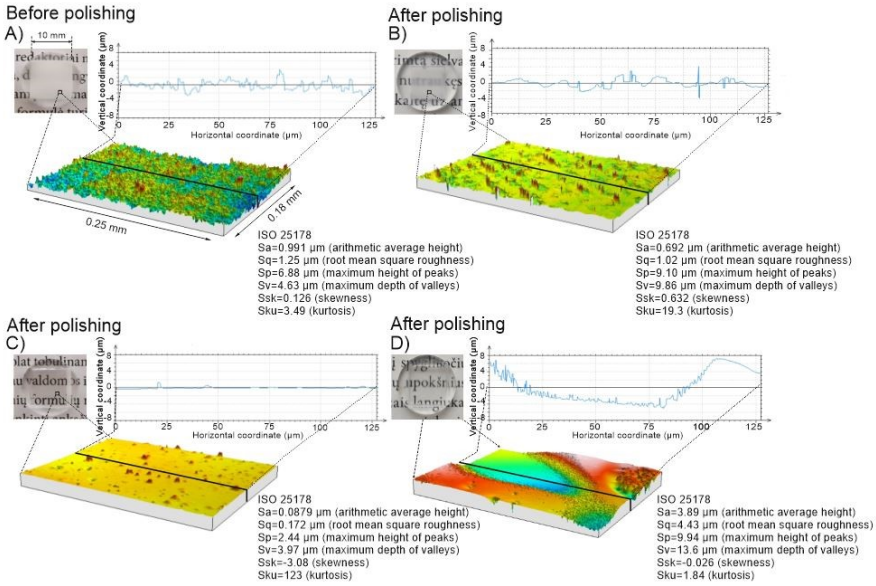


Fig. 7.5 Surface before laser polishing (A). Surface after single scan laser polishing with bursts of femtosecond pulses, with P = 12 W, v = 1000 mm/s, dy = 5 μm and N_p = 10 (B); P = 29 W, v = 1000 mm/s, dy = 10 μm and N_p= 10 (C); and P = 29 W, v = 1000 mm/s, dy = 5 μm, N_p= 10 (D).

To further investigate how the number of sub-pulses in a burst influences polishing quality, we examined its correlation with the sample's surface temperature by monitoring the temperature during processing using an IR camera. The results are given in figure 7.6. The figure indicates that increasing the number of sub-pulses within a burst from 1 to 3 raises the surface temperature from 285 to 355 °C, while simultaneously reducing the sample roughness to R_a < 100 nm. Further increasing the number of sub-pulses per burst does not lead to any additional reduction in surface roughness. These observations suggest that when splitting a single pulse into at least three sub-pulses, a certain energy threshold per pulse is reached and thermodynamical processes are stimulated which result in the remelting of the surface and its smoothening. The minimum achieved roughness value here $R_a \approx 20$ nm, was obtained when N_p value of 3 was used, and the surface was scanned twice. In part B of the figure, the microscope pictures of laser polished surfaces using different P and N_p values are shown. The upper row shows that an average power in the range of 16 W < P < 24 W yields the most effective surface melting and the smoothest finish. At higher laser powers P > 25 W, it was observed that the average surface

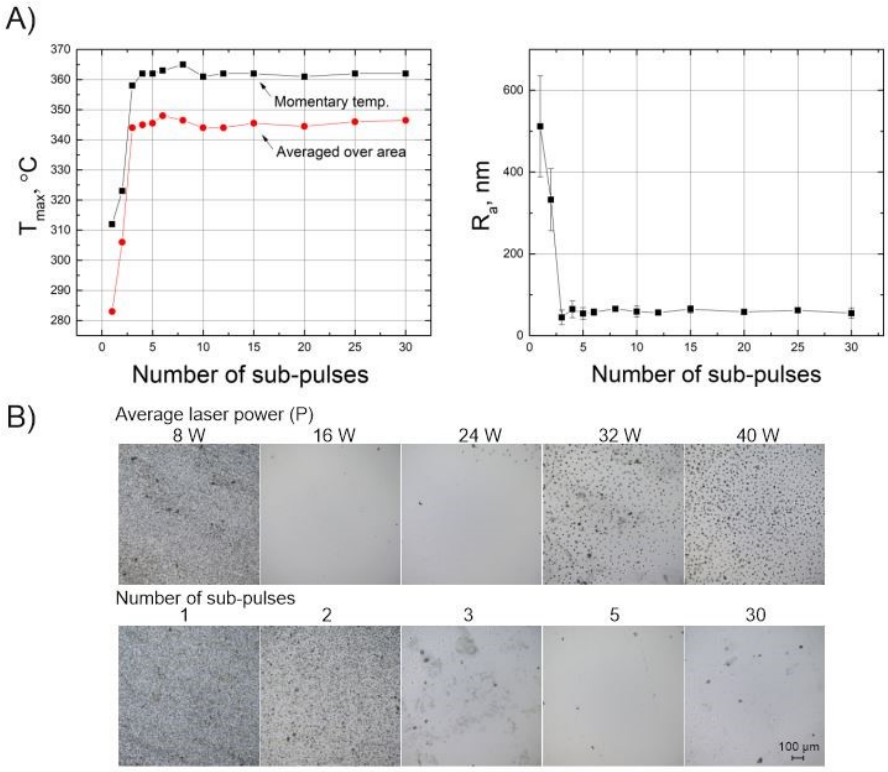


Fig. 7.6 (A) Surface temperature dependence on the number of sub-pulses within a burst (on the left), R_a dependence on the number of sub-pulses within a burst (on the right). Other parameters: P = 16 W, dy = 10 μm, v = 700 mm/s and number of scans = 2. (B) The microscope pictures of laser polished surfaces using different P values, with the remaining parameters of N_p = 10, dy = 10 μm, v = 700 mm/s and number of scans = 2 (upper row). The microscope pictures of laser polished surfaces using different numbers of sub-pulses. Remaining parameters P = 16 W, dy = 10 μm, v = 700 mm/s and number of scans = 2 (bottom row).

temperature rises above 360°C, which initiates the formation of bubbles below the surface (seen as black circles in the figure). The bubbles are the release of gas trapped inside the volume which explode upon reaching the surface. It causes sputtering of the molten material and creates micro-valleys, resulting in an increase of surface roughness [230]. The findings indicate that the success of laser polishing lies in heating the surface to an optimal temperature, measured here as T_{optimal} = 357,° C (when processing acrylic polymer).

7.2.3 Summary

The results presented in this section conclude that bursts of femtosecond pulses can be efficiently used to perform laser polishing of the acrylic polymer. The analysis of the surface temperature during laser processing showed that the polishing process depends on the thermal heat flux, which initiates thermodynamic processes that change the surface roughness of the sample. The optimal surface temperature was found to be approximately 357 °C, at which it was possible to polish the material down to $R_a \approx 20$ nm, resembling a transparent surface that meets optical-quality standards. It was shown that in order to reach the stated temperature level, it is necessary to split the single pulse into at least more than three sub-pulses (with temporal separation of 400 ps). However, if the number of sub-pulses is increased above three, similar results in terms of surface temperature are achieved. If the surface is overheated to above 360 °C, micro bubbles form which rise to the surface and produce surface craters upon exploding, thereby reducing the surface quality.

7.3 Non-thermal ablation

Another novel method that preserves ultra-fine surface roughness while performing laser processing was introduced by a research group led by Jie Qiao. Four years ago, the authors published their first paper on this topic [231], demonstrating the capabilities of laser processing of Borofloat 33 (BF33) glass while maintaining a surface roughness of $S_a < 1$ nm. They reported achieving a non-thermal ablation regime, in which material is removed at a rate of less than 1 nm per layer while preserving exceptional surface quality. The authors have established the numerical model based on the formulation in ref. [232], to predict the evolution of free-electron density and surface temperature during the interaction with multiple femtosecond laser pulses that are scanned across the BF33 sample surface. They then demonstrated that the main condition for achieving such a regime is maintaining the surface temperature between material softening and melting temperatures. In figure 7.7, part B, surface temperature dynamics when using two different fluence values are shown. When $F = 4.26$ J/cm^2, the peak temperature is higher than melting $T_m = 1923$ K, as a result, during the processing, the surface is heavily modified (see part (a) of the figure). Whereas, when $F = 2.76$ J/cm^2, the peak surface temperature is below that of

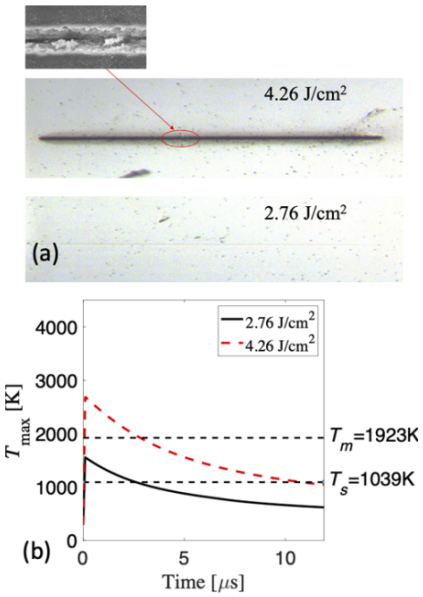


Fig. 7.7 (a) Microscopy images of line-scan-based processing, and (b) predicted surface temperature evolution for two laser fluences [231].

the melting and above the softening $T_m < T_{peak} < T_s$, resulting in an ablation regime, where the initial glass surface roughness is maintained. Facilitating on these findings, the authors have demonstrated the ability to form various structures on the surface, while maintaining the surface quality of $S_a < 1$ nm. One of such structures - the staircase is given in the figure 7.8. From the figure, it is evident that the authors have achieved precise control over the removed depth while maintaining surface roughness comparable to that of the glass before processing. Surprisingly, the authors managed to achieve the material removal without the formation of nanoripples, which was determined to be the limiting factor in achieving $S_a < 100$ nm (see chapter 4) when performing conventional laser ablation. It suggests that the formation of nanoripples might be heavily influenced by surface melting. Although the proposed non-thermal ablation regime enables the preservation of ultra-fine surface roughness ($S_a < 1$ nm), it also presents certain limitations. Authors have demonstrated that for the realization of this non-thermal regime, the scanning speed of $v = 1$ mm/s is required. To scan a 1x1 mm rectangle a single time, with a realistic scanning pitch of $dy = 5$ μm, would take 200 seconds. Ablating such a cavity to a practical depth of 10 μm (given an ablation rate of 0.6 nm per layer) would take

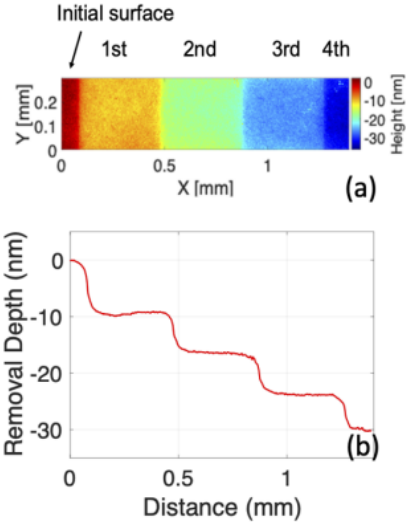


Fig. 7.8 (a) Surface profile of the staircase structure and (b) vertically integrated line profile [231].

approximately 925 hours, which is an unreasonably long duration. Furthermore, it is unclear whether this regime can be sustained when scanning to such depths, or if it would eventually break down. Additionally, the successful application of this regime on initially rough surfaces has not yet been demonstrated and may even prove infeasible. Despite the limitations, the authors continue exploring this regime and have already demonstrated its use for mid-spatial frequency error correction [233], micropisrm array formation [234], and formation of free form optics [235]. Furthermore, last year, they demonstrated the successful implementation of this regime on fused silica glass [236], demonstrating that the presented technique is not limited to a single material. Although this regime is still in an early stage of development - lacking a detailed understanding of the governing material removal mechanisms and requiring a significant increase in throughput for practical application - it demonstrates considerable promise.

Outlooks

With the main findings discussed and the literature reviewed, this brief chapter aims to put everything into perspective and outline potential directions for future endeavors.

The figure 7.9, part (a), provides a collected overview of attainable surface roughness values using different laser-based processes, including conventional laser ablation, non-thermal laser ablation, CW/pulsed laser polishing, fs burst polishing, and others. For better evaluation of the practical value of different processes, the material removal rates R_t were given when available. The relationship between the attainable surface roughness levels and the material removal rates R_t (for references when available) is given in part (b) of the figure. As data points are scattered, no strict correspondence between the two parameters can be derived. The overall trend shows that a higher material removal rate usually corresponds to higher surface roughness. This rough approximation holds true across several orders of magnitude. Focusing back onto the (a) part of the figure, we see that by utilizing different laser processes, the surface roughness levels spanning 6 order of magnitude can be obtained. The minimum roughness to date is achieved using non-thermal ablation [231]. However, while this novel approach offers exceptional S_a values ($S_a \sim 0.1 - 1$ nm), it can only be realized on surfaces with extremely low initial roughness ($S_a \sim 1-10$ nm), and its ablation rate is approximately seven orders of magnitude lower ($R_t \sim 10^{-7}$ mm^3/min) than that of conventional fs ablation, limiting its practical applicability. An order or two higher in magnitude roughness level ($S_a \sim 1 - 100$ nm) can be achieved utilizing laser polishing, using CW, pulsed or burst laser regimes [10, 222, 25]. Such a level of surface finish is still considered very good, as surfaces with such low roughness are typically already optically transparent, satisfying the requirements for most of optical components. The downside of laser polishing is that it can only be used as a

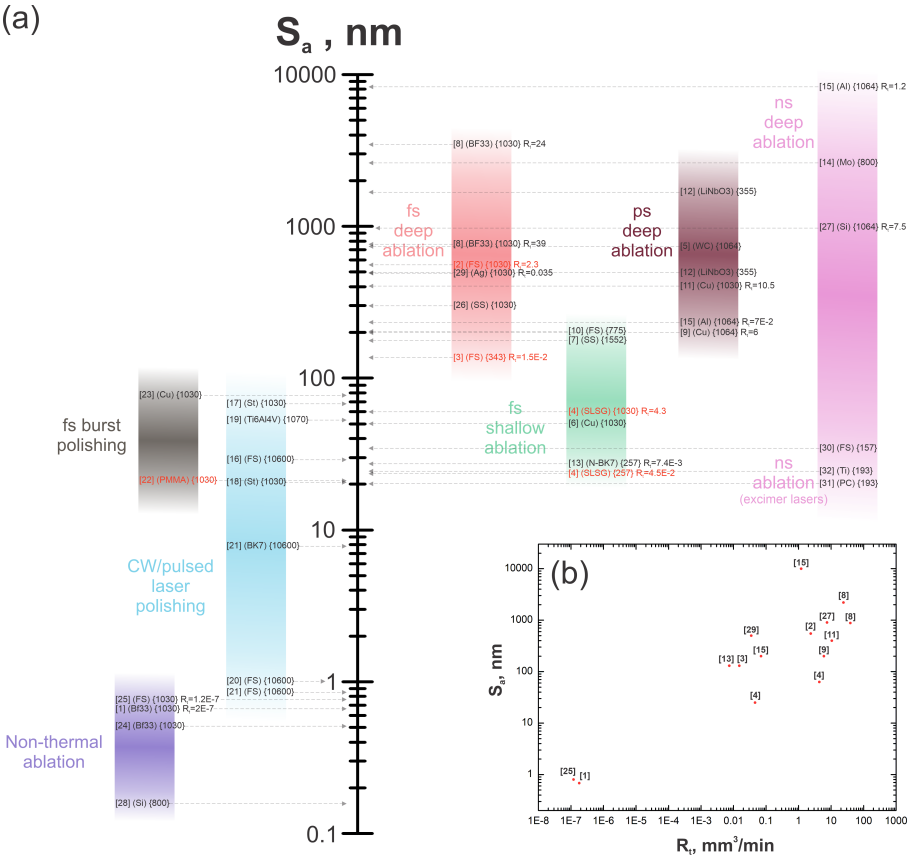


Fig. 7.9 Part (a) of the figure overviews the attainable surface roughness (S_a) levels when different laser processing techniques are used. Next to the reference from which the value is taken, additionally the processed material abbreviation, together with laser radiation wavelength (in nm) and ablation rate (in mm^3/min units), when available, are given. Red references correspond to the results achieved in this work. The part (b) of the figure plots the S_a dependence on material removal rate R_t from the references containing both values. 1 - [231]; 2 - [237]; 3- [36]; 4 - [66]; 5 -[35]; 6 - [172] ; 7 - [34]; 8 -[33]; 9 - [162]; 10 - [160]; 11 - [156]; 12 - [154]; 13 - [152] 14 - [148]; 15 - [147]; 16 - [10]; 17 - [217]; 18 - [26]; 19 - [218]; 20 - [221]; 21 - [222]; 22 - [25] 23 - [238]; 24 - [233]; 25 - [236]; 26 - [170]; 27 - [165]; 28 - [239]; 29 - [240]; 30 - [241]; 31 - [242]; 32 - [224]. FS- fused silica; SLSG - soda lime; BF33 - borofloat33; WC- tungsten carbide; Cu -copper; SS - stainless steel; Mo - Molybdenum; Al - Aluminum; St - steel; PMMA - hydrophilic acrylic polymer, Ag - silver, Ti - titanium, PC- polycarbonate.

post-process, since during such a procedure no material is removed from the surface. Furthermore, during the remelting of the surface, residual stresses may be induced making the material more prone to cracking [243]. Comparable level of roughness ($S_a \sim 20 - 50$ nm [66, 152]) can be achieved using shallow fs laser ablation (typically values for number of scans $N < 10$, resulting depth

$h < 2$ μm) and using UV laser radiation as laser source. The relatively low ablation rates ($R_t \sim 10^{-2} - 10^{-3}$ mm^3/min) and the limited achievable ablation depth constrain the applicability of this regime for full shape retrieval; however, it remains well suited for shallow ablation and fine surface roughening needs. Such level of roughness ($S_a \sim 20 - 40$ nm [241, 242, 224]) can also be achieved using nanosecond excimer lasers, owing to their short ultraviolet wavelengths ($\lambda \sim 100 - 300$ nm), which promote strong material absorption and enable precise surface modification. However, due to the need for complex high-pressure gas systems involving toxic and corrosive halogen mixtures, as well as significant maintenance requirements and gradual gas degradation, excimer lasers nowadays are being used less frequently and are increasingly being replaced by modern solid-state UV laser sources [144]. The most versatile and well-rounded regime to date remains laser ablation using ultrashort laser pulses (ps,fs). It enables the achievement of moderate surface roughness values in the range of $S_a \sim 100$–1000 nm [36, 33] without limitations on achievable depth. In addition, the reasonable ablation rates ($R_t \sim 10^{-2}$–10^2 mm^3/min) make the process practical, while the fine tunability of the resulting surface roughness demonstrated in this thesis further establishes this regime as a true "jack of all trades". With the advent and dominance of ultrashort laser processing, IR nanosecond laser ablation is used less frequently, primarily retained for the fabrication of surfaces, where high surface finish is not required ($S_a > 1000$ nm [148, 147]).

Regarding future prospects, it is evident that a rapid technological development further facilitates the need for surfaces with extremely low surface roughness levels ($S_a \lesssim 10$ nm) attainable at any depth and with much higher throughput ($R_t \gtrsim 10^2$ mm^3/min). While such conditions are currently unattainable using a single process, combining multiple processes (e.g., ultrashort laser ablation with CW or pulsed laser polishing) offers a close approximation. Considering the potential of future technologies, non-thermal ablation and ultrashort burst polishing demonstrate significant promise with the potential of becoming leading laser processing techniques. Regarding ultrashort laser ablation, the primary limitation in achieving lower roughness levels remains the formation of laser-induced periodic surface structures (LIPSS), also known as nanoripples. Solving that would open entirely new avenues for ultrashort laser processing. Additionally, the literature review and obtained results suggest that employing even shorter pulse durations together with shorter-wavelength UV

laser radiation could facilitate the achievement of lower roughness levels. In that sense, attosecond lasers, currently in the development state, show considerable promise. Finally, considering the throughput, adopting faster scanning systems - such as polygon scanners paired with higher laser repetition rates ($f_r \geq 2$ MHz) - could significantly improve processing speed, although this may also increase the risk of undesirable thermal effects. Additional increase in throughput could be achieved by utilizing full potential of high average laser power lasers by implementing beam splitting. While the most of named technological means are already present, their successful implementation is still yet to be achieved on an industrial scale.

The future shines as bright as it is smooth.

Main results and Conclusions

- It was demonstrated that during femtosecond laser ablation of dielectric materials the surface roughness is greatly determined by the overlap of the craters $\Omega_{x,y}$, with parameter values in the range of 10-25 % resulting in minimum surface roughness (here $Ra_x \sim 20$ nm). The tendency is maintained in single and multi scan regimes, when using different laser radiation wavelengths ($\lambda = 257 - 1030$ nm) and varying fluence values ($F = 4.6 - 24$ J/cm^2). Such $\Omega_{x,y}$ values result in minimal roughness, as under these conditions, ablation occurs only at the crater sidewalls, that exhibit significantly greater slopes than the nearly flat crater bottoms. The precise optimal $\Omega_{x,y}$ value is determined by the taper and overall geometry of the individual crater.

- It was demonstrated that the precise control ($\delta S_a = 20$ nm) of surface roughness over a broad range of roughness values ($\Delta S_a \approx 500$ nm) can be attained during multilayer femtosecond laser ablation of fused silica. This is achieved by stabilizing the S_a value through the implementation of the scanning strategies: rotation of the layers (where angle of rotation $\alpha = 73°$) and the displacement of the layers (with maximum displacement of $\Delta \geq dx$). The stabilized S_a level is further tuned by controlling the crater overlap and crater depth, where the former is achieved through the variations in fluence or laser wavelength.

- When performing femtosecond laser ablation of fused silica surfaces with varying initial roughness levels ($S_{q\_int} = 0.02 - 8.07$ μm), it was shown that, after prolonged engraving all surfaces converge to the same state corresponding identical S_q values. The evolution rates of S_q, along with the number of scans N required to reach the final state, depend on the initial spatial spectrum and roughness of the processed surfaces. This

is due to non-uniform amplitude decay coefficients of different spatial frequencies $k(f_r)$, with increased values at the high-frequency end of the spatial spectrum and reduced values at low frequencies.

- It was shown that the formation of high amplitude (PV $\gtrsim$ 3 μm), low spatial frequency ($f \lesssim 3$ mm^{-1}) features (HALSFF) observed in the laser deep engraving of fused silica using femtosecond pulses is governed by the laser pulse generated acoustic wave perturbation of the consecutive laser beam wavefront, resulting in the reduced local ablation rate ($\delta R_t \lesssim 5\%$). The formation of these features can be mitigated by fabricating cavities with shallow sidewalls ($\alpha \geq 45°$), which redirect laser-induced acoustic waves out of the processing region and prevent their interaction with subsequent laser pulses.

- It was demonstrated that bursts of femtosecond pulses (with intraburst repetition rate of 2.5 GHz) can be effectively used for polishing of acrylic polymer surfaces (from $R_a = 0.99$ μm down to $R_a \sim 20$ nm). The use of femtosecond GHz bursts enables the heating of the polymer surface to the optimal temperature ($T_{opt.} = 357$ C°), at which the surface effectively remelts and smoothens, without overheating.

Santrauka lietuvių kalba

Įvadas

Paviršiaus apdirbimas, siekiant išgauti formą arba pakeisti paviršiaus optines, chemines, mechanines ir kitas fizines savybes, išlieka paklausiu ir plačiai taikomu procesu pramonėje, bei skirtingose mokslinių tyrimų srityse. Apdirbamų paviršių mastelis svyruoja nuo mikrostruktūrų iki didelių plotų, užimančių kvadratinius metrus. Didžioji dalis šiuolaikinės pramonės vis dar yra paremta tradiciniais mechaniniais paviršiaus apdirbimo metodais, tokiais kaip CNC (kompiuterinio skaitmeninio valdymo) frezavimas, tekinimas, ar abrazyvinis poliravimas [1], nors sudėtingesnės technologijos, kaip cheminis apdorojimas, elektrocheminis poliravimas ar litografija, taip pat išlieka paklausios, tačiau mažesnėse ir labiau nišinėse srytise [2–4]. Pastaraisiais dešimtmečiais sparčiai tobulėjant lazerinėms technologijoms, lazerinė spinduliuotė tampa vis labiau patrauklia alternatyva įvairių medžiagų paviršiaus apdirbimui. Lyginant su tradiciniais metodais, lazerinis apdirbimas pasižymi didesniu tikslumu, universalumu, bei atsparumu įrankių devėjimuisi, kadangi tai yra nekontaktinis paviršiaus apdirbimo būdas [5]. Femtosekundinių lazerių išvystymas ir jų pritaikymas lazeriniam medžiagų apdirbimui suteikė papildomų privalumų. Naudojant juos pasiekiama aukštesnė formuojamų modifikacijų kontrolė, praplečiamas apdirbamų medžiagų spektras (pvz. skaidrios medžiagos), sumažinamos indukuojamų šilmos paveiktų zonų ribos ir kt. [6]. Femtosekundinė lazerinė abliacija plačiai taikoma medicinoje, mikrofluidikoje, MEMS bei mikrooptikoje [7–11], tiek paviršiaus modifikcaijai, tiek gilaus graviravimo poreikiams. Atlikus vos keletą lazerinių skenavimų, galima formuoti funkcinius paviršius, pasižyminčius antibakterinėmis ar atsparumo užšalimui savybėmis [12, 13]. Tuo tarpu selektyviai šalinant medžiagą sluoksnis po sluoksnio, formuojamos struktūros, kurių gylis siekia nuo šimtų nanometrų iki dešimčių milimetrų, taip

sukuriant sąlygas sudėtingų trimačių struktūrų kūrimui. Toks lazerinis graviravimas plačiai taikomas prabangos prekių pramonėje, pavyzdžiui, laikrodžių ir juvelyrinių dirbinių graviravimui [14], kur formuojamų struktūrų gylis dažnai viršija 100 μm [15]. Ši technologija taip pat naudojama sudėtingų, kompleksinės formos padėklų gamyboje, kurie vėliau naudojami formų liejime. Papildomi taikymai apima medicininių komponentų, įskaitant ortapedinių bei akių implantų, gamybą bei kt. [16, 17].

Formuojant sudėtingas geometrinės struktūras lazerinio apdirbimo būdu, lygiagrečiai yra veikiamas apdirbamos medžiagos paviršius, keičiant jo paviršiaus tekstūrą. Tokiu būdu suformuota paviršiaus tekstūra, kuri yra apibrėžiama kaip paviršiuje esančių edrvinių dažnių visuma [18], gali daryti įtaką daugeliui to paviršiaus savybių. Tyrimai rodo, kad paviršiaus šiurkštumas (apibrėžiamas, kaip aukštų erdvinių dažnių tekstūros sritis) turi įtakos paviršiaus biosuderinamumui [22], korozinėms, drėkinimo, bei kitoms nepaminėtoms paviršiaus paviršiaus savybėms [19–21]. Be to, pastebima, kad atskiri paviršiaus funkcionalumai yra realizuojami prie skirtingų paviršiaus šiurkštumo lygių. Pavyzdžiui, formuojant optinius elementus, svarbu, kad suformuotos struktūros šiurkštumas būtų minimalus, norint užtikrinti paviršiaus skaidrumą ir sumažinti sklaidos nuostolius [25]. Prabangos prekių sektoriuje vyrauja vienodas poreikis tiek blizgiems, tiek matiniams paviršiams, taip parodant, kad dominuoja paklausa ne tik lygiem bet ir šiurkštiems paviršiams [26]. Kitose srityse, tokiose kaip antibakterinių paviršių formavime, efektyviam paviršiaus funkcijos realizavimui reikalingas konkretus šiurkštumo lygis ($R_q \approx 400$ nm) [27]. Tuo tarpu didinant šilumos išskalaidymo spartą šilumokaičiuos būtinas kuo didesnis šiurkštumas ($R_a \gg 1$ μm) [28]. Panšus šiurkštumo lygis taip pat reikalingas gerinant paviršių tarpusavio sukibimą, bei dažų adheziją [29]. Platus skirtingų šiurkštumo lygių poreikis minėtiems taikymams pabrėžia gebėjimo tiksliai valdyti paviršiaus šiurkštumą svarbą bei poreikį. Be tikslios paviršiaus tekstūros kontrolės, lazerinio apdirbimo metu suformuoti paviršiai gali vygdyti savo funkciją netinkamai ir būti išbrokuoti.

Siekiant spręsti šį iššūkį, buvo atlikta daug tyrimų, nagrinėjančių kaip lazerio parametrai, tokie kaip energijos tankis, skenavimo greitis ar impulsų perklojimas, veikia galutinį paviršiaus šiurkštumą [30–32]. Papildomos įžvalgos buvo gautos tiriant, kaip paviršiaus šiurkštumas priklauso nuo lazerio pluošto skenavimo strategijos. Skenavimo algoritmai, įskaitant radialinį skenavimą, skenuojančių sluoksnių sukimą pasirinktu kampu, kiekvieno sekančio sluoksnio perstumimą

ir kt. [33–36] buvo ištestuoti ant plataus spektro medžiagų, siekiant ištirti jų daromą įtaką paviršiaus šiurkštumui. Vis dėlto, nepaisant didelio kiekio atliktų tyrimų, didžioji jų dalis nagrinėja paviršiaus šiurkštumą atliekant parametrinius tyrimus, apsiribojant siaura, juos dominančia parametrų erdve su pagrindiniu tikslu - nustatyti optimalius parametrus, o ne įgauti gilesnį supratimą apie patį šiurkštumo formavimąsi ir jo kitimą. To pasekoje, paviršiaus šiurkštumas vis dar yra interpretuojamas kaip baigtinis proceso rezultatas, apibrėžtas tiksliomis parametrų vertėmis, be gilesnio supratimo kaip jis buvo suformuotas ar kaip jį kontroliuoti. Be to, didžiojoje dalyje literatūros šiurkštumas yra vertinamas tik erdviniais parametrais, tokiais kaip R_a ar S_a, o naudoti filtrai atliekant erdvinio spektro filtravimą yra nutylimi. Dėl ko, tokia paviršiaus šiurkštumo analizė suteikia tik ribotą informaciją apie paviršiaus netolygumus, yra sunkiai palyginama bei gali būti netesingai interpretuojama. Vyraujančios šiurkštumo studijos, kurios apsiriboja tik parametriniais tyrimais, kartu su ribota paviršiaus tekstūros analize, lemia tai, kad fundamentiniai procesai, nulemiantys tekstūros ir šiurkštumo formavimąsi lazerinio apdirbimo metu vis dar yra nesuprasti. Atsižvelgiant į žinių stoką šioje srityje bei reguojant į vis didėjančius pramonės poreikius skirtingo šiurkštumo paviršių formavimui, būtina tobulinti paviršiaus šiurkštumo kontrolės galimybes lazerinio apdirbimo metu, bei plėsti supratimą apie vyraujančius fundamentinius, paviršiaus tekstūrą formuojančius procesus.

Darbo tikslas

Šis disertacinis darbas skirtas ištirti fizikinius procesus, lemiančius paviršiaus šiurkštumo formavimąsi ir paviršiaus tekstūros raidą lazerinio mikroapdirbimo metu, siekiant išvystyti metodus, kurie įgalintų tikslią šiurkštumo, bei tekstūros kontrolę.

Sprendžiami uždaviniai

- Ištirti paviršiaus šiurkštumo formavimąsi femtosekundinės lazerinės abliacijos metu, vieno ir daugelio skenavimų sąlygomis, nagrinėjant šiurkštumo raidą erdvinėje srityje bei atliekant spektrinę apdirbtų paviršių analizę.

- Ištirti paviršiaus šiurkštumo valdymo galimybes femtosekundinės lazerinės abliacijos metu, taikant integruotus metodus, apjungiančius skenavimo strategijų variacijas ir lazerinio apdirbimo parametrų koregavimą.
- Ištirti paviršiaus šiurkštumo raidą femtosekundinės lazerinės abliacijos metu, kai lazerinis apdirbimas atliekamas ant paviršių, turinčių skirtingą pradinį šiurkštumo lygį.

Mokslinis darbo naujumas

Ši disertacija pateikia naujų įžvalgų apie paviršiaus šiurkštumo bei tekstūros formavimąsi ir jų raidą femtosekundinės lazerinės abliacijos metu.

- Šioje disertacijoje, pirmą kartą pademonstruota tiksli paviršiaus šiurkštumo kontrolė daugiasluoksnės femtosekundinės abliacijos metu, pakartotinai, pagal poreikį padidinant bei sumažinant šiukštumo lygį giluminio graviravimo metu. Tai buvo pasiekta išvystant naujo tipo skenavimo strategijas, apjungiančias skirtingas skenavimo trajektorijas bei kintančius lazerio parametrus.
- Atliekant išsamų paviršiaus šiurkštumo evoliucijos lazerinio apdirbimo metu tyrimą, buvo nustatyta, kad mažiausią pasiekiamą paviršiaus šiurkštumo lygį sąlygojantis veiksnys yra lazerio indukuotų periodinių struktūrų neišvengiamas formavimasis.
- Šioje disertacijoje nuodugniai ištirta, iki šiol nežinota, pradinio paviršiaus šiurkštumo įtaka jo tolimesnei raidai daugiasluoksnės lazerinės abliacijos metu.
- Atliekant išsamią eksperimentinę ir skaitmeninę analizę, šios disertacijos metu buvo nustatytos, iki šiol nežinotos, aukštos amplitudės, žemo dažnio paviršiaus struktūrų (dar geriau žinomų kaip banguotumo) formavimosi priežastys daugiasluoksnės femtosekundinės abliacijos metu. Pademonstruota, kad šių struktūrų formavimasis yra nulemtas erdviškai selektyvia akustinių bangų sąveika su krintančia lazerine spinduliuote.

Praktinė darbo vertė

Disertacijos darbo metu sugeneruotos žinios ir sukurti metodai neša didelę praktinę vertę ir gali būti taikomi daugelyje sričių, tokiems tikslams kaip:

- Tikslaus paviršiaus šiurkštumo valdymo dėka galima formuoti paviršius, pasižyminčius skirtingomis skaidrumo savybėmis. Dėka aukšto lazerinio apdirbimo tikslumo galima tiksliai reguliuoti paviršiaus sklaidos ir pralaidumo balansą, taip formuojant difuzinius ir kitokio pobūdžio paviršius.
- Išvystyti paviršiaus šiurkštumo kontrolės metodai įgalina apdirbimo metu pasiekti norimą šiukštumo lygį, taip optimizuojant paviršių funkcines savybes (atsparumą bakterijų adhezijai ar biosuderinamumą), kurios pagal literaūrą, realizuojamos prie konkrečių šiukrštumo verčių.
- Tiksli paviršiaus šiurkštumo kontrolė įgalina erdviškai moduliuotą paviršiaus tekstūros modifikaciją. Tokiu būdu galima lokaliai padidinti paviršiaus adheziją pasirinktose paviršiaus vietose, bei sumažinti kitur. Praktiškai tai naudinga stiprinant sukibimą arba dangos adheziją tik tam tikrose vietose, tuo pačiu išlaikant mažą trintį arba didelį atsparumą užterštumui kitose srityse.
- Naudojant išvystytą paviršiaus šiurkštumo valdymą, gali būti įmanoma kurti vizualiai neatskiriamus paviršius, turinčius skirtingas šiluminio spinduliavimo savybes. Tokie paviršiai galėtų būt naudojami apsaugos nuo vagysčių srityje.

Ginamieji teiginiai

- Stiklų paviršiaus apdirbime, naudojant femtosekundinę lazerinę abliaciją, mažiausias paviršiaus šiurkštumas pasiekiamas išlaikant mažą kraterių perklojimo vertę, tipiškai apie $\Omega_{x,y} \sim 10 - 25\%$.
- Tikslus ($\delta S_a = 20$ nm) paviršiaus šiurkštumo valdymas plačiame verčių diapazone ($\Delta S_a \approx 500$ nm) gali būti pasiektas daugiasluoksnės femtosekundinės lazerinės abliacijos metu, taikant integruotus metodus, apjungiančius skenavimo strategijų (sluoksnių posūkio bei sluoksnių

postūmio) variacijas ir lazerinio apdirbimo parametrų (pažeidimų perklojimo $\Omega_{x,y}$, energijos tankio F bei spinduliuotės bangos ilgio λ) koregavimą.

- Paviršiaus šiurkštumo (S_q) raidos sparta femtosekundinės lazerinės abliacijos metu priklauso nuo pradinio paviršiaus erdvinio spektro, dėl nevienodų skirtingų erdvinių dažnių slopinimo koeficientų $k(f_r)$.

- Didelės amplitudės ($PV \gtrsim 3$ μm), žemo erdvinio dažnio ($f_r \leq 3$ mm^{-1}) struktūrų formavimasis giluminio graviravimo metu kyla dėl liekamųjų, pirminės lazerio ir medžiagos sąveikos metu indukuotų akustinių bangų sąveikos su sekančiais lazerio impulsais.

Trumpa pagrindinių rezultatų apžvalga

Pirmame skyriuje aprašomas tyrimas, kuriame nagrinėjama kaip kinta ir formuojasi paviršiaus šiurkštumas priklausomai nuo naudojamų skirtingų skenavimų strategijų, kai paviršius skenuojamas vieną kartą. Eksperimentai atliekami ant silikatinio stiklo, naudojant skirtingus energijos tankius ($F = 4.6 - 24$ J/cm^2) bei skirtingo bangos ilgio lazerinę spinduliuotę ($\lambda = 257 - 1030$ nm). Tiriamos skenavimo strategijos:

- Kintamas kraterių perklojimas Ω x ir y kryptimis.

- Linijų pozicionavimo neapibrėžtumas.

- Kas antros linijos poslinkis per fiksuotą atstumą.

Be atliekamų eksperimentų, pirmame skyriuje pristatomas disertacijos metu sukurtas lazerinės abliacijos skaitmeninis modelis. Modelis, remdamasis eksperimentiškai išmatuotais parametrais - lazerio pluošto skirstiniu bei pavienio pažeidimo geometrija, geba simuliuoti lazerinę paviršiaus abliaciją ir nuspėti galutinį paviršiaus šiurkštumą.

Tyrimo metu parodoma, kad pažeidimų persiklojimas $\Omega_{x,y}$ vienasluoksnės abliacijos metu daro didelę įtaką galutiniam paviršiaus šiurkštumui. Eksperimentiniai rezultatai ir skaitmeniniai modeliavimai atskleidžia, kad mažiausias paviršiaus šiurkštumas ($Ra_x \sim 20$ nm) pasiekamas, prie pažeidimų perklojimo vertės $\Omega = 16.6$ % (kai $F = 4.6$ J/cm^2, o $\lambda = 257$ nm). Toliau demonstruojama, kad naudojant kitus lazerio apdirbimo parametrus, gaunamos optimalios

pažeidimų perklojimo vertės, prie kurių pasiekiamas minimalus šiurkštumas, išlieka panašios - $\Omega_{opt.} = 10.8$ %, kai $F = 24$ J/cm^2, o $\lambda = 1030$ nm bei $\Omega_{opt.} = 23$ %, kai $F = 17.3$ J/cm^2, o $\lambda = 343$ nm. Gauti rezultatai rodo bendrą tendenciją, kad nepriklausomai nuo naudojamų lazerio parametrų, mažiausias paviršiaus šiurkštumas pasiekiamas, kai pažeidimų perklojimas yra $\Omega_{x,y} \sim 10 - 25$ % ribose. Toks pastebėjimas, aiškinamas tuom, kad perklojant kraterius nurodytose ribose, nuabliuojami tik statūs jų kraštai, o palyginti lygus dugnai lieka nepaveikti. Tai patvirtina suskaičiuotos kraterio sienelės ir diametro skersinių matmenų santykių $\Gamma = (\Delta r_{sw}/D) \times 100\%$ vertės, kurios koreliuoja su optimaliom kraterių perklojimo vertėmis (pvz. $\Gamma(F = 17.3$ J/cm^2, $\Omega = 343$nm) = 21.7 %, o $\Omega_{opt.}(F = 17.3$ J/cm^2, $\Omega = 343$nm) = 23 %). Tokiu būdu suformutoi paviršiai pasižymi mažiausiu šiurkštumu, o tiksli optimali kraterių perklojimo vertė $\Omega_{opt.}$ priklauso nuo kraterių sienelių statumo ir dugno plokštumo.

Toliau pirmajame skyriuje nagrinėjama kokią įtaką paviršiaus šiurkštumui turi lazerio ir skenavimo sistemos sinchronizacija. Esant sinchronizacijai - krateriai skenuojamame paviršiuje išdėstomi taisyklingai, tuo tarpu kai jos nėra, atsiranda atsitiktinis pirmo impulso eilutėje pozicijos neapibrėžtumas δ ribose ($\delta \in [0, dx]$), kur $dx = v/f$ yra kraterių skenavimo atstumas, apibrėžtas skenavimo greičio v ir lazerio pasikartojimo dažnio f. Parodoma, kad sinchronizacijos nebuvimas, gali nulemti tai, kad matuojamas paviršiaus šiurkštumas skirtingomis kryptimis Ra_x ir Ra_y bus skirtingas. Nustatyta, kad maksimalus skirtumas tarp skirtingomis kryptimis matuojamų šiukrštumo verčių gali siekti iki 37 % (pasiekta prie $\Omega_{x,y} = 5.4$ %).

Galiausiai, pirmame skyriuje apžvelgiama, kaip kinta paviršiaus šiurkštumas naudojant sąmoningą, kas antros eiltuės poslinkio (Δx_2 atstumu) skenavimo strategiją. Nustatyta, kad perslinkus lygines eilutes per dydį $\Delta x_2/dx \sim 0.5$, galima pasiekti papildomą paviršiaus šiurkštumo sumažinimą, siekiantį 20 % (nuo $Ra_x = 57$ nm iki $Ra_x = 45$ nm). Tai pasiekiama, nes perstūmus lygines eilutes nurodytu atstumu, realizuojamas šachmatų lentos skenavimo modelis, kurio metu efektyviai pašalinama, įprastai 4 kraterių sandūroje liekanti nepaveikta medžiagos dalis.

Antrame skyriuje nagrinėjama kokią įtaką paviršiaus šiukštumui daugesluoksnės abliacijos metu (kai paviršius skenuojamas daugiau nei vieną kartą $N \geq 1$) daro šios skenavimo strategijos:

- Kintamas kraterių perklojimas Ω x ir y kryptimis.
- Kiekvieno sekančio sluoksnio posūkis aplink jo centrinę ašį (kampu α).
- Kiekvieno sekančio sluoksnio atsitiktinis postūmis x ir y kryptimis, kur maksimalus galimas postūmis apibrėžiamas Δ parametru.

Be nurodytų skenavimo strategijų įtakos šiurkštumui nagrinėjimo, šiame skyriuje taip pat tyrinėjami metodai, kurie įgalintų tiksliai valdyti paviršiaus šiurkštumą giluminio graviravimo metu.

Tyrimo metu nustatoma, kad pasiekti šiurkštumo kontrolę, pirma būtina stabilizuoti, įprastai vis augantį širkštumo lygį (įvertinamą per S_a). Įprasto rastrinio skenavimo metu, nenaudojant pagalbinių skenavimo strategijų, formuojamos periodinės struktūros, kurių kontrastas (apibrėžiamas PV verte, kuri nurodo ablsoliutų skirtumą tarp mažiausios ir didžiausios paviršiaus verčių) auga su kiekvienu skenuojamu sluoksniu. Parodoma, kad šių struktūrų formavimą galima sustabdyti pritaikant sluoksnių posūkio (kampu $\alpha = 73°$) ir sluoksnių postūmio (kur $\Delta \geq dx$) skenavimo strategijas. Nustatyta, kad sluoksnių posūkio strategiją efektyviausiai stabdo periodinių struktūrų formavimąsi, kai posūkio kampas α yra ne 90° kartotinis (geriausiai tinkantys kampai $\alpha \in \mathbb{P}$,). Vis dėlto, dėl fiksuotos sukimosi ašies, pilnai pašalinti periodinių struktūrų formavimąsi vien su sluoksnių posūkiais nepavyksta. Pilnas šių struktūrų eliminavimas pasiekiamas, kai sluoksniai papildomai (kartu su jų centrine posūkio ašimi) yra perstumiami x ir y kryptimis atsitiktiniu atstumu, kur galima maksimali postūmio vertė $\Delta \geq dx$, čia dx atstumas tarp pavienių kraterių. Taikant šias strategijas, tikimybė skenuojant pozicionuoti lazerio pluoštą į tas pačias vietas kaip praeituose sluoksniuose yra sumažinama iki minimalios, ko pasekoje periodinių struktūrų formavimas yra eliminuojamas. Per pirmus 20-30 skenavimo sluoksnių (naudojant darbe nurodytus lazerinius parametrus) yra suformuojamas statistiškai stabilus ir atsikratojantis paviršius, kurio šiurkštumas toliau nebekinta - pasiekiama šiukrštumo lygio stabilizacija.

Toliau, antrame skyriuje pristatomi metodai, kaip galima keisti jau stabilizuoto šiurkštumo lygį. Pristatomi du metodai tam pasiekti - keičiant kraterių perklojimo vertę $\Omega_{x,y}$ bei pavienio kraterio gylį. Parodoma, kad keičiant $\Omega_{x,y}$ vertę galima derinti stabilizuoto šiukštumo lygi, o norint pasiekti mažiausią S_a vertę daugesluoksnės abliacijos metu, būtina naudoti kraterių perklojimo vertes $\Omega_{opt.} \sim 0-40$ % (palyginamos su $\Omega_{opt.}$ vertėmis, nustatytomis vienasluoksnės

abliacijos metu). Vis dėlto, šiukštumo derinimas keičiant Ω, gali būti gan grubus ($\delta S_a \sim 500$ nm, kai Ω kinta nuo 70 iki 80 %). Tikslesnis derinimas pasiekiamas varijuojant pavienių kraterių gyli bei išlaikant optimalų jų perklojimą. Kraterio gylio derinimas atliekamas keičiant energijos tankio F bei λ vertes. Tokiu būdu šiurkštumo stabilizacijos lygis gali būti derinamas labai tiksliai ($\delta S_a \sim 20$ nm).

Galiausiai, pademonstruojama, kad naudojant pristatytus metodus, galima tiksliai valdyti S_a vertę giluminio graviravimo metu. Graviruojant lydyto kvarco paviršių iki 800 μm gylio, S_a vertė buvo varijuojama tarp dviejų pasirinktų šiurkštumo lygių ($S_{a1} = 420$ nm bei $S_{a2} = 700$ nm). Proceso metu šiurkštumas buvo pakeistas (sumžinamas ar padidinamas) 6 kartus, demonstruojant galimybę tiksliai kontroliuoti paviršiaus šiurkštumą.

Trečiame skyriuje nagrinėjamas paviršiaus šiurkštumo kitimas daugesluoksnės abliacijos metu atliekant apdirbtų paviršių spektrinę analizę. Papildomai šiame skyriuje tiriama pradinio paviršiaus šiurkštumo įtaka tolimesnei jo raidai apdirbimo metu. Lazerinis apdirbimas atliekamas ant mechaniškai pašiaušių paviršių, kurių S_{q_int} vertės: 0.02 , 0.62, 1.64, 3.53, 8.07 μm.

Pradžioje nagrinėjama S_q evoliucija iš erdvinės bei spektrinės perspektyvos, kai lazerinis apdirbimas atliekamas ant $S_{q\_int} = 0.02$ μm. Nustatoma, kad S_q evoliucija turi 3 pagrindinius etapus - inicijaciją, stabilizaciją bei augimą. Inicijacijos metu (kai skenavimo skaičius $N < 10$), dėl stochastinės paviršiaus modifikacijos, naudojant praeitame skyriuje pristatytus metodus, yra formuojama paviršiaus tekstūra. Kai $N > 10$ (naudojant darbe pateiktus lazerinius parametrus), pasiekiamas statistiškai stabilus paviršius ir jo šiurkštumas toliau nebekinta. Prie didelių gylių (kai $N > 500$, o gylis $h \gtrsim 350$ μm) stebimas paviršiaus šiurkštumo augimo atsinaujinimas. Spektrinė analizė atskleidžia, kad toks S_q augimas yra nulemtas aukštos maplitudės (PV $\gtrsim 3$ mm^{-1}), žemo dažnio ($f_r \lesssim 3$ mm^{-1}) struktūrų formavimosi (dar kitaip vadinamo - banguotumu), kuris pasireiškia tik prie didelių graviravimo gylių.

Toliau tyrimas tęsiamas atliekant lazerinį apdirbimą ant paviršių su kitais pradinio šiurkštumo lygiais (S_{q_int} - 0.62, 1.64, 3.53, 8.07 μm). Nustatoma, kad lazerinis graviravimas keičia pradinę paviršių tekstūrą taip, kad po prailginto apdirbimo ji supanašėja su bazine paviršiaus tekstūra, kuri pasiekiama kai apdirbimas atliekamas ant lygaus paviršiaus. Stebima, kad sluoksnių skaičius, reikalingas pasiekti bazinę paviršiaus tekstūrą, priklauso nuo pradinės medžiagos S_{q_int} vertės ir pradinio paviršiaus erdvinio spektro. Kuo didesnė S_{q_int} vertė, tuo daugiau sluoksnių reikia skenuoti paviršių, norint pasiekti bazinę paviršiaus

tekstūros būseną (pvž. paviršiui su S_{q_int} = 0.62 μm, reikia N = 32, tuo tarpu S_{q_int} = 1.64 μm, reikia N = 512). Spektrinė analizė atskleidžia, kad lazerinis apdirbimas keičia visų erdvinių dažnių amplitudes, bet jų kitimo spartos yra nevienodos ir priklauso nuo tikslios erdvinio dažnio vertės f_r. Stebima, kad dažnio amplitudės slopinimo koeficientas $k(f_r)$ yra didesnis aukštiems dažniams ($k(200\ mm^{-1}) = 0.74$) ir mažesnis - žemiems ($k(10\ mm^{-1}) = 0.01$). Tai paaiškina, kodėl paviršiaus, kurio pradinę tekstūrą sudaro daug žemų dažnių, S_q evoliucija yra lėta, o paviršiaus, kurio pradinėje tekstūroje dominuoja aukšti dažniai, S_q raida yra sparti.

Ketvirtame skyriuje plačiau tiriamas trečiajame skyriuje pastebėtas aukštos amplitudės (PV $\gtrsim$ 3 mm^{-1}), žemo dažnio ($f_r \lesssim$ 3 mm^{-1}) paviršiaus struktūrų formavimasis giluminio graviravimo sąlygomis. Papildomai, šio skyrio rėmuose, sukuriamas skaitmeninis, lazerio indukuotų akustinių bangų sklidimą nagrinėjantis modelis. Tyrimas atliekamas pradžioje nustatant tikslias eksperimentines sąlygas (lazerio parametrus ir kt.), kuriomis formuojasi šios struktūros. Vėliau remiantis eksperimentiniais rezultatais ir skaitmeniniais modeliavimais nustatomos šių struktūrų formavimosi priežastys.

Eksperimentiniai tyrimai atskleidžia, kad šių struktūrų formavimuisi būtinos šios sąlygos: aukštas energijos tankis ($F \gtrsim$ 6.8 J/cm^2), stačios (kampas tarp vertikalės ir sienelės $\alpha \sim 10°$) graviruojamos struktūros sienelės (paaiškina, kodėl efektas stebimas tik giluminio graviravimo metu) bei aukštas lazerio pasikartojimo dažnis ($f \geq$ 33 kHz). Toliau demonstruojama, kad formuojamų struktūrų periodas ir forma yra tiesiogiai nulemiami graviruojamos struktūros kontūro, bei matmenų. Graviruojant kvadaratinio kontūro plotą, fiksuojamas aukštos amplitudės, žemo dažnio gardelės formos struktūrų formavimasis, su sienelėm lygiagrečiais vieną kitą kertančiais paviršiaus iškilimais. Pastebimas, fiksuotų skersinių matmenų sąryšis tarp pirmo periodinės struktūros maksimumo ir struktūros sienelės (atstumas tarp šių paviršiaus dalių - 1.78 mm). Toliau, nagrinėjant kaip šios paviršiaus struktūros priklauso nuo pažeidimų perklojimo Ω, nustatyta, kad nepriklausomai nuo Ω vertės, šios struktūros formuojasi visais atvejais, išlaikant identišką formą. Vis dėlto, atkreipiama dėmesį, kad prie didesnių pažeidimų perklojimo verčių (Ω = 60 %), pagrindinė struktūros forma išlaikoma, bet stebimi jos išdarkymai, indikuojantys apie padidėjusį paviršiaus šiurkštumą. Išmatuotos šiurkštumo vertės tą patvirtina ($S_q(N_{ic} = 2.5\ \text{mm}^{-1}) =$ 0.835 μm prie Ω = 10 %, o prie Ω = 60 %, $S_q(N_{ic} = 2.5\ \text{mm}^{-1}) = 1.075\ \mu$m).

Toliau ketvirtame skyriuje, naudojantis sukurtu skaitmeniniu modeliu, įvertinamas liekamojo akustinio lauko pasiskirstymas virš apdirbamos erdvės tuo momentu, kai atkeliauja sekantis lazerinis impulsas. Palyginus eksperimentiškai suformuotas aukštos amplitudės, žemo dažnio struktūras su skaitmeniniais modeliavimais sukuriama šio reiškinio kilmės hipotezė. Indukuotų struktūrų maksimumai sutampa su modelivimuose stebimais akustinių bangų indukuotais erdviškai ribotais slėgio padidėjimais. Tai sufleruoja, kad lazerio pluoštas sklisdamas per padidėjusio slėgio erdvę (su pakitusiu lužio rodikliu per $\Delta n \approx 10^{-5} - 10^{-3}$), patiria lokalius bangos fronto iškraipymus, dėl ko abliacijos sparta lokaliai sumažėja (įvertintas spartos sumažėjimas per $\delta R_t \leq 5$ %). Tokiu būdu per daugelį skenavimų ($N \gtrsim 500$), paviršiaus vietose, kuriose vyksta šis reiškinys, pašalinama mažiau medžiagos, ko pasekoje stebimi iškilimai.

Toliau, skyriuje pateikiami metodai, kaip išvengti šių, paviršiaus S_q vertę didinančių, struktūrų formavimosi. Pristatomi du būdai. Pirmas būdas - vygdyti paviršių apdirbimą stipirai sumažinus lazerio pasikartojimo dažnį ($f < 30$ kHz). Tokiu būdų iki atvykstant sekančiam lazerio impulsui, akustinės bangos spėja pasišalinti iš apdirbamo paviršiaus, ko pasekoje pluoštų bangos frontai nėra darkomi. Vis dėlto, toks būdas stipriai prailgina apdirbimo trukmę (bent 2.5 kartų). Kitas metodas paremtas struktūrų su nuožulniomis kraštinėmis formavimu (kur kampas tarp vertikalės ir kraštinės $\alpha > 45$). Šiuo atveju, dėl nuožulnios kraštinės, atsispindėjusios akustinės bangos nukreipiamos už apdirbamos zonos ribų, dėl ko pluoštų darkymas taip pat nevyksta. Pademonstruota, kad naudojantis šia prevencine strategija, galima sumažinti galutinę paviršiaus S_q vertę 10 kartų ($S_q = 5.66$ μm, kai $\alpha - 14°$, tuo tarpu kai $\alpha - 58°$, $S_q = 0.58$ μm).

Penktame skyriuje apžvelgiami femtosekundinei abliacijai alterantyvus lazeriniai procesai, kuriu metu galimas paviršiaus šiurkštumo keitimas. Ši apžvalga leidžia disertacijos metu pasiektus rezultatus palyginti platesniame kontekste.

Skyrius pradedamas pristatant lazerinio poliravimo technologiją. Jos metu, pasitelkiant lazerinę spinduliuotę, perlydomas medžiagos paviršių, o lydalas, veikiamas paviršiaus įtempimo jėgų pasiskirsto po paviršių, taip efektyviai sumažinant paviršiaus šiurkštumą. Šiam tikslui naudojami tiek nuolatinės veikos (kaip CO2), tiek impulsiniai (ilgų impulso trukmių $\tau \sim ns$, pvž. Nd:YAG) lazeriai. Šiuo metodu pasiekimos žemos šiurkštumo vertė ($S_a = 10 - 100$ nm), tačiau jo metu medžiaga nuo paviršiaus nėra pašalinama, todėl jis nėra

tinkamas struktūrų formavimui ir gali būti taikomas tik kaip antrinis procesas, tolimesniam paviršiaus šiurkštumo kitimui.

Toliau penktame skyriuje pristatomas lazerinio poliravimo metodas pasitelkiant Ghz (2.5 GHz) femtosekundines papliūpas. Tai toks lazerio operavimo režimas, kada pavieniai femtosekundiniai impulsai yra išskaidomi į vorą sub-impulsų, kurių suintegruota energija atitinka pirminio impulso energiją. Lazerinis poliravimas naudojant GHz papliūpas atliekamas ant akrilinio polimero paviršių, kurie prieš tai buvo pašiaušti naudojant įprastinę femtosekundinę abliaciją iki $R_a \sim 1$ μm lygio. Poliravimo, pasirinktuoju metodu, galimybių ribos buvo tiriamos atliekant parametrinį tyrimą, kur keičiami šie parametrai: vidutinė galia P, skenavimo greitis v, skenuojamų linijų atstumas dy bei sub-impulsų papliūpoje skaičius N_p. Nustatyta, kad parinkus tinkamus lazerio parametrus, įmanomą sumažinti galutinį paviršiaus šiurkštumą iki $R_a \sim 20$ nm (kai parametrai $P = 16$ W, $dy = 10$ μm, $v = 700$ mm/s, o $N_p = 3$). Stebint atliekamus eksperimentus su termovizoriumi, pastebėta, kad poliravimo efektyvumas priklauso nuo gebėjimo užkelti paviršiaus temperatūrą iki optimalios temperatūros (šiai medžiagai - $T_{opt.} = 360\ ^\circ C$), kada vyksta paviršiaus perlydymas, jo neperkaitinant.

Galiausiai, skyriuje apžvelgiama neterminės abliacijos technologija, kurios metu įmanoma vygdyti abliaciją, išlaikant ypač mažą paviršiaus širukštumą ($S_a < 1$ nm). Apžvelgtų šaltinių autoriai nurodo, kad šis režimas pasiekiamas, kaitinant paviršių iki temperatūros, kuri yra aukštesnė nei medžiagos mikštėjimo, bet neviršyja medžiagos lydymosi temperatūros $T_M < T < T_L$. Technologijos sėkmingas pritaikymas pademonstruotas ant BF33 ir FS stiklų. Pažymima, kad dirbant tokiame režime, nors ir išlaikomas idealus paviršiaus šiurkštumas, abliacijos sparta yra ypač maža ($R_t \sim 10^{-7}$ mm^3/min), ko pasekoje, toks paviršiaus apdirbimas yra nepraktiškas. Taip pat atkreipiama dėmėsį į tai, kad po kol kas šio metodo veiksmingumas buvo pademonstruotas tik ant paviršių, su ypač mažu pradiniu paviršiaus šiurkštumu ($S_{q\_int} \lesssim 10$ nm).

Pagrindiniai rezultatai ir išvados

- Buvo nustatyta, kad dielektrinių medžiagų apdirbimo metu, naudojant femtosekundinius lazerinius impulsus, gautas paviršiaus šiurkštumas stipriai priklauso nuo pažeidimų perklojimo $\Omega_{x,y}$, o mažiausio šiurkštumo paviršiai pasiekiami, kai $\Omega_{x,y} \sim 10 - 25$ %. Ši tendencija buvo stebima vieno bei daugelio sluoksnių apdirbimo metu, naudojant skirtingus bangos ilgius ($\lambda = 257 - 1030$ nm), bei energijos tankio vertes ($F = 4.6 - 24$ J/cm^2). Šios perklojimo vertės leidžia formuoti mažiausio šiurkštumo paviršius dėl to, kad perklojant kraterius tokiose ribose, yra pašalinamos tik palyginamai stačios kraterių kraštines, o lygus dugnai išlieka nepaveikti. Tiksli optimali perklojimo vertė $\Omega_{opt.}$ priklauso nuo pavienio pažeidimo geometrijos, ypač nuo jo sienelių statumo.

- Daugesluoksnės abliacijos metu pademonstruota tiksli ($\delta S_a = 20$ nm) paviršiaus šiurkštumo kontrolė plačiame verčių diapazone ($\Delta S_a \approx 500$ nm). Tai pasiekiama stabilizuojant paviršiaus S_a vertę pasitelkiant kombinuotas skenavimo strategijas - sluoksnių posūkį (kur posūkio kampas $\alpha = 73°$) bei sluoksnių postūmį (su maksimalia postūmio verte $\Delta \geq dx$). Stabilizuota S_a vertė toliau derinama keičiant pažeidimų perklojimą $\Omega_{opt.}$ bei pavienio pažeidimo gylį, kur šio kitimas realizuojamas varijuojant energijos tankį F arba lazerinės spinduliuotės bangos ilgį λ.

- Taikant femtosekundinę lazerinę abliaciją ant paviršiu su skirtingu pradiniu šiurkštumo lygiu ($S_{q\_int} = 0.02 - 8.07$ μm), buvo pademonstruota, kad nepriklausomai nuo pradinio paviršiaus širukštumo, ilgo lazerinio apdirbimo metu, visi paviršiai konverguoja į vienodos tekstūros ir S_q vertės bazinę būseną. S_q vertės kitimo sparta bei reikalingas sluoksnių skaičius iki kol pasiekiama bazinė būsena priklauso nuo pradinio paviršiaus erdinio spektro bei S_{q_int} vertės. Tą sąlygoja nevienodas, skirtingų erdinių dažnių, amplitudės atenuacijos koeficientas, kuris yra didesnis aukštiems dažniams bei mažesnis - žemiems.

- Pademonstruota, kad aukštos amplitudės (PV $\gtrsim 3$ μm), žemo dažnio ($f \lesssim 3$ mm^{-1}) erdvinių struktūrų formavimasis giluminio graviravimo metu yra nulemtas lazerio ir medžiagos sąveikos metu indukuotų akustinių bangų sekančių lazerinių impulsų darkymų, dėl ko lokaliai sumažinama abliacijos sparta ($\delta R_t \lesssim 5\%$). To galima išvengti formuojant apdirbamas

struktūras su nuožulniom kraštinėm ($\alpha \geq 45°$). Tokiu atveju, lazerio indukuotos akustinės bangos yra nukreipiamos už apdirbamo ploto ribų, eliminuojant jų sąveiką su sekančiais lazeriniais impulsais.

- Buvo pademonstruota, kad femtosekundinės papliūpos (su papliūpos dažniu - 2.5 GHz) gali būti naudojamos efektyviam akrilinių polimerų paviršiaus poliravimui (sumažinant šiurkštumą nuo $R_a = 0.99$ μm iki $R_a \sim 20$ nm). GHz papliūpu naudojimas įgalina polimero paviršiaus kaitinimą iki optimalios temperatūros ($T_{opt.} = 357$ C°), kada paviršius yra efektyviai perlydomas ir išlyginamas, be papildomo perkaitinimo.

BIBLIOGRAPHY

[1] I. Okokpujie, C. Bolu, O. Ohunakin, E. Akinlabi, D. Adelekan, A review of recent application of machining techniques, based on the phenomena of CNC machining operations, Procedia Manuf. **35**, 1054–1060 (2019).

[2] C. Hsu, F. Chang, Y. Huang, Surface machining of stainless steel cardiovascular stents by fluid abrasive machining and electropolishing, Key Eng. Mater. **897**, 3–13 (2021).

[3] C. Baley, F. Busnel, Y. Grohens, O. Sire, Influence of chemical treatments on surface properties and adhesion of flax fibre–polyester resin, Compos. - A: Appl. Sci. Manuf. **37**(10), 1626–1637 (2006).

[4] M. Colburn, T. Bailey, B. Choi, J. Ekerdt, S. V. Sreenivasan, C. Willson, Development and advantages of step-and-flash lithography, Solid State Technol. **44**(7) (2001).

[5] N. Ahmed, S. Darwish, A. M. Alahmari, Laser ablation and laser-hybrid ablation processes: A review, Mater. Manuf. Process **31**(9), 1121–1142 (2016).

[6] A. H. Hamad, Effects of different laser pulse regimes (nanosecond, picosecond and femtosecond) on the ablation of, High energy and short pulse lasers 303 (2016).

[7] D. Gomez, I. Goenaga, I. Lizuain, M. Ozaita, Femtosecond laser ablation for microfluidics, Optical Engineering **44**, 1105– (2005).

[8] J. Linden, N. Melech, I. Sakaev, O. Fogel, S. Krylov, D. Nuttman, Z. Zalevsky, M. Sirota, Femtosecond laser-assisted fabrication of piezoelectrically actuated crystalline quartz-based mems resonators, Microsystems & Nanoengineering **9**(1), 38 (2023).

[9] J.-G. Hua, S.-Y. Liang, Q.-D. Chen, S. Juodkazis, H.-B. Sun, Free-form micro-optics out of crystals: Femtosecond laser 3d sculpturing, Advanced Functional Materials **32**(26), 2200255 (2022).

[10] L. Zubauskas, E. Markauskas, A. Vyšniauskas, V. Stankevič, P. Gečys, Comparative analysis of microlens array formation in fused silica glass by laser: Femtosecond versus picosecond pulses, Journal of Science: Advanced Materials and Devices **9**(4), 100804 (2024).

[11] D. Stonyte, V. Jukna, I. Lukosiunas, P. Zakarauskas, H.-H. Huang, T. Katkus, N. Zheng, N. H. A. Le, S. Juodkazis, D. Gailevicius, et al., Four-level diffractive photon sieves by deep-uv femtosecond laser ablation, Optics Express **32**(24), 43102–43117 (2024).

[12] S.-j. Li, L.-p. Kong, Y.-c. Liu, Y.-z. Huang, K. Chen, Y.-c. Li, J.-h. Qiao, H.-t. Liu, Y. Luo, X.-W. Li, et al., Uv laser-ablated cu superwetting surface with improved anti-icing and antibacterial properties, Colloids and Surfaces A: Physicochemical and Engineering Aspects **639**, 128282 (2022).

[13] A. H. A. Lutey, L. Gemini, L. Romoli, G. Lazzini, F. Fuso, M. Faucon, R. Kling, Towards laser-textured antibacterial surfaces, Scientific Reports **8**(1), 10112 (2018).

[14] P. Khatami, S. F. Nabavi, A. Farshidianfar, A comprehensive review of laser marking: an in-depth exploration of processes, methods, parameters, materials, and applications, Welding in the World **69**(11), 3415–3442 (2025).

[15] D. Pallarés-Aldeiturriaga, P. Claudel, J. Granier, J. Travers, L. Guillermin, M.-O. Flaissier, P. B. d'Augeres, X. Sedao, Femtosecond laser engraving of deep patterns in steel and sapphire, Micromachines **12**(7) (2021).

[16] F. Agalianos, S. Patelis, P. Kyratsis, E. Maravelakis, E. Vasarmidis, A. Antoniadis, Industrial applications of laser engraving: influence of the process parameters on machined surface quality, World Academy of Science, Engineering and Technology **59**, 1242–1245 (2011).

[17] S. Pattanayak, A. K. Sahoo, R. Routray, S. K. Sahoo, Micro engraving on ti-6al-4v using fiber laser for orthopedic implant-a study, Optical Fiber Technology **67**, 102745 (2021).

[18] D. J. Whitehouse, *Surfaces and their Measurement* (CRC Press, 2002).

[19] T. Hong, M. Nagumo, Effect of surface roughness on early stages of pitting corrosion of type 301 stainless steel, Corrosion Science **39**(9), 1665–1672 (1997).

[20] W. Li, D. Li, Influence of surface morphology on corrosion and electronic behavior, Acta Materialia **54**(2), 445–452 (2006).

[21] K. Kubiak, M. Wilson, T. Mathia, P. Carval, Wettability versus roughness of engineering surfaces, Wear **271**(3), 523–528, the 12th International Conference on Metrology and Properties of Engineering Surfaces (2011).

[22] M. M. Hatamleh, X. Wu, A. Alnazzawi, J. Watson, D. Watts, Surface characteristics and biocompatibility of cranioplasty titanium implants following different surface treatments, Dental Materials **34**(4), 676–683 (2018).

[23] M. Auinger, P. Ebbinghaus, A. Blümich, A. Erbe, Effect of surface roughness on optical heating of metals, J. Eur. Opt. Soc. **9** (2014).

[24] J. Jiang, R. Arnell, The effect of substrate surface roughness on the wear of dlc coatings, Wear **239**(1), 1–9 (2000).

[25] E. Kažukauskas, S. Butkus, P. Tokarski, V. Jukna, M. Barkauskas, V. Sirutkaitis, Micromachining of transparent biocompatible polymers applied in medicine using bursts of femtosecond laser pulses, Micromachines **11**(12) (2020).

[26] A. Temmler, E. Willenborg, K. Wissenbach, Laser polishing, in *Laser applications in microelectronic and optoelectronic manufacturing (LAMOM) XVII* (SPIE, 2012), volume 8243, 171–183.

[27] M. Mu, S. Liu, W. DeFlorio, L. Hao, X. Wang, K. S. Salazar, M. Taylor, A. Castillo, L. Cisneros-Zevallos, J. K. Oh, Y. Min, M. Akbulut, Influence of surface roughness, nanostructure, and wetting on bacterial adhesion, Langmuir **39**(15), 5426–5439 (2023).

[28] Y. You, B. Zhang, S. Tao, Z. Liang, B. Tang, R. Zhou, D. Yuan, Effect of surface microstructure on the heat dissipation performance of heat sinks used in electronic devices, Micromachines **12**(3) (2021).

[29] C. Söğütlü, P. Nzokou, I. Koc, R. Tutgun, N. Döngel, The effects of surface roughness on varnish adhesion strength of wood materials, Journal of Coatings Technology and Research **13**(5), 863–870 (2016).

[30] A. Mohammad, M. K. Mohammed, A. M. Alahmari, Effect of laser ablation parameters on surface improvement of electron beam melted parts, The International Journal of Advanced Manufacturing Technology **87**(1), 1033–1044 (2016).

[31] M. N. F. B. Haron, F. R. B. M. Romlay, Parametric study of laser engraving process of AISI 304 stainless steel by utilizing fiber laser system, IOP Conf. Ser.: Mater. Sci. Eng. **469**(1), 012124 (2019).

[32] S. Campanelli, G. Casalino, N. Contuzzi, A. Ludovico, Taguchi optimization of the surface finish obtained by laser ablation on selective laser molten steel parts, Procedia CIRP **12**, 462–467 (2013).

[33] K. L. Wlodarczyk, J. Schille, L. Naumann, A. A. Lopes, I. Bitharas, P. Bidare, S. D. Dondieu, P. Blair, U. Loeschner, A. J. Moore, M. Mercedes Maroto-Valer, D. P. Hand, Investigation of an interlaced laser beam scanning method for ultrashort pulse laser micromachining applications, Journal of Materials Processing Technology **285**, 116807 (2020).

[34] L. Romoli, Flattening of surface roughness in ultrashort pulsed laser micromilling, Precision Engineering **51**, 331–337 (2018).

[35] C. Daniel, J. Manderla, S. Hallmann, C. Emmelmann, Influence of an angular hatching exposure strategy on the surface roughness during picosecond laser ablation of hard materials, Physics procedia **83**, 135–146 (2016).

[36] E. Kažukauskas, S. Butkus, V. Jukna, D. Paipulas, Surface roughness control in deep engraving of fused silica using femtosecond laser ablation, Surfaces and Interfaces **50**, 104471 (2024).

[37] R. Walter, B. K. Mathan, Influence of surface roughness on the corrosion behaviour of magnesium alloy, Materials Design - MATER DESIGN **32**, 2350–2354 (2011).

[38] M. Cabrini, A. Cigada, G. Rondell, B. Vicentini, Effect of different surface finishing and of hydroxyapatite coatings on passive and corrosion current of ti6al4v alloy in simulated physiological solution, Biomaterials **18**(11), 783–787 (1997).

[39] R. N. Wenzel, Resistance of solid surfaces to wetting by water, Industrial & Engineering Chemistry **28**(8), 988–994 (1936).

[40] A. Cassie, S. Baxter, Wettability of porous surfaces, Transactions of the Faraday society **40**, 546–551 (1944).

[41] L. Ponsonnet, K. Reybier, N. Jaffrezic, V. Comte, C. Lagneau, M. Lissac, C. Martelet, Relationship between surface properties (roughness, wettability) of titanium and titanium alloys and cell behaviour, Materials Science and Engineering: C **23**(4), 551–560 (2003).

[42] C. N. Elias, Y. Oshida, J. H. C. Lima, C. A. Muller, Relationship between surface properties (roughness, wettability and morphology) of titanium and dental implant removal torque, Journal of the Mechanical Behavior of Biomedical Materials **1**(3), 234–242, biological Materials Science (2008).

[43] U. Ulusoy, M. Yekeler, Correlation of the surface roughness of some industrial minerals with their wettability parameters, Chemical Engineering and Processing: Process Intensification **44**(5), 555–563 (2005).

[44] P. Spijker, G. Anciaux, J.-F. Molinari, Relations between roughness, temperature and dry sliding friction at the atomic scale, Tribology International **59**, 222–229, eNERGY AND HEALTH (2013).

[45] S. Tomlinson, R. Lewis, M. Carré, The effect of normal force and roughness on friction in human finger contact, Wear **267**(5), 1311–1318, 17th International Conference on Wear of Materials (2009).

[46] L. Skedung, K. Danerlöv, U. Olofsson, C. Michael Johannesson, M. Aikala, J. Kettle, M. Arvidsson, B. Berglund, M. W. Rutland, Tactile perception: Finger friction, surface roughness and perceived coarseness, Tribology International **44**(5), 505–512, special Issue: ECOTRIB 2009 (2011).

[47] C. Hendriks, S. Franklin, Influence of surface roughness, material and climate conditions on the friction of human skin, Tribology Letters **37**, 361–373 (2009).

[48] Y. Bellouard, A. A. Said, M. Dugan, P. Bado, High strength fused silica flexures manufactured by femtosecond laser, in *Commercial and Biomedical Applications of Ultrafast Lasers IX* (SPIE, 2009), volume 7203, 84–91.

[49] W. Grzesik, Prediction of the functional performance of machined components based on surface topography: State of the art, Journal of Materials Engineering and Performance **25**(10), 4460–4468 (2016).

[50] D. Bergström, J. Powell, A. F. Kaplan, The absorption of laser light by rough metal surfaces, J. Appl. Phys. **103**(10), 103515 (2008).

[51] N. Pinel, B. Christophe, J. Saillard, Degree of roughness of rough layers: Extensions of the rayleigh roughness criterion and some applications, Progress In Electromagnetics Research B **19**, 41–63 (2010).

[52] S. Butkus, V. Jukna, E. Kažukauskas, Ž. Svirksas, D. Paipulas, V. Sirutkaitis, High-Contrast marking of Stainless-Steel using bursts of femtosecond laser pulses, Micromachines (Basel) **14**(1) (2023).

[53] K. A. Barth, J. D. Waterfield, D. M. Brunette, The effect of surface roughness on raw 264.7 macrophage phenotype, Journal of Biomedical Materials Research Part A **101A**(9), 2679–2688 (2013).

[54] M. Hatamleh, X. Wu, A. Alnazzawi, J. Watson, D. Watts, Surface characteristics and biocompatibility of cranioplasty titanium implants following different surface treatments, Dental materials : official publication of the Academy of Dental Materials **34** (2018).

[55] L. Le Guéhennec, A. Soueidan, P. Layrolle, Y. Amouriq, Surface treatments of titanium dental implants for rapid osseointegration, Dental Materials **23**(7), 844–854 (2007).

[56] T. Silva, D. Cantarelli Machado, C. Viezzer, A. Júnior, M. Oliveira, Effect of titanium surface roughness on human bone marrow cell proliferation and differentiation. an experimental study, Acta cirúrgica brasileira / Sociedade Brasileira para Desenvolvimento Pesquisa em Cirurgia **24**, 200–5 (2009).

[57] R. Mukherjee, K. Chaudhury, S. Das, S. Sengupta, P. Biswas, Posterior capsular opacification and intraocular lens surface micro-roughness characteristics: an atomic force microscopy study., Micron **43 9**, 937–47 (2012).

[58] M. Lombardo, M. P. De Santo, G. Lombardo, R. Barberi, S. Serrao, Analysis of intraocular lens surface properties with atomic force microscopy, J Cataract Refract Surg **32**(8), 1378–1384 (2006).

[59] O. Nishi, K. Nishi, Y. Osakabe, Effect of intraocular lenses on preventing posterior capsule opacification: design versus material, J Cataract Refract Surg **30**(10), 2170–2176 (2004).

[60] E. Abbott, F. Firestone, Specifying surface quality—a method on accurate measurement and comparison, Mechanical Engineering ASME **55**, 569–572 (1933).

[61] R. E. Bach, Selecting rc values for active filters, Electronics **33**, 82–85 (1960).

[62] B. J. Albers, T. C. Schwendemann, M. Z. Baykara, N. Pilet, M. Liebmann, E. I. Altman, U. D. Schwarz, Three-dimensional imaging of short-range chemical forces with picometre resolution, Nat Nanotechnol **4**(5), 307–310 (2009).

[63] Y. Gong, J. Xu, R. C. Buchanan, Surface roughness: A review of its measurement at micro-/nano-scale, Physical Sciences Reviews **3**(1), 20170057 (2018).

[64] U. Abou El-Atta, *Surface roughness assessment in three-dimensional machined surfaces for some manufacturing operations*, Ph.D. thesis, M. Sc. Thesis, Industrial Production Engineering Department, University of . . . (1991).

[65] T. Pancewicz, I. Mruk, Holographic contouring for determination of three-dimensional description of surface roughness, Wear **199**(1), 127–131 (1996).

[66] E. Kažukauskas, S. Butkus, V. Jukna, D. Paipulas, V. Sirutkaitis, Scanning algorithm optimization for achieving low-roughness surfaces using ultrashort laser pulses: A comparative study, Materials **16**(7), 2788 (2023).

[67] M. Harcarik, R. Jankovych, Relationship between values of profile and areal surface texture parameters, MM Science Journal **2016**, 1659–1662 (2016).

[68] E. Gadelmawla, M. Koura, T. Maksoud, I. Elewa, H. Soliman, Roughness parameters, Journal of Materials Processing Technology **123**(1), 133–145 (2002).

[69] International Organization for Standardization, Iso 4287: Geometrical product specifications (gps) - surface texture: Profile method - terms, definitions and surface texture parameters, https://www.iso.org/standard/53860.html, iSO standard 4287 (1997).

[70] N. D. Boscher, V. Vaché, P. Carminati, P. Grysan, P. Choquet, A simple and scalable approach towards the preparation of superhydrophobic surfaces – importance of the surface roughness skewness, J. Mater. Chem. A **2**, 5744–5750 (2014).

[71] M. Sedlaček, B. Podgornik, J. Vižintin, Correlation between standard roughness parameters skewness and kurtosis and tribological behaviour of contact surfaces, Tribology International **48**, 102–112, 14th Nordic Symposium on Tribology, NORDTRIB 2010 (2012).

[72] A. B. Meireles, F. de Souza Bastos, T. P. Cornacchia, J. A. Ferreira, E. B. de Las Casas, Enamel wear characterization based on a skewness and kurtosis surface roughness evaluation, Biotribology **1-2**, 35–41 (2015).

[73] International Organization for Standardization, Iso 25178-2: Geometrical product specifications (gps) surface texture: Areal, part 2: Terms, definitions and surface texture parameters, https://www.iso.org/standard/74591.html, iSO standard 25178-2:2021 (2021).

[74] J. Rudzitis, N. Bulaha, J. Lungevics, O. Linins, K. Berzins, Theoretical analysis of spacing parameters of anisotropic 3d surface roughness, Latvian Journal of Physics and Technical Sciences **54** (2017).

[75] A. P. Nagalingam, M. S. Vohra, P. Kapur, S. H. Yeo, Effect of cut-off, evaluation length, and measurement area in profile and areal surface texture characterization of as-built metal additive manufactured components, Applied Sciences **11**(11) (2021).

[76] K. Palová, T. Kelemenová, M. Kelemen, Measuring procedures for evaluating the surface roughness of machined parts, Applied Sciences **13**(16) (2023).

[77] International Organization for Standardization, Iso 4288: Gps – surface texture: Profile method. rules and procedures for the assessment of surface texture, https://www.iso.org/standard/2096.html, iSO standard 4288 (1996).

[78] International Organization for Standardization, Iso 3274: Geometrical product specifications (gps) surface texture: Profile method. nominal characteristics of contact (stylus) instruments, https://www.iso.org/standard/1916.html, iSO standard 3274 (1996).

[79] International Organization for Standardization, Iso 25178-3: Geometrical product specifications (gps) surface texture: Areal, part 3: Specification operators, https://www.iso.org/standard/42895.html, iSO standard 25178-3:2023 (2023).

[80] International Organization for Standardization, Iso 166110-1:2015 geometrical product specifications (gps) filtration: Overview and basic concepts, https://www.iso.org/standard/61375.html, iSO standard 16110-1 (2015).

[81] International Organization for Standardization, Iso 11562:1996 geometrical product specifications (gps) surface texture: Profile method, metrological characteristics of phase correct filters, iSO standard 11562:1996, howpublished=https://www.iso.org/standard/21977.html, (1996).

[82] J. Seewig, *Areal Filtering Methods* (Springer Berlin Heidelberg, Berlin, Heidelberg, 2013), 67–106.

[83] J. Raja, B. Muralikrishnan, S. Fu, Recent advances in separation of roughness, waviness and form, Precision Engineering **26**(2), 222–235 (2002).

[84] L. Skedung, M. Arvidsson, J. Y. Chung, C. M. Stafford, B. Berglund, M. W. Rutland, Feeling small: Exploring the tactile perception limits, Scientific Reports **3**(1), 2617 (2013).

[85] T. R. Thomas, *Rough surfaces* (Imperial College Press London, London, 1999), 2nd ed edition.

[86] S. W. Paddock, K. W. Eliceiri, *Laser Scanning Confocal Microscopy: History, Applications, and Related Optical Sectioning Techniques* (Springer New York, New York, NY, 2014), 9–47.

[87] A. D. Elliott, Confocal microscopy: Principles and modern practices, Current Protocols in Cytometry **92**(1), e68 (2020).

[88] M. Marvin, Microscopy apparatus (1961).

[89] S. T. Holmström, U. Baran, H. Urey, Mems laser scanners: a review, Journal of microelectromechanical systems **23**(2), 259–275 (2014).

[90] P. De Groot, Principles of interference microscopy for the measurement of surface topography, Advances in Optics and Photonics **7**(1), 1–65 (2015).

[91] D. Haas, D. Birnie, M. Zecchino, J. Figueroa, The effect of radial position and spin speed on striation spacing in spin on glass coatings, Journal of materials science letters **20**(19), 1763–1766 (2001).

[92] S. Adi, H. Adi, H.-K. Chan, P. M. Young, D. Traini, R. Yang, A. Yu, Scanning white-light interferometry as a novel technique to quantify the surface roughness of micron-sized particles for inhalation, Langmuir **24**(19), 11307–11312 (2008).

[93] E. Meyer, Atomic force microscopy, Progress in Surface Science **41**(1), 3–49 (1992).

[94] B. Voigtländer, *Introduction* (Springer International Publishing, Cham, 2019), 1–13.

[95] W. Sun, *Principles of Atomic Force Microscopy* (Springer Singapore, Singapore, 2018), 1–28.

[96] Y. Gong, J. Xu, R. Buchanan, Surface roughness: A review of its measurement at micro-/nano-scale, Physical Sciences Reviews **3** (2018).

[97] H.-J. BUTT, P. SIEDLE, K. Seifert, K. Fendler, T. SEEGER, E. BAMBERG, A. WEISENHORN, K. GOLDIE, A. Engel, Scan speed limit in atomic force microscopy, Journal of Microscopy **169**, 75 – 84 (2011).

[98] R. Leach, Chapter 6 - surface topography measurement instrumentation, in R. Leach (ed.), *Fundamental Principles of Engineering Nanometrology (Second Edition)* (William Andrew Publishing, Oxford, 2014), Micro and Nano Technologies, 133–204, second edition edition.

[99] W. Zhou, R. Apkarian, Z. L. Wang, D. Joy, Fundamentals of scanning electron microscopy (sem), in *Scanning microscopy for nanotechnology: techniques and applications* (Springer, 2006), 1–40.

[100] R. Le Harzic, D. Dörr, D. Sauer, M. Neumeier, M. Epple, H. Zimmermann, F. Stracke, Formation of periodic nanoripples on silicon and germanium induced by femtosecond laser pulses, Physics Procedia **12**, 29–36, lasers in Manufacturing 2011 - Proceedings of the Sixth International WLT Conference on Lasers in Manufacturing (2011).

[101] R. E. Russo, X. Mao, J. Yoo, J. Gonzalez, Chapter 3 - laser ablation, in J. P. Singh, S. N. Thakur (eds.), *Laser-Induced Breakdown Spectroscopy (Second Edition)* (Elsevier, Amsterdam, 2007), 41–70, second edition edition.

[102] D. F. Swinehart, The beer-lambert law, Journal of chemical education **39**(7), 333 (1962).

[103] M. Fox, *Optical properties of solids*, volume 3 (Oxford university press, 2010).

[104] V. Devanathan, et al., Electron energy bands in solids, Journal of Chennai Academy of Sciences **3**(1), 39–56 (2021).

[105] T. DiStefano, D. Eastman, The band edge of amorphous sio2 by photoinjection and photoconductivity measurements, Solid State Communications **9**(24), 2259–2261 (1971).

[106] L. A. Moore, C. M. Smith, Fused silica as an optical material, Optical Materials Express **12**(8), 3043–3059 (2022).

[107] A. L'HUILLIER, Multiple ionization of atoms through multiphoton absorption, Le Journal de Physique Colloques **48**(C9), C9–415 (1987).

[108] C. B. Schaffer, A. Brodeur, E. Mazur, Laser-induced breakdown and damage in bulk transparent materials induced by tightly focused femtosecond laser pulses, Measurement Science and Technology **12**(11), 1784–1794 (2001).

[109] M. R. Marks, K. Y. Cheong, Z. Hassan, A review of laser ablation and dicing of si wafers, Precision Engineering **73**, 377–408 (2022).

[110] L. Schlessinger, J. Wright, Inverse-bremsstrahlung absorption rate in an intense laser field, Physical Review A **20**(5), 1934 (1979).

[111] B. C. Stuart, M. D. Feit, S. Herman, A. Rubenchik, B. Shore, M. Perry, Nanosecond-to-femtosecond laser-induced breakdown in dielectrics, Physical review B **53**(4), 1749 (1996).

[112] A. Bogatskaya, Y. Gulina, N. Smirnov, I. Gritsenko, S. Kudryashov, A. Popov, An experimental study of multiphoton ionization in fused silica at ir and visible wavelengths, Photonics **10**(5) (2023).

[113] M. V. Ammosov, N. B. Delone, V. P. Krainov, Tunnel ionization of complex atoms and atomic ions in an alternating electromagnetic field, Soviet Physics JETP **64**(6), 1191–1194 (1986).

[114] M. Perry, B. Stuart, P. Banks, M. Feit, V. Yanovsky, A. Rubenchik, Ultrashort-pulse laser machining of dielectric materials, Journal of applied physics **85**(9), 6803–6810 (1999).

[115] A. Q. Wu, I. H. Chowdhury, X. Xu, Femtosecond laser absorption in fused silica: Numerical and experimental investigation, Physical Review B—Condensed Matter and Materials Physics **72**(8), 085128 (2005).

[116] M. Lebugle, N. Sanner, N. Varkentina, M. Sentis, O. Utéza, Dynamics of femtosecond laser absorption of fused silica in the ablation regime, Journal of Applied Physics **116**(6) (2014).

[117] S. Nolte, C. Momma, H. Jacobs, A. Tünnermann, B. N. Chichkov, B. Wellegehausen, H. Welling, Ablation of metals by ultrashort laser pulses, Journal of the Optical Society of America B **14**(10), 2716–2722 (1997).

[118] P. Balling, J. Schou, Femtosecond-laser ablation dynamics of dielectrics: basics and applications for thin films, Reports on Progress in Physics **76**(3), 036502 (2013).

[119] A. Ben-Yakar, A. Harkin, J. Ashmore, R. L. Byer, H. A. Stone, Thermal and fluid processes of a thin melt zone during femtosecond laser ablation of glass: the formation of rims by single laser pulses, Journal of Physics D: Applied Physics **40**(5), 1447 (2007).

[120] M. Saghebfar, M. Tehrani, S. Darbani, A. Majd, Femtosecond pulse laser ablation of chromium: experimental results and two-temperature model simulations, Applied Physics A **123**(1), 28 (2017).

[121] X. Zeng, X. Mao, R. Greif, R. Russo, Experimental investigation of ablation efficiency and plasma expansion during femtosecond and nanosecond laser ablation of silicon, Applied Physics A **80**(2), 237–241 (2005).

[122] S. Laville, F. Vidal, T. Johnston, M. Chaker, B. Le Drogoff, O. Barthelemy, J. Margot, M. Sabsabi, Modeling the time evolution of laser-induced plasmas for various pulse durations and fluences, Physics of Plasmas **11**(5), 2182–2190 (2004).

[123] M. Park, Y. Gu, X. Mao, C. P. Grigoropoulos, V. Zorba, Mechanisms of ultrafast ghz burst fs laser ablation, Science advances **9**(12), eadf6397 (2023).

[124] C. Wu, L. V. Zhigilei, Microscopic mechanisms of laser spallation and ablation of metal targets from large-scale molecular dynamics simulations, Applied Physics A **114**(1), 11–32 (2014).

[125] L. V. Zhigilei, Z. Lin, D. S. Ivanov, Atomistic modeling of short pulse laser ablation of metals: connections between melting, spallation, and phase explosion, The Journal of Physical Chemistry C **113**(27), 11892–11906 (2009).

[126] S. S. Harilal, J. R. Freeman, P. K. Diwakar, A. Hassanein, *Femtosecond Laser Ablation: Fundamentals and Applications* (Springer Berlin Heidelberg, Berlin, Heidelberg, 2014), 143–166.

[127] S. Li, S. Li, F. Zhang, D. Tian, H. Li, D. Liu, Y. Jiang, A. Chen, M. Jin, Possible evidence of coulomb explosion in the femtosecond laser ablation of metal at low laser fluence, Applied Surface Science **355**, 681–685 (2015).

[128] N. LaHaye, S. Harilal, P. Diwakar, A. Hassanein, P. Kulkarni, The effect of ultrafast laser wavelength on ablation properties and implications on sample introduction in inductively coupled plasma mass spectrometry, Journal of applied physics **114**(2) (2013).

[129] R. Stoian, D. Ashkenasi, A. Rosenfeld, E. Campbell, Coulomb explosion in ultrashort pulsed laser ablation of al 2 o 3, Physical review B **62**(19), 13167 (2000).

[130] P. Lorazo, L. J. Lewis, M. Meunier, Short-pulse laser ablation of solids: from phase explosion to fragmentation, Physical review letters **91**(22), 225502 (2003).

[131] M. V. Shugaev, M. He, Y. Levy, A. Mazzi, A. Miotello, N. M. Bulgakova, L. V. Zhigilei, Laser-induced thermal processes: heat transfer, generation of stresses, melting and solidification, vaporization, and phase explosion, in *Handbook of laser micro-and nano-engineering* (Springer, 2021), 83–163.

[132] M. He, C. Wu, M. V. Shugaev, G. D. Samolyuk, L. V. Zhigilei, Computational study of short-pulse laser-induced generation of crystal defects in ni-based single-phase binary solid–solution alloys, The Journal of Physical Chemistry C **123**(4), 2202–2215 (2019).

[133] S. V. Starikov, V. V. Pisarev, Atomistic simulation of laser-pulse surface modification: predictions of models with various length and time scales, Journal of Applied Physics **117**(13) (2015).

[134] M. V. Shugaev, L. V. Zhigilei, Thermodynamic analysis and atomistic modeling of subsurface cavitation in photomechanical spallation, Computational Materials Science **166**, 311–317 (2019).

[135] K. A. Laverty, B. D. Chalifoux, Ultrafast laser stress generation landscape in fused silica, Optics Express **33**(12), 24787–24799 (2025).

[136] F. Dahmani, A. W. Schmid, J. C. Lambropoulos, S. Burns, Dependence of birefringence and residual stress near laser-induced cracks in fused silica on laser fluence and on laser-pulse number, Applied optics **37**(33), 7772–7784 (1998).

[137] G. Torun, Y. Bellouard, Femtosecond laser interaction with ule® glass, Acta Materialia 122355 (2026).

[138] M. Bergler, K. Cvecek, F. Werr, M. Brehl, D. De Ligny, M. Schmidt, Cooling rate calibration and mapping of ultra-short pulsed laser modifications in fused silica by raman and brillouin spectroscopy, International Journal of Extreme Manufacturing **2**(3), 035001 (2020).

[139] J. E. Shelby, *Introduction to glass science and technology* (Royal society of chemistry, 2020).

[140] L. Skuja, H. Hosono, M. Hirano, Laser-induced color centers in silica, in *Laser-Induced Damage in Optical Materials: 2000* (SPIE, 2001), volume 4347, 155–168.

[141] H.-B. Sun, S. Juodkazis, M. Watanabe, S. Matsuo, H. Misawa, J. Nishii, Generation and recombination of defects in vitreous silica induced by irradiation with a near-infrared femtosecond laser, The Journal of Physical Chemistry B **104**(15), 3450–3455 (2000).

[142] A. Dwivedi, Recent advances in pulsed laser ablated plasma plumes: A review, Surface review and letters **14**(01), 57–69 (2007).

[143] D. Gupta, J. Kim, V. Kulagin, H. Suk, Laser pulse distortion in a plasma of the weakly relativistic regime, Laser Physics Letters **11**(5), 056003 (2014).

[144] D. Bäuerle, *Laser processing and chemistry* (Springer Science & Business Media, 2013).

[145] B. N. Chichkov, C. Momma, S. Nolte, F. von Alvensleben, A. Tünnermann, Femtosecond, picosecond and nanosecond laser ablation of solids, Applied Physics A **63**(2), 109–115 (1996).

[146] Y. Zhou, D. Wu, G. Luo, Y. Hu, Y. Qin, Efficient modeling of metal ablation irradiated by femtosecond laser via simplified two-temperature model coupling molecular dynamics, Journal of Manufacturing Processes **77**, 783–793 (2022).

[147] A. Žemaitis, P. Gečys, M. Gedvilas, High throughput and low surface roughness laser layer-by-layer milling using nanosecond (ns), picosecond (ps), and hybrid ns-ps pulses: A comparative study, Optics and Lasers in Engineering **176**, 108046 (2024).

[148] M. M. Mathew, R. N. Bathe, G. Padmanabham, R. Padmanaban, S. Thirumalini, A study on the micromachining of molybdenum using nanosecond and femtosecond lasers, The International Journal of Advanced Manufacturing Technology **104**(9), 3239–3249 (2019).

[149] O. Utéza, N. Sanner, B. Chimier, A. Brocas, N. Varkentina, M. Sentis, P. Lassonde, F. Légaré, J. Kieffer, Control of material removal of fused silica with single pulses of few optical cycles to sub-picosecond duration, Applied Physics A **105**(1), 131–141 (2011).

[150] N. Muhammad, D. Whitehead, A. Boor, W. Oppenlander, Z. Liu, L. Li, Picosecond laser micromachining of nitinol and platinum–iridium alloy for coronary stent applications, Applied Physics A **106**(3), 607–617 (2012).

[151] S. Prakash, S. Kumar, 6 - microchannel fabrication via direct laser writing, in J. P. Davim (ed.), *Microfabrication and Precision Engineering* (Woodhead Publishing, 2017), Woodhead Publishing Reviews: Mechanical Engineering Series, 163–187.

[152] A. Sassmannshausen, M. Kratz, F. Withake, D. Podkatilov, Laser ablation of optical glasses in the linear and non-linear absorption regime using ultrashort pulsed laser radiation from deep uv to ir, Journal of Laser Micro/Nanoengineering. Online journal (2026).

[153] C. Varghese, M. Ochoa, G. Hehl, O. Pronin, Ablation of transparent materials using 515 nm and 80 fs pulses., in *Laser Applications in Microelectronic and Optoelectronic Manufacturing (LAMOM) XXXI* (SPIE, 2026), PC138800O.

[154] L. EL Fissi, V. Xhurdebise, L. A. Francis, Effects of laser operating parameters on piezoelectric substrates micromachining with picosecond laser, Micromachines **6**(1), 19–31 (2015).

[155] R. Vilar, S. Sharma, A. Almeida, L. Cangueiro, V. Oliveira, Surface morphology and phase transformations of femtosecond laser-processed sapphire, Applied Surface Science **288**, 313–323 (2014).

[156] A. Žemaitis, P. Gecys, M. Barkauskas, G. Raciukaitis, M. Gedvilas, Highly-efficient laser ablation of copper by bursts of ultrashort tuneable (fs-ps) pulses, Scientific Reports **9**, 12280 (2019).

[157] B. Neuenschwander, B. Jaeggi, M. Schmid, V. Rouffiange, P.-E. Martin, Optimization of the volume ablation rate for metals at different laser pulse-durations from ps to fs, in *Proc. SPIE* (2012), volume 8243, 1–13.

[158] X. Li, H. Wang, B. Wang, Y. Guan, Machine learning methods for prediction analyses of 4H–SiC microfabrication via femtosecond laser processing, J. Mater. Res. Technol. **18**, 2152–2165 (2022).

[159] A. Caggiano, R. Teti, V. Alfieri, F. Caiazzo, Automated laser polishing for surface finish enhancement of additive manufactured components for the automotive industry, Prod. Eng. **15** (2020).

[160] D. F. Farson, H. W. Choi, B. Zimmerman, J. K. Steach, J. J. Chalmers, S. V. Olesik, L. J. Lee, Femtosecond laser micromachining of dielectric materials for biomedical applications, Journal of Micromechanics and Microengineering **18**(3), 035020 (2008).

[161] T.-L. Chang, Micromachining of microfluidic channels in glass by microjoule femtosecond laser pulses, Microelectronic engineering **110**, 450–456 (2013).

[162] A. Žemaitis, M. Gaidys, P. Gečys, G. Račiukaitis, M. Gedvilas, Rapid high-quality 3d micro-machining by optimised efficient ultrashort laser ablation, Optics and Lasers in Engineering **114**, 83–89 (2019).

[163] M. Domke, G. Piredda, J. Zehetner, S. Stroj, Minimizing the surface roughness for silicon ablation with ultrashort laser pulses, Journal of Laser Micro Nanoengineering **11**(1), 100 (2016).

[164] D. Kam, L. Shah, J. Mazumder, Femtosecond laser machining of multi-depth microchannel networks onto silicon, Journal of Micromechanics and Microengineering **21**(4), 045027 (2011).

[165] H. Le, P. Penchev, A. Henrottin, D. Bruneel, V. Nasrollahi, J. A. Ramos-de Campos, S. Dimov, Effects of top-hat laser beam processing and scanning strategies in laser micro-structuring, Micromachines **11**(2), 221 (2020).

[166] G. Račiukaitis, E. Stankevičius, P. Gečys, M. Gedvilas, C. Bischoff, E. Jäger, U. Umhofer, F. Völklein, Laser processing by using diffractive optical laser beam shaping technique., Journal of laser micro/nanoengineering **6**(1) (2011).

[167] O. Homburg, T. Mitra, Gaussian-to-top-hat beam shaping: an overview of parameters, methods, and applications, Laser Resonators, Microresonators, and Beam Control XIV **8236**, 62–70 (2012).

[168] H. Bai, J. G. Manni Sr, D. C. Muddiman, Transforming a mid-infrared laser profile from gaussian to a top-hat with a diffractive optical element for mass spectrometry imaging, Journal of the American Society for Mass Spectrometry **34**(1), 10–16 (2022).

[169] G. Pallier, J.-F. Poisson, Beam shaping to scale up microprocessing: Combining multiplane light conversion with an industrial femtosecond laser to increase performance, PhotonicsViews **20**(1), 32–35 (2023).

[170] N. Li, P. Fan, Q. Zhu, B. Cui, J.-F. Silvain, Y. F. Lu, Femtosecond laser polishing of additively manufactured parts at grazing incidence, Applied Surface Science **612**, 155833 (2023).

[171] K. L. Wlodarczyk, A. A. Lopes, P. Blair, M. M. Maroto-Valer, D. P. Hand, Interlaced laser beam scanning: a method enabling an increase in the throughput of ultrafast laser machining of borosilicate glass, Journal of Manufacturing and Materials Processing **3**(1), 14 (2019).

[172] C. Chen, C. K. Ng, F. Zhang, X. Xiong, B.-F. Ju, Y. Zhang, H. N. Hansen, Y.-L. Chen, Towards obtaining high-quality surfaces with nanometric finish by femtosecond laser ablation: A case study on coppers, Optics & Laser Technology **155**, 108382 (2022).

[173] S. Campanelli, A. Ludovico, C. Bonserio, P. Cavalluzzi, M. Cinquepalmi, Experimental analysis of the laser milling process parameters, J. Mater. Process. Technol. **191**(1), 220–223 (2007).

[174] J. Martin, 4 - glasses and ceramics, in J. Martin (ed.), *Materials for Engineering (Third Edition)* (Woodhead Publishing, 2006), 133–158, third edition edition.

[175] B. Deng, Y. Shi, F. Yuan, Investigation on the structural origin of low thermal expansion coefficient of fused silica, Materialia **12**, 100752 (2020).

[176] W. Bylsma, Spatial and frequency domain calculation of terrain roughness metric root-mean-square (rms), Technical report (2014).

[177] S. E. Hough, On the use of spectral methods for the determination of fractal dimension, Geophysical Research Letters **16**(7), 673–676 (1989).

[178] B. B. Mandelbrot, The fractal geometry of nature/revised and enlarged edition, New York (1983).

[179] H. E. Schepers, J. H. Van Beek, J. B. Bassingthwaighte, Four methods to estimate the fractal dimension from self-affine signals (medical application), IEEE Engineering in Medicine and Biology Magazine **11**(2), 57–64 (1992).

[180] R. F. Voss, Random fractals: Self-affinity in noise, music, mountains, and clouds, Physica D: Nonlinear Phenomena **38**(1-3), 362–371 (1989).

[181] C. L. Giusca, J. D. Claverley, W. Sun, R. K. Leach, F. Helmli, M. P. Chavigner, Practical estimation of measurement noise and flatness deviation on focus variation microscopes, CIRP Annals **63**(1), 545–548 (2014).

[182] B. E. A. Saleh, M. C. Teich, *Fundamentals of photonics; 2nd ed.*, Wiley series in pure and applied optics (Wiley, New York, NY, 2007).

[183] I. Saklakoglu, Kasman, Investigation of micro-milling process parameters for surface roughness and milling depth, International Journal of Advanced Manufacturing Technology **54**, 567–578 (2010).

[184] G. Schnell, U. Duenow, H. Seitz, Effect of laser pulse overlap and scanning line overlap on femtosecond laser-structured ti_6Al_4V surfaces, Materials **13**(4) (2020).

[185] L. Torrisi, A. Borrielli, D. Margarone, Study on the ablation threshold induced by pulsed lasers at different wavelengths, Nuclear Instruments and Methods in Physics Research Section B: Beam Interactions with Materials and Atoms **255**(2), 373–379 (2007).

[186] B.-Y. Cao, M. Chen, Z.-Y. Guo, Effect of surface roughness on gas flow in microchannels by molecular dynamics simulation, International Journal of Engineering Science **44**(13-14), 927–937 (2006).

[187] M. E. Thompson, S. R. Brown, The effect of anisotropic surface roughness on flow and transport in fractures, Journal of Geophysical Research: Solid Earth **96**(B13), 21923–21932 (1991).

[188] A. Rosenfeld, M. Lorenz, R. Stoian, D. Ashkenasi, Ultrashort-laser-pulse damage threshold of transparent materials and the role of incubation, Applied Physics A **69**(Suppl 1), S373–S376 (1999).

[189] A. Ben-Yakar, R. L. Byer, Femtosecond laser ablation properties of borosilicate glass, J. Appl. Phys. **96**(9), 5316–5323 (2004).

[190] T. Wang, J. Bian, X. Li, H. Kong, L. Wang, X. Wang, X. Sun, Enhanced absorptance of 45 steel by laser-induced periodic surface structures (lipss), Metals **10**(9) (2020).

[191] R. Buividas, M. Mikutis, S. Juodkazis, Surface and bulk structuring of materials by ripples with long and short laser pulses: Recent advances, Progress in Quantum Electronics **38**(3), 119–156 (2014).

[192] B. Jaeggi, S. Remund, R. Streubel, B. Goekce, S. Barcikowski, B. Neuenschwander, Laser micromachining of metals with ultra-short pulses: Factors limiting the scale-up process., Journal of Laser Micro/Nanoengineering **12**(3) (2017).

[193] M. Domke, V. Matylitsky, S. Stroj, Surface ablation efficiency and quality of fs lasers in single-pulse mode, fs lasers in burst mode, and ns lasers, Applied Surface Science **505**, 144594 (2020).

[194] J. Bonse, S. Höhm, S. V. Kirner, A. Rosenfeld, J. Krüger, Laser-induced periodic surface structures— a scientific evergreen, IEEE J. Sel. Top. **23**(3) (2017).

[195] F. Liang, R. Vallée, S. L. Chin, Physical evolution of nanograting inscription on the surface of fused silica, Opt. Mater. Express **2**(7), 900–906 (2012).

[196] F. Liang, R. Vallée, Physical origin of nanograting formation on fused silica with femtosecond pulses, Appl. Phys. Lett. **105**(13), 131904 (2014).

[197] W. M. Haynes, *CRC handbook of chemistry and physics* (CRC press, 2016).

[198] M. E. Shaheen, J. E. Gagnon, B. J. Fryer, Laser ablation of iron: A comparison between femtosecond and picosecond laser pulses, J. Appl. Phys. **114**(8), 083110 (2013).

[199] A. Abou-Saleh, E. Karim, C. Maurice, S. Reynaud, F. Pigeon, F. Garrelie, L. Zhigilei, J. Colombier, Spallation-induced roughness promoting high spatial frequency nanostructure formation on cr, Applied Physics A **124**(4), 308 (2018).

[200] F. Babadjanov, U. Specht, T. Lukasczyk, B. Mayer, Heat accumulation-induced surface structures at high degrees of laser pulse overlap on ti6al4v surfaces by femtosecond laser texturing, Materials **16**(6), 2498 (2023).

[201] T. Lippert, Interaction of photons with polymers: From surface modification to ablation, Plasma processes and polymers **2**(7), 525–546 (2005).

[202] J. Cao, G. Yang, J. Wang, S. Gao, Y. Lu, R. Sun, P. Yan, Enhanced optical absorption of monolayer ws2 using ag nanograting and distributed bragg reflector structures, Superlattices and Microstructures **112**, 218–223 (2017).

[203] A. Di Bucchianico, Coefficient of determination (r 2), Encyclopedia of statistics in quality and reliability (2008).

[204] F. Liang, R. Vallée, S. L. Chin, Mechanism of nanograting formation on the surface of fused silica, Optics express **20**(4), 4389–4396 (2012).

[205] A. Rudenko, J.-P. Colombier, T. E. Itina, From random inhomogeneities to periodic nanostructures induced in bulk silica by ultrashort laser, Physical Review B **93**(7), 075427 (2016).

[206] T. W. Hodapp, P. R. Fleming, Modeling topology formation during laser ablation, Journal of Applied Physics **84**(1), 577–583 (1998).

[207] R. O. Esenaliev, A. A. Oraevsky, V. S. Letokhov, A. A. Karabutov, T. V. Malinsky, Studies of acoustical and shock waves in the pulsed laser ablation of biotissue, Lasers in Surgery and Medicine **13**(4), 470–484 (1993).

[208] L. Savioja, U. P. Svensson, Overview of geometrical room acoustic modeling techniques, Journal of the Acoustical Society of America **138**(2), 708–730 (2015).

[209] F. G. Friedlander, The diffraction of sound pulses i. diffraction by a semi-infinite plane, Proceedings of the Royal Society A **186**(1006), 322–344 (1946).

[210] Q. Qin, K. Attenborough, Characteristics and application of laser-generated acoustic shock waves in air, Applied Acoustics **65**(4), 325–340 (2004).

[211] O. Koritsoglou, D. Loison, O. Uteza, A. Mouskeftaras, Characteristics of femtosecond laser-induced shockwaves in air, Opt. Express **30**(21), 37407–37415 (2022).

[212] S. P. Banerjee, Z. Chen, R. Fedosejevs, Femtosecond laser plasma plume characteristics in the nanojoule ablation regime, Journal of Applied Physics **113**(18) (2013).

[213] F. L. Pedrotti, L. M. Pedrotti, L. S. Pedrotti, *Introduction to optics* (Cambridge University Press, 2017).

[214] H. E. Bennett, J. O. Porteus, Relation between surface roughness and specular reflectance at normal incidence, J. Opt. Soc. Am. **51**(2), 123–129 (1961).

[215] E. Ukar, A. Lamikiz, L. López de Lacalle, D. del Pozo, J. Arana, Laser polishing of tool steel with co2 laser and high-power diode laser, International Journal of Machine Tools and Manufacture **50**(1), 115–125 (2010).

[216] T. L. Perry, D. Werschmoeller, X. Li, F. E. Pfefferkorn, N. A. Duffie, Pulsed laser polishing of micro-milled ti6al4v samples, Journal of Manufacturing Processes **11**(2), 74–81 (2009).

[217] A. Sassmannshausen, A. Brenner, J. Finger, Ultrashort pulse laser polishing by continuous surface melting, Journal of Materials Processing Technology **293**, 117058 (2021).

[218] F. E. Pfefferkorn, N. A. Duffie, X. Li, M. Vadali, C. Ma, Improving surface finish in pulsed laser micro polishing using thermocapillary flow, CIRP Annals **62**(1), 203–206 (2013).

[219] S. Kou, C. Limmaneevichitr, P. Wei, Oscillatory marangoni flow: a fundamental study by conduction-mode laser spot welding, Welding Journal **90**(12), 229–240 (2011).

[220] E. V. Bordatchev, A. M. K. Hafiz, O. R. Tutunea-Fatan, Performance of laser polishing in finishing of metallic surfaces, The International Journal of Advanced Manufacturing Technology **73**(1), 35–52 (2014).

[221] C. Weingarten, A. Schmickler, E. Willenborg, K. Wissenbach, R. Poprawe, Laser polishing and laser shape correction of optical glass, Journal of Laser Applications **29**(1), 011702 (2017).

[222] C. Weingarten, S. Heidrich, Y. Wu, E. Willenborg, Laser polishing of glass, in J. L. Bentley, S. Stoebenau (eds.), *Optifab 2015*, International Society for Optics and Photonics (SPIE, 2015), volume 9633, 963303.

[223] R. M. Meffert, B. Langer, M. E. Fritz, Dental implants: a review, J Periodontol **63**(11), 859–870 (1992).

[224] M. Bereznai, I. Pelsöczi, Z. Tóth, K. Turzó, M. Radnai, Z. Bor, A. Fazekas, Surface modifications induced by ns and sub-ps excimer laser pulses on titanium implant material, Biomaterials **24**(23), 4197–4203 (2003).

[225] M.-H. Lai, K. S. Lim, D. S. Gunawardena, Y.-S. Lee, H. Ahmad, Co2 laser applications in optical fiber components fabrication and treatment: A review, IEEE Sensors Journal **17**, 2961–2974 (2017).

[226] A. Žemaitis, M. Gaidys, P. Gečys, M. Barkauskas, M. Gedvilas, Femtosecond laser ablation by bibursts in the mhz and ghz pulse repetition rates, Opt. Express **29**(5), 7641–7653 (2021).

[227] W. Becker, *Advanced time-correlated single photon counting techniques* (Springer, 2005).

[228] M. Barkauskas, K. Neimontas, V. Butkus, Device and method for generation of high repetition rate laser pulse bursts, https://patents.google.com/patent/US11276985B2/en, uS Patent 11,276,985 B2 (2022).

[229] International Organization for Standardization, Geometrical product specifications (gps)—surface texture: Areal—part 1: Definitions and surface texture parameters, ISO 25178-1:2016, geneva, Switzerland (2016).

[230] Y. Huang, S. Liu, W. Yang, C. Yu, Surface roughness analysis and improvement of pmma-based microfluidic chip chambers by co2 laser cutting, Applied surface science **256**(6), 1675–1678 (2010).

[231] G. Chen, J. Qiao, Femtosecond-laser-enabled simultaneous figuring and finishing of glass with a subnanometer optical surface, Opt. Lett. **47**(15), 3860–3863 (2022).

[232] P. K. Sahoo, T. Feng, J. Qiao, Dynamic pulse propagation modelling for predictive femtosecond-laser-microbonding of transparent materials, Optics express **28**(21), 31103–31118 (2020).

[233] G. Chen, J. Qiao, Optical structuring and finishing toward mid-spatial-frequency errorreduction using femtosecond lasers, Opt. Lett. **49**(6), 1560–1562 (2024).

[234] G. Chen, M. A. Qadeer, J. C. Lambropoulos, J. Qiao, Fabrication of microprism arrays using direct femtosecond-laser figuring and finishing, Opt. Express **33**(11), 23252–23259 (2025).

[235] M. A. Qadeer, J. Qiao, Femtosecond laser figuring of freeform optics using iterative tool path optimization, in *Laser Applications in Microelectronic and Optoelectronic Manufacturing (LAMOM) XXXI* (SPIE, 2026), PC1388006.

[236] C. Otieno, J. Qiao, Femtosecond laser figuring and polishing of fused silica with ghz-burst mode, Opt. Mater. Express **15**(7), 1510–1519 (2025).

[237] E. Kažukauskas, S. Butkus, T. Latvys, V. Jukna, D. Paipulas, Spectral domain analysis of surface roughness evolution during femtosecond laser deep engraving of glass, Opt. Express **34**(6), 10334–10350 (2026).

[238] M. Gaidys, A. Žemaitis, P. Gečys, M. Gedvilas, Efficient surface polishing using burst and biburst mode ultrafast laser irradiation, RSC advances **13**(6), 3586–3591 (2023).

[239] H. Zhong, T. Zou, Z. Huang, K. Xu, X. Sun, C. Wang, J. Yang, W. Deng, Z. Zhang, Frequency-selective smoothing of amorphous silicon via femtosecond laser polishing, in *11th International Symposium on Advanced Optical Manufacturing and Testing Technologies (AOMATT 2025)* (SPIE, 2026), volume 13992, 441–447.

[240] L. Leggio, Y. Di Maio, A. Pascale-Hamri, G. Egaud, S. Reynaud, X. Sedao, C. Mauclair, Ultrafast laser patterning of metals commonly used in medical industry: Surface roughness control with energy gradient pulse sequences, Micromachines **14**(2) (2023).

[241] A. A. Tseng, Y.-T. Chen, C.-L. Chao, K.-J. Ma, T. Chen, Recent developments on microablation of glass materials using excimer lasers, Optics and Lasers in Engineering **45**(10), 975–992 (2007).

[242] Y.-T. Chen, K. Naessens, R. Baets, Y.-S. Liao, A. A. Tseng, Ablation of transparent materials using excimer lasers for photonic applications, Optical Review **12**(6), 427–441 (2005).

[243] A. Gusarov, M. Pavlov, I. Smurov, Residual stresses at laser surface remelting and additive manufacturing, Physics Procedia **12**, 248–254, lasers in Manufacturing 2011 - Proceedings of the Sixth International WLT Conference on Lasers in Manufacturing (2011).

Curriculum Vitae

Name: Evaldas
Surname: Kažukauskas

Education

2016–2020	Vilnius University, Faculty of Physics Bachelor's degree in Applied Physics
2020–2022	Vilnius University, Faculty of Physics Master's degree in Laser Technologies
2022–Present	Vilnius University, Faculty of Physics PhD studies in Physics

Work Experience

2019-2020	Quality Assurance Analyst at Eksma Optics
2020-2022	Project Specialist at Vilnius University, Laser Research Center
2023-2023	Junior Assistant at Vilnius University, Laser Research Center
2022-Present	Application Engineer at Akoneer
2022-Present	Junior Researcher at Vilnius University, Laser Research Center

Research Projects

2020–2022	**SMART** (Project No. 01.2.2-LMT-K718-03-0029) Research Council of Lithuania (LMT) Investigated UV femtosecond laser processing and its influence on surface roughness.
2024–Present	**SURFEMTEC** (Project No. S-MIP-24-105) Research Council of Lithuania (LMT) Research on surface roughness development and control during multilayer femtosecond laser ablation.

Internships and Research Visits

2023 08 27 – 09 02	Summer school “Trends and New Developments in Laser Technology” (Germany)
2025 04 15 – 06 15	Visiting Researcher, Shizuoka University (Japan)

Acknowledgements

I would like to express my sincere gratitude to my supervisor, dr. Simas Butkus, for his continuous guidance, support, and valuable feedback throughout the course of this work. Furthermore, I would like to thank dr. Vytautas Jukna, whose assistance was invaluable throughout my PhD, both in terms of advice and direct contributions. Additionally, I am grateful for the advice and feedback provided by all other academic colleagues, including but not limited to Domas Paipulas, Valdemar Stankevič, Paulius Gečys, Darius Gailevičius, Mangirdas Malinauskas, and others.

Special thanks go to the head of the institute, dr. Dalia Kaškelytė, who cared for us PhD candidates as if we were her own children, offering encouragement and support in every possible way. On the same note, I'd like to express my gratitude to prof. Vygantas Mizeikis, who took care of me during my research visit in Shizuoka University. Being able to have daily coffee talks in Lithuanian while being in Japan, made 12,000 km distance feel less heavy.

Next, I would like to express my deepest gratitude to my fellow PhD candidates and members of the Zenius Committee — Ignas Lūkošiūnas, Jonas Banys, and Marius Navickas. The coffee talks, lunch breaks, and doing the most ridiculous things together helped lift the weight of the PhD and made these four years much more enjoyable - Whee.

Last but not least, I thank my family for supporting and believing in me. My friends, colleagues, former and present students for the encouraging words and finally, I am deeply grateful to my partner, Milda, for her love, care, and unwavering support.

Evaldas Kažukauskas
2026, Vilnius

Notes

Notes

Notes

Vilnius University Press
Saulėtekio av. 9, Bld. III, LT-10222 Vilnius
e-mail: info@leidykla.vu.lt, www.leidykla.vu.lt
bookshop.vu.lt, journals.vu.lt
Print run copies 20